# Investigation on natural and synthetic polymers as an aqueous binder for anodes of lithium-ion batteries (LIBs)

THESIS
SUBMITTED IN PARTIAL FULFILMENT OF THE REQUIREMENTS
FOR THE AWARD OF THE DEGREE OF

*Doctor of Philosophy*

IN CHEMISTRY

By

**V. V. N. Phanikumar**
(Roll No. 701450)

RESEARCH SUPERVISORS

**Dr. K. V. Gobi**

**Professor, NITW**

**Dr. R. Prakash**

**Scientist - F, ARCI**

**Department of Chemistry**
**NATIONAL INSTITUTE OF TECHNOLOGY WARANGAL**
**WARANGAL-506004, TELANGANA, INDIA**
**January 2021**

# DECLARATION

This is to declare that the work presented in the thesis entitled ***"*Investigation on natural and synthetic polymers as an aqueous binder for anodes of lithium-ion batteries (LIBs)*"*** is a bonafide work done by me under the supervision of **Dr. R. Prakash**, Scientist 'F', Centre for Automotive Energy Materials, ARCI, Chennai and **Prof. K. V. Gobi**, Professor, Department of Chemistry, NIT Warangal and was not submitted elsewhere for the award of any degree.

I declare that this written submission represents my ideas in my own words and where others ideas or words have been included, I have adequately cited and referenced the original sources. I also declare that I have adhered to all principles of academic honesty and integrity and have not misrepresented or fabricated or falsified any idea/data/fact/source in my submission.

I understand that any violation of the above will be a cause for disciplinary action by the institute and can also evoke penal action from the sources which have thus not been properly cited or from whom proper permission has not been taken when needed.

V. Phanikumar

Date: 18-01-2021 **(V. V .N. Phanikumar)**

Place: **Chennai** Roll Number: **701450**

# CERTIFICATE

This is to certify that the work presented in the thesis entitled ***"*Investigation on natural and synthetic polymers as an aqueous binder for anodes of lithium-ion batteries (LIBs)*"*** is a bonafide work carried out by **Mr. V. V. N. Phanikumar** under our supervision and was not submitted elsewhere for the award of any degree.

Signature of the thesis Supervisor
**Dr. R. Prakash**
Scientist - F, Team Leader
Centre for Automotive Energy Materials,
ARCI, Chennai

Signature of the thesis Supervisor
**Dr. K. V. Gobi**
Professor
Department of Chemistry
NIT Warangal

# ACKNOWLEDGEMENTS

It is with immense pleasure that I express my deep sense of gratitude to my supervisors ***Dr. R. Prakash***, ARCI, Chennai and ***Prof. K. V. Gobi***, National Institute of Technology, Warangal for their inspiring guidance and invaluable cooperation in the course of my research. The fruitful discussions I had with them on the subject gave me the needed insight into the subject and were very helpful in the preparation of this thesis. I consider myself as very fortunate for being their student and it would have been impossible to achieve this goal without their support and care.

I am grateful to ***The Directors***, International Advanced Research Centre for Powder metallurgy and New materials (ARCI), Hyderabad and National Institute of Technology, Warangal for giving me the opportunity to carry out the work and allowing me to submit in the form of thesis. I would like to thank ***Dr. R. Gopalan***, Regional Director, ARCI, Chennai and Associate Directors of ARCI, Hyderabad for their encouragement and constant support. I am also grateful to former director of ARCI, Dr. G. Sundararajan for his valuable support by all means.

I greatly acknowledge Department of Science and Technology, Govt. Of India for the financial support under Grant number (TRC project AI/1/65/ARCI/2014 (C)).

I express my gratitude to the Doctoral Scrutiny Committee members, namely ***Dr. Vishnu Shanker***, Chairman and Head, Department of Chemistry, NIT Warangal, ***Dr. Raghu Chitta***, Department of Chemistry, NIT Warangal and ***Dr. Bonta Srinivasa Rao***, Department of Metallurgical & Materials Engineering, NIT Warangal for their fruitful suggestions. I specially thank ***Prof. B. V. Appa Rao***, Retired Professor and my former mentor for his constant encouragement and valuable suggestions. I also thank to other faculty members from the Department of Chemistry, namely, ***Prof. A. Ramachandraiah, Prof. V. Rajeshwar Rao, Dr. Venkatathri Narayanan, Dr. D. Kashinath, Dr. B. Srinivas, Dr. K. Hari Prasad, Dr. S. Nagarajan, Dr. Ch. Jugun Prakash, Dr. Ravinder Pawar, Dr. Mukul Pradhan, Dr. Rajeshkhanna Gaddam, Dr. V. Rajeshkumar*** and all the other faculty members for their valuable advice and encouragement throughout the research work.

I would like to extend my sincere gratitude to ***Dr. N. Rajalakshmi, Dr. T. Mohan, Dr. D. Sivaprahasam, Dr. M. B. Sahana, Dr. D. Prabhu, Dr. Manjusha Battabyal, Dr. S. Kavita,***

***Dr. Bijoy Kumar Das, Dr. K. Ramya, Dr. R. Balaji, Dr. V. Raman, Dr. Sathiya Mariyappan, Dr. Thrinath Reddy, Dr. M. Pavana, Dr. Sonia, Dr. S. R. Sahu, Dr. N. Sasikala, Dr. S. Bhuvaneshwari, Dr. K. Nannaji, Dr. Manjula reddy, Mrs. N. Aparna Rao, Mr. A. Srinivasa Rao*** and ***Prof. U.V. Varadaraju*** for their motivation in all regards.

I would like to express my concern to other colleagues and friends of ARCI namely, *R. Vallabha Rao, L. Babu, S. Vasu, K. Kumari, P. Lakshman Mani Kanta, P. Mahender, Ravi Gautam, V. V. Ramakrishna, M. Siva kumar, M. Venkatesh, Vijaya ragavan, B. Priyadarshini, G. Mrinalini, S. Harish, B. Jayachandran, B. Prasanth, V. Trivedi, D. Nikhil, G. Priya, A. R. Dilipan, T. Ramesh, J. Prithi, R. Archana, Ramya, and K. Tanuja*.

I would like to thank *K. Shanmugam, T. P. Sarangan, Sivaraj, Sambhu Jana, Gowtham, Debendranath, Vignesh, and Kannadasan,* for their support during experiments and characterizations. Further I also show my special thanks to *Mr. Sampath kumar, Mr. Bhargavan, Mrs. Geeta,* and *Mrs. Vijayalakshmi*.

I convey my special thanks from the bottom of my heart to my NIT-Warangal friends *Dr. K. Chaitanya Kumar, Dr. M. Narsimha Reddy, Dr. K. Vimal Kumar, Dr. K. Koteshwara Reddy, Dr. M. Satyanarayana, Dr. K. Yugender Goud, Dr. V. Sunil, Dr. E. Hari Mohan, Dr. Vikram Sagar, Dr. A. Varun, Mr. K. Shekher, Mr. K. Sampath, Mrs. S. Manasa, Ms. G. Aarti and Mrs. Divya.*

I also owe my gratitude to all my family members for my professional and personal life, without them my journey is unachievable. I am also privilege to thank my mother, father, sister, brother-in-law, niece, nephew, wife and daughter in this journey.

Finally, a big thanks to the Almighty God, who has blessed me in the heavenly realms, which helped me a lot to work for hours together tirelessly.

V. Phanikumar

Date: 18-01-2021 **(V. V .N. Phanikumar)**

# CONTENTS

# Table of contents

# LIST OF SYMBOLS AND ABBREVIATIONS

LIBs : Lithium-ion Batteries
PVDF : Polyvinylidene difluoride
PTFE : Polytetrafluoroethylene
NMP : N-methyl-2-pyrrolidone
SEM : Scanning Electron Microscopy
TEM : Transmission Electron Microscopy
XPS : X-ray Photoelectron Spectroscopy
XRD : X-ray Diffraction
TGA : Thermogravimetric analysis
CV : Cyclic Voltammetry
CA : Contact angle
CD : Charge/Discharge
ED : Energy Density
$mAh\ g^{-1}$ : Milli ampere Hour Per Gram
V : Volt
$mV\ s^{-1}$ : Millivolt per Second
EIS : Electrochemical Impedance Spectroscopy
EDLC : Electrical double layer capacitor
EDS : Energy Dispersive X-ray spectroscopy
CPE : Constant Phase Element
Cdl : Double layer capacitance
SEI : Solid electrolyte interface
eV : Electron Volt
Z' : Real Impedance
Z" : Imaginary Impedance
W : Warburg Impedance
$R_{ct}$ : Charge Transfer Resistance

$R_s$ : Solution Resistance

Ω : Ohm

ºC : Degree Celsius

PVA : Polyvinyl Alcohol

Na-Alg : Sodium Alginate

TKP : Tamarind kernel powder

FG : Fenugreek powder

CMC : Carboxy methyl cellulose

SBR : Styrene butadiene rubber

mg : milligram

s : Seconds

h : Hour

i : Current

mA : Milliampere

mV : Millivolt

µA : Microampere

M : Molarity

υ : Scan Rate

cm : Centimeter

nm : Nanometer

Tg : Glass transition temperature

# Chapter 1

# Introduction

# 1. Introduction

Universally, the living standards of human race are changing day by day, due to the presence of the enormous technologies in the concerned field. At most, all the adept technologies are converted to products only by manufacturing in industries. To run those industries, energy is a vital source without any interruption to scale up the required products and to utilize workforce and machinery efficiently. For all the deeds, energy sector is forefront in the form of oil, coal, and also by renewable energies like solar and wind. Specifically, efficient and sustainable energy storage systems are highly focused arenas. For electrochemical energy storage, rechargeable batteries, electrochemical double layer capacitors (EDLCs) as well as electrochemical supercapacitors are considered to be the feasible technologies [1]. Explicitly, above all the rechargeable batteries, lithium-ion batteries (LIBs) have been deployed widely worldwide in various electronic devices as well as in electric vehicle (EV) applications because of the lightweight, lower self-discharge, no memory effect, high energy density and prolonged cyclic life as compared to other existing rechargeable batteries [2-3]. Hence, lithium-ion batteries are represented as preferred energy storage systems as compared to other available energy systems. In addition, different energy storage systems further can be elucidated by Ragone plot (Specific power vs Specific energy) [4] as shown in Fig. 1.1. Based on these advantages, LIBs have become the most successful energy storage devices for the on-road as well as off-road applications i.e., EVs, digital gadgets like smartphones and laptops etc. Although these batteries have high attention in the current market, the tendency has been changing for the further development towards high energy density and better power density along with prolonged cyclic life. As of now, these batteries are able to deliver the energy density of 250-693 Wh/l and specific energy of 100-265 Wh/kg for a cyclic stability of ~ 2000 cycles in the potential range of 3.60-3.85 V. The output criteria for the energy density and cycle number will be differed by changing the active material and its composition. Furthermore, in the realistic conditions, many companies do make their own auto engineering in view of extended cyclic stability of the batteries.

The research is systematically focused on exploring the high energy density with better cyclic stability for various types of LIBs. To achieve this, the development of active electrode materials, enhancement in electrolyte voltage window and cost-effective binders are of high concern research fields to meet the required criteria. In addition, once the active materials were decided to make the cell or battery, the next main objective is fabrication of the respective electrodes. In LIBs, the electrode fabrication method can be done in two ways: 1) Non-Aqueous binder method, and 2) Aqueous binder method.

Non-Aqueous binder method: In this method, active material, conductive carbon and binder (Polyvinylidene difluoride) (PVDF) are dispersed in an organic solvent i.e., 1-methyl-2-pyrrolidone (NMP) to prepare a homogenous slurry. After the preparation, the slurry is casted on respective foil for the required thickness and subsequently dried in an oven at a temperature of 120 °C.

Aqueous binder method: In this method, active material, conductive carbon and aqueous binders are dispersed in aqueous media i.e., Water is used to prepare the homogenous slurry. After the preparation, the slurry is casted on respective foil for the required thickness and subsequently dried in an oven at a temperature of 120 °C.

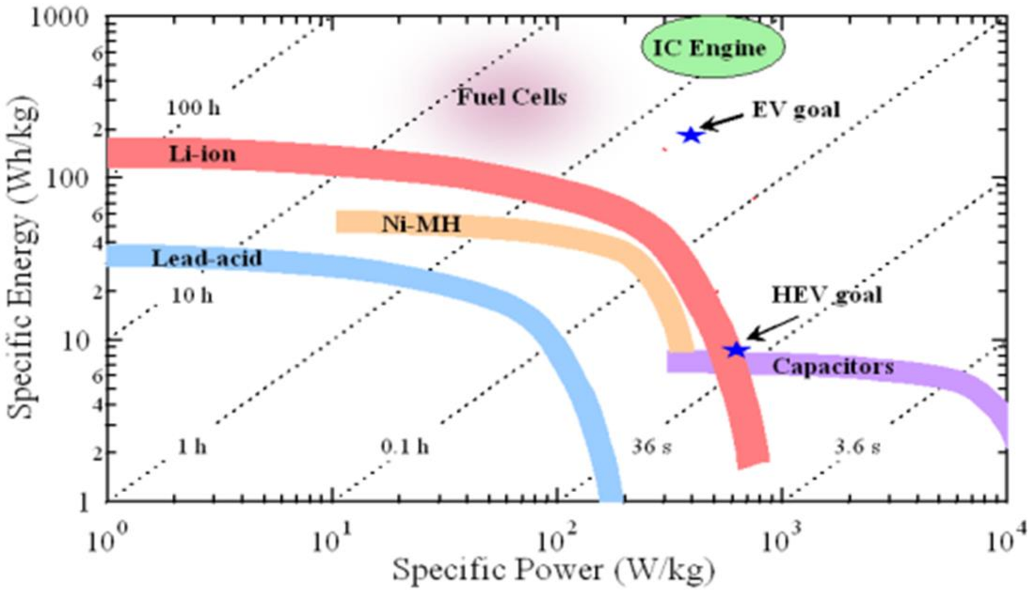

Figure 1.1. Ragone plot for different energy storage solutions

### 1.1. Principle of lithium-ion battery

Typically, the lithium-ion battery consists of four main components such as cathode, anode, separator and the electrolyte [5]. The charge/discharge mechanism of LIB is represented in Fig. 1.2. During the charge process, both electrodes are connected to an external power supply. Thus, the electrons do move from cathode to anode through the circuit, and, at the same time, lithium-ions would travel in the same direction through the electrolyte from cathode to anode. By this process, the external energy is electrochemically stored in battery in the form of chemical energy in electrode materials with a difference in electrochemical potential. Further, the opposite action takes place during the discharge process: electrons do move from anode to the cathode via the external load to carry the work and lithium-ion moves from anode to cathode in the electrolyte. This process is called as rocking chair mechanism, where the lithium-ion shuffles between the cathode and anode during the charge/discharge cycles. However, the electrochemical reactions at the two electrodes open the stored chemical potential energy. A change in Gibbs free energy is noticed due to the electrochemical reactions on the two electrodes depends on the electrode materials selected. Hence, the energy of the overall electrochemical reaction can be estimated using the theoretical cell voltage, as $\Delta E = -\Delta G/nF$.

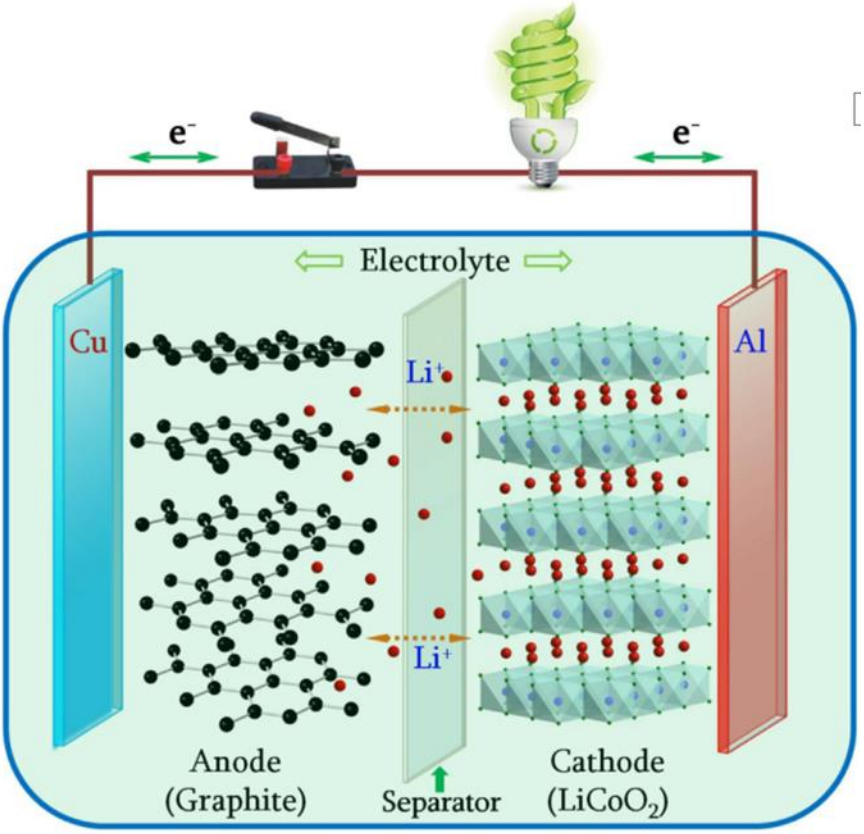

**Figure 1.2.** Charge/ discharge mechanism of LIB

The theoretical capacity of the materials can also be calculated based on the electrochemical reactions involved. For an instance, the cathode of $LiCoO_2$ with 50% of lithium-ion and corresponding electrons transferred would give the capacity, as shown in Eqn. 1.1.

$$LiCoO_2 \leftrightarrow 0.5\ Li^+ + 0.5\ e^- + Li_{0.5}CoO_2 \text{ ------------------ } 1.1$$

The theoretical specific capacity ($C_{specific}$) calculation is as given below.

$$\text{Specific capacity} = \frac{x\text{F}}{\text{nM}} = \frac{0.5 \times 96485\ \text{C/mol}}{1 \times\ 98\ \text{g/mol}} = 137\ \text{mAh g}^{-1}$$

In the case of anode, i.e., graphite can intercalate with lithium reversibly to form $LiC_6$ as given in Eqn. 1.2.

$$Li^+ + e^- + C_6 \leftrightarrow LiC_6 \text{ -------------------------------------- } 1.2$$

The theoretical specific capacity calculation is as given below.

$$\text{Specific capacity} = \frac{x\text{F}}{\text{nM}} = \frac{1 \times 96485\ \text{C/mol}}{6 \times\ 12\ \text{g/mol}} = 372\ \text{mAh g}^{-1}$$

where $x$ is number of electrons transferred in Eqn. 1.1 and 1.2 (0.5 and 1, respectively), $F$ = 96,485 C/mol is Faraday's constant, n is number of moles of a chosen electroactive material that take place in the reaction, and $M$ is the molecular weight of the same electroactive material. Furthermore, to find the specific capacity of the lithium-ion cell or battery, the other factors involved also need be taken into the consideration, other than the cathode and anode materials. The other vital components of the battery are binder, conductive carbon, separator, electrolyte, current substrates, tabs and battery management system (BMS). Thus, the practical capacity is always lesser than the theoretical capacity of battery [6].

## 1.2. Requirements and challenges of lithium-ion battery

Mileage is major requirement for EVs, and it again depends on gravimetric and volumetric capacities. Space and weight are further limitations to LIBs. Although LIBs have highest energy densities, still they are inferior to the gasoline. Hence, large number of batteries is required to meet the 200 to 300 mileage range. Batteries such as Lithium-Sulphur and Li-$O_2$ possess highest energy densities, but they do suffer from other issues like safety and low cyclic life. The cost of the batteries is main challenge for EV technology; hence the reduction of battery cost is highly prioritized to make inexpensive batteries. It is estimated that the cost of battery pack and cell would be \$125 and \$100 per kWh. These prices can be reduced further by innovative engineering or by indigenous supply source of raw materials. From the materials side also, the cost of the battery can be cut down, if cobalt-based materials are replaced with other metals. The absence of cobalt can lead to thermal issues and specific capacity reduction during the cycling. Hence, challenge does lie to minimize the battery cost by keeping an equivalent performance [7].

Fast charging and power factors are considerably challenged for LIBs. At present, electric vehicles take long time for charging, hence it is always an obstacle for long distance drive which require the battery charging several times. Currently, EVs have improvised the charge capability and reduced the charging time effectively. Lithium ions will transfer between cathode and anode during charge/discharge cycles, and their speed is controlled by intercalation rate and diffusivity of lithium-ions. High charging rate guides the lithium plating at anode side, which further escalates the raise in cell temperature. In addition, optimized charge programme allows quick charge by not hampering the battery life and safety of the future EVs. The power factor is also crucial concern for the EV utility. The influence of power is crucial for heavy duty vehicles with different power requirements. Other aspect of LIBs is its performance in different climatic conditions. Electrochemical performance is always being affected with environmental conditions, especially at high temperatures. High and low temperatures do cause the change in the solid electrolyte interface (SEI) thicknesses, which pave way for low cyclic life and lithium plating in LIBs at different environmental conditions. Hence, thermal management is optimal method to regulate the batteries at different working conditions to prolong the cyclic life and rate capability of the batteries [8].

## 1.3. Literature survey on lithium-ion battery materials like cathode, anode, binders and electrolyte

### 1.3.1. Literature survey on cathode materials

The cathode materials are highly crucial in terms of energy to power density, cycling life and safety issues. These are broadly classified into three major types, such as intercalation/de-intercalation, alloying/de-alloying and conversion-based materials. The importance has mainly been given for the intercalation-based materials. Among the intercalation materials, Lithium cobalt dioxide ($LiCoO_2$, layered structure), Lithium iron phosphate ($LiFePO_4$, olivine family), Lithium nickel manganese cobalt dioxide ($LiNi_{0.33}Mn_{0.33}Co_{0.33}O_2$, layered structure), Lithium manganese tetraoxide ($LiMn_2O_4$, spinel oxides), $LiMn_{1.5}Ni_{0.5}O_4$ (spinel oxides) and Lithium nickel cobalt aluminium dioxide ($LiNiCoAlO_2$, layered structure) are mostly being used cathode materials in LIBs [9]. The crystal structure and properties of these materials are illustrated in Fig. 1.3 and in Table 1.1.

**Table 1.1.** Properties of various cathode intercalation materials

| **Type of frame work** | **Material** | **Theoretical / Practical capacity (mAh g$^{-1}$)** | **Average potential (V Vs. Li/Li$^+$)** |
|---|---|---|---|
| Layered | $LiCoO_2$ | 272/140 | 4.2 |
| Layered | $LiNi_{0.33}Mn_{0.33}Co_{0.33}O_2$ | 272/200 | 4.0 |
| Spinel | $LiMn_2O_4$ | 148/120 | 4.1 |
| Spinel | $LiMn_{1.5}Ni_{0.5}O_4$ | 148/120 | 4.7 |
| Olivine | $LiFePO_4$ | 170/160 | 3.4 |

### 1.3.2. Layered compounds ($LiMO_2$, M = Co)

It is as same as to the layered α-$NaFeO_2$ with a space group of R3m. In this compound, the oxygen ions are close-packed in a cubic arrangement, where cobalt and lithium ions have occupied in octahedral sites of alternating layers with an ABCABC system, called the O3-type structure, as depicted in Fig. 1.3. The cobalt is adopted with trivalent electronic configuration $(t_{2g})^6$ $(e_g)^0$ of low spin state S = 0. Besides, this layered oxide is in rhombohedral symmetry containing lithium in 3a, cobalt in 3b, and oxygen in 6c sites. The unit cell of the hexagonal crystal contains three formula units. During the electrochemical cycling, the lithium-ions are reversibly shuffled into the framework by creating vacancies within the lithium planes, as shown in Fig. 1.3. The formed vacancies are responsible for driving electronic transitions in lithium cobalt dioxide and organizing the ordered lithium vacancy structures on a triangular lattice of sites. In this compound, no coupling between cobalt $e_g$ and Li:2s energy levels occur and the lowest energy would reach in the interplanar stacking that leads to as many equivalent Co sites as possible. The cobalt (+3 and +4 oxidation states) has a tendency for charge delocalization at x = 0.5. It also has an intermediate oxidation state of +3.5, which is responsible for the monoclinic structure [9]. Even more, the $LiCoO_2$ suffers from dissolution of the metal ion in the electrolyte which induces the oxygen release. However, this will suppress by adopting metal oxide coating like $ZrO_2$, $Al_2O_3$, $TiO_2$ etc.

### 1.3.3. Spinel compound ($LiMn_2O_4$)

The spinel compound has $A[B_2]O_4$ spinel type system and crystallizes in the Fd3m space group with the cubic lattice parameter a = 8.239 Å. This spinel compound describes Mn and Li cations on the 16d and 8a sites and the oxygen ions are situated on the 32e sites, which form almost similar to cubic close packed (ccp) sublattice. The half of the octahedral sites are occupied with Mn ions forming a three-dimensional framework of edge sharing $MnO_6$ octahedra. The lithium-ions are at tetrahedral sites by sharing common faces with four neighbouring empty octahedral sites at the 16c position as shown in Fig. 1.3. It provides the three-dimensional network path 16c-8a-16c through which lithium ions can migrate during the intercalation and de-intercalation reactions. However, in the case of $LiMn_{1.5}Ni_{0.5}O_4$ spinel, nickel is substituted with 25%, and it keeps the oxidation state of manganese in +4 to avoid the Jahn-Teller distortion associated to $Mn^{3+}$. Thus, the redox activity is only due to the $Ni^{2+}$ ions by transferring the $2e^-$ per nickel ion. It crystallizes in two crystallographic structures with cationic sub lattice. One is face-centred spinel with a space group of Fd3m, which is also named as disordered spinel, and the other one is called simple cubic phase having a space group of $P_4332$ also called as ordered spinel. Further, the cation distribution in the $P_4332$ symmetry is then Li on 8c, Ni on 4b, Mn on 12d, and O(1) and O(2) oxygen ions have filled the 24e and 8c Wyckoff positions, respectively. However, the phase pure spinel is difficult to prepare due to NiO and $Li_yNi_{1-y}O$ impurities and they also commonly existed in the prepared compound. The substitution of Ni and Mn by Cr in $LiNi_{0.5-y}Cr_{2y}O_4$ is a fruitful way to suppress the problem of oxygen loss generating $Mn^{3+}$ ions in the spinel framework with a voltage of 4 V vs. $Li/Li^+$ [9].

### 1.3.4. Lithium iron phosphate ($LiFePO_4$)

Lithium iron phosphate belongs to olivine family, and it crystallizes in the orthorhombic system with Pnma space group. It has distorted hexagonal close packed (hcp) oxygen framework with lithium and iron are placed in half of the octahedral sites and phosphorous in one eighth of the tetrahedral sites [9]. The $FeO_6$ octahedra is distorted and lowers the regular octahedral $O_h$ to the $C_s$ symmetry. $FeO_6$ corner shared octahedra is linked together in the bc-plane, whereas $LiO_6$ octahedra forms the edge sharing chains along the b-axis, as shown in Fig. 1.3. The tetrahedral $PO_4$ group also connect the $FeO_6$ octahedra by sharing a common edge with one $FeO_6$ octahedra and two edges with $LiO_6$ octahedra. It also contains the three non-equivalent O sites, in which most of them are filled by 4c Wyckoff position, but O(3) which stays in the general 8d position and $Li^+$ ions occupy only in 4a Wyckoff position ($M_1$ site on an inversion centre). However, at the other side, Fe magnetic ions are in +2 oxidation state and occupy only the 4c Wyckoff position ($M_2$ site in a mirror plane) i.e., the centre of the $FeO_6$ units. Therefore, Fe is dispersed so as to form $FeO_6$ octahedra isolated from each other in $TeOc_2$ layers as perpendicular to the (001) hexagonal direction. This lattice has strong two-dimensional property, since above a $TeOc_2$ layer comes another one vertical to the previous one to build the (100) layers of $FeO_6$ octahedra sharing corner and mixed layers of $LiO_6$ octahedra and $PO_4$ octahedra. In addition, the back bonding between phosphorous and oxygen gives the stable crystal structure for LFP during the cycling.

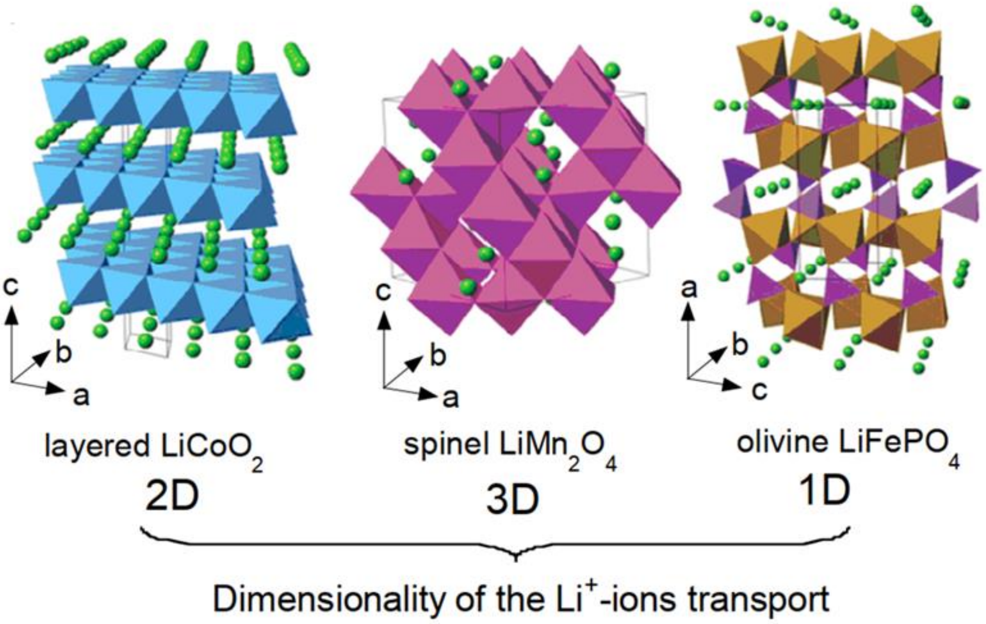

**Figure 1.3.** Crystal structure of the intercalation compounds in which the $Li^+$ ions travel through the 2-D (layered), 3-D (spinel) and 1-D (olivine) frameworks.

### 1.3.5. Literature survey on anode materials

In the case of anode materials also, lithiation and de-lithiation during the cycling occurs by intercalation/de-intercalation, alloying/de-alloying and conversion-based mechanisms. But, the potential of anode materials lies below 3.0 V vs. $Li/Li^+$. The anode materials have highest specific capacity than the cathode materials. Especially, for anode materials, at the first discharge (i.e., lithium intercalation) a thin layer will form, called solid electrolyte interface (SEI) in order to insert the lithium-ions in to the crystal structure during the cycling.

**Table 1.2.** Anode properties for the intercalation/de-intercalation, alloying/de-alloying and conversion-based materials

| **Type of frame work** | **Material** | **Theoretical / Practical capacity (mAh $g^{-1}$)** | **Volume change (%)** | **Average potential (V vs. $Li/Li^+$)** |
|---|---|---|---|---|
| Layered | Graphite | 372 | 12 | 0.05 |
| Spinel | Lithium titanium oxide | 175 | ~1 | 1.60 |
| Body centered cubic | Silicon | 4200 | 410 | 0.40 |
| Body centered cubic | Tin | 993 | 260 | 0.60 |
| - | Metal oxides | ~500 to 1000 | - | - |

### 1.3.6. Graphite (C)

Carbon materials are usually described in two forms i.e., $sp^3$ (Diamond) or $sp^2$ (Graphite). In the graphite case, the $sp^2$ hybridized graphene layers are linked with weak van der Waals forces and π- π interactions of delocalized electron orbitals. In addition, these layers would be stacked either in thermodynamically more stable ABAB structure with hexagonal symmetry or in thermodynamically less stable ABCABC structure with rhombohedral symmetry, as shown in Fig. 1.4 (a, b). But the rhombohedral symmetry holds for only 30% due to its mediocre thermodynamic stability. The resultant layered structure of graphite particles is generally described by flake like particle morphology with two different kinds of surfaces i.e., edge and basal planes. The edge plane illustrated in Fig. 1.4c is also called as prismatic plane. The prismatic plane can be further classified as zig-zag surface and armchair surface, as depicted in Fig. 1.4d. It is known that the edge surface plane exhibits a higher surface activity than the basal plane due to higher surface energy of the edge surface. In general, the 2D layered structure does not only influence forefront anisotropy concerning surface energy, but it has more influences on electronic, optical, physicochemical and mechanical properties. The weak van der Waals force is responsible for the lithium intercalation/de-intercalation by expansion and compression of the interlayer distance of the graphene layers [10].

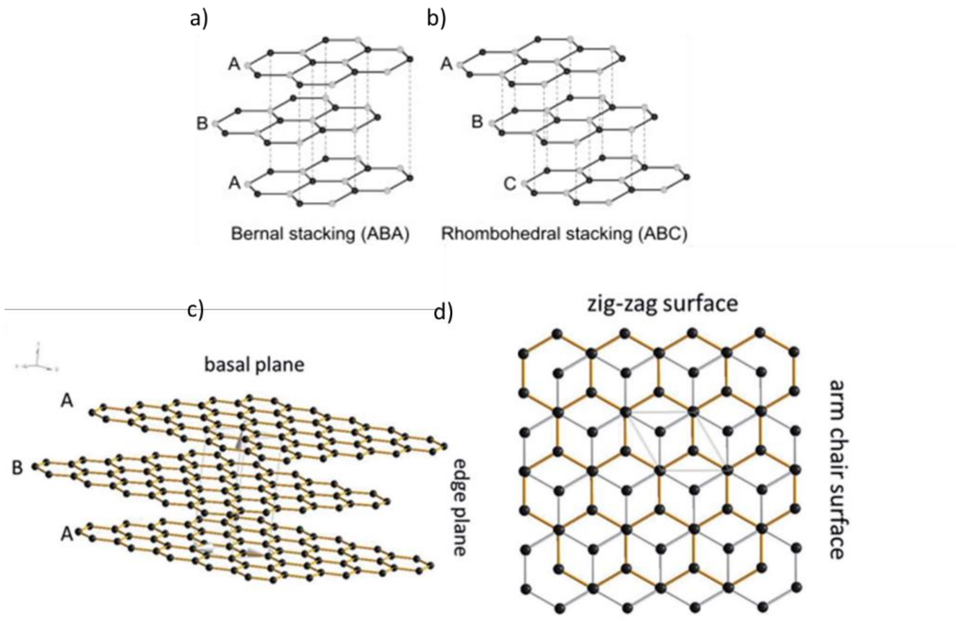

**Figure 1.4.** a-d) Schematic pictures of a) Bernal stacking, b) Rhombohedral stacking, c) basal/edge plane, d) zig-zag/arm chair surface.

1.3.7. Lithium titanium oxide (LTO)

LTO is considered as one of the promising material due to the excellent safety and prolonged life time. It can accommodate up to three lithium ions per formula unit and provides the theoretical capacity of 175 mAh g$^{-1}$ in the LTO structure with a minimum volume change during the charge/discharge. It has spinel crystal structure with the Fd3m space group and cubic symmetry. In the crystal structure, the lithium-ions occupy the tetrahedral 8a sites and 1/6 of the octahedral 16d sites, whereas the rest of the octahedral 16d sites are occupied by tetravalent Ti$^{4+}$ ions. The ratio of lithium to titanium is to be 1:5. It can be expressed as $Li_{8a}[Li_{1/3}Ti_{5/3}]_{(16d)}O_{4(32e)}$ in space representation. The octahedral 16c sites and the tetrahedral 8b and 48f lattices are vacant and also used for lithium charge/discharge as displayed in Fig. 1.5. Actually, $TiO_6$ is main frame work for the lithium-ion insertion/de-insertion. The Li$^{+}$ ions occupy the 8a sites forming the spinel structure at the initial stage of discharge. When the lithium insertion (lithiation) initiates, three lithium-ions from the 8a sites transfer to the 16c sites, simultaneously three lithium-ions move to the 16c sites through 8a sites. Whereas, during the charge (de-intercalation), lithium-ions are removed out from the 16c sites through the same 8a sites and the other lithium atoms go back to 8a sites from 16c sites. The redox reaction of Ti$^{4+}$/Ti$^{3+}$ takes place in octahedral coordinated framework. Finally, the spinel LTO structure

($Li_4Ti_5O_{12}$) changes to the rock salt structure ($Li_7Ti_5O_{12}$) during the electrochemical cycling as shown in Eqn. 1.3.

$$Li_4Ti_5O_{12} + 3\ Li^{+} + 3\ e^{-} \leftrightarrow Li_7Ti_5O_{12} \text{ ------------------ } 1.3$$

The LTO during the charge/discharge provides a flat potential of 1.55 V vs. $Li/Li^+$ due to the stable $Ti^{4+}/Ti^{3+}$ redox couple. Generally, SEI layer occurred at a voltage below 0.8 V vs. $Li/Li^+$. In the case of LTO, the potential was above the reduction potential of all organic electrolytes. Therefore, the SEI film can be prevented on the surface by employing LTO anode for the rechargeable cells. LTO can also show better thermal stability than the other anodes [11].

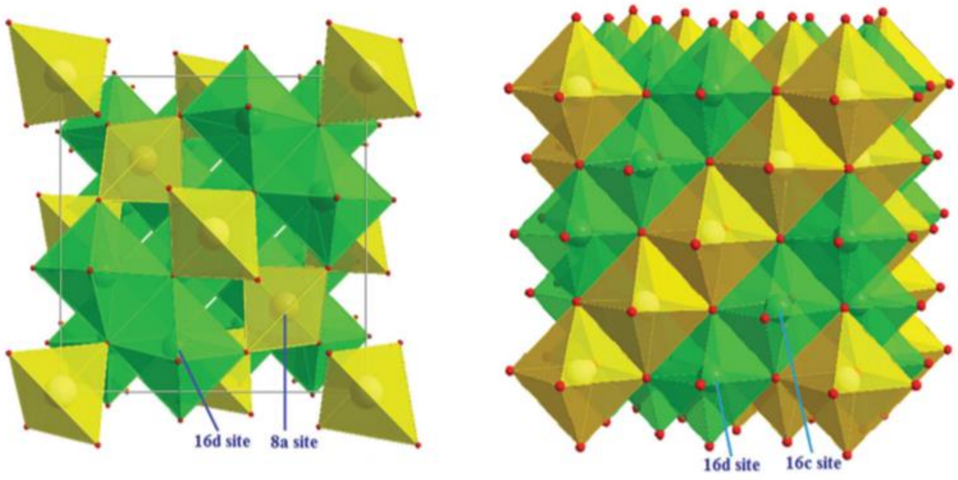

**Figure 1.5.** Lithiation/de-lithiation sites during cycling in LTO structure.

### 1.3.8. Silicon (Si)

Silicon is contemplated to be prominent anode material for LIBs due to the high theoretical capacity of 4200 mAh $g^{-1}$ than the graphite anode (372 mAh $g^{-1}$). It is abundantly existed in the earth crust than the graphite. But, this silicon by accommodating lithium atom results a huge volume change of ~400% and leads pulverization during the electrochemical cycling. To reduce the silicon pulverization, many reports have been investigated in literature. The recent theoretical studies are mainly concentrated on the modeling of lithium insertion and de-insertion of silicon anode, $Li_xSi$ phases and amorphous $Li_xSi$ alloys. Additionally, lithium silicide crystalline phases like LiSi, $Li_{12}Si_7$, $Li_7Si_3$, $Li_{13}Si_4$, $Li_{15}Si_4$, $Li_{17}Si_4$, and $Li_{22}Si_5$ are reported to be stable and formed only at high temperature lithiation. Room temperature lithiation of c-Si creates the amorphous lithium silicides like a-$Li_xSi$. The constrain for the formation of crystalline c- $Li_xSi$ alloys at room temperature is due to the kinetics of lithium, hence c-Si lithiation at room temperature is a nonequilibrium process. But several groups have reported that the crystalline c-$Li_{15}Si_4$ could be formed through an amorphous $Li_xSi$ phase. However, few works describe only about the formation of amorphous $Li_xSi$ phase [12]. During the lithiation, the generation of cracks and isolated silicon particles could be seen for silicon anode in Fig. 1.6.

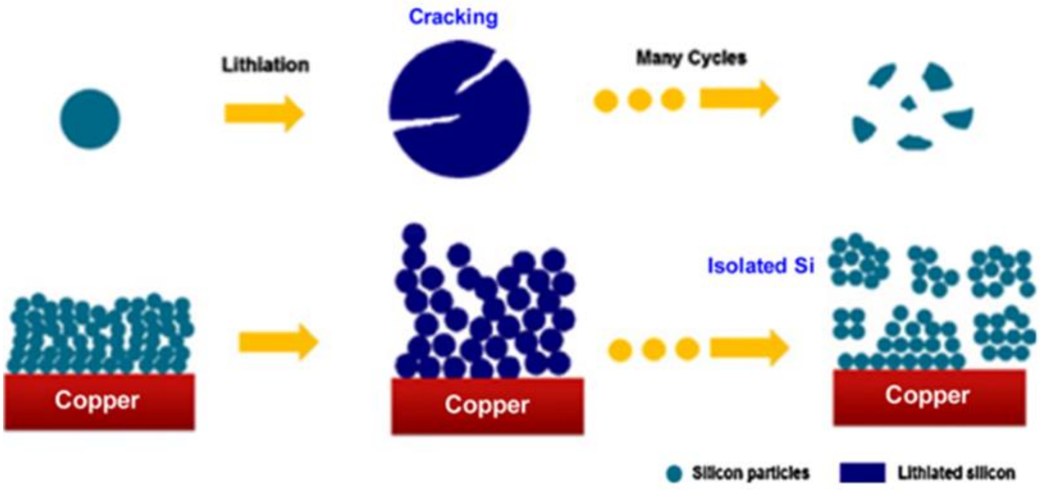

**Figure 1.6.** Cracks generation and isolated silicon particles for silicon anode from copper substrate after the cycling.

### 1.3.9. Tin (Sn)

Tin is one of the actively studied anodes in LIBs due to its highest theoretical capacity (991 mAh/g), low cost, high abundance and electronic conductivity. But, like silicon anode, tin also exhibits huge volume change during electrochemical cycling [13]. It further leads to pulverization, aggregation and loss of the electrical interphase contact for the active materials, as depicted in Fig. 1.7. $SnO_2$ anode stores lithium reversibly, but it irreversibly reduced to $Li_2O$ and metallic Sn at the initial discharge, as revealed by Idoda et al. It directs to low initial Coulombic efficiency as well as main obstacle for not promoting to the commercial level for LIBs. Dahn et al. have proved that lithium storage in $SnO_x$ is by alloying and de-alloying mechanisms. For the tin anode, two reactions are mostly referred for performing the electrochemical cycling, as given in the Eqn. 1.4 and 1.5. In addition, the band gap of the tin anode is 3.6 eV. The electrical resistivity of tin is about 1.1 x $10^{-7}$ Ω m at room temperature, which is little lower value than that of graphite. To overcome the volume expansion issues, few attempts have been done like reducing the sizes from micron to nano scale level for lessening the volume change and facilitate the lithium/electron diffusion. Furthermore, it is observed that increasing the surface area to volume ratios decrease the diffusion lengths. Currently, tin based nanomaterials display improved cycling performance compared to their micron size materials, even then they can't be considered for the real LIB applications because of aforementioned concerns. For tin anode, research is being explored in order to maximize the cyclic stability by increasing the tap/packing density and gravimetric/ areal/volumetric capacities [14].

$$SnO_2 + x\,Li^+ + x\,e^- \leftrightarrow Li_2O + Sn \text{ ------------------ } 1.4$$

$$Sn + x\,Li^+ + x\,e^- \leftrightarrow Li_xSn\ (0 \leq x \leq 4.4) \text{ ------------------} 1.5$$

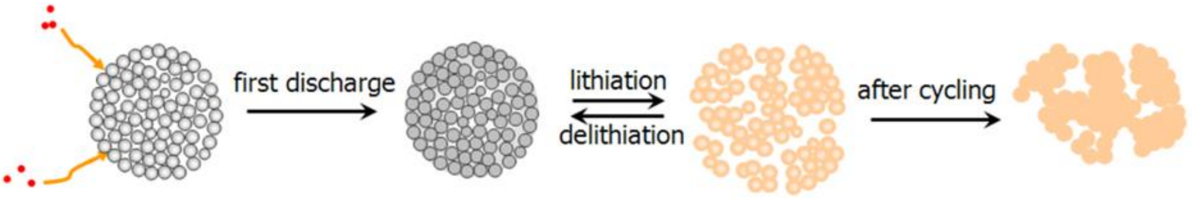

**Figure 1.7.** Pictorial representation of $SnO_2$ during lithiation/de-lithiation and after cycling.

### 1.3.10. Metal oxides

Many potential metal oxides have been explored for LIBs due to their physiochemical properties, and also, they could deliver high reversible capacities of 500 and 1000 mAh $g^{-1}$. These oxides can also be categorized in to three types depending on their reaction mechanism: a) Li-alloy reaction mechanism, b) insertion/extraction mechanism, and c) conversion reaction mechanism. Some of the metal oxides like $Fe_2O_3$, $Fe_3O_4$, $Co_3O_4$, CuO, NiO, and $RuO_2$ are the prominent metal oxides. However, these oxides have their own issues in terms of low Coulombic efficiency at the initial cycle, non-homogenous SEI film formation, large potential hysteresis, and very low-capacity retention [15]. The SEM images of as synthesized $Fe_2O_3$ and carbon coated $Fe_2O_3$/$Fe_3O_4$ spindles and TEM image of carbon coated $Fe_3O_4$ spindles are given in Fig. 1.8 (a-d).

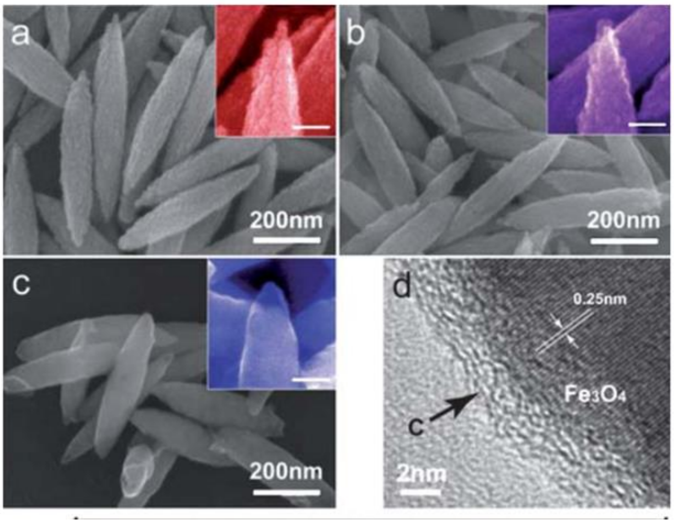

**Figure 1.8.** SEM images of a) as synthesized $Fe_2O_3$ and b, c) carbon coated $Fe_2O_3/Fe_3O_4$ spindles, and d) TEM image of carbon coated $Fe_3O_4$ spindles.

### 1.3.11. Binders and its mechanism

Binder is a main network connecting each part of the electrode. It has two major roles: 1) It acts cohesive to active materials and conducting carbon into integrity as well as binds the matrix laminate and to the current collector together. 2) The other one is to keep electron and ion circuits together for effective lithiation and de-lithiation. Hence, it has pivotal role for good stability and cyclic performance of electrodes. The mechanism of binder action also exists by two routes. The primary one is mechanical meshing force, which occurs at the coarse surface for all ingredients of electrode that includes binder polymer, active material, carbon black and current collectors. It is known that mechanical strength at the interface between binder and active material is lower than that between the inter active materials. Whenever the binder is dispersed with solvent, the solvent molecules will carry the binder polymer dispersed same in to the tissue of active materials. Therefore, the binder will join two objects together by pulling on each other after the drying. Always, the binder and adherend should mix homogeneously to give the robust mechanical meshing with required contact area as shown in Fig. 1.9. The second route is interfacial forces which are van der Walls forces, hydrogen bonding force, electrovalent force bonding, covalent bonding and co-ordinate covalent bonding. All these can ensure the contact between binder and other components of the electrode [16]. Some functional groups like -OH, -COOH, -RCOOR, $-NH_2$ and $-CONH_2$ of backbone polymer can interact between lone pair of electrons in functional group of binder and unoccupied orbital of -H on active material along with dipoles as well as induced dipoles between polar groups across the interface. Further, the chemical binding has been registered into the following approach; dot-to-surface contact, segment-to-surface contact and network-to-surface contact according to the interaction mode between binders and active powders, as represented graphical representation in Fig. 1.10.

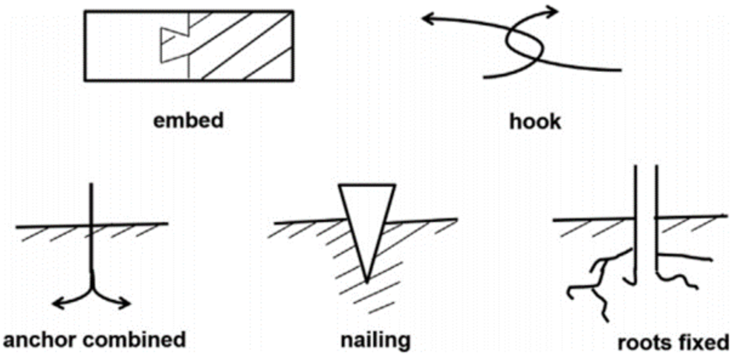

**Figure 1.9.** Mechanical connection for the binders.

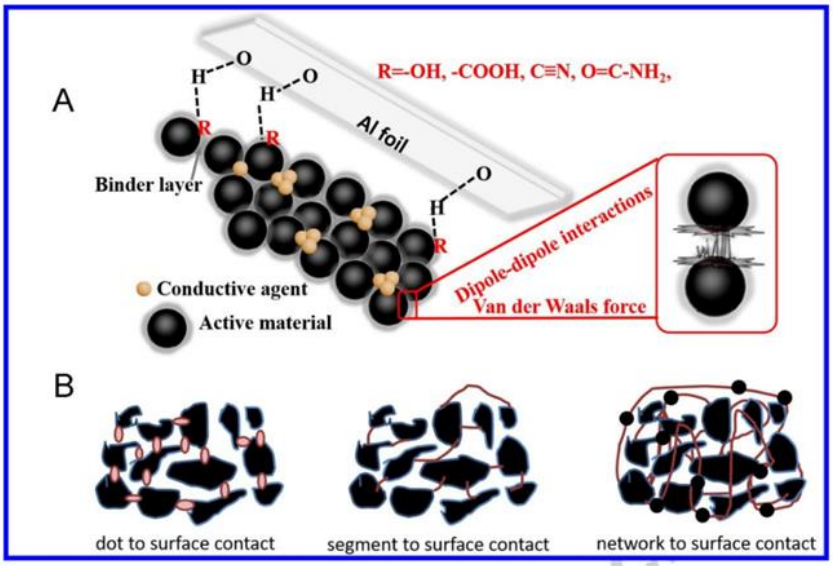

**Figure 1.10.** Graphical representation of dot-to-surface contact, segment-to-surface contact and network-to-surface contact according to the interaction mode between binders and active powders.

The selection of binding agents follows the below criteria:

1) It must be suitable for cohesion between the active material particles and conductive black components
2) It should provide strong adhesion for the electrode coating to the current collector
3) It maintains the facile properties during the electrode processing
4) Importantly the binder must be insoluble in electrolyte with desired swelling behavior is advantageous
5) It maintains the high chemical, thermal and electrochemical stability
6) Finally, the low cost, homogenously dispersed and environmental benign binders are highly prioritized for selecting the binders in LIB applications.

Generally, in the electrode fabrication process, the binder content need be very minimal. But it plays a vital role in the electrochemical cycling of battery systems. Some of the important physical properties desired for binder are thermal stability, conductivity, mechanical, and dispersion properties. In addition, chemical and electrochemical stability will emphasize the stability of binder in tough environments along with wide voltage windows [17].

### 1.3.11.1. Thermal properties

Thermal property can influence the change in physical and chemical performance of polymers, when heat is provided or removed because the property of polymers is associated with thermodynamics. For practical approach of LIBs, thermal stability, diffusivity and expansion rate of binders are vital considerations, since they can affect the electrochemical cycling and cycle life of electrodes in energy storage applications for different operating temperatures. The other affecting factor in this regard is the strength of binding forces between binders, composition and various functional groups with respect to molecular weight.

### 1.3.11.2. Mechanical properties

Mechanical properties of binder that involve mainly during the electrode fabrication and operation are the strength, flexibility, hardness, cohesion and adhesion of materials. The strength of material relates to its strength under tension or compression with the same material adept to display different tensile and compressive strengths. It is also known that tensile strength will be the main focus of the properties relate to the strength. Since, tensile strength is based on polymer molar mass and functional groups, it is proved that the tensile strength of aqueous binder is better than that of PVDF binder and that aqueous binder would provide long cyclic life for the active materials. By the tension measurements, materials elasticity and flexibility can be determined. Elasticity refers to a material's ability to bring it to the original position after a stress is applied and removed. Flexibility tells the ability of a material to handle bending without breaking. Hence, along with tensile strength, polymer's molar mass and functional groups largely would define its elasticity and flexibility. As of now, research is devoted for developing flexible binders in order to improve the mechanical properties for future flexible and wearable electronic applications [17].

### 1.3.11.3. Electrical and ionic conductivity

Electrical and ionic conductivities are crucial for all the batteries. It is known that polymers are insulators, but after the first conductive link was attached, i.e., conjugated frame work and free charge carries, they being used as conductive binders. The polymers conductivity is believed to be due to the presence of conjugated polymeric network. At present, some of the binders are in developed stage, like polypyrrole (PPy), polyaniline (PANI), poly(3,4-ethylenedioxythiophene) (PEDT, PEDOT), polythiophene (PTh), polyisoprene (PIP), and poly(p-phenylene-terephthalamide) (PPTA). The polymers also demonstrate neutral conductivity in the range of $10^{-10}$ to $10^{-5}$ S $cm^{-1}$. Further, other factors like self-doping, ion exchange doping, solution doping are also adopted to enhance the polymer conductivity. Interestingly, these polymers may replace the conductive additives which are being used in the LIB applications. The ionic conductivity of polymers is depended on the segmental motion of solvated ions through the polymer chains. Some of the measured ionic conductivities present in literature are $6.3 \times 10^{-7}$, $4.6 \times 10^{-6}$, and $1.4 \times 10^{-6}$ S/cm for SPEEK-PSA-Li, SPEEK-PSI-Li and PSU-PSI-Li, respectively.

### 1.3.11.4. Swelling nature

Binders should require a chemical stability to avoid the corrosion from electrolyte during the charge/discharge. As of now, PVDF is majorly used stable binder for all LIBs. But it reacts with lithiated graphite and lithium metal at elevated temperature and getting swelled in organic solvents i.e., ethylene carbonate (EC), diethyl carbonate (DEC), and dimethyl carbonate (DMC). The semi-crystalline PVDF binder's reaction with lithiated carbon ($Li_xC_6$) is ascribed to the exothermic reaction of lithiated carbon materials and it also forms LiF and hydrogen on the surface of electrodes. Sometimes, PVDF-NMP solution even turns in to the dark kind of gel. Binders may also cause to collapse the electrodes and trigger the safety issues. Hence, the chemical stability of binders for battery systems including different electrode materials, electrolytes and electrochemical cycling potential ranges are believed to be required prerequisites for electrode design to ensure better cyclic and rate capability of batteries [17].

### 1.3.11.5. Electrochemical stability window

The electrodes get cycled in a wide scan of voltage window; they are expected to stay stable in the complete range of potential window. Binders should not show redox nature neither at high reduction potential nor at high oxidation potential. The electrochemical stability of binder actually governed by Nernst and Arrhenius reactions, importantly activation energy is one of the determining factors for electrochemical stability of binders. The operating potential for high voltage materials, like LNMO, spinel layered oxides and solid-state electrolytes, presents a bigger challenge for electrochemical stability of binders.

### 1.3.11.6. Electrolytes for LIB

Electrolyte plays a major role in LIBs. It acts as a medium for all the lithium-ion batteries. The lithium-ions will shuffle from cathode to anode and vice versa through the electrolyte. Three different types of electrolytes are available in LIBs. 1) liquid systems (solution of lithium salt in aprotic solvents), 2) polymer electrolytes (solid or gel electrolytes) and 3) solutions of lithium salts in ionic liquids. As of now, the commercial used electrolyte for LIBs is liquid electrolyte. The other two are being researched for better voltage window and for the redox stability [18].

The ideal electrolyte should consist the below mentioned points.

a) It should able to dissolve lithium salts for required concentrations.
b) The viscosity of the electrolyte must be lower in order to provide fast ion transport and rapid filling of electrolyte in the LIB commercial line.
c) Electrolyte should be inert with all other components of LIBs.
d) Sufficient wettability is needed to wet the electrodes and separator.
e) Importantly, it should be featured with high dielectric constant and ability to complex minimum one of the ions disassociated from the electrolyte salt.

Although many commercial electrolytes are available for LIBs, the most used one is 1 M $LiPF_6$ in EC: DMC: DEC (1:1:1). The ionic conductivity for the same is 8.5 mS $cm^{-1}$ at 20 $^{O}$C.

1.3.11.7. Cost effectiveness of aqueous binder over the non-aqueous binder

Although PVDF is a better binder for LIBs, intensive steps are taken towards the cost reduction for LIBs by implementing aqueous binders instead of non-aqueous binders during the electrode fabrication. Currently, the electrode fabrication is being carried out with non-aqueous and aqueous binders by dissolving them in NMP and water solvents, respectively. But, NMP is volatile, toxic and explosive organic solvent. Therefore, the replacement of organic solvent with aqueous solvent is considered for electrode fabrication in LIB applications. In recent times, electrodes with aqueous binders have shown better electrochemical performance than the non-aqueous binders and they also reduce the overall cost of LIBs [19]. Moreover, the advantages of aqueous binders over non-aqueous binder are as follows.

1) Cost effective: Aqueous binder minimizes the manufacturing cost of electrodes as water is used as the solvent instead of expensive NMP. In addition, there is no need for a solvent recovery plant for water-based electrode processing. For non-aqueous based process, more processing energy is required to remove the solvent during electrode drying. Hence, aqueous binders are cheaper than PVDF binder.

2) Eco-friendly process: The implementation of aqueous solvent instead of NMP brings the entire process environmentally friendly. Furthermore, it also reduces the carbon foot print which is released out from the NMP solvent.

3) Higher energy density: Electrode peel strength can be improved with aqueous binder. Thus, binder usage goes minimum with effective increase in active material percentage. It results an increase in energy density of the batteries.

4) No stringent humidity conditions are required during the electrode fabrication.

5) Fast drying conditions: Since, the boiling point (BP) of water is very much lesser than that of NMP (202 °C), electrodes with aqueous binders can be dried faster than the non-aqueous based electrodes. So, the production rate can be increased with aqueous binder rather than PVDF binder during the electrode fabrication.

6) Furthermore, aqueous based binders would reduce the formation time during initial cycling of cells due to its higher electrolyte wettability than the non-aqueous binders.

7) Majorly the cost of the binders also will decrease by adopting aqueous binders instead of non- aqueous binders.

Based on these advantages, many aqueous binders have been explored for LIBs as summarized in Table 1.3.

**Table 1.3.** Aqueous binders and their chemical structures used for LIB studies.

| Binder | Molecular structure | Electrode materials | Characteristics | References |
|---|---|---|---|---|
| PVDF (Polyvinylidene difluoride) | 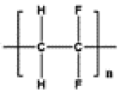 | Graphite, Silicon, Sn, $Fe_2O_3$, NiO, $SnO_2$, LTO and Sulphur. | Linear polymer | [20], [21], [22], [23], [24], [25], [26], [27] |

| | | | | |
|---|---|---|---|---|
| Na-CMC<br>(Sodium carboxymethyl cellulose) | 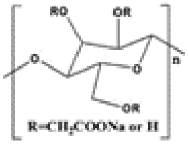 | Graphite, Silicon, Sn, LTO, LFP, $LiMn_2O_4$, and $LiCoO_2$. | Linear polymer modified from natural polymer, high viscous and low ionic impedance, $T_g$ = 75 $^{O}$C ($T_g$= Glass transition temperature | [28], [21], [22], [26], [29], [30], [31] |
| SBR<br>(Styrene butadiene rubber) | 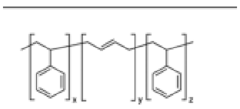 | Graphite and $LiCoO_2$ | Copolymer of styrene and butadiene, low cost and better elasticity, Tg = 65 $^{O}$C | [32], [33] |
| PAA<br>(Poly acrylic acid) | 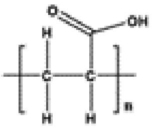 | Graphite, Silicon, LFP and LMO | Linear polymer, tunable mechanical properties, $T_g$ = 106 $^{O}$C | [34], [35], [30] |
| PVA<br>(Poly vinyl alcohol) | 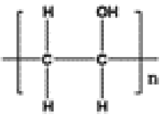 | Silicon, LTO | Linear polymer, enhances the adhesion strength, Tg = 80 $^{O}$C | [36], [37] |
| PVAc<br>(Poly vinyl acetate) | 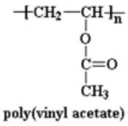 | LFP | Linear polymer<br>$T_g$ = 80 $^{O}$C | [38] |
| XG<br>(Xanthan gum) | 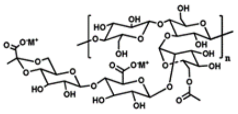 | Graphite, Silicon, LFP | Natural polymer, strong adhesion, Self-healing effect, | [39], [40], [41] |

| | | | | |
|---|---|---|---|---|
| | | | Double helical backbone | |
| Na-Alg<br>(Sodium alginate) | 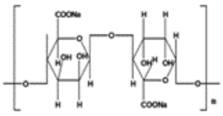 | Silicon, LTO, NMC | Self-healing effect, carboxyl group evenly distributed, lower ionic impedance, high stiffness in electrolyte | [42], [38], [43] |
| Carrageenan | 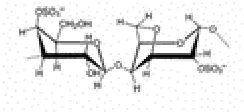 | Graphite | Linear sulfated polysaccharide forms stable conductive networks with carbon conductive additives | [39] |
| Agar-agar | 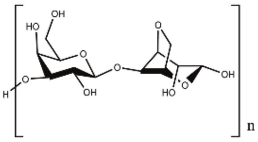 | Graphite | Natural polymer | [39] |
| PNVF<br>(Poly-N-vinyl formamide) | 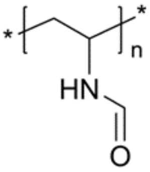 | Graphite | Functional group capable of forming hydrogen bonding with the active material | [44] |
| PEG<br>(Poly ethylene glycol) | 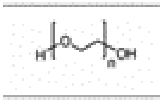 | LTO, LFP | Able to coordinate with metal salts | [45], [46] |

| | | | | |
|---|---|---|---|---|
| PTFE<br>(Poly tetrafluoro ethylene) | 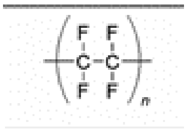 | Carbon, LFP | Good chemical resistance and thermal stability | [47] |

## 1.4. Focused binder literature which are investigated for the thesis

### 1.4.1. Polyvinyl alcohol (PVA)

PVA is a linear polymer available in various molecular weights. The presence of numerous hydroxyl groups enables strong hydrogen bonding with the active material. Thus, it has been used as a binder for cathode and anode active materials in LIBs [48]. In few studies, degree of saponification (DS) was varied in order to achieve better electrochemical performance. Oh et al. have demonstrated stable electrochemical performance for silicon/graphite anode with optimized molecular weight, swelling ratio and degree of saponification [49]. Liang et al. have studied the blend of PVA/PAA as an aqueous binder for $LiFePO_4$/C cathode. Further, the electrochemical performance for individual PVA and PAA was also studied and compared with blended binder. The optimized electrode with 2% PAA/1% PVA blended binder shows a higher rate capability of 130 mAh $g^{-1}$ at 5 C and retained excellent cycling stability of nearly >99% capacity retention even after 300 cycles at 5 C-rate. The stable performance of blend PVA/PAA is ascribed due to increased hydrogen bonding interactions with active material and current collector and also by enhanced amount of binder coverage on surface of the active materials. In addition, the blend polymer gives lower charge transfer resistance and higher diffusion coefficient due to the aforementioned bonding interactions than the other aqueous binder-based electrodes mentioned in Fig. 1.11(a, b) [50].

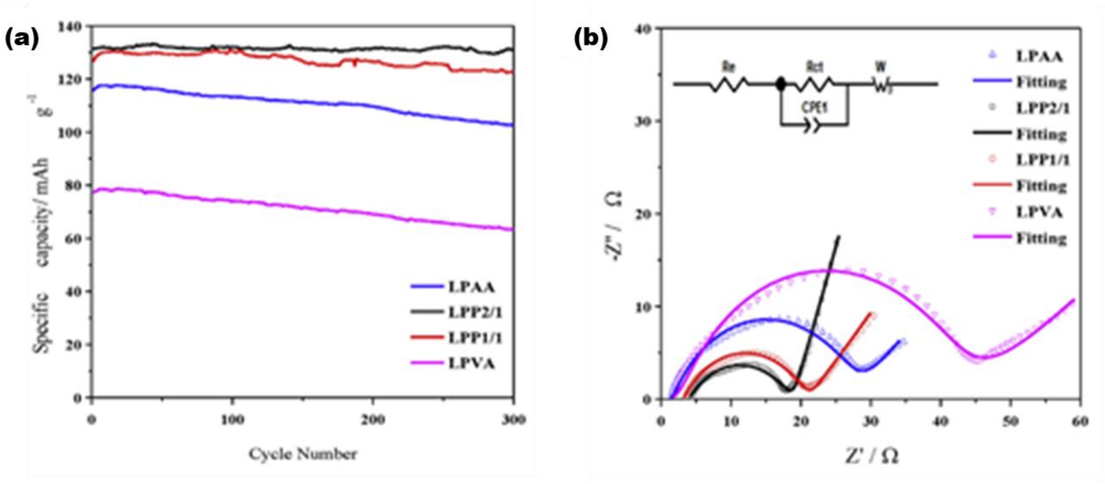

**Figure 1.11.** (a, b) Cycling stability curves at 5C-rate, b) Nyquist plots of $LiFePO_4/C$ electrodes with various binders.

The other study reveals that grafted PVA with PAA investigated as an aqueous binder for silicon anode had exhibited better adhesion and electrochemical performance compared to the CMC based silicon anodes. By this grafting route, for silicon anode, authors have improved the properties like Coulombic efficiency, excellent rate capability, high electrical conductivity, low SEI/charge transfer resistance and fast lithium-ion diffusion coefficient. Even more, for long-term charge-discharge test of 1000 cycles at 400 mA $g^{-1}$, it displayed a charge capacity (de-intercalation) of 1315.8 mAh $g^{-1}$ with capacity retention of 40.3% as shown in Fig. 1.12. The superior charge capacity, high capacity retention and the average CE value have directed the crucial role of optimized binder percentage in forming a stable SEI layer on silicon surface [51]. In addition, the increased binding capability and flexibility on its grafted PVA/PAA polymeric network is shown in Fig. 1.12. Recently, Chung et al. have evaluated the frictional properties of PVA polymer using atomic force microscopy (AFM) to improve the mechanical integrity of the silicon anode for LIBs. For this, the interfacial shear strength of the polymer binder was studied with silicon to understand the contact shearing and sliding behaviours. It was observed that decrease in mechanical and adhesion properties in the electrolyte would be responsible for the decrease in the frictional properties of PVA polymer [52].

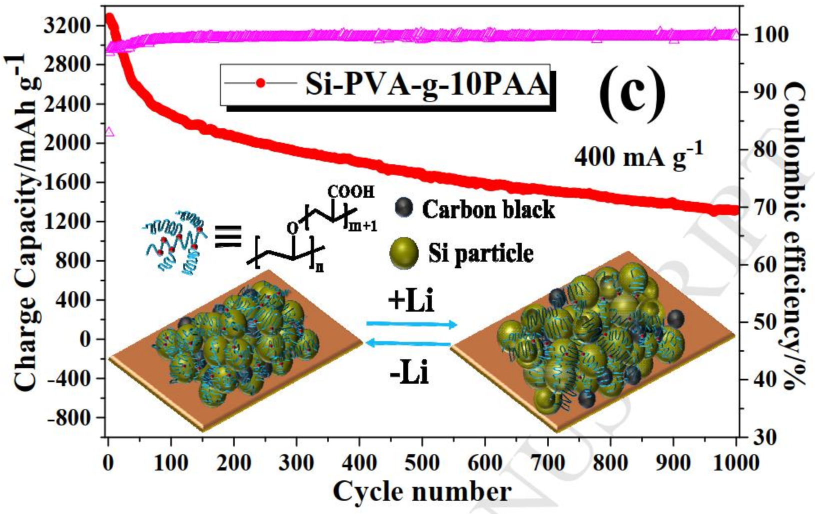

**Figure 1.12.** Charge capacity of Si-PVA-g-10PAA electrode in the voltage range of 0.01-1.5 V vs. $Li/Li^+$ for 1000 cycles at 400 mA $g^{-1}$.

### 1.4.2. Sodium alginate (Na-Alg)

Sodium alginate is a natural polysaccharide extracted from sea algae. Carboxylic groups are attached with each algae polymer monomeric unit. It is a branched polymer consists of 1,4-linked β-D-mannuronic acid (M) and α-L-glucuronic acid (G) chains. Different compositions of M and G monoblocks in alginate give either excess or surplus physical and biological properties. It is understood that algae grow in coastal areas have more G percentage than the similar algae growing in running waters. The high G percent makes alginate gels stiffer. Furthermore, multivalent ions from seawater able to cross link the matrix and enhance the stiffness of the plant backbone. Having these glue properties, it is used as an aqueous binder for LIBs. Since then, it is used for different cathode and anode materials for LIBs. At first, Kovalenko et al. have studied sodium alginate binder for nano silicon anode and showed a stable capacity of ~2000 mAh $g^{-1}$ at a high current density of 4200 mA $g^{-1}$ for 100 cycles. In addition, cycling performed with lithium insertion capacity limited to 1200 mAh $g^{-1}$ for silicon anode demonstrated the stable performance of more than 1300 cycles as shown in Fig. 1.13. Importantly, an ideal silicon binder should be able to provide access of lithium-ions to the silicon surface. Therefore, if a binder is not permeable to solvent electrolyte molecules, it should either cover only a portion of the silicon surface or remain permeable to lithium-ions. The small size silicon nanopowder with high surface curvature results the number of binding points between binder polymeric chains and silicon particles restricted, suggesting that a small area of the silicon surface should certainly be directly exposed to the electrolyte. In sodium alginate, carboxylic groups are aligned evenly to the polymeric chain, which causes better lithium-ion movement at the peripheral of silicon anode for better SEI and stable electro chemical performance [53].

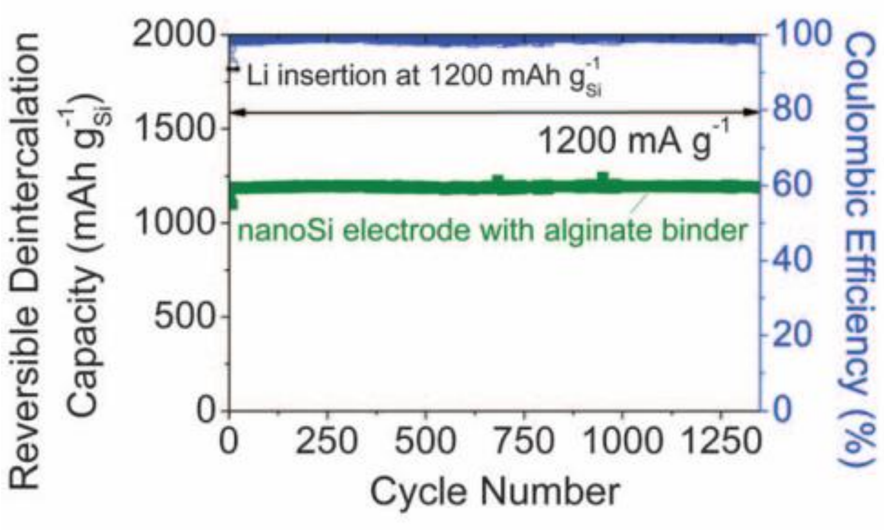

**Figure 1.13.** Electrochemical stability of nano Si electrode with alginate binder for 1300 cycles at current density of 1200 mA $g^{-1}$.

Sun et al. have shown suppressions of voltage and capacity fading for lithium rich metal oxide (LRMO) cathode using the sodium alginate binder. For this, pure sodium alginate binder (SA) was dissolved in aqueous solutions of different concentrations of Barium ($Ba^{2+}$) and Aluminium ($Al^{3+}$). Subsequently, electrodes were fabricated with LRMO, carbon black and the prepared binder solutions. The schematic picture of molecular structure of binder, binder interaction of $Al^{3+}$ and $Ba^{2+}$ ions with LRMO and corresponding viscosities of different binders are shown in Fig. 1.14 (a-c). The bonding of alginate molecules with cations is further explained by the presence of mannuronate group (M) and glucuronate group (G), which lead to prominent inter-molecular crosslinking between both – OH and the cations that connects – COOH groups of the mannuronate residues and guluronate residues by ionic bonding [54]. This further increases the viscosities of $Al^{3+}$ and $Ba^{2+}$ doped sodium gel as compared to the PVDF binder one, as depicted in Fig. 1.14c. FESEM shows the typical morphologies of the LRMO pristine electrodes fabricated with different binders including PVDF, sodium alginate and $Ba^{2+}/Al^{3+}$ doped sodium alginate binders in Fig. 1.15 (a-f). The electrodes of LRMO with sodium alginate, $Ba^{2+}/Al^{3+}$ doped sodium alginate gel binders had shown uniform morphologies without any agglomerations with fabricated electrodes. But, the FESEM image of PVDF electrode with LRMO and conductive carbon was quite inconsistent with the others with isolated individual particles, as marked in red circles (Fig. 1.15(b)). Moreover, all particles were quite agglomerated as evidenced by SEM morphology. Finally, among the fabricated electrodes, the optimized $Al^{3+}$ doped electrode showed the excellent cyclic stability, capacity retention of 99% for 150 cycles and voltage decay of only 0.208 V, respectively. Similarly, the $Ba^{2+}$ doped electrodes also displayed the stable specific capacity and lower voltage decay than the electrodes with pure sodium alginate and PVDF binder. This work also reveals the inhibition of manganese dissolution during the cycling process; hence it endows the LRMO cathodes with better cycling stability and negligible voltage decay [54].

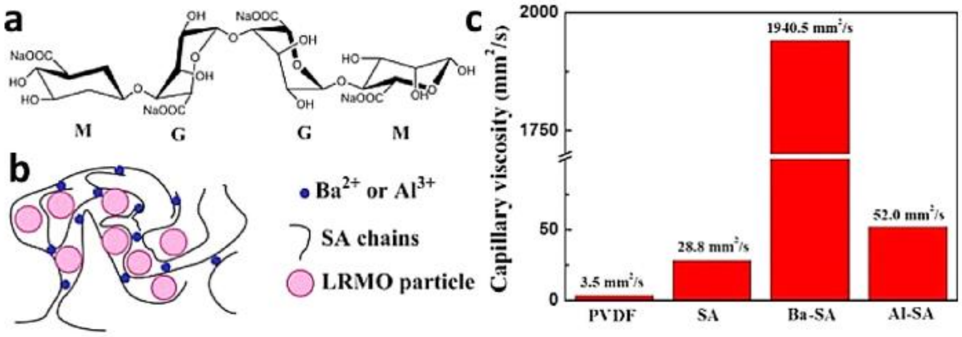

**Figure 1.14.** (a-c) a) Molecular structure of the sodium alginate binder, b) Polymer interaction of $Ba^{2+}$-SA/$Al^{3+}$-SA with LRMO particles and c) capillary viscosity of the PVDF, SA, Ba-SA and Al-SA solutions.

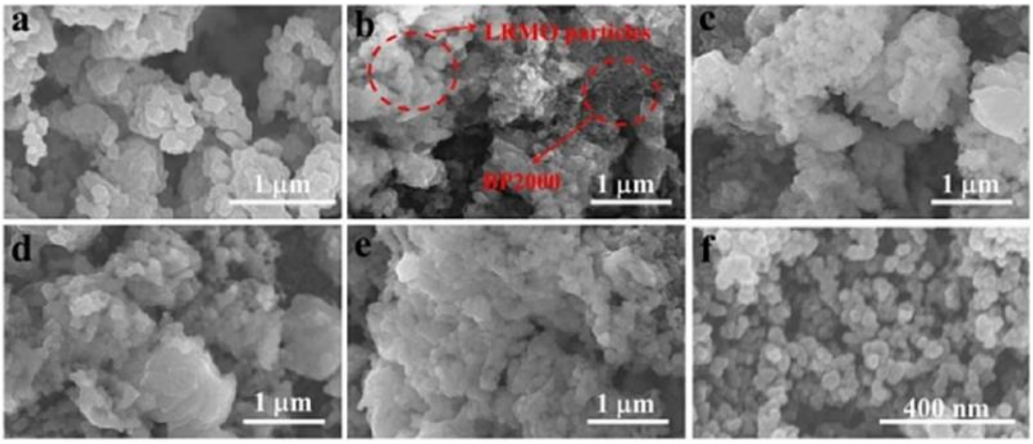

**Figure 1.15.** FESEM images of a) as synthesized LRMO material, b-f) Electrodes before the cycling test which are prepared with b) PVDF, c) SA, d) Na-SA-2, e) Al-SA-1, f) conductor BP2000.

### 1.4.3. Tamarind kernel powder (TKP)

It is also one of the natural and biodegradable polysaccharides extracted from the seeds of *Tamarindus indica* Linn. The TKP belongs to the Leguminosae family having a branched structure with a molecular weight of 720–880 kDa, and it forms a viscous solution in water. It constitutes of (1→4) β-D-glucan backbone with a link of α-D-xylopyranose and β-D-galactopyranosyl linked (1→2)-α-D-xylopyranose linked (1→6) to glucose residues. The groups like glucose, xylose, and galactose are present in the ratios of 2.8:2.25:1.0, respectively [55-56]. In addition, it is also used as a thickening, stabilizing and gelling agents for the various food industries. TKP has wide pH tolerance, high solubility, good ionic conductivity, good thermal/electrochemical stabilities and good mechanical strength. Considering all these properties, it has been employed as an aqueous binder for LIBs. However, it has already been used in various applications in LIBs. Sometimes TKP is also termed as tamarind seed polysaccharide (TSP). Sun et al. have reported the suppression of lithium dendrite by a protective biopolymeric film from tamarind seed polysaccharide for high-performance lithium metal anode. To perform that, 0.5 wt.% TSP solution was mixed for 5 h at ambient temperature and then was casted on copper foil for different thicknesses. Then, it was dried at 100 $^{O}$C for 5

h. Thereafter, the TSP thickness was optimized for 800 nm with compromised mechanical strength and same has been assembled into a symmetric battery with a lithium foil for electrochemical deposition of lithium on to the coated copper foil to get the Li@TSP-Cu electrode. Galvanostatic charge/discharge studies were performed with 2032-coin cells, in which bare copper foil and Li@TSP-Cu as working electrodes and lithium metal as reference electrode at different current densities, and the voltage time profiles were monitored for instabilities in the cells. After initial trails of charge/discharge with a lower current density of 0.5 mA cm$^{-2}$ and stripping/ plating capacity of 1 mAh cm$^{-2}$ (not shown), they were cycled at current densities of 1, 2, and 5 mA cm$^{-2}$ and stripping/ plating capacities of 1 and 2 mAh cm$^{-2}$ as shown in Fig. 1.16 (a-c). It was noticed that the cell with Li@TSP-Cu electrode was able to maintain the stable voltage loop rather than the cell with Li@Cu for long cycling in all the cases. Moreover, the inconsistent voltage profiles to both the electrodes for respective cycle were also clearly seen in the insert Fig. 1.16 (a-c). The better performance in the case of Li@TSP-Cu is due to the less decomposition of electrolyte during the initial cycling. Further, the protective layer minimizes direct contact between lithium metal and electrolyte, which helps to keep the SEI stable for prolonged cycling. The same has not been observed in the case of bare copper and hence lithium dendrites would have been generated and reduced the cyclic stability during the cycling [57]. Recently, TSP has also been used as lithium-ion conducting membranes in polymer electrolytes. Premalatha et al. have used the TSP polymer along with LiBr and showed the ionic conductivity of 4.83 × 10$^{-4}$ S cm$^{-1}$ [58].

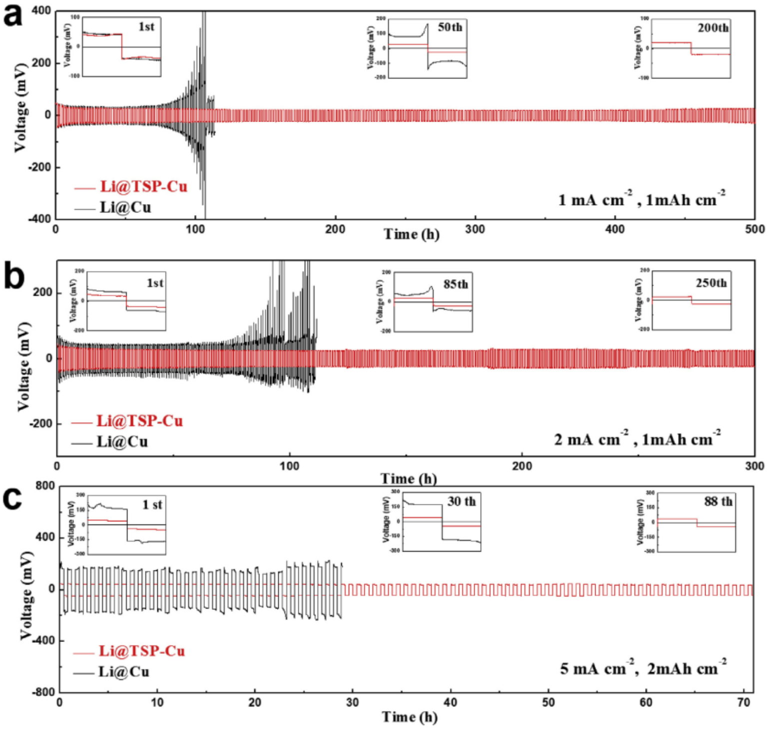

**Figure 1.16.** Galvanostatic cycling of fabricated cells using Li@Cu and Li@TSP-Cu at a current density of a) 1 mA $cm^{-2}$, b) 2 mA $cm^{-2}$ and c) 5 mA $cm^{-2}$ with a stripping/plating capacity of (a, b) 1 mAh $cm^{-2}$ and c) 2 mAh $cm^{-2}$.

In addition, the same polymer together with lithium triflate ($LiCF_3SO_3$) bestowed the ionic conductivity of $8.37 \times 10^{-4}$ S $cm^{-1}$ [59]. Hence, this TKP polymer might further be utilized along with other inorganic salts to enhance the conductivity in the field of solid polymer electrolytes.

### 1.4.4. Fenugreek powder/gum (FG)

It is also called as Methi or *Trigonellafoenum-graecum* Linn. It is abundantly available in India, Middle East, Southern Europe, North Africa, North America, etc. The contents of seed on dry basis are as follows: moisture 3.6%; protein 25-30%; ether extract 7-9%; steroidal saponins 5-7%; galactomannans 25-30%; insoluble fibre 20-25%; and ash 3-4%. Fibrous material entails of insoluble cellulose fibre, while the endosperm galactomannan would be soluble in water. Generally, galactomannans do have strong characteristic to bind and hold moisture. It is noticed that solvent-removed and protein-free FG is in whitish and odourless colour. In addition, it lowers blood sugar and blood lipid levels. It also encourages the growth of prebiotic colon bacteria, which is good for human health. The chemical structure of FG galactomannan consists of β-1,4-linked linear mannan backbone, to which single galactose grafts are linked randomly by α-1,6-glycoside bond. FG has highest galactose (~ 48%; M: G, 1.02:1) in its seed, and its linear mannan backbone has α-1,6-linked single galactose grafts on nearly all the mannose groups of the main chain [60]. The molecular weight of FG is 30 kDa. The linear mannan backbone of fenugreek polysaccharide was made up of 90-95, β-1,4-linked mannopyranosyl units and each backbone monomer carries an α, 1-6 linked galactopyranosyl group. In addition, the cold-water solubility of FG is 80%. The viscosity of FG solution decreases (shear thinning) with increase in temperature. FG is a fully substituted backbone and hence does not interact with other polymers to show synergism for the enhancement of viscosity and gelling. But it can be gelled by borate ions which is due to the presence of cis-hydroxyl groups. Therefore, these properties can be considered to use FG as an aqueous binder for LIBs. At first, Wang et al. have used the carboxymethyl FG gum as an aqueous binder for silicon anode [61]. The carboxymethyl FG gum was synthesized with pure FG gum and monochloroacetic acid. A total of three samples were prepared and studied by varying the degree of substitution (DS) to the fenugreek gum. Pure and derivatives (Different DSs) were identified as FG and CFGs in the present study. The bare and derivative gums had been studied for FTIR and rheology measurements, also they were studied along with silicon anode by cyclic voltammetry and galvanostatic charge/discharge analyses. The FTIR analysis for pure binder unveils the reduction in intensity of hydroxyl groups present in the FG polymer. Hence, it implies that carboxyl groups replaced the hydroxyl groups in the FG gum polymer. Both pure and derivatives have shown non-Newtonian behaviour with shear thinning property. It concludes that both could be used as an aqueous binder for LIBs. Interestingly, the increase in DS exhibits higher viscosity recovery rate i.e., the increase in DS influence the quick recovery of structural viscosity. Further, pure as well as each derivative with different binder weight percentages i.e., 3, 5 and 10 wt.% were mixed with silicon anode and fabricated the electrodes for electrochemical charge/discharge studies of 1000 mA/g between 0.01 and 1.50 V. The fabricated electrodes displayed the different initial Coulombic efficiencies with increase in binder content, and finally the electrode with higher DS and optimum binder content (i.e., CFG-3) showed the higher specific capacity and CE i.e., 2686 mAh $g^{-1}$and ~ 91.3%, respectively as given in Fig. 1.17a. Even more, the same electrode had given the 2175 mAh $g^{-1}$ at 50th cycle with better cyclic stability and rate capability, as depicted in Fig. 1.17. The higher capacity and better CE were attributed to the increased carboxymethyl groups in CFG that offered strong hydrogen bonding interactions between the CFG and silicon anode [61]. In addition, the volume expansion and cracks were also minimized for CFG based silicon anodes. Hence, this study was quite useful to use FG as an aqueous binder for LIB applications. In recent times, Mo et al. have deployed FG gum for lithium sulphur (Li-S) battery. In their study, the cathode S/CNFs composite was fabricated with FG gum binder and displayed higher initial capacity of 900 mAh $g^{-1}$ at 2C-rate and reversible capacity retention of 45% even after 1300 cycles. The same electrode had also been compared with conventional PVDF as well as GG binder and noticed better performance with FG binder. The higher performance with FG binder was ascribed due to the formation of the S-O and Li-O bonds between the oxygen functional groups from the binder and also from the polysulfides in sulphur cathode as obtained from XPS data [62].

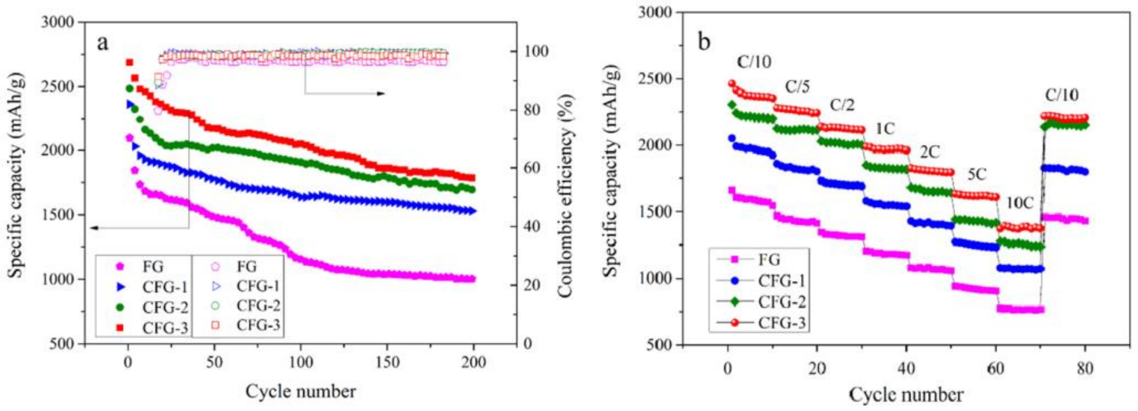

**Figure 1.17.** a) Electrochemical stability at 1000 mA/g between 0.01 and 1.50 V with specific capacity and Coulombic efficiency, b) cycling stability at different C rates of silicon electrodes with different degrees of substitution containing 5 wt.% of FG binder and CFG binders.

### 1.4.5. Sodium Carboxymethyl cellulose and Styrene butadiene rubber (CMC/SBR)

Among all the binders, CMC/SBR is the main one which used as an aqueous binder for LIBs. CMC is generally used for stabilizers, emulsifiers, thickening as well as binding agents in aqueous solutions. The physical and chemical characteristics of cellulose polymers are relying on the polymer molecular weight, particle size, nature of substituents and the degree of substitution (DS) [63]. It is a linear polymer consists of glucose units attached via glycosidic β-(1,4) linkages. The characteristic of CMC depends strongly on the DS, which implies the conformation and charge density of the polymeric chains in water. Hence, CMC is essentially used in LIB fabrication. Preliminarily, CMC was employed for graphite anode. But, hydrophobic water suspensions of natural graphite were found unstable. Even then, the interactions between the graphite anode and CMC backbone were established. It was also determined that a lower DS results in higher hydrophobic and stronger interaction with graphite. The carboxylic groups of Na-CMC adsorbed on the graphite surface separate and stabilize the suspension. Thus, Na-CMC acted as thickening agent as well as surfactant by avoiding graphite sedimentation. The same had not achieved if only SBR was used for graphite anode. However, the coupled CMC/SBR retained graphite sedimentation and also form denser and less brittle electrodes. Electrodes which were prepared with CMC/SBR exhibited the lower first cycle irreversibility than PVDF based electrodes. It was due to the faster SEI formation induced by the interactions between carbon and Na-CMC. The presence of hydroxyl and carboxyl groups was responsible for the improved cyclic performance. In one of the studies, authors proved that the reactivity of CMC with the electrolyte forms the protective surface layer consisting of R-O-$PF_4$ and lithium fluoride groups. The aforementioned layer (artificial SEI) augments for better cyclic stability in sulfolane based electrolytes for graphite electrodes fabricated with CMC binder as compared to the non-aqueous PVDF binder [1]. Lee et al. have explained the role of CMC and SBR binders using natural graphite (NG) and artificial graphite (AG) for electrode fabrication in LIBs. The physiochemical behaviour of CMC and SBR binders during the electrode fabrication process were revealed by direct monitoring of binder distribution of graphite electrodes with low binder content of 2 to 3wt.%. Laser-ablation laser induced breakdown spectroscopy (LA-LIBS) and time-of-flight secondary-ion mass spectrometry (TOF-SIMS) were employed to characterize the electrodes. Initially, three kinds of CMC binder adsorption were investigated during the slurry mixing for natural and artificial graphite. In the case of natural graphite, slurry mixing process was associated for the absorption of CMCs on the graphite anode by the interactions of hydrocarbon polymer structure or functional carboxylic groups of the CMCs. In addition, the surface of natural graphite with few defects enunciate the CMCs adhered by noncovalent interactions. Hence, van der Waals interactions between the CMC structure and the graphitic surface were happened between them. Whereas, the adhesion of CMC on the artificial graphite surface was materialized by cross linking between the dangling bonds of artificial graphite and functional moieties of CMCs. The binding mechanisms in the slurry could affect the migration of the binder during electrode fabrication and the resultant distribution of binders in electrodes, as shown in Fig. 1.18 (A and B). Further, LA-LIBS exhibits better detection capability for elements of O and H. During the process, the pulse ablates a few amounts of sample and generates an array of holes on its surface as shown in Fig. 1.19 (A-C). The elements of O and H after ablation from the surface could be visualized in the form of 2D mapping images, as seen from the same picture. Figure 1.19 (A-E) also shows the vertical distribution of O and H atoms in the NG/CMC-B/SBR and AG/CMC-H/SBR electrodes. It is found that the distribution of O from CMC was reduced gradually in vertical direction from surface to the current collector for both NG and AG electrodes. Whereas, the H atoms from CMC and SBR were quite uniform for the same. Hence, LA-LIBS revealed that migration of SBR not affected either by evaporating water or CMC and remained same throughout the concerned area; especially at the bottom surface it was higher than the top surface. TOF-SIMS also indicated that the SBR was more concentrated towards the current collector rather than the top surface, hence it is coherent with LA-LIBS data [64].

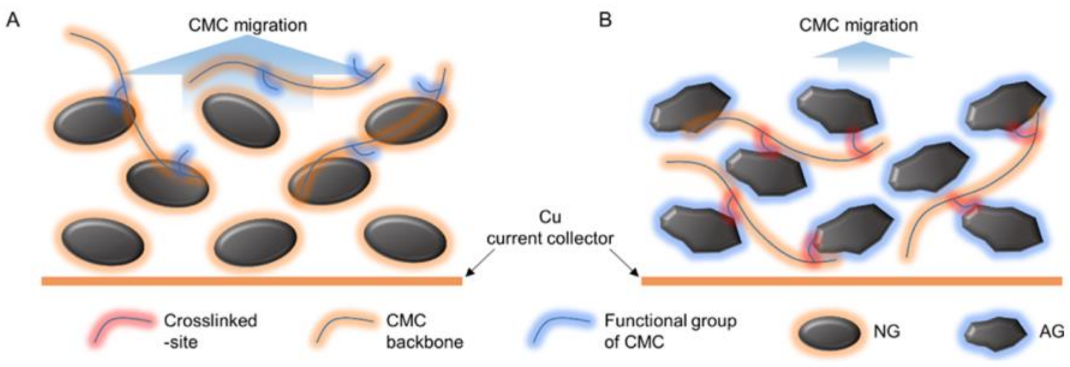

**Figure 1.18.** CMC binder migration during drying A) NG/CMCs B) AG/CMCs electrodes

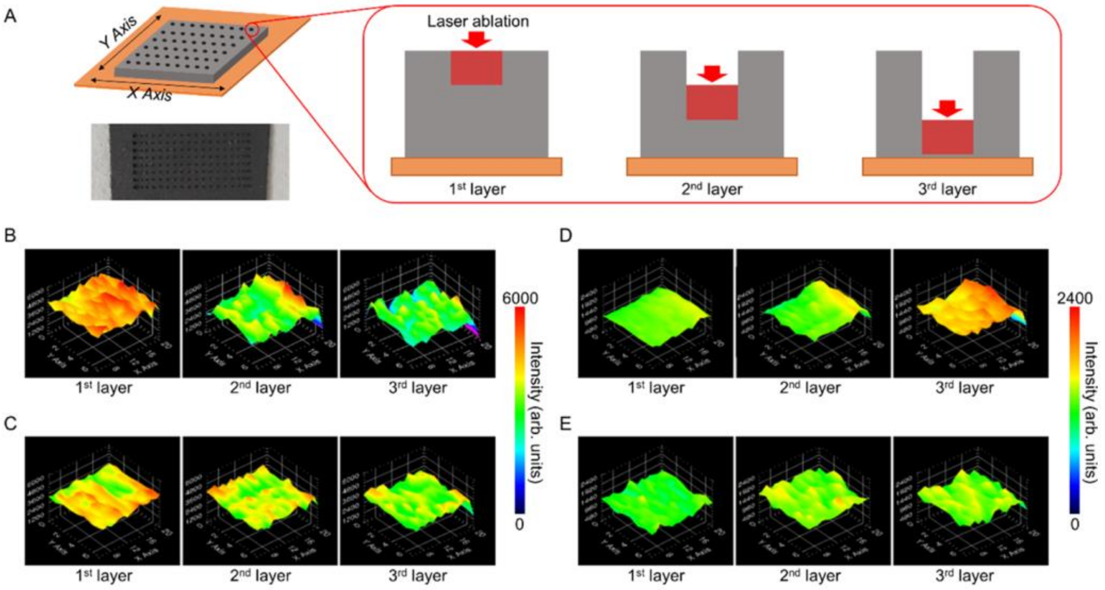

**Figure 1.19.** (A) Schematic pictures of graphite electrode for LA-LIBS. LA-LIBS mapping in vertical distribution of (B) O and (D) H for NG/CMC-B/SBR electrode and (C) O and (E) H of AG/CMC-H/SBR electrode.

### 1.5. Objectives of the present study

The objective of the thesis for each individual aqueous binder for corresponding anode is as follows.

- PVA and Na-Alg binders: To evaluate the stability of these binders as an alternative to the existing non-aqueous PVDF binder for the electrode fabrication of LTO anode.
- TKP binder: To find the electrochemical stability of TKP binder and its effect during the charge/discharge with graphite anode for LIB applications.

- ➢ FG binder: To study the effect of inter and intra hydrogen bonding interactions of FG binder with graphite anode in terms of cycling stability, and rate capability for LIBs.
- ➢ CMC/SBR binder: To determine the binder effect for large scale graphite electrode fabrication and its electrochemical performance by fabricating the full cells with different cathode materials of LIBs.

### 1.5.1. Scope of the present study

Electrode fabrication for lithium-ion batteries is being made with polyvinylidene difluoride (PVDF) binder using NMP medium due to the robust, adhesive and cohesive nature of the binder. In addition, it has excellent compatibility with cathode and anode active materials available for LIBs. But it has several drawbacks like excessive binder swelling during electrochemical cycling, environmental pollution, high process cost, etc. Hence, a suitable and versatile alternate binder material needs to be adopted for the electrode fabrication of LIBs. Aqueous binders are the best replacement for PVDF binder in the fabrication of LIB electrodes. With the use of aqueous binders, cost-effective, easy handling and environmentally benign electrodes can be fabricated using an aqueous medium. Furthermore, aqueous-binder based electrodes are more flexible and conducive than non-aqueous based electrodes. The adhesive and cohesive binding of these electrodes is equivalent to the electrodes which are being prepared with a PVDF binder. So far, cyclic stability and rate capability of aqueous-based LIB electrodes have been reported better than corresponding non-aqueous based electrodes [65]. In this thesis, an elaborate research on anode materials for lithium-ion batteries using different aqueous-binders has been carried out. Structural, morphological and electrochemical performances of these electrodes have been compared with that of equivalent non-aqueous based electrodes.

## 1.6. References

[1] D. Bresser, D. Buchholz, A. Moretti, A. Varzi, S. Passerini, *Energy Environ. Sci.* **2018**, 11, 3096-3127.

[2] J. B. Goodenough, K. S. Park, *J. Am. Chem. Soc.* **2013**, 135, 4, 1167-1176.

[3] V. Etacheri, R. Marom, R. Elazari, G. Salitra, D. Aurbach, *Energy Environ. Sci*. **2011**, 4, 3243-3262.

[4] M. M. Kabir, D. E. Demirocak, *Int. J. Energy Res*. **2017**, 41, 1963-1986.

[5] C. Liu, Z. G. Neale, G. Cao, *Materials Today*. **2016**, 19, 2, 109-123.

[6] D. Deng, *Energy Science & Engineering* **2015**, 3(5), 385-418.

[7] J. Deng, C. Bae, A. Denlinger, T. Miller, *Joule* **2020**, 4, 3, 511-515.

[8] S. Ma, M. Jiang, P. Tao, C. Song, J. Wu, J. Wang, T. Deng, W. Shang, *Progress in Natural Science: Materials International* **2018**, 653-666.

[9] C. M. Julien, A. Mauger, K. Zaghib, H. Groult, *Inorganics* **2014**, 2, 132-154.

[10] J. Asenbauer, T. Eisenmann, M. Kuenzel, A. Kazzazi, Z. Chen, D. Bresser, *Sustainable Energy Fuels* **2020**, 4, 5387-5416.

[11] X. Sun, P. V. Radovanovic, B. Cui, *New J. Chem*. **2015**, 39, 38-63.

[12] A. Lyalin, V. G. Kuznetsov, A. Nakayama, I. V. Abarenkov, I. I. Tupitsyn, I. E. Gabis, K. Uosaki, T. Taketsugu, *J. Phys. Chem. C*. **2018**, 122, 20, 11096-11108.

[13] B. Luo, T. Qiu, D. Ye, L. Wang, L. Zhi, *Nano Energy* **2016**, 22, 232-240.

[14] X. W. Guo, X. P. Fang, Y. Sun, L. Y. Shen, Z. X. Wang, L. Q. Chen, *J. Power Sources* **2013**, 226, 75-81.

[15] L. Ji, Z. Lin, M. Alcoutlabi, X. Zhang, *Energy Environ. Sci*. **2011**, 4, 2682-2699.

[16] Y. Ma, J. Ma, G. Cui, *Energy Storage Materials* **2019**, 20, 146-175.

[17] H. Chen, M. Ling, L. Hencz, H. Y. Ling, G. Li, Z. Lin, G. Liu, S. Zhang, *Chem. Rev*. **2018**, 118, 18, 8936-8982.

[18] M. Yuan, K. Liu, *Journal of Energy Chemistry* **2020**, 43, 58-70.

[19] P. S. Salini, S. V. Gopinadh, A. Kalpakasseri, B. John, M. T. Devassy, *ACS Sustainable Chem. Eng*. **2020**, 8, 4003-4025.

[20] J. Chong, S. Xun, H. Zheng, X. Song, G. Liu, P. Ridgway, J. Q. Wang, V. S. Battaglia, *J. Power Sources* **2011**, 196, 18, 7707-7714.

[21] H. Buqa, M. Holzapfel, F. Krumeich, C. Veit, P. Novak, *J. Power Sources* **2006**, 161, 1, 617-622.

[22] S. L. Chou, X. W. Gao, J. Z. Wang, D. Wexler, Z. X. Wang, L. Q. Chen, H. K. Liu, *Dalton Trans*. **2011**, 40, 12801-12807.

[23] J. Li, H. M. Dahn, L. J. Krause, D. B. Le, J. R. Dahn, *J. Electrochem. Soc*. **2008**, 155, A812-A816.

[24] C. Zhong, J. Z. Wang, S. L. Chou, M. M. Rahman, S. X. Dou, H. K. Liu, *J. Appl. Electrochem*. **2010**, 40, 1415.

[25] S. L. Chou, J. Z. Wang, C. Zhong, M. M. Rahman, H. K. Liu, S. X. Dou, *Electrochim. Acta* **2009**, 54(28), 7519.

[26] S. L. Chou, J. Z. Wang, H. K. Liu, S. X. Dou, *J. Phys. Chem. C* **2011**, 115, 16220-16227.

[27] M. M. Rao, X. Y. Song, H. G. Liao, E. J. Cairns, *Electrochim.Acta* **2012**, 65, 228.

[28] J. H. Lee, U. Paik, V. A. Hackley, Y. M. Choi, *J. Electrochem. Soc*. **2005**, 152, A1763-A1769.

[29] J. He, H. Zhong, L. Zhang, *J. Appl. Polym. Sci*. **2018**, 135(14), 46132.

[30] Z. Zhang, T. Zeng, Y. Lai, M. Jia, J. Li, *J. Power Sources* **2014**, 247, 1-8.

[31] N. Yabuuchi, Y. Kinoshita, K. Misaki, T. Matsuyama, S. Komaba, *J. Electrochem. Soc*. **2015**, 162, A538-A544.

[32] S. Lim, S. Kim, K. H. Ahn, S. Lee, *J. Power Sources* **2015**, 299, 221-230.

[33] C. C. Li, J. T. Lee, Y. L. Tung, C. R. Yang, *J. Mater. Sci*. **2007**, 42, 5773-5777.

[34] J. Chong, S. Xun, H. Zheng, X. Song, G. Liu, P. Ridgway, J. Q. Wang, V. S. Battaglia, *J. Power Sources* **2011**, 196, 7707-7714.

[35] Z. P. Cao, Y. Liang, W. S. Li, L. D. Xing, Y. H. Liao, *J. Power Sources* **2009**, 189, 547-551.

[36] B. D. Assresahegan, D. Belanger, *J. Power Sources* **2017**, 345, 190-201.

[37] V. V. N. Phanikumar, V. R. Rikka, B. Das, R. Gopalan, B. V. Appa Rao, R. Prakash, *Ionics* **2019**, 25, 2549.

[38] P. P. Prosini, M. Carewska, C. Cento, A. Masci, *Electrochim.Acta* **2014**, 150, 378-383.

[39] N. Cuesta, A. Ramos, I. Camean, C. Antuna, A. B. Garcia, *Electrochim. Acta* **2015**, 155, 140-147.

[40] D. Chen, R. Yi, S. Chen, T. Xu, M. L. Gordin, D. Wang, *Solid State Ionics* **2014**, 254, 65-71.

[41] J. He, H. Zhong, J. Wang, L. Zhang, *J. Alloys Compd*. **2017**, 714, 409-418.

[42] G. Liu, S. Xun, N. Vukmirovic, X. Song, P. O. Velasco, H. Zheng, V. S. Battaglia, L. Wang, W. Yang, *Adv. Mater*. **2011**, 23, 4679-4683.

[43] J. Xu, S. L. Chou, Q. F. Gu, H. K. Liu, S. X. Dou, *J. Power Sources* **2013**, 225, 172-178.

[44] M. Lis, K. Chudzik, M. Bakierska, M. Swietoslawski, M. Gajewska, M. Rutkowska, M. Molenda, *J. Electrochem.Soc*. **2019**, 166, A5354-A5361.

[45] B. Tran, O. I. Oladeji, Z. Wang, J. Calderon, G. Chai, D. Atherton, L. Zhai, *Electrochim. Acta* **2013**, 88, 536-542.

[46] A. Fedorkova, R. Orinakova, A. Orinak, I. Talian, A. Heile, H. D. Wiemhofer, D. Kaniansky, H. F. Arlinghaus, *J. Power Sources* **2010**, 195, 3907-3912.

[47] S. Gao, Y. Su, L. Bao, N. Li, L. Chen, Y. Zheng, J. Tian, J. Li, S. Chen, F. Wu, *J. Power Sources* **2015**, 298, 292-298.

[48] J. Liao, Z. Liu, J. Wang, Z. Ye, *ACS Omega* **2020**, 5, 8272-8282.

[49] P. H. Kyoung, K. B. Seon, O. E. Suok, *Electrochemistry Communications* **2011**, 13, 10, 1051-1053.

[50] J. Sun, X. Ren, Z. Li, W. Tian, Y. Zheng, L. Wang, G. Liang, *J. Alloy. Compd*. **2019**, 783, 379-386.

[51] J. He, L. Zhang, *J. Alloy. Compd.* **2018**, 763, 30, 228-240.

[52] Q. D. Nguyen, K. H. Chung, *Appl. Phys. Lett.* **2020**, 116, 061604.

[53] I. Kovalenko, B. Zdyrko, A. Magasinski, B. Hertzberg, Z. Milicev, R. Burtovyy, I. Luzinov, G. Yushin, *Science* **2011**, 334, 75-79.

[54] S. J. Zhang, Y. P. Deng, Q. H. Wu, Y. Zhou, J. T. Li, Z. Y. Wu, Z. W. Yin, Y. Q. Lu, C. H. Shen, L. Huang, S. G. Sun, *ChemElectroChem.* **2018**, 5, 1321-1329.

[55] M. Razavi, S. Nyamathulla, H. Karimian, S. Z. Moghadamtousi, M. I. Noordin, *Molecules* **2014**, 19, 13909-13931.

[56] L. S. Kumar, P. C. Selvin, S. Selvasekarpandian, R. Manjuladevi, S. Monisha, P. Perumal, *Ionics* **2018**, 24, 3793-3803.

[57] J. H. You, S. J. Zhang, L. Deng, M. Z. Li, X. M. Zheng, J. T. Li, Y. Zhou, L. Huang, S. G. Sun, *Electrochim. Acta* **2019**, 299, 636-644.

[58] M. Premalatha, T. Mathavan, S. Selvasekarapandian, S. Monisha, S. Selvalakshmi, D. V. Pandi, *Ionics* **2017**, 23, 2677-2684.

[59] L. S. Kumar, P. C. Selvin, S. Selvasekarapandian, *Polym. Bull.* **2020**.

[60] V. Mathur, N. K. Mathur, *J. Scientific & Industrial Research* **2005**, 64, 475-481.

[61] L. Qiu, Y. Shen, H. Fan, X. Yang, C. Wang, *Int. J. Biol. Macromol*. **2018**, 115, 672-679.

[62] Y. X. Mo, Y. J. Wu, Z. W. Yin, W. F. Ren, Z. G. Gao, P. F. Zhang, J. X. Lin, Y. Zhou, J. T. Li, L. Huang, S. G. Sun, *ChemistrySelect* **2020**, 5, 8969-8979.

[63] C. Clasen, W. M. Kulicke, *Prog. Polym. Sci*. **2001**, 26, 1839-1919.

[64] W. J. Chang, G. H. Lee, Y. J. Cheon, J. T. Kim, S. Lee, J. Kim, M. Kim, W. Park, Y. J. Lee, *ACS Appl. Mater. Interfaces* **2019**, 11, 41330-41337.

[65] Y. Yang, S. Wu, Y. Zhang, C. Liu, X. Wei, D. Luo, Z. Lin, *Chem. Eng. J*. **2021**, 406, 126807.

# Chapter 2

# Materials, Methodology and Characterization Techniques

# 2. Materials, Methodology and Characterization Techniques

## 2.1. Introduction

This chapter expresses the materials, adopted methodology for electrode fabrication and various physiochemical and electrochemical characterization techniques which are being involved in the current study. Aqueous and non-aqueous binder materials used for fabricating the electrodes were obtained from chemical precursors as well as from natural bio-sources. To characterize the materials and fabricated electrodes, the following techniques have been employed in the present study. (i) X-ray diffraction (XRD), (ii) Thermal gravimetric analysis (TGA)/ Differential scanning calorimetry (DSC), (iii) Contact angle measurements (CA), (iv) Peel strength, (v) Field emission scanning electron microscopy (FE-SEM) and Energy dispersive spectroscopy (EDS), (vi) Fourier transform infrared spectroscopy (FTIR), (vii) Four probe conductivity measurements, (viii) Optical microscopy, (ix) X-ray photoelectron spectroscopy (XPS), (x) Confocal Raman spectroscopy, (xi) Electrochemical measurements like Cyclic voltammetry (CV), Galvanostatic charge/discharge, electrochemical impedance spectroscopy (EIS), etc. An elaborated process for all the above methodologies and used techniques are mentioned in the appropriate sections below. Figure 2.1 represents the schematic diagram for the sequence of materials, characterizations, cell fabrication and the electrochemical performance studies adopted for the thesis.

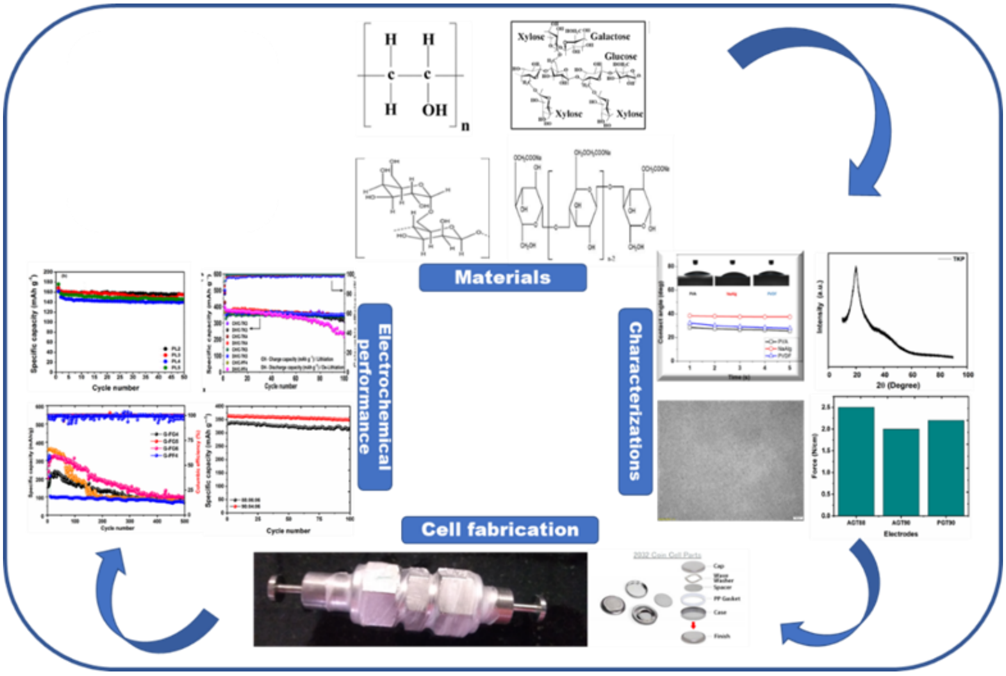

**Figure 2.1.** Schematic diagram for the sequence of materials, physicochemical characterization, cell fabrication and electrochemical performance studies adopted for the thesis.

## 2.2. Materials

The chemical precursors and reagents required for the thesis work are put together along with purities and suppliers in Table 2.1.

**Table 2.1.** List of different materials used in the experiments.

| Chemicals/Materials (Purity %) | Supplier |
|---|---|
| Carboxymethyl cellulose (CMC), (99%) | Merck, India |
| Styrene butadiene rubber (SBR), (>98%) | MTI Corporation, USA |
| Polyvinyl alcohol (PVA), (99%) | Sigma Aldrich, India |
| Sodium alginate (Na-Alg), (99%) | Merck, India |
| Tamarind kernel powder (TKP) | A. K. Products, India |
| Fenugreek powder (FG) | Local market, India |
| TRD202A and TRD102A | JSR Corporation, Japan |
| Copper foil | Gelon, China |
| Aluminium foil | Gelon, China |
| 1M Lithium hexafluorophosphate ($LiPF_6$) in EC: DMC: DEC (or) EMC (Ethylene carbonate, Dimethyl carbonate, Diethyl carbonate / ethyl methyl carbonate 1:1:1 v/v) | BASF, Germany (or) enchem, Korea |
| Lithium titanium oxide (LTO), (99%) | Linyi Gelon LIB Co, Ltd, China |
| Polyvinylidene difluoride (PVDF), (99%) | Kynar, USA |
| Super C65 (Carbon black) (>98%) | Timcal, Belgium |
| Potato shaped graphite (99%) | Superior graphite, USA |
| Ultra-pure water (18 MΩ) | Millipore system Thermofischer, India |
| Lithium nickel manganese cobalt oxide (NMC532) (99%) | Targray, Canada |
| Coin cells (CR2032) | Eager Corporation, Japan |
| Swagelok cells | Swagelok, India |
| Glass Micro fiber paper | GE Healthcare Whatman, India |
| Lithium metal, (99.9%) | Alfa Aesar, USA |
| N-methyl-2-pyrrolidone (NMP) (99.5%) | Merck, India |
| Glove Box | Innovative Technology, USA |

## 2.3. Methodologies (or) Physiochemical Characterization Techniques

Various physiochemical characterization techniques used for the thesis, instrument details, experimental details and the nature of the resulting information are given together in this section of Table 2.2.

**Table 2.2.** Characterization techniques, instrument details and the resulting information.

| Characterization technique | Equipment model | Expected information |
|---|---|---|
| Powder X-ray diffraction (XRD) | Rigaku equipped with monochromatic Cu $K_\alpha$ radiation | To analyze the crystalline nature and phase of pure binders and coated electrodes |
| Thermal gravimetric analysis (TGA) / Differential scanning calorimetry (DSC) | STA 4497, QMS403C; NETZSCH, in argon atmosphere and SDT Q600, TA instruments, (USA) | To analyze the thermal stability of materials as well as to observe the endo/exo thermic processes |
| Contact angle (CA) | Kyowa 601 (Kyowa Interface Science Co., Ltd.) equipped with USB 3.0 CCD Camera | To check the wettability of pure binders |
| Peel strength | Mecmesin, UK | To find the adhesiveness of electrodes |
| Field emission scanning electron microscopy (FE-SEM) | Carl Zeiss, Germany | To check the morphology of coated electrodes |
| Energy dispersive spectroscopy (EDS) | Carl Zeiss, Germany | To detect the elemental composition of electrodes |
| Fourier transform infra-red spectroscopy (FTIR) | Attenuated Total Reflectance (ATR) method, Perkin Elmer analyzer, (USA) | To identify the various functional groups and vibrational bands |
| Four probe conductivity meter | Keithely Model 6621 current source and 2180 voltage source | To check the electrical resistance of the coated electrodes |
| Conductivity meter | Metrohm, Switzerland | To find the ionic conductivity of pure binder solutions |
| Optical microscopy | Olympus, GX51, Japan | To find the morphology of the pure binder electrodes |
| X-ray photoelectron spectroscopy (XPS) | Omicron Nanotechnology, UK | To investigate the surface nature of the cycled electrodes |
| Confocal Raman spectroscopy | WITEC, Germany | To check the ordered nature and disorderness of coated graphite electrodes |

Details of the experimental conditions, analytical tools and analytical ranges of the various equipments with regard to the characterization of materials have been explained.

### 2.3.1. X-ray Diffraction (XRD)

Crystalline nature and phase of pure binders and coated electrodes were analyzed by X-ray diffraction studies using Rigaku X–ray diffractometer equipped with monochromatic Cu $K_\alpha$ radiation. Powder materials and electrode films were scanned in the 2θ range between 10–90$^o$ with a scan rate of 0.02$^o$ $s^{-1}$ using Cu $K_\alpha$ ($\lambda$ =0.15408 nm) with an applied potential of 40 kV and 30 mA current.

### 2.3.2. Thermogravimetric analysis (TGA)/ Differential scanning calorimetry (DSC)

Thermal stability of materials as well as the endo/exo thermic processes of all binder materials were analyzed using STA 4497, QMS403C, NETZSCH and SDT Q600, TA instruments, (USA) in argon atmosphere. Temperature range was 30 to 900 $^o$C under inert atmosphere to evaluate the thermal stability of the binders.

### 2.3.3. Contact angle measurements

Wettability of pure binders were examined using Kyowa 601 (Kyowa Interface Science Co., Ltd.) equipped with USB 3.0 CCD Camera. Electrolyte solution of 1M $LiPF_6$ in EC: DMC: DEC (or) EMC 1:1:1 v/v was placed (dropped) on the surface of binder film. A typical volume of 100 μl electrolyte was mechanically placed using a microneedle from a height of 3 cm, and contact angle of the drop on the film surface was measured at different time periods.

### 2.3.4. Peel strength tester

Adhesiveness of electrodes were examined using Mecmesin, UK. Peel strength of the electrodes was determined using a 180$^o$ peel tester by applying a constant speed of 30 mm/min from 0 to 100 mm length. The adhesive tape is used for the peel strength measurements.

### 2.3.5. Fourier transform infrared spectroscopy (FTIR)

Various functional groups and vibrational bands were identified by attenuated total reflectance (ATR) method using Perkin Elmer analyzer, (USA). Powder and thin film samples were placed on ATR crystal surface, and FTIR spectra was recorded in transmission mode with a resolution of 4 $cm^{-1}$ in the wavelength range between 500 and 4500 $cm^{-1}$.

### 2.3.6. Field emission scanning electron microscopy (FE-SEM)

Surface morphology of coated electrodes were examined by Field emission scanning electron microscopy (FE-SEM, Carl Zeiss, Germany). Powder samples and electrode films were placed on a conducting carbon tape before mounting on the sample holder for characterization, and the operating potential range was 10 – 20 KeV.

### 2.3.7. Energy Dispersive X-ray spectroscopy (EDS)

Elemental mapping of various active materials was done by using energy dispersive X-ray spectroscopy (EDS, Carl Zeiss, Germany). For elemental mapping of the electrochemically cycled samples, the cells were decrimped inside a glove box and the electrodes were washed with dimethyl carbonate (DMC) for 4–5 h. Then, the electrodes were used for recording elemental mapping.

### 2.3.8. Optical microscope

Surface morphology of the pure binder films coated on glass substrates were imagined by optical microscope (Olympus, GX51, Japan).

### 2.3.9. Four probe measurements

Four probe measurements were done in order to determine the electrical resistance of coated electrodes. Electrical resistance was measured with reference to the current collector using Four probe conductivity meter (Keithley 6621 Current source and 2180 Voltage source, Tektronix Inc, USA). An AC current was applied in the range of 10 – 70 µA, and the corresponding voltage was measured across the electrode thickness. The experiments were repeated for three times and the average resistance was measured.

### 2.3.10. Conductivity meter

Ionic conducivity was measured for pure binder solutions using Metrohm 914 pH/Conductometer.

### 2.3.11. X-ray photoelectron spectroscopy (XPS)

XPS analysis was used to investigate the surface nature of the electrochemically cycled electrodes. XPS analysis was carried out using a multiprobe system (Omicron Nanotechnology, UK) equipped with a Mg–$K_\alpha$ radiation operating at 300 W and 15 kV and a hemispherical analyzer operating in constant analyzer energy (CAE) mode. High–resolution spectra was obtained at a kinetic energy range of 20 eV with an energy step of 0.1 eV.

### 2.3.12. Calculation for Swelling analysis

The swelling measurements are performed by immersion of electrodes in electrolyte solution at room temperature for required time. The formula to calculate the swelling is given below.

$$Swelling\ (\%) = \frac{m - m_o}{m_o} \times 100$$

where $m_o$ and m are the parameters of dry and wet electrode films.

## 2.4. Electrochemical Characterization Techniques

Electrochemical characterization plays an important role to investigate the performance of the materials in order to find the electrochemical reactions and their mechanistic aspects like charge transfer, mass transport, electrode-electrolyte interaction, electron transport, etc. The electrochemical and energy storage characterization techniques such as a) Cyclic voltammetry (CV), b) Galvanostatic charge/discharge, and c) Electrochemical impedance spectroscopy (EIS) have been carried out using the electrochemical workstations like Biologic SP200, PARSTAT 4000 and Arbin BT-2000.

### 2.4.1. Cyclic voltammetry studies

Cyclic voltammetric studies were performed by using Biologic battery tester (Biologic SP200, France). The cathode and anode materials were tested in the potential range of 2.5 to 4.2 V and 0.005 to 3.0 V, respectively, with respect to $Li/Li^+$ at various scan rates. CV measurements were done with Swagelok or coin cells.

### 2.4.2. Galvanostatic charge/discharge studies

Galvanostatic charge/discharge studies were performed by using Arbin battery testing station (Arbin instruments, BT–2000, USA) in the voltage range of 1.0 to 3.0 V vs. $Li/Li^+$ for $Li_4Ti_5O_{12}$ anode, and 0.005 to 3.0 V vs. $Li/Li^+$ for graphite anode half cells. Whereas, the applied voltage range for full cells was 3.0 to 4.2 V for NMC vs. Graphite and 2.5 to 3.65 V for LFP vs. Graphite in CC/CV conditions.

### 2.4.3. Electrochemical impedance spectroscopy

AC impedance studies of the LIB electrodes were carried out by electrochemical impedance analyzer (PARSTAT 4000, USA) in the frequency range of 1MHz to 0.01 Hz with an AC signal amplitude of 10 mV.

## 2.5. Electrode Preparation and Cell Fabrication

### 2.5.1. Electrode preparation process

Working electrode (cathode/anode) was prepared by mixing of active material in the range of 80 – 90wt.%, carbon black 8 –10 wt.%, and aqueous binder 3 – 6wt.% in aqueous medium.

For comparison, an equivalent non-aqueous electrode was prepared by dissolving PVDF binder in N–methyl–2–pyrrolidone (NMP) organic medium. For aqueous electrode fabrication, initially, required binder solution was prepared either at room temperature or at temperature of 80 °C followed by dry mixing of carbon black and active material. Subsequently, all these were mixed thoroughly in a mortar and pestle for homogenizing the slurry, and then it was cast on appropriate substrate using doctor blade as shown schematically in Fig. 2.2. Afterwards, the electrodes were kept for drying in an oven at 120 °C for 24 h. The dried electrodes were used for cell fabrication after cutting it as 15 mm diameter disc.

### 2.5.2. Cell fabrication process

Cells of CR 2032 or Swagelok type were assembled in argon filled glove box with moisture level of <0.1 ppm and $O_2$ of <0.1 ppm as shown in Fig. 2.3. The active material coated on the current collector was used as working electrode, and lithium foil was used as both reference and counter electrode. Both the electrodes were separated by using Whatman GF/D borosilicate glass microfiber separator. The electrolyte used was 1M of $LiPF_6$ in EC: DMC: DEC (or) EMC (1:1:1 v/v). All fabricated cells were kept for an equilibration time of 10 – 12 h in order to dissipate the electrolyte uniformly on the electrode surface. In the case of full cell, the lithium metal was replaced with a suitable cathode.

### 2.5.3. Calculations for LIB cell or battery

Specific capacity of the cells was calculated by using the formula given below.

$$\text{Specific Capacity} = \frac{I * \Delta t}{m * 3600}$$

where I is the charge/discharge current in amperes, Δt is the charge/discharge time in seconds and m is the mass of active material in grams.

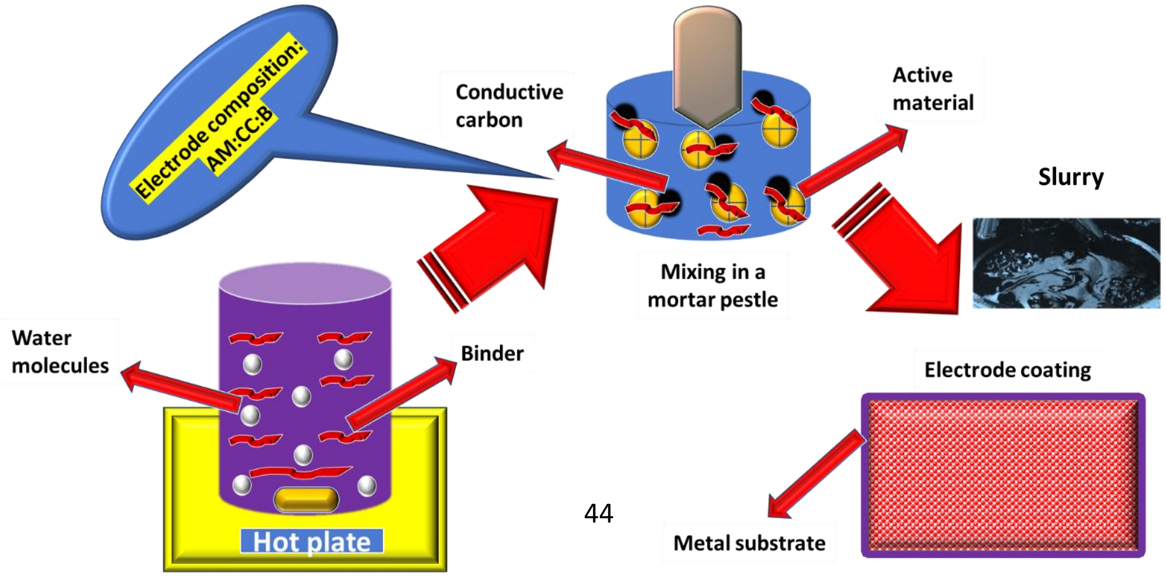

**Figure 2.2.** Schematic diagram for aqueous electrode fabrication.

**Figure 2.3.** Schematic illustrations of Swagelok and CR 2032-coin cells.

# Chapter 3

# Investigation on polyvinyl alcohol and sodium alginate as aqueous binders for lithium titanium oxide anode in lithium-ion batteries

## 3. Investigation on polyvinyl alcohol and sodium alginate as aqueous binders for lithium titanium oxide anode in lithium-ion batteries

### 3.1. Introduction

Lithium ion batteries (LIBs) are considered as superior energy storage systems due to their versatile applications in portable electronics, stationary energy storage and electric mobility (hybrid and pure electric vehicles) [1]. Most of the developments in LIBs are focused on battery electrode materials (intercalation as well as conversion) for improved electrochemical performance [2-5]. Apart from the electrode development, enormous efforts have also been made to develop suitable electrolytes and their additives for LIBs [6-7]. So far, research on binders was paid less attention while compared to electrodes and electrolytes, even though the binders have been reported to be the most significant components for improving the electrochemical stability and rate performance of LIBs [8]. Tarascon et al. have reported that the selection of binder is a primary choice to prepare electrodes with high efficiency [9]. Zheng et al. also reported that binder is one of the pre-requisites for electrode preparation since it integrates the active material and conducting additive to ease the electron transport as well as lithium-ion diffusion in the electrodes [10]. Polyvinylidene fluoride (PVDF) is widely used as binder in LIBs due to its good thermal and electrochemical stability [11]. However, the major problem associated with this binder is the use of toxic solvent N-methyl-2-Pyrrolidone (NMP) for dissolution of PVDF during electrode fabrication [12].

Moreover, the high cost and difficulty of disposing it at the end of the battery life make the PVDF unsuitable for LIBs. Hence, alternative binders which are environmental friendly are explored as substitutes for PVDF. Aqueous binders are preferred over non-aqueous binders as they do not require humidity-controlled condition for LIB electrode fabrication process [13,14]. Given the environmental and cost considerations, aqueous binders are gaining importance and have drawn the attention of researchers in the field of LIBs [15]. Many potential aqueous binders have come into existence for the preparation of LIB electrodes *viz*. carboxymethyl cellulose (CMC) [16,17], sodium alginate (Na-Alg) [18], polyvinyl alcohol (PVA) [19], polyacrylic acid (PAA) [20] cyclodextrin [21], polyurethane [22], etc.

Unlike PVDF, until now it is not clear which type of aqueous binder will be suitable for the preparation of cathodes, anodes or both. Nevertheless, aqueous binders are more flexible and ductile, which can accommodate the stress generated during lithiation/de-lithiation process. Furthermore, the binder content in the electrode should be within an optimal value in order to achieve high energy density as well as prolonged cyclic stability [13, 23]. These ameliorated properties of aqueous binders ensure the electrodes to exhibit high electrochemical performance profoundly at higher current rates [24]. The adhesion properties of the binders to the current collector, i.e., peel strength analysis, determines the electrochemical performance and longevity of the electrodes [25]. CMC, widely used aqueous binder, has a cellulose backbone structure which significantly enhances the cohesive properties of the electrode as well as good adhesion to the current collector. It is well reported in the literature that CMC is used along with low-viscous styrene butadiene rubber (SBR) as a thickening agent for the preparation of aqueous binder-based electrodes [26]. The major drawback associated with CMC-binder based electrode is prone to bacterial growth on ageing, which causes electrode to peel-off from the substrate material, hence deteriorate the cell performance.

In general, anodes operate within the potential range of 0.01-3.0 V. Graphite is currently used as anode in the commercial LIB due to its low working potential and low volume expansion upon lithium insertion and de-insertion reaction [27]. The problems associated with the graphite anode are the cyclic instability due to improper formation of the solid electrolyte interface (SEI) layer as well as poor rate capability due to the structural disintegration of graphite layers. Henceforth, researchers are looking for an alternative anode matereial, which could show good cyclic and high C-rate performances. In this context, lithium titanium oxide (LTO) would be a viable option among other available LIB anodes. Since the intercalation and deintercalation potential of LTO is around 1.55 V, there will be no (SEI) layer formation during the lithiation and de-lithiation processes. In addition, these electrodes exhibit long cyclic life and high-rate capability, hence it is considered as one of the potential anodes for EV applications [28-31]. Despite of these advantages, LTO has drawback of poor electrical conductivity and insulation behaviour leading to the low diffusion coefficient [32-33]. To enhance the electrical conductivity and diffusion coefficient of LTO, aqueous binders would be a choice for LIBs. Surprisingly, a few reports are available on aqueous binders for LTO anode, e.g. CMC, LA132, guar gum and pectin [31, 34-35]. In addition, the effect of binders has been studied for alloying and de-alloying materials such as CuO, Si, etc. [36, 37]. Furthermore, a comprehensive review on the role of water-soluble binders for high energy density electrode materials in LIB applications is reported in the literature [38]. Na-Alg and PVA were broadly studied either individually or cross linked with other aqueous binders, and the robust behaviour has been retained for many other cathode and anode materials as effective binders. To our knowledge, no report is available on Na-Alg and PVA binders for the fabrication of LTO anode.

Herein, we report the fabrication of LTO anodes using PVA and Na-Alg binders and their electrochemical performance against Li/Li$^+$. In addition, thermal stability and wettability of the binders, as well as variation of binder concentrations, electrical resistance, electrochemical impedance, morphology and swelling studies of electrodes have been investigated and correlated with its electrochemical performance.

## 3.2. Experimental

### 3.2.1. Materials

Polyvinyl alcohol (PVA, $M_W$ = 1,46,000-1,86,000 g/mol), sodium alginate (Na-Alg, $M_w$ = 1,20,000-1,90,000 g/mol) were received from Sigma-Aldrich, and $Li_4Ti_5O_{12}$ (LTO, d= 0.5-1.0 µm; purity 99%) was obtained from Linyi Gelon LIB Co., Ltd. Polyvinylidene fluoride (PVDF, $M_w$ = 1,56,000 g/mol) was purchased from Kynar. The Super C65 carbon black obtained from Timcal; Belgium was used as a conductive additive. The electrolyte solution of 1M $LiPF_6$ in a mixture of solvents namely ethylene carbonate (EC), diethyl carbonate (DEC) and dimethyl carbonate (DMC) in the ratio of 1:1:1 was purchased from BASF. All these chemicals were used as in received condition.

### 3.2.2. Characterization of electrodes

X-ray diffraction (XRD) analyses were carried out using Smart lab Rigaku X-ray diffractometer equipped with monochromatic Cu $K_\alpha$ radiation in the scan range of 10-85$^o$ for phase identification of the coated electrodes. All morphological analyses were performed by field emission scanning electron microscope (FE-SEM), Carl Zeiss, Germany. X-ray photoelectron spectroscopy (XPS) was performed with Omicron Nanotechnology, UK for the surface analysis of the cycled electrode.

### 3.2.3. Thermal, adhesive and swelling studies of the binders

Thermogravimetric analyses were performed by using Simultaneous Thermal Analyser (STA) STA 4497, QMS403C, NETZSCH, in argon atmosphere to determine the thermal stability of the binders. Adhesion strength test was conducted using a 180$^o$ peel tester (Mecmesin peel tester) with a speed of 30 mm/min. Swelling studies of the coated electrodes were carried out to observe the increased weight percentage of electrodes soaked in the 1M $LiPF_6$ in EC: DEC: DMC (1:1:1) electrolyte for 7 days.

### 3.2.4. Contact angle for pure binder electrodes

Contact angle (CA) measurements were performed inside the dehumidified room (<10% relative humidity) in order to minimize the influence of humidity on the electrolyte droplets. Pure binder solutions of PVA (3wt.%), Na-Alg (4wt.%) and PVDF (4wt.%) were coated on copper foil and CA was measured by using Kyowa - 601 (Kyowa Interface Science Co., Ltd.) with USB 3.0 CCD Camera. The coated binders on the copper foil 10 µm was exposed to electrolyte droplet for 5 seconds and measured their contact angle.

### 3.2.5. Resistance/Conductive measurements for coated electrodes

The electrode resistance was measured using four probe method (Keithely Model 6621 current source and 2180-volt source). The electrical resistance of the electrode was measured with reference to the current collector. An AC current was applied in the range of 10-70 µA and the corresponding voltage was measured across the electrode thickness. The experiments were repeated for three times and the average resistance was measured.

### 3.2.6. Cell preparation and electrochemical measurements

Electrochemical studies of all the electrodes were carried out in half-cell mode using Swagelok/coin cells, in which Li metal was used as the reference electrode. The electrode had a mixture of active material (LTO) in the range of 85-88 wt.% with conductive carbon (Super C65) of 10wt.% and the binder in the range of 2-5 wt.%. A homogenous slurry was prepared by manual mixing of the active material, conductive carbon and binder in water/N-methyl-2-Pyrrolidone (NMP) in a mortar and pestle. PVA was dissolved at high temperature (~100 $^{o}$C), whereas Na-Alg dissolved in water at room temperature. To this solution, a mixture of active material and conductive carbon was added and stirred continuously to get homogenous slurry. Electrodes were fabricated by coating the slurry onto the copper foil by doctor blade technique and dried in vacuum oven at 60-110 $^{o}$C for 12 h. To reduce the thickness and porosity, the electrodes were calendered by applying a pressure of 500 psi at room temperature and slit into15 mm diameter for cell fabrication. The active material loading was found to be 4.8 mg cm$^{-2}$. Cells using LTO cathode and lithium metal anode were fabricated inside the argon filled glove box (where $O_2$ and $H_2O$ were maintained <1ppm). Whatman glass microfiber filter paper (grade GF/D) was used as separator, and 1M $LiPF_6$ dissolved in (EC:DMC:DEC) (1:1:1 by v/v) was used as an electrolyte. LTO electrodes prepared by various binder compositions are given in Table 3.1.

**Table 3.1.** Aqueous binder electrodes and their composition.

| S.No | Material / Binder | Composition<br>(LTO: CB: B)<br>(AM: CC: B) | Name of Electrode |
|---|---|---|---|
| 1 | LTO/ PVA | 88:10:2 | PL2 |
| 2 | LTO/ PVA | 87:10:3 | PL3 |
| 3 | LTO/ PVA | 86:10:4 | PL4 |
| 4 | LTO/ PVA | 85:10:5 | PL5 |
| 5 | LTO / Na-Alg | 88:10:2 | NL2 |
| 6 | LTO / Na-Alg | 87:10:3 | NL3 |
| 7 | LTO / Na-Alg | 86:10:4 | NL4 |
| 8 | LTO / Na-Alg | 85:10:5 | NL5 |
| 9 | LTO/PVDF | 86:10:4 | PF4 |

Galavanostatic charge / discharge cycling was carried out using BT-2000 Arbintester in the voltage range of 1.0 – 3.0 V *vs.* Li/Li$^+$. Further, cyclic stability study at 0.1C and 1C-rates was carried out for 100 and 500 cycles. Rate capability studies were performed up to 5C-rate. Cyclic voltammetry (CV) studies for pure binders as well as electrodes were conducted at scan rates of 0.05 and 0.1 mV s$^{-1}$, respectively, in the range of 1.0 – 3.0 V *vs.* Li/Li$^+$. The CV of bare copper foil was also recorded under identical conditions as reference. Electrochemical impedance spectroscopy (EIS) measurements were carried out with Parstat MC electrochemical workstation (Princeton applied research, USA) in the frequency range of 1 MHz to 0.01 Hz.

### 3.2.7. Characterization of cycled electrodes

Post mortem analyses were carried out for electrodes of PL3, NL4 and PF4 after charge/discharge at 1C rate after 100 cycles for SEM analyses. Furthermore, PL3 electrode was characterized for XPS analyses. For this, Swagelok cell was disassembled in the glove box after the cycling, and the electrode was washed with DMC for removal of electrolyte from the electrode and dried in glove box.

## 3.3. Results and discussion

Thermal analysis of PVA, Na-Alg and PVDF binders was done by thermal gravimetric analysis (TGA). The weight of the binder as a function of temperature for different binders and the corresponding derivative weight *vs*. temperature plots are shown in Fig. 3.1(a, b). The observed data are in good agreement with the reported values in the literature [8, 39-40]. Compared to PVDF, both these aqueous binders exhibited relatively less thermal stability. However, the aqueous binders did not show any appreciable weight loss up to 200 $^{o}$C, which suggests that they can be used for LIB electrode fabrication wherein the drying temperature will be < 150 $^{o}$C.

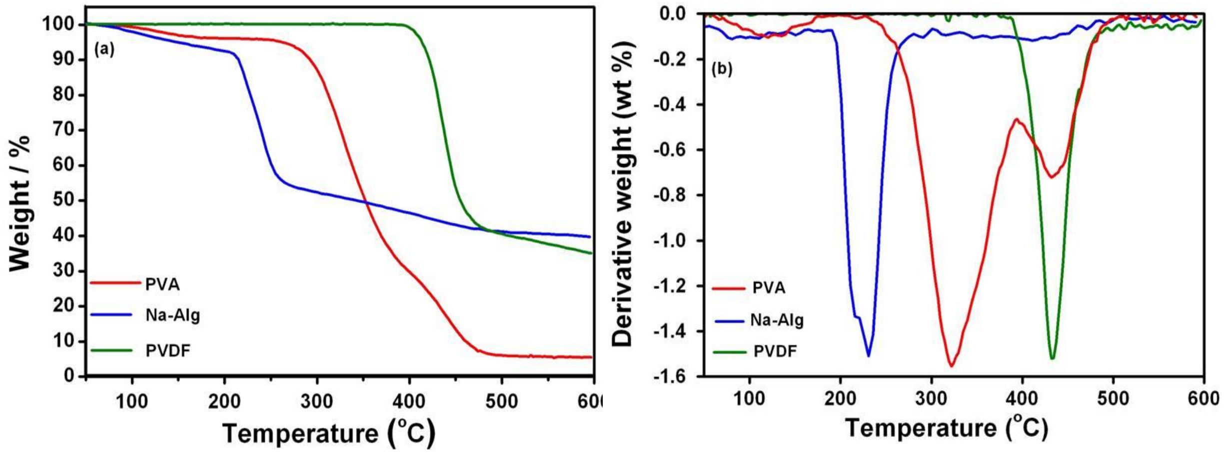

**Figure 3.1.** TGA plots of the binders: (a) Weight of the binder as a function of temperature (b) derivative weight as a function of temperature.

In order to study the electrochemical stability of PVA, Na-Alg and PVDF, thin films of these binders were coated on copper foils and CV studies were carried out in the potential range of 1.0 – 3.0 V *vs*. Li/Li$^{+}$ at a scan rate of 0.05 mV s$^{-1}$ (Fig. 3.2(a, b)). The CV profile of copper foil did not show any redox wave. Whereas, the thin film electrodes exhibited small reduction peaks (nA range) in the potential range between 1.2 and 1.7 V, after successive cycles, which correspond to the reduction of residual moisture present in the electrolyte [41, 42]. Thus, the CV characteristics indicate that the binders have excellent electrochemical stability in the given potential window.

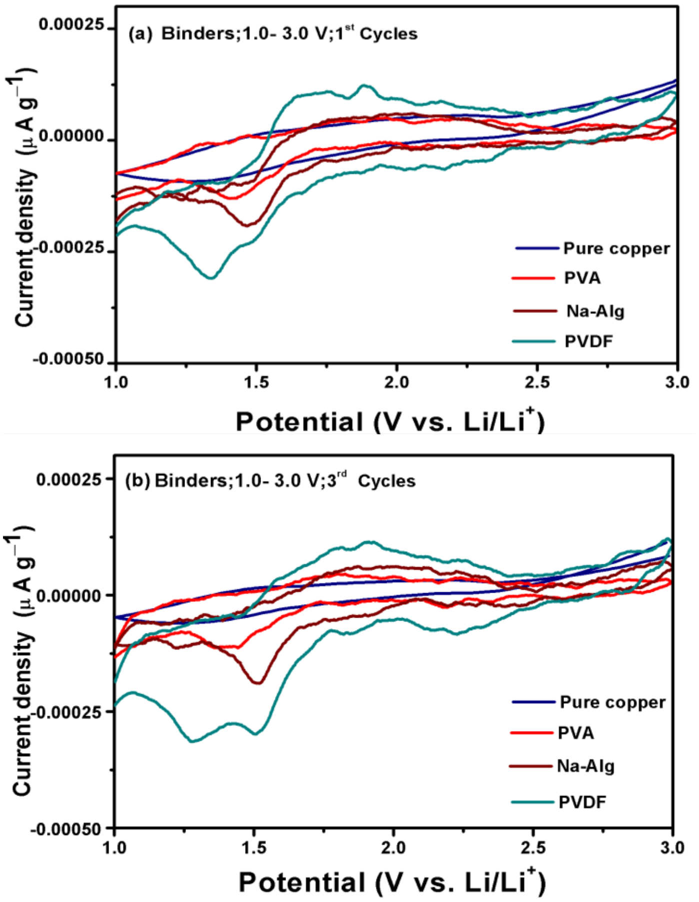

**Figure 3.2.** Cyclic voltmmaograms of copper foil and binders (a) first cycle and (b) third cycle.

Electrolyte absorption on electrode plays a crucial role in the good ionic movement with aqueous as well as non-aqueous binders. Figure 3.3 displays the CA measurements obtained for electrolyte (1M $LiPF_6$ in EC:DMC:DEC) drop placed on the surface of the binder films. It can be seen from Fig. 3.3 that the CA values were observed as 28.5, 38.4 and 32.2 for PVA, Na-Alg, and PVDF, respectively. The PVA film has shown the lower angle than Na-Alg and PVDF films. This indicates that PVA film has a high degree of wettability due to the hydroxyl groups and some amount of acetate groups present as the degree of saponification. So the acetate group may weaken the PVA hydroxyl groups as similar to the carboxymethyl group that affects in CMC. Hence the decrease in the hydrogen bonding helps to increase in the infiltration of electrolyte rapidly [43]. In Na-Alg, the presence of intra hydrogen bonding between hydroxyl groups and carboxylic groups are stronger compared to that of PVA. Due to this, the hydrogen bonding between the binder and the active material has increased, which leads to the decrease in the electrolyte absorption. Due to the high molecular weight of PVDF, the entanglement of polymer chains may impede the electrolyte wetting. Hence it shows the less uptake of the electrolyte with binder film. These results indicated that the PVA binder shows better wettability than Na-Alg and PVDF binders. Table 3.1 presents the details of LTO electrodes that have been prepared using different binder contents along with different compositions of active materials and conductive carbon. X-ray diffraction patterns of all electrodes have shown the line characteristics of pure phase LTO (JCPDS card no: 49-0207) with high crystallinity as reflected from the narrow diffraction peaks, seen in representative graph given in Fig. 3.4. The characteristic lines are due to the cubic crystal structure with $Fd\bar{3}m$ space group with spinel structure of LTO [44].

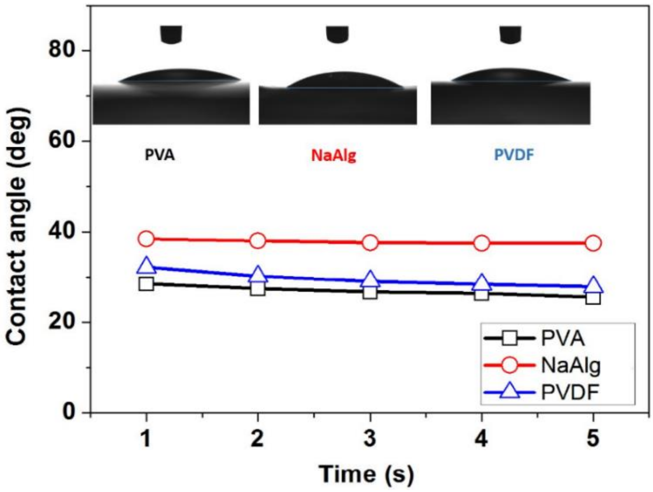

**Figure 3.3.** Contact angle measurement of an electrolyte with binder films and their contact angle after 5 s.

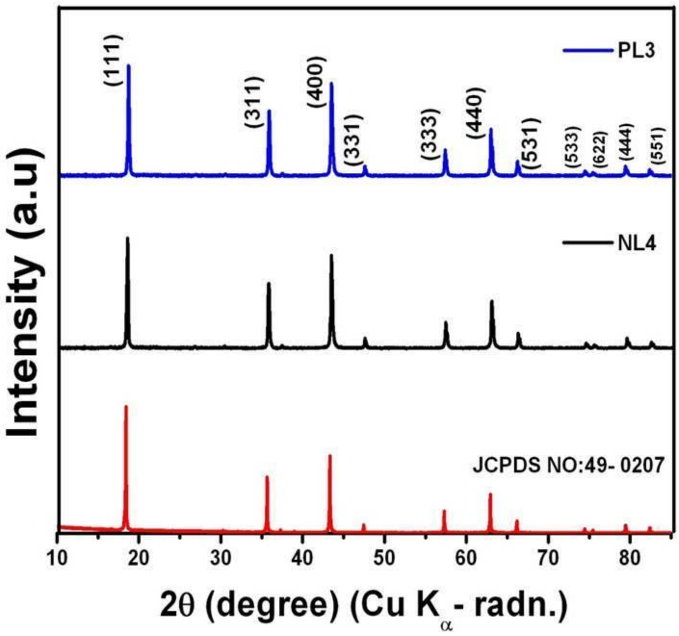

**Figure 3.4.** XRD pattern for LTO electrodes with PL3 and NL4.

Since binder plays a vital role in achieving better adhesion and cohesion of active materials, optimization of its composition is crucial for the fabrication of electrodes. Electrodes were fabricated with the binder content in the range of 2 to 5 wt.% and their electrochemical performances are given in Fig. 3.5. Figure 3.5(a) shows the first discharge/charge profile of PL electrodes with different binder concentrations in the voltage range of 1.0 – 3.0 V at 0.1C-rate. The discharge/charge voltage plateau at ~1.55 V is due to insertion/de-insertion of $Li^+$ into LTO [45]. Electrodes PL2 and PL3 showed almost same initial discharge/charge capacities of 168/159 and 167/156 mAh $g^{-1}$, respectively (Table 3.2). Whereas, PL4 and PL5 electrodes exhibited the initial discharge/charge capacities of 161/146 mAh $g^{-1}$ and 175/157 mAh $g^{-1}$, respectively. In all the four cases, a higher discharge capacity was observed in the first cycle when compared to charge capacity, which could be due to the presence of titanium oxide impurities in the active material [46, 47]. The capacity *vs*. cycle number plots for the electrodes up to 50 cycles at 0.1C-rate are depicited in Fig. 3.5(b).

Both PL2 and PL3 showed higher capacities without any noticeable capacity degradation. A reversible capacity of 155 mAh $g^{-1}$ with capacity retention of 96% was achieved at the end of 50 cycles for both of them. In the case of PL4, a capacity of 140 mAh $g^{-1}$ after 50 cycles with the retention of capacity 93% was obtained. Despite higher initial capacity of 175 mAh $g^{-1}$, PL5 electrode did not show good cyclic stability as its capacity reduced to 140 mAh $g^{-1}$ with capacity retention of 92% at 50th cycle. At 0.1C-rate, there is no clear indication of the influence of the binder content on the electrochemical performance of the electrode. However, it is to be noted that PL2 and PL3 electrodes showed better cyclic stability when compared to the other electrodes.

**Table 3.2.** Electrochemical performance for various electrodes at 0.1C-rate.

| **S.No** | **Electrode** | **Discharge capacity (mAh$g^{-1}$)** | | | **Irreversible capacity (mAh $g^{-1}$)** | **Capacity retention (%)** |
|---|---|---|---|---|---|---|
| | | **1st cycle** | **2nd cycle** | **nth cycle** | | |
| 1 | PL2 | 168 | 162 | 155 (50) | 10 | 96 |
| 2 | PL3 | 167 | 161 | 154 (50) | 11 | 96 |
| 3 | PL4 | 161 | 150 | 140 (50) | 07 | 93 |
| 4 | PL5 | 175 | 157 | 145 (50) | 16 | 92 |

| | | | | | | |
|---|---|---|---|---|---|---|
| 5 | NL2 | 139 | 139 | 66 (20) | 03 | 48 |
| 6 | NL3 | 147 | 143 | 101 (20) | 05 | 71 |
| 7 | NL4 | 172 | 159 | 139 (50) | 16 | 87 |
| 8 | NL5 | 131 | 131 | 129 (50) | 02 | 98 |
| 9 | PF4 | 154 | 150 | 128 (30) | 09 | 85 |

The discharge/charge cycling of PL2, PL3, and PL5 electrodes were carried out at 1C-rate, and the capacity *vs*. cycle number plots for PL2 and PL3 are shown in the inset of Fig. 3.5(b). The electrode PL2 showed an initial discharge capacity of 130 mAh g$^{-1}$ which decreased to 100 mAh g$^{-1}$ in first 10 cycles. The capacity is found to be stable for the remaining cycles. In the case of PL3, a capacity of 139 mAh g$^{-1}$ was observed in the initial cycle, and the same capacity was retained even after 100 cycles. On the other hand, PL5 at 1C-rate showed an initial specific capacity of 115 mAh g$^{-1}$, which dropped to 52 mAh g$^{-1}$ at 100th cycle (Figure not shown). These results reveal that PL3 having a binder content of 3wt.% showed better cyclic performance than any other binder compositions. The stable cycling performance of the electrode with PVA aqueous binder is possibly due to the strong hydrogen bonding of hydroxyl groups with active materials as well as better adhesion of active materials with the current collector [19].

The electrochemical performance of NL electrodes with varied binder concentrations was studied. Figure 3.5(c) shows the initial discharge/charge profiles of NL electrodes at 0.1C-rate and their capacity *vs*. cycle number plots are depicted in Fig. 3.5(d). The first discharge/charge capacities of the NL2 electrode were 139/136 mAh g$^{-1}$. The capacity of NL2 decreases with an increase in a number of cycles and after 20 cycles it was found to be 60 mAh g$^{-1}$ with capacity retention of 48%. In the case of NL3, the first cycle capacity was 147/142 mAh g$^{-1}$, which follows a similar trend as of NL2, and it exhibited 100 mAh g$^{-1}$ with capacity retention of 70% at the end of 20 cycles. NL4 showed the highest 1st cycle discharge/charge capacity of 172/156 mAh g$^{-1}$. The second cycle discharge capacity was found to be 159 mAh g$^{-1,}$ and it gradually decreased to 139 mAh g$^{-1}$ at the end of 35 cycles with capacity retention of 87% and thereafter it remained stable for 50 cycles with capacity retention of >99%.

On the other hand, the first cycle capacity of 131/129 mAh $g^{-1}$ was observed for the NL5 electrode, and the electrode exhibited the stable capacity up to 50 cycles with >95% capacity retention. With an increase in cycle number, NL2 and NL3 have undergone capacity degradation, while NL4 and NL5 showed better cyclic stability. However, during initial cycles the specific capacity of NL4 electrode was higher than the NL5 electrode. Hence, the high specific capacity of NL4 is due to the strong chemical interaction of alginate and LTO particles, as reported by others with different electro active materials. Nevertheless, the discharge capacities of all PL electrodes were quite stable than the NL electrodes for all weight percentages at 0.1C rate.

In order to test the feasibility of using these aqueous binders as alternatives to PVDF binder, further studies such as cyclic stability and charge/discharge cycling studies at high C-rates were carried out with PL3, NL4, and PF4 electrodes. The discharge/charge and cyclic stability plots at 0.1C-rate for PL3, NL4 and PF4 electrodes in the potential range between 1.0 and 3.0 V *vs*. $Li/Li^+$ are shown in Fig. 3.6. It can be seen from Fig. 3.6(a) that the first cycle profiles of PL3 and NL4 show flat plateau with negligible polarization when compared to that of PF4 electrode. The first cycle specific capacities of PL3 (167/156 mAh $g^{-1}$), NL4 (172/156 mAh $g^{-1}$) are higher than that of PF4 (154/145mAh $g^{-1}$). The LTO electrode with poly-acrylonitrile aqueous binder has been reported to give an initial capacity of 152 mAh $g^{-1}$ [48]. Among all the electrodes, the PL3 electrode showed a better electrochemical performance and lower polarization potential with a specific capacity of 154 mAh $g^{-1}$ at the end of the 50th cycle as shown in the Fig. 3.6(b). Although the NL4 showed higher initial capacity than PL3, the capacity decreased gradually to 139 mAh $g^{-1}$ at the end of the 50th cycle. On the other hand, the PF4 electrode experienced a high-capacity degradation and showed only 128 mAh $g^{-1}$ after 30 cycles as exhibited in Fig. 3.6(c).

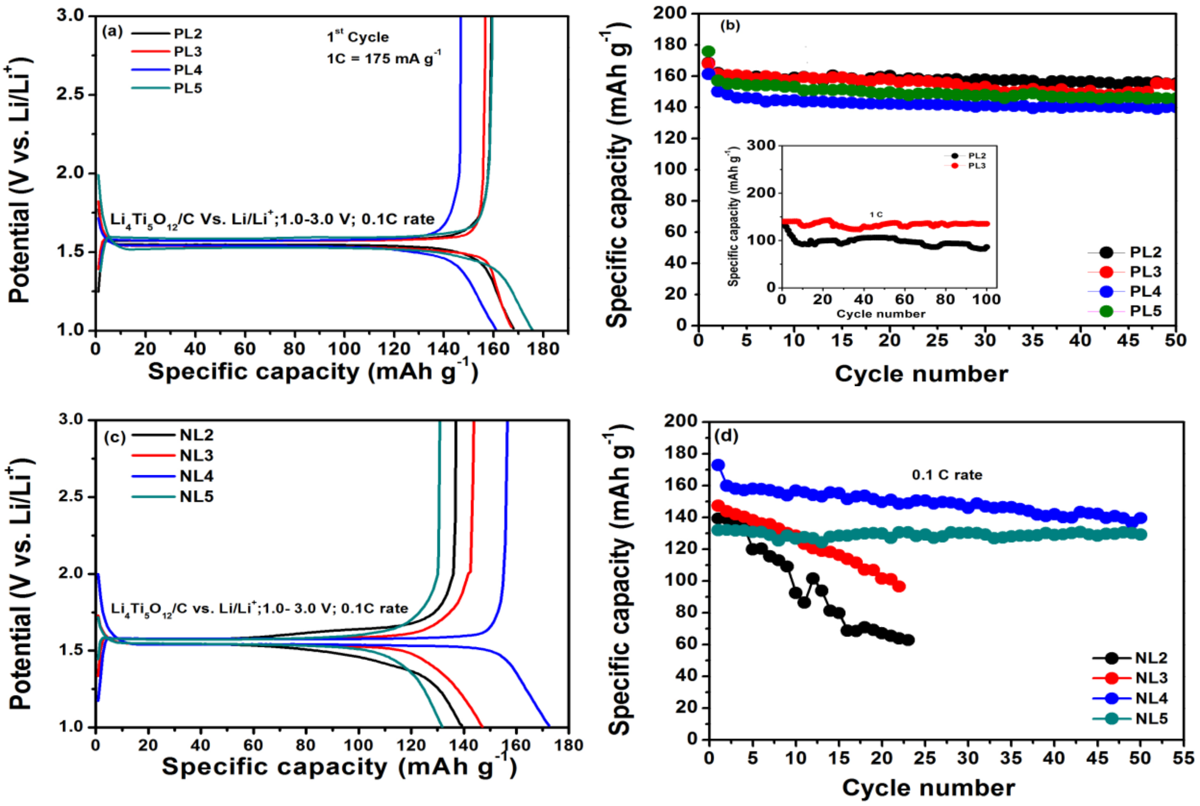

**Figure 3.5.** (a), (c) Galvanostatic cycling of PL (2-5 at 0.1C-rate) NL (2-5 at 0.1C rate), (b), (d) Cyclic stability of PL (2-5) and NL (2-5 at 0.1C-rate).

Figure. 3.6(d) shows the charge/discharge and cyclic stability profiles of PL3, NL4 and PF4 electrodes at 1C-rate. PL3 electrode showed 1st discharge specific capacity of 139 mAh $g^{-1}$ and the specific capacity was maintained at ≥140 mAh $g^{-1}$ for 100 cycles, with capacity retention of >99%. In the case of NL4, the initial cycle capacity was 112 mAh $g^{-1}$, which got reduced to 97 mAh $g^{-1}$ at the end of the 100th cycle with 86% capacity retention. Similarly, PF4 also exhibited the first cycle capacity of 112 mAh $g^{-1}$ while at 100th cycle the capacity was 80 mAh $g^{-1}$ with capacity retention of 71%. Higher capacity retention and stable capacity of PL3, when compared to the other two binders, are effectively due to the presence of optimized hydroxyl groups in PVA, which ensures better electrode binding and electrolyte infiltration as reported by Eunsuok Oh et al. [19].

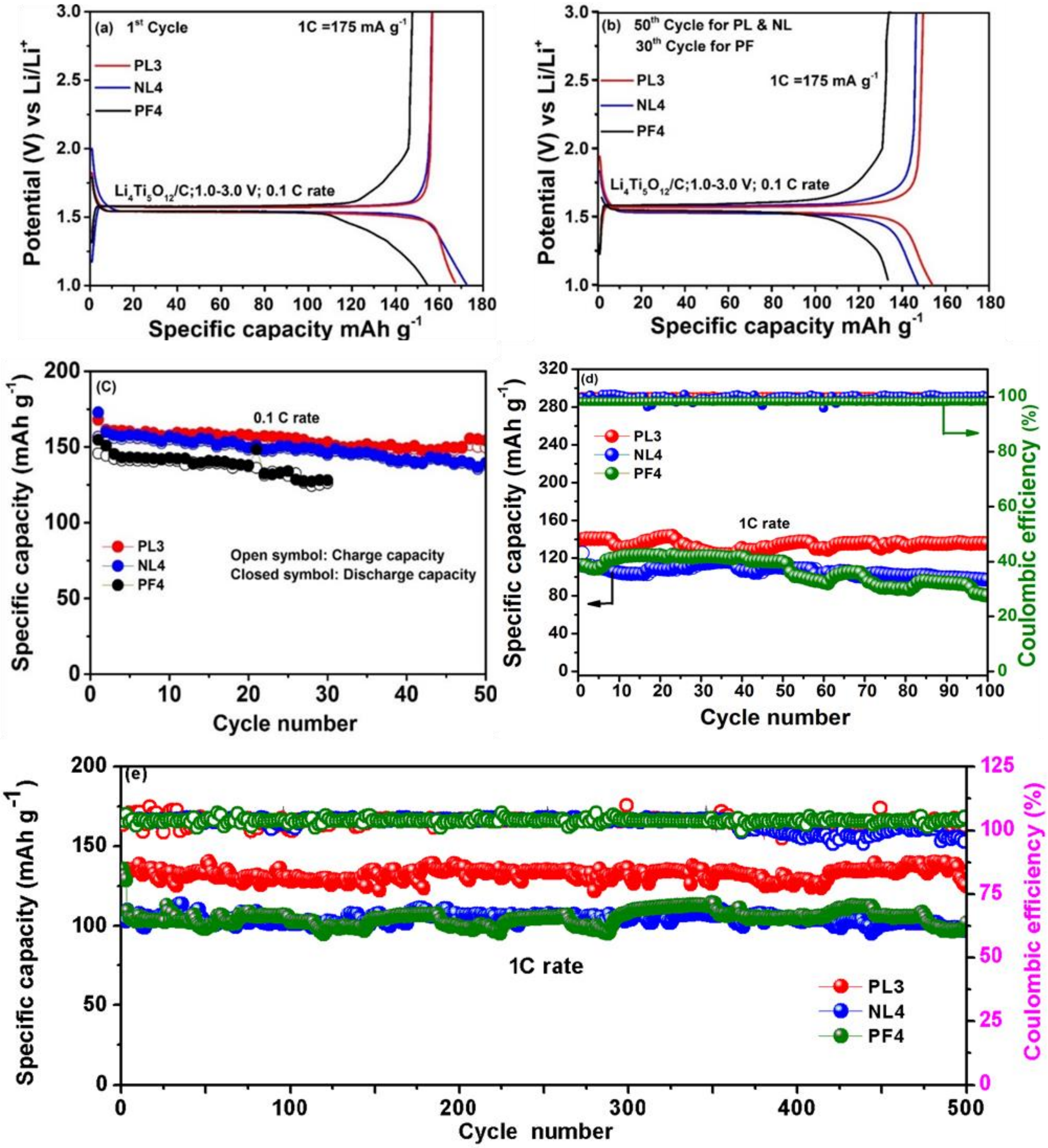

**Figure 3.6.** Galvanostatic cycling of PL3, NL4 and PF4 at 0.1C and 1C-rate a) First cycle at 0.1C b) 30th and 50th cycles at 0.1C c) Cyclic stability profiles at 0.1C and d) at 1C for 100 cycles e) discharge specific capacitites at 1C for 500 cycles.

Nevertheless, the columbic efficiencies in all the three cases were in the range of 98-100%. In the case of PL3, the binder concentration is lower than NL4 and PF4. Lower binder concentration increases the loadings of active materials and hence increases the specific capacity as explained by Lu et al. [49]. Further, higher binder concentration in PF4 and NL4 possibly minimizes the contact between active materials and conductive carbon. Even though, Na-Alg has both carboxylic and hydroxyl groups, the low electrochemical performance at high C-rate might be due to the low adhesion and high electrical resistance of NL4 electrode. The higher specific capacity and better retention at 0.1 and 1C-rates makes PVA electrode as promising aqueous binder electrode for LIBs. Further, we have also performed the charge/discharge cycles for PL3, NL4 and PF4 electrodes for 500 cycles at 1C-rate as shown in Fig. 3.6(e). PL3 electrode exhibits a stable discharge capacity of 130 mAh $g^{-1}$ with a capacity retention of ≥96% after 500 cycles. Whereas, the NL4 and PF4 electrodes showed the initial specific discharge capacitates of 104 and 135 mAh $g^{-1}$ with capacity retentions of ≥93 and ≥77% at the end of 500 cycles, respectively. In all cases, coulombic efficiences are in the range of 97- 99%.

The cycling performance at different current rates was performed for all three electrodes. The plots of specific capacity *vs*. cycle number for PL3, NL4 and PF4 electrodes at current rates from 0.1 to 5C-rates are shown in Fig. 3.7(a). At 0.1C-rate, PL3 showed an initial discharge capacity of 167 mAh $g^{-1}$, which is very close to the initial discharge capacity of 172 mAh $g^{-1}$ for NL4. Both the electrodes have shown higher initial discharge capacities when compared to PF4; the latter showed initial discharge capacity of 138 mAh $g^{-1}$. In the range of current rates from 0.5 to 2C, both NL4 and PF4 electrodes have shown nearly the same discharge capacity. However, at 2C and 5C-rates, NL4 exhibited specific discharge capacities of 56 and 10 mAh $g^{-1}$, and PF4 delivered 52 and 36 mAh $g^{-1}$, respectively. On the other hand, PL3 yielded the specific capacities of 96 mAh $g^{-1}$ at 2C and 80 mAh $g^{-1}$ at 5C-rate. A distinctly stable cycling performance was noticed for PL3 electrode at high C-rates compared to NL4 and PF4 counterpart. After that, the cells were cycled back to 1C-rate. In all three cases, the capacities are reproducible, indicating the rate capable behaviour of these electrodes. Recently, Kalaiselvi et al. has reported the high specific capacity of 116 mAh $g^{-1}$ at 5C-rate with LA132 for LTO anode, which is close to the obtained capacity of our PL3 electrode at the same rate [32]. Further, Eun-Suok Oh and Stefano Passerini et al. have shown a very high capacity of 140 and 157 mAh $g^{-1}$ at 4C/5C-rates with Galactomannan gum and Pectin/PA binders for LTO anode [33]. Apart from this, recent literature survey of LTO with aqueous binders has summarized in Table 3.3.

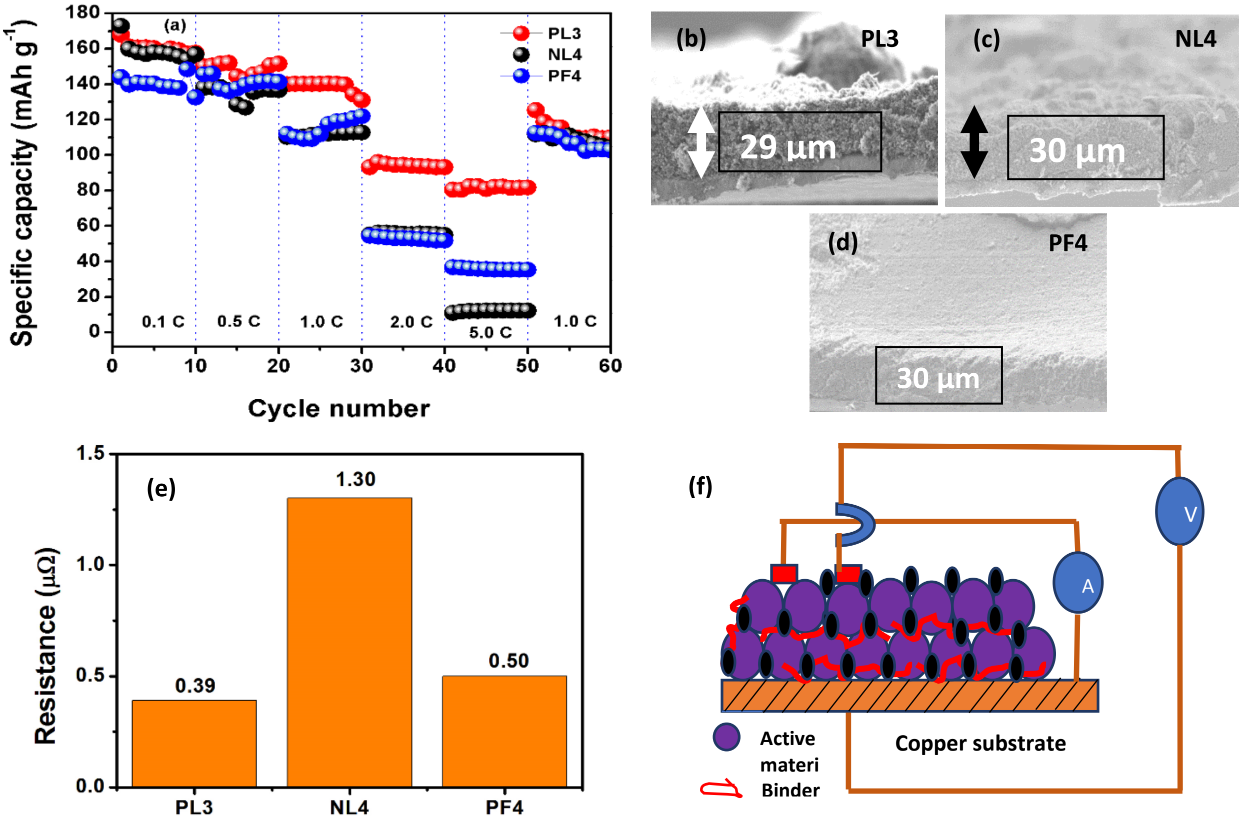

**Figure 3.7.** a) Rate capability of PL3, NL4 and PF4 electrodes, (b, c and d) SEM cross sections of PL3, NL4 and PF4 electrodes e) Resistance profiles of the electrodes f) Schematic diagram for four probe measurement.

**Table 3.3.** Literature reported values for LTO with different aqueous binders.

| **S.No** | **Aqueous Binder used with LTO** | **Specific discharge capacity (mAh g$^{-1}$) at different C-rates** | | | | | **Reference** | **Binder (wt.%)** |
|---|---|---|---|---|---|---|---|---|
| | | 0.1 | 0.5 | 1.0 | 2.0 | 5.0 | ----------- | |
| 01 | CMC | ------ | 150 | 150 | 140 | 130 | [32] | 10 |
| 02 | LA132 | 175 | 160 | 155 | 145 | 116 | [33] | 10 |
| 03 | CMC | 175 | 160 | 150 | 130 | 90 | [41] | 5 |
| 04 | GG | 180 | 168 | 160 | 158 | 140/ 4C | [48] | 5 |
| 05 | TG | 165 | 155 | 150 | 145 | 130/ 4C | [48] | 5 |
| 06 | Pectin/ PA | 178 | 170 | 170 | 167 | 157 | [48] | 5 |

|  |  |  |  |  |  |  |  |  |
|---|---|---|---|---|---|---|---|---|
| 07 | PVA | 167 | 149 | 140 | 96 | 80 | This work | 3 |
| 08 | NaAlg | 172 | 137 | 110 | 56 | 10 | This work | 4 |

In order to understand better the capacity retention of PL3 electrode at high C-rate, porosity calculation and electrical resistance of the electrodes were performed. The percentage of porosity was calculated according to equation given by V.S. Battaglia et al. [50]. The electrodes PL3, NL4, and PF4 exhibited porosities of 40%, 41% and 40%, respectively. Binder plays a crucial role in the electrical resistance of the electrode. The thickness of all the three calendared electrodes were maintained at ~30µm and the measurements were carried out across the electrode thickness to understand the resistance behaviour across the electrode and current collector. Figure 3.7(b, c, d, e and f) shows the SEM cross sectional images and resistance profile of the electrodes, and schematic diagram for four probe measurement setup, respectively. These experiments were repeated for three times for each sample at every current range and they showed the consistent value (Fig. 3.7 (e) with an error limit of ± 0.2%). The data confirmed that the resistance is in the order of PL3< PF4< NL4.

It is evidenced from the Fig. 3.7(e) that the resistance value of PF4 is marginally greater than PL3, whereas the resistance of NL4 is much higher than the both PL3 and PF4. Thus, it suggests that the electrodes PL3 and PF4 are anticipated to perform well at high C-rate applications. At 5C-rate, the capacity retention of PL3, PF4 and NL4 was 48, 26 and 6% with respect to that of 0.1C-rate. The enhanced rate capability of PL3 could be due to the better percolation of the electrolyte, and good lithium-ion diffusion kinetics than NL4 and PF4. The CV profiles of PL3, NL4 and PF4 electrodes at a scan rate of 0.05 mV $s^{-1}$ in the potential range of 1.0-3.0 V *vs*. Li/$Li^+$ are shown in the Fig. 3.8(a). The electrode PL3 shows an anodic peak at 1.66 V and a cathodic peak at 1.44 V. The potential difference between the anodic and cathodic peaks ($\Delta E$ = 220mV) corresponds to the redox process of LTO. The electrode NL4 exhibited anodic wave at 1.66 V and a cathodic wave at 1.44 V ($\Delta E$ = 220mV). The PF4 electrode has exhibited the oxidation peak at 1.65 V and the reduction peak at 1.49 V ($\Delta E$ = 160mV). It is known that $\Delta E$ is a measure of polarization of the electrode, which is inversely proportional to the ionic conductivity. NL4 electrode experiences more polarization than the PL3 electrode, hence the ionic conductivity of PL3 is higher than NL4.

To empathise the $Li^+$ ion kinetics for LTO electrode with PVA, Na-Alg and PVDF binders, CV studies were carried out at different scan rates from 0.05-5.0 mV $s^{-1}$, in the potential window of 1.0 – 3.0 V *vs*. Li/$Li^+$ electrode. The voltammograms for PL3 has been shown in Fig. 3.8(b), and the peak current *vs*. square root of scan rate is depicted in Fig. 3.8 (c). For both NL4 and PF4 electrodes, CVs at diferent scan rates and the plots of peak current *vs*. square root of scan rate of NL4 and PF4 are shown in Fig. 3.9.

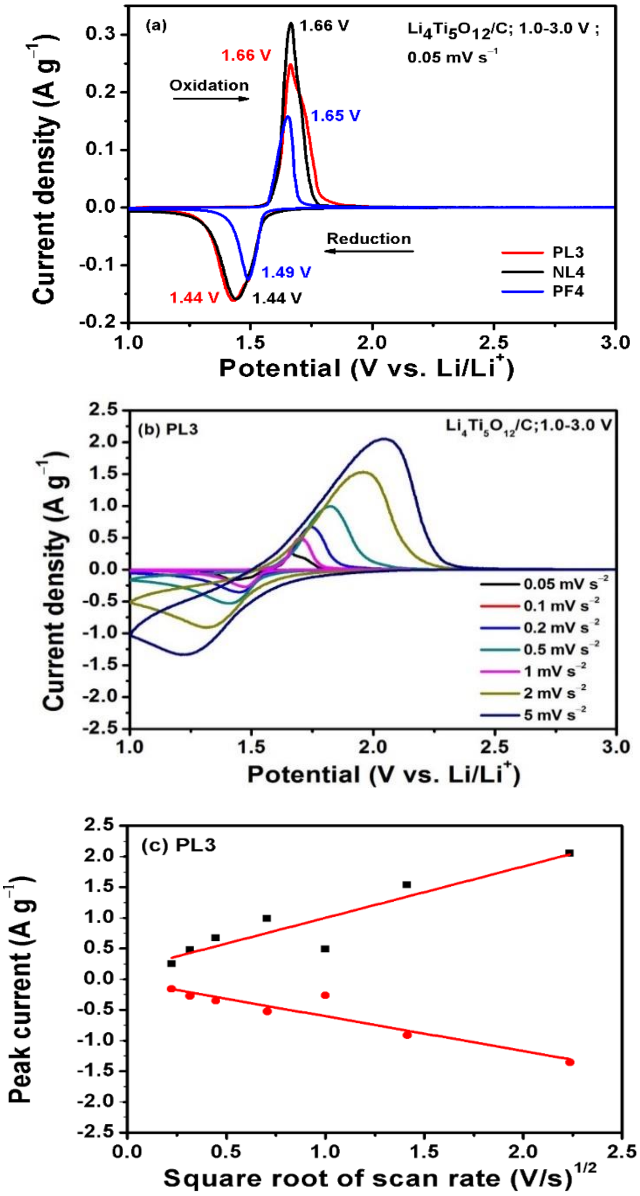

**Figure 3.8.** a) Cyclic voltammetry analysis of PL3**,** NL4 and PF4 electrodes at 0.05mV s$^{-1}$ and (b-c) cyclic voltammograms of different scan rates and peak current *vs*. square root of the scan rate of PL3**.**

In all the three cases, as the scan rate increases, the anodic peak potential shifts towards more positive values and the cathodic peak potential shifts towards less positive values. In addition, the cathodic and anodic peak currents increase with an increase in the scan rate.

The peak current increased linearly with the square root of the scan rates suggesting that the intercalation of $Li^+$ ion within LTO electrode is a diffusion-controlled process. It is also observed that among three electrodes, PF4 has shown more sharp peaks than the PL3 and NL4 due to the high crystalline nature of PVDF rather than Na-Alg and PVA. Further, $Li^+$ ion diffusion coefficients ($D_{Li^+}$) for PL3, NL4 and PF4 were calculated from the CV data using the Randles-Sevcik equation, given in Equation (3.1)

$i_p = 2.69 \times 10^5 n^{3/2} A D^{1/2} C_{Li^+} \nu^{1/2}$ ---------------------------------------------------------- 3.1

where, $i_p$= Peak current

n = No of electrons involved in the reaction; A= Area of the electrode;

D= Diffusion Coefficient ($D_{Li^+}$); C= Concentration in mol/cm$^3$; $\nu$ = Scan rate in V $s^{-1}$

The parameters such as n, A, C and ν calculated from the CV data are used to determine the $D_{Li^+}$. The $D_{Li^+}$ values for PL3, NL4 and PF4 electrodes are found to be $2.34\times10^{-13}$, $3.02\times10^{-15}$ and $9.6\times10^{-15}$ cm$^2$s$^{-1}$, respectively. These data's are in coherence with the reported lithium diffusion coefficient values for LTO electrodes in the literature [51, 52]. It is well known that electrodes with low glass transition temperature binder exhibits the higher lithium diffusion coefficient due to free mobile $Li^+$ ion as reported by Wang et al. [53]. PVA binder has shown good wettability and lower glass transition temperature (Tg,~85 $^{O}$C) than Na-Alg (Tg~110 $^{O}$C). In addition, PL3 electrode shows less swelling behavior, better adhesive and optimum porosity compared to that of the other two electrodes. Hence, these behaviors might strongly influence the better percolation of electrolyte, as a result, the better ionic diffusion can be expected. The higher diffusion coefficient of PL3 electrode suggests that it facilitates better $Li^+$ ion transport within the LTO electrode when compared to NL4 and PF4 electrodes. As a result, the PL3 electrode showed an improved electrochemical performance.

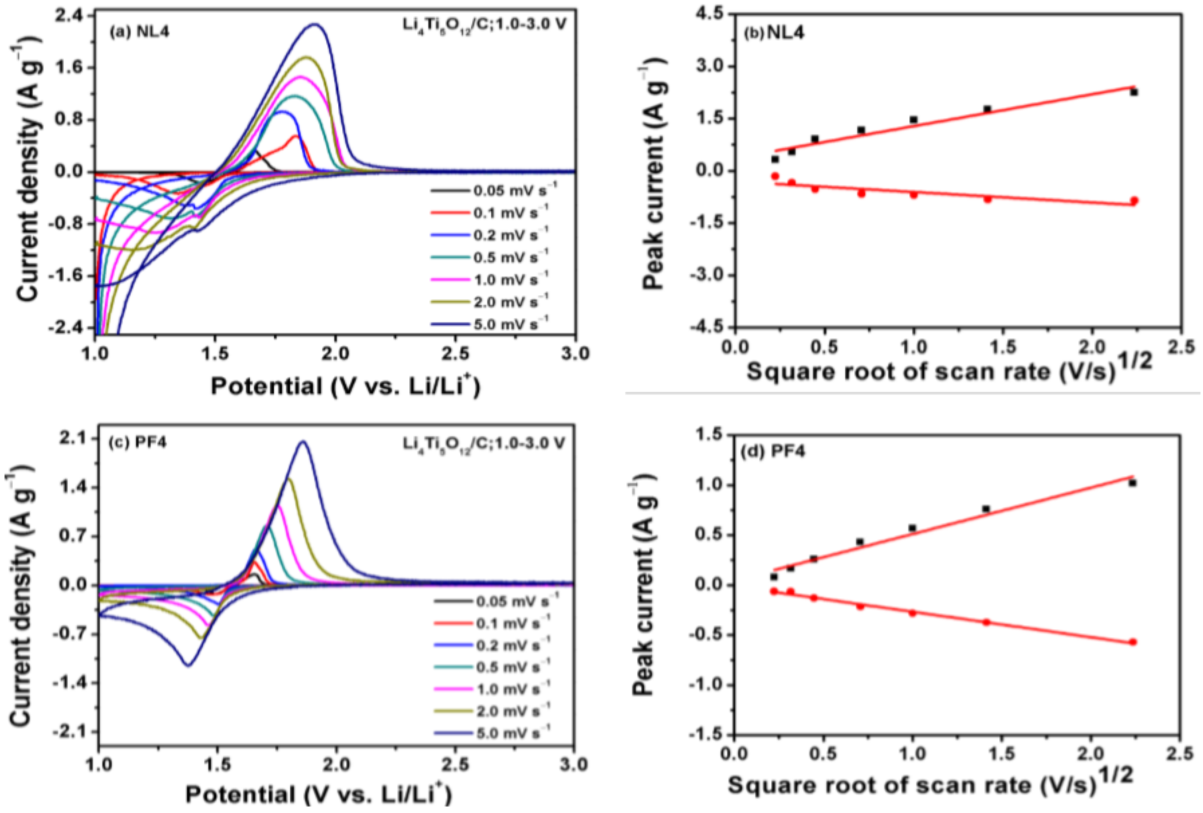

**Figure 3.9.** a, c) CVs at different scan rates and b, d) plot of peak current *vs*. square root of scan rate for NL4 and PF4 electrodes.

Further to assess the performance of these electrodes, EIS analyses were performed for pristine and cycled cells. Nyquist plots for the LTO electrodes with PL3, NL4, and PF4 were recorded before OCV analysis and after cycling of 100 cycles at 1C-rate and are shown in Fig. 3.10(a, b). The plots were fitted using an equivalent circuit model as shown in Fig. 3.10(c) and the fitted data are shown in Table 3.4. Where, $R_s$ is the solution resistance, $R_f$ is the film resistance, $C_f$ is the film capacitance, $R_{ct}$ is the charge transfer resistance, $CPE_{dl}$ is the double layer capacitance and $W_o$ is the Warburg impedance. In all cases, the spectra show a depressed semicircle and a sloped straight line. The depressed semicircle at high to moderate frequency region (Fig. 3.10) is due to the charge transfer resistance ($R_{ct}$) and double layer capacitance ($CPE_{dl}$) between the electrode and electrolyte interface. The linear line at an angle of 45° at low frequency region is ascribed to Warburg impedance ($W_o$), which is due to the $Li^+$ ion diffusion within the solid electrode.

It can be seen from Fig. 3.10 and Table 3.4. that the PL3 electrode showed lowest $R_{ct}$ while compared to that of NL4 and PF4 electrodes at open circuit voltage (OCV) and the same trend was maintained for the electrodes after 100 cycles. But in the case of NL4 and PF4 electrodes, the $R_{ct}$ values are quite closer and exhibited the similar trend. Moreover, the solution resistance of $R_s$ was quiet low for PL3 than the NL4 and PF4 electrodes. This result corroborated the improved electrochemical performance observed for the PL3 electrode. This in turn correlates with the enhanced conductivity for PL3 electrodes as compared to NL4 and PF4 (rate capability section). This result infers the increase in the $Li^+$ ion kinetics of PL3 which enhances the conductivity by a decrease in the resistance as mentioned by Eunsukoh et al. [19]. Apart from this, the high $R_{ct}$ of PF4 is correlated to the more swelling nature of PVDF, hence reduction in the specific capacity of the electrode.

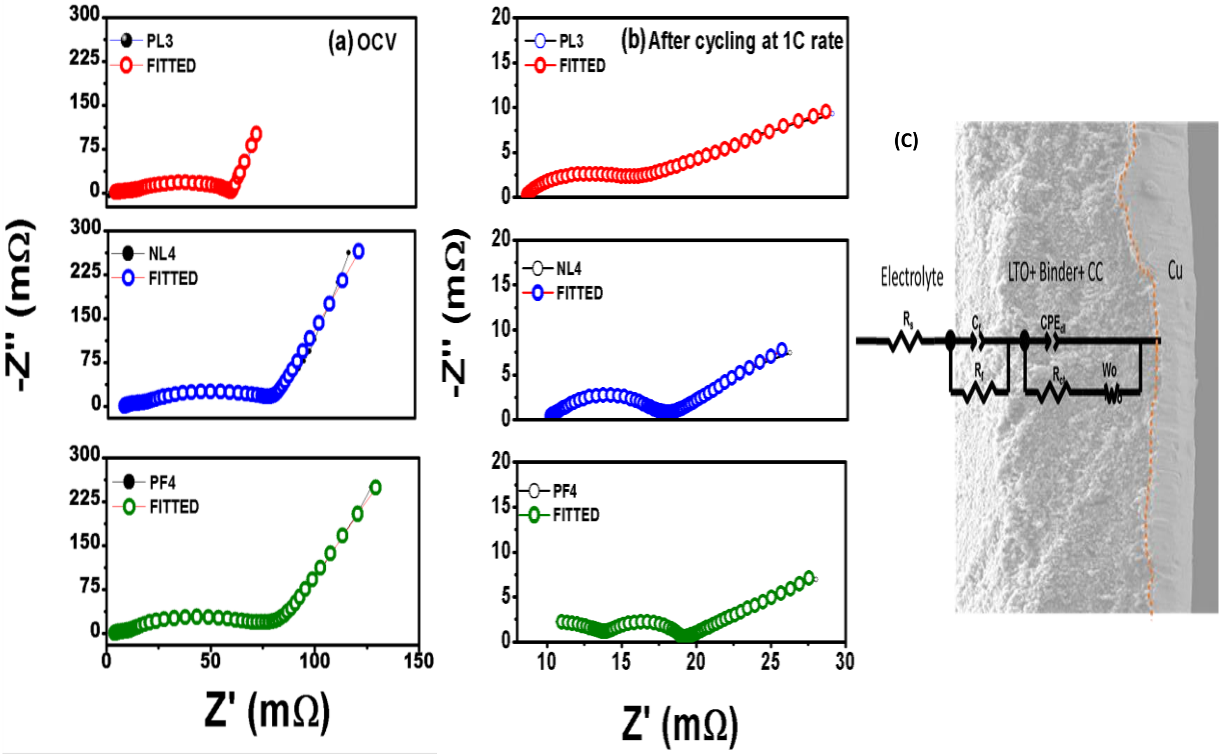

**Figure 3.10.** EIS spectra of PL3, NL4 and PF4 Electrodes a) Nyquist plots of OCV electrodes b) Nyquist plots for electrodes after 100 cycles at 1C rate c) Equivalent circuit for fitting of PL3, NL4 and PF4 Electrodes for both OCV and cycled electrodes.

**Table 3.4.** Impedance parameters after the galvanostatic cycling at 1C-rate for PL3, NL4 and PF4 electrodes.

| S.No | Binder | $R_s$ (mΩ) | $R_{ct}$ (mΩ) | $CPE_{dl}$ (μF) | % Error for $R_{ct}$ |
|---|---|---|---|---|---|
| 1 | PL3 | 0.04 | 3.60 | $1.37 \times 10^{-4}$ | 5.65 |
| 2 | NL4 | 0.09 | 6.92 | $4.17 \times 10^{-5}$ | 2.78 |
| 3 | PF4 | 0.23 | 7.40 | $4.33 \times 10^{-5}$ | 2.47 |

Since the effect of binders can be distinctly revealed from the surface morphology, the electrode surfaces with different binders were seen using scanning electron microscope (SEM) before and after charge/discharge tests (100 cycles) at 1C-rate (Fig. 3.11). The images of all the pristine electrodes exhibited smooth surfaces without any cracks as shown in Fig. 3.11(a, c, e). The homogeneous distributions of LTO particles within the binder matrix for all the cycled electrodes are evident from the elemental mapping (Fig. 3.12-3.14). The SEM image of PL3 electrode after cycling showed no noticeable cracks on the electrode surface as well as no significant change in the particle size or agglomeration (Fig. 3.11b). However, in the case of the NL4 electrode after cycling, severe cracks (Fig. 3.11d) and delamination were observed. Although SEM micrographs of PF4 electrode after cycling appeared as smooth surface with no visible cracks (Fig. 3.11f), the images at higher magnification (Fig. 3.11f inset) confirm the presence of cracks and agglomerations.

This was further corroborated by the peel strength test conducted by the conventional 180° peel test. The force at which maximum detachment occurred for the PL3, NL4 and PF4 electrodes are 3.20, 1.20 and 4.55 N, respectively. It can be seen that the NL4 has the low mechanical strength of the coating layer to the current collector. Due to the low bond strength in NL4, major cracks were formed during cycling. The PL3 shows better mechanical stability due to 2-D hydrogen bonding interaction with polymer network of PVA. Even though the PF4 electrode exhibited higher mechanical stability when compared to aqueous binder electrodes, micro cracks were formed during cycling, which might be due to the agglomeration of the active materials with PVDF binder. It indicates that both NL4 and PF4 electrode particles sparingly would have lost the contact with the current collector and deteriorates the specific capacities gradually. Thus, PVA is found to be a better binder for LTO when compared to Na-Alg and PVDF.

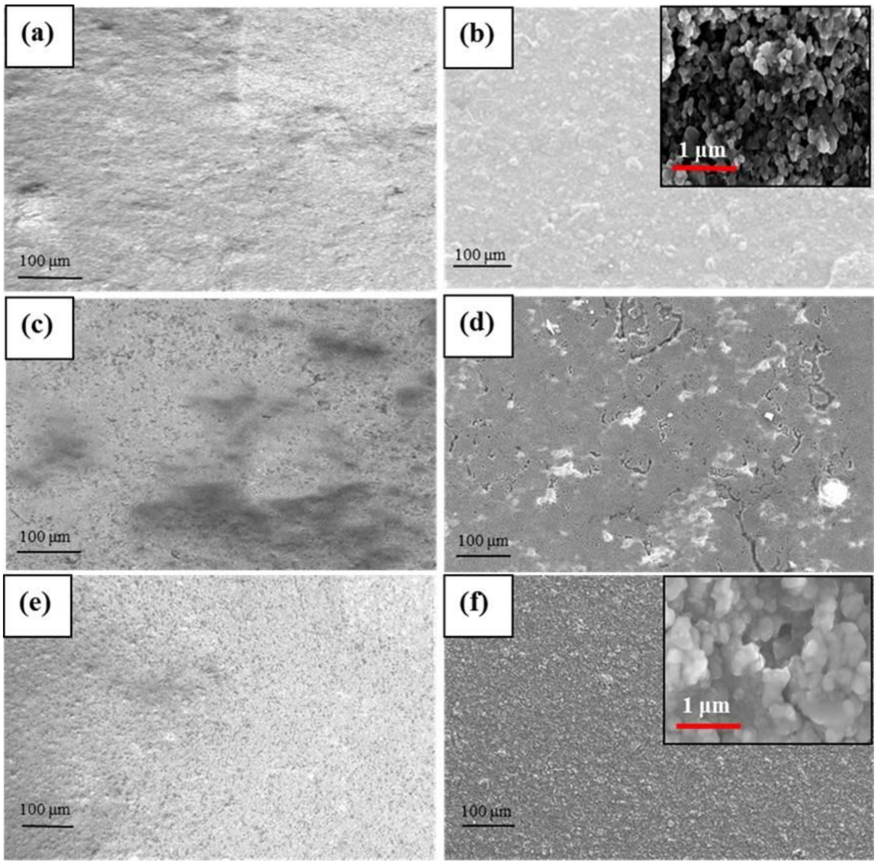

**Figure 3.11.** SEM images of LTO electrodes a), c), e) are PL3, NL4 and PF4 before cycling and b), d), f) are PL3, NL4 and PF4 after cycling at 1C-rate.

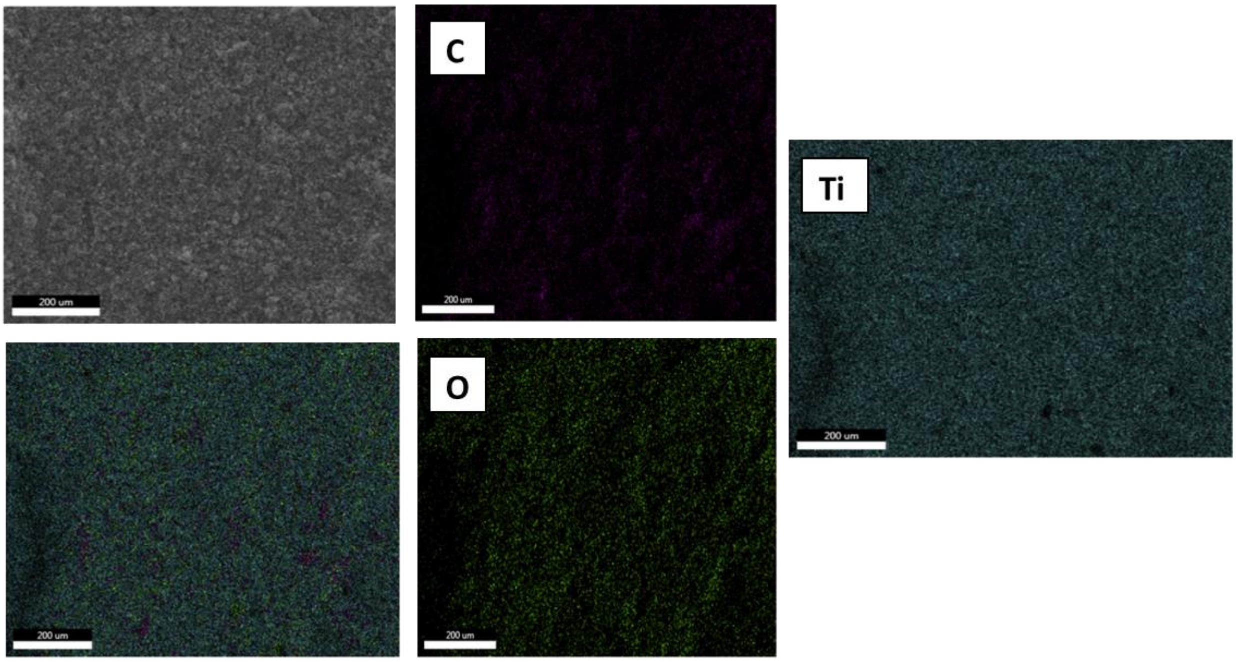

**Figure 3.12.** SEM elemental mapping of PL3 electrode after 100 cycles at 1C-rate.

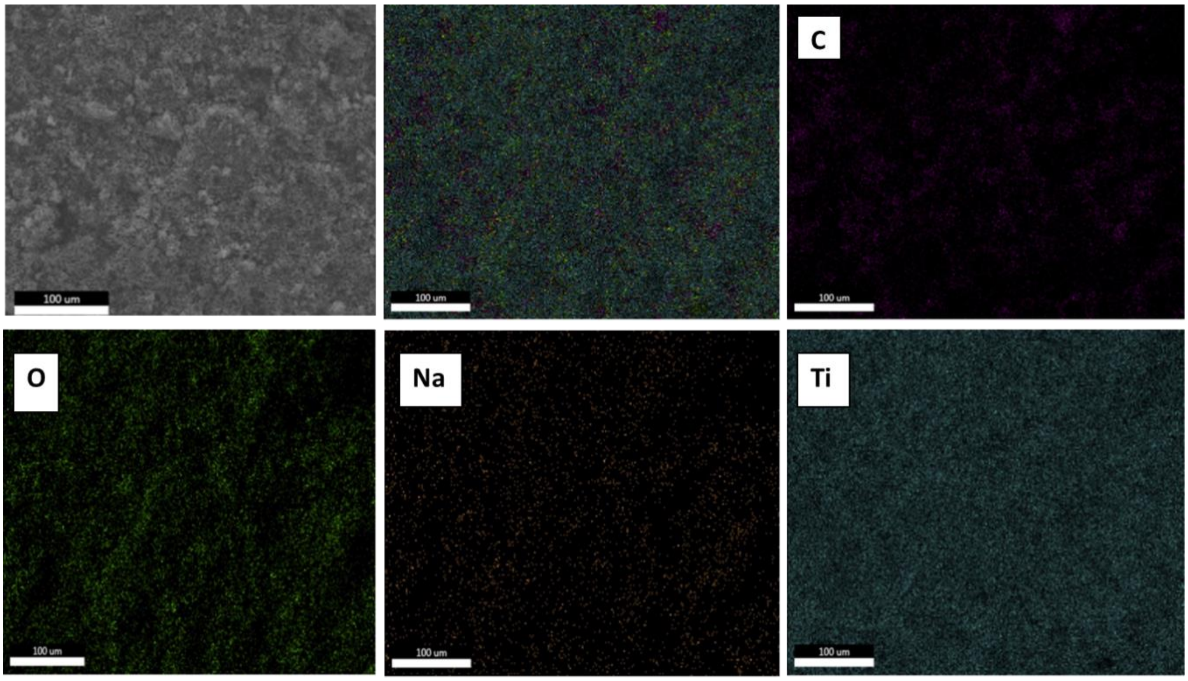

**Figure 3.13.** SEM elemental mapping of NL4 electrode after 100 cycles at 1C-rate.

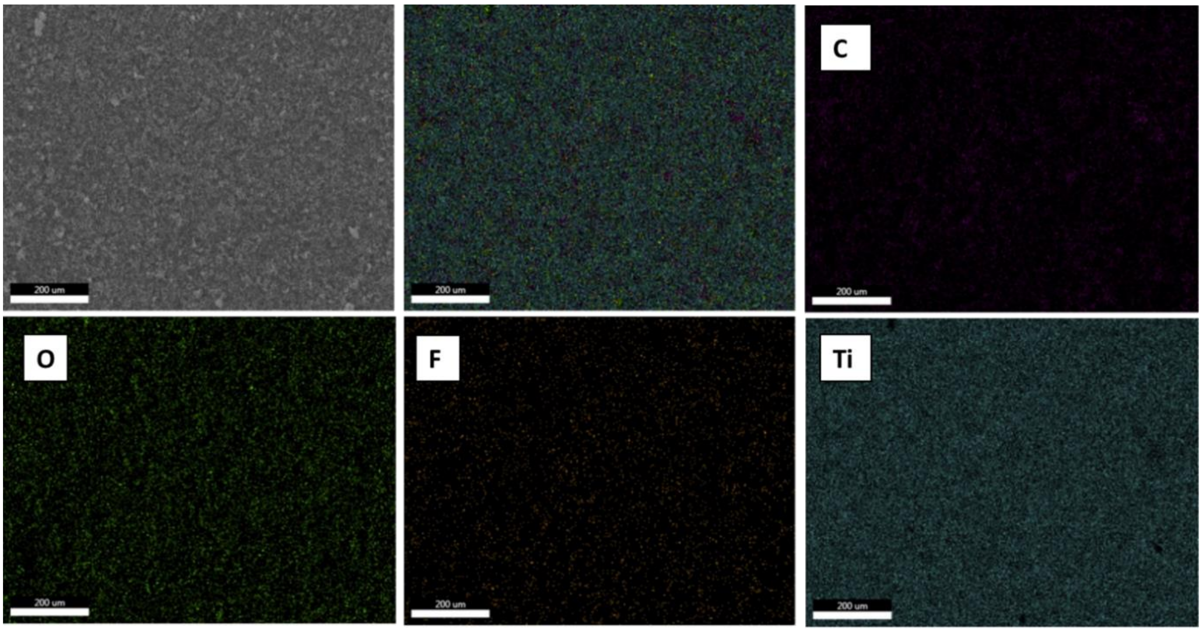

**Figure 3.14.** SEM elemental mapping of PF4 electrode after 100 cycles at 1C-rate.

In addition, XPS analysis (Figure 3.15) of the cycled PL3 electrode was carried out on the surface and the obtained results indicated the presence of Ti 2p3, C 1s, F 1s, O 1s and Li 1s, as shown in the survey spectrum of Fig. 3.15a. Although cycled electrode exhibits other associated products, our main focus is only to study the titanium and carbon peaks. The de-convoluted spectral peaks of Ti 2p and C 1s (Fig. 3.15b, c) have displayed as reported in the literature [32]. The high intense peaks of Ti (458.77 for Ti $2p_{3/2}$ and 464.61 eV for Ti $2p_{1/2}$)

manifested the exposure of LTO surface with electrolyte. The corresponding peaks of C 1s at 284.72 and 289.76 eV could be ascribed as sp$^2$ carbon of super C65 and C-H from the binder, respectively. Thus it indicates the distribution of PVA binder throughout the surface of the electrode and it might effectively increase the kinetics of lithium-ions and result better performance, as noticed in the different C-rates. Swelling analysis was performed for all the three electrodes by soaking the electrodes in the electrolyte for a period of 7 days. Calculation of swelling rates was done according to the procedure described in the literature [54]. The swelling values were found to be 27.0%, 27.2% and 37.6% for PL3, NL4 and PF4, respectively. PVDF (i.e., PF4) exhibits more swelling percentage due to its linear and flexible than the other two aqueous binder electrodes. Figure 3.16 shows the images of the samples before and after immersing them in the 1M LiPF$_6$ in (EC: DEC: DMC) electrolyte. The PL3 and NL4 electrodes have showed lower swelling behavior than the PF4 electrode. It evidences that the PL3 and NL4 electrodes have more affinity with electrolyte carbonate groups rather than the PF4. The chemical structures of all the three binders were given in Fig. 3.17.

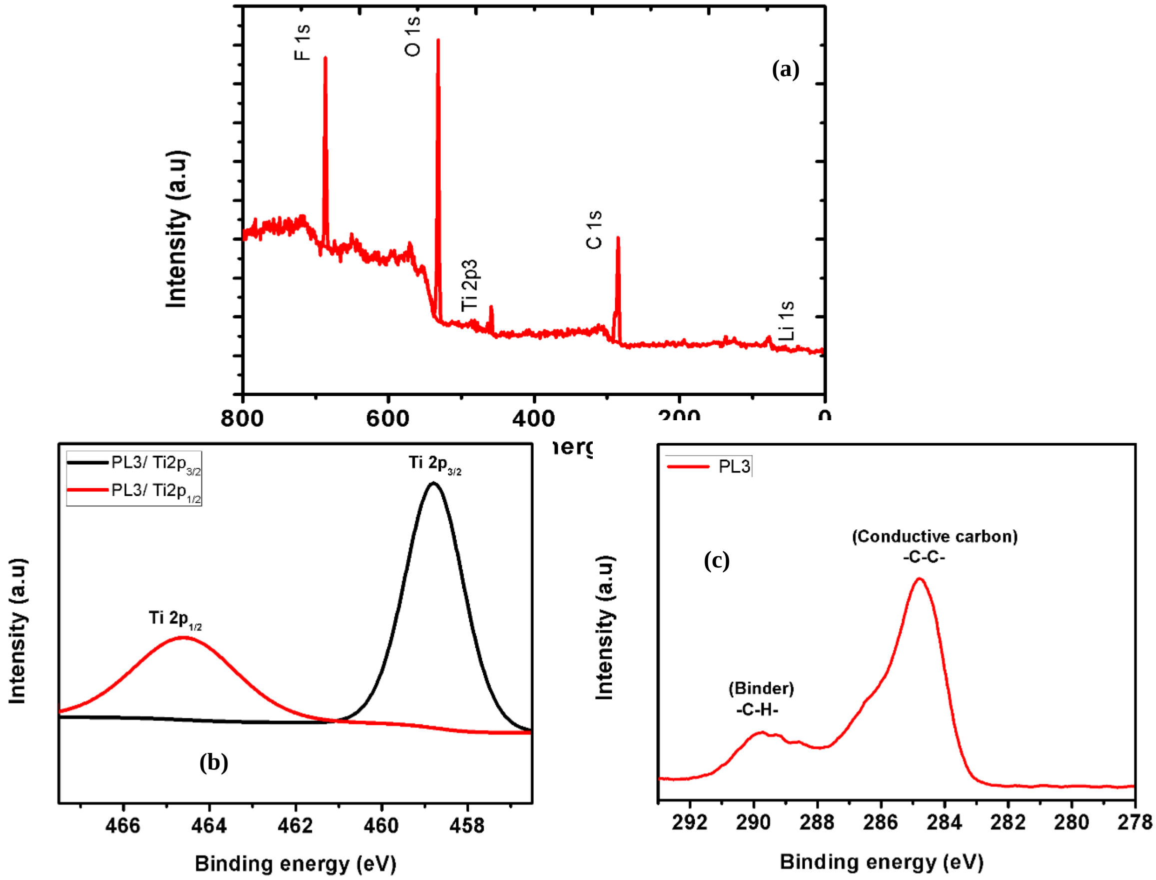

**Figure 3.15.** XPS specrtra of cycled PL3 electrode. a) Survey spectrum b) Ti 2p and c) C 1s peaks.

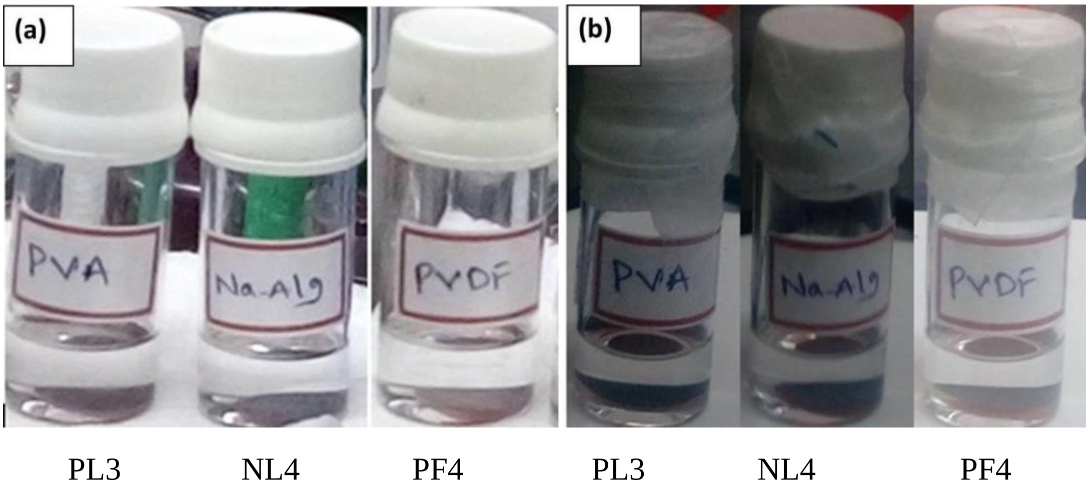

**Figure 3.16.** Swelling analysis of PL3, NL4 and PF4 a) before and b) after immersing the eletrodes in 1M $LiPF_6$ in EC:DEC:DMC (1:1:1) electrolyte.

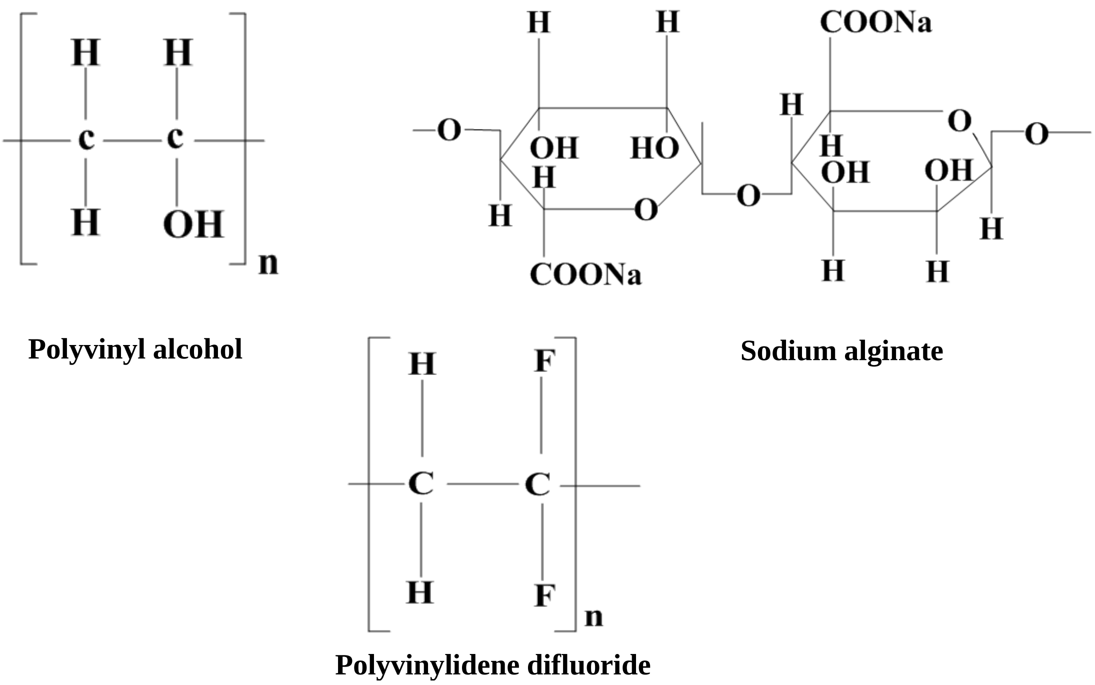

**Figure 3.17.** Chemical structures of polyvinyl alcohol, sodium alginate & polyvinylidene difluoride.

Overall, the properties of binders which mainly influence the electrochemical performance of LTO electrodes are adhesion strength, swelling, viscosity, contact angle and amorphocity. Adhesion strength plays a vital role in enhancing the cyclic stability of the electrodes, which can bind the active materials to the current collector strongly to withstand the stress during penetration of electrolyte solution as well as volume change during charge/dishcharge cycling. From our data, the obtained adhesive strength of PL3 is higher than NL4 due to the presence of more hydroxyl groups in PVA, and as a result PL3 electrode remains intact even after extended cycles. Swelling is an important parameter which effect the reversibility; as the swelling of LIB electrode increases, the specific capacity decreases as reported in the literature [55]. In the present work, PL3 electrode has shown the least swelling behaviour than other electrodes and exhibited better reversibility. Viscosity of a slurry plays a vital role in dispersion of the electrode, which leads to the uniform distribution of porosity through out the electrode for better electrolyte percolation and enhance the better electrochemical performance. Wettability helps in spreading of the electrolyte uniformly through out the electrode for good ionic movement during charge/discharge of the cell. Hence, pure PVA binder has shown low contact angle which implies good electrode wettability in PL3 electrode. Furthermore, PVA and Na-Alg are low crystalline powders as characterized by FTIR and XRD data reported [56, 57]. Crystalline polymers are effectively reduced the binding due to its main chains are bundled together in their crystalline region during drying [55]. However, the difference in crystallinity and molecular structures of binders influence the binding capabilities. Although PVA inherently possess little more crystallinity than Na-Alg, better electrochemical performace was observed in PL3, which might be due to the lower $T_g$ of PVA than Na-Alg. Hence, PL3 electrode having good adhesion, lower swelling, good dispersion and exhibited better electrochemical performance than other electrodes.

## 3.4. Conclusions

We have investigated PVA and Na-Alg as aqueous binders for LTO electrode in lithium-ion batteries. Both the binders exhibit good thermal and electrochemical stability in the operating temperature as well as potential window of LIBs. The LTO electrodes with aqueous binders have shown lower charge transfer resistance, less polarization behaviour than the corresponding electrode prepared with PVDF. The electrical resistance measurement revealed that the PL3 has lower resistance (0.39 $\mu\Omega$) compared to that of NL4 (1.30 $\mu\Omega$) and PF4 (0.50 $\mu\Omega$) electrodes. PL3 and NL4 electrodes have shown the discharge capacities of 130 mAh $g^{-1}$ and 104 mAh $g^{-1}$ after 500 cycles at 1C-rate with the capacity retention of 96% and 93%, respectively.

Both PL3 and NL4 electrodes have exhibited better rate capability performance and higher Coulombic efficiency than PF4. The PL3 electrode exhibits least swelling nature and good wettability to electrolyte. SEM analysis of PL3 electrode shows uniform distribution of LTO and conductive carbon and the distribution remains intact even after 100 charge/discharge cycles. The obtained discharge capacity of PL3 is in good agreement with that of LTO electrodes at 1C-rate with other aqueous binders as reported in the literature. This enhanced performance of LTO electrode with PVA binder compared to that of Na-Alg and PVDF can be attributed to the presence of more hydroxyl groups in PVA, which in turn leads to better adhesive and cohesive properties. Also, the diffusion coefficient of lithium- ion in PL3 is higher than the other two electrodes. Hence, the low-cost and environmentally benign PVA and Na-Alg can be used as aqueous binders for LTO anode, which may lead to more economical process of LIB fabrication for electric vehicle as well as energy storage applications.

## 3.5. References

1. M. Armand, J. M. Tarascon, *Nature* **2008**, 451:652-657.
2. R. Prakash, A. K. Mishra, A. Roth, C. Kubel, T. Scherer, M. Ghafari, H. Hahn, M. Fichtner, *J. Mater. Chem*. **2010,** 20:1871-1876.
3. R. Prakash, C. Wall, A. K. Mishra, C. Kübel, M. Ghafari, H. Hahn, M. Fichtner, *J. Power Sources* **2011,** 196:5936-5944.
4. J. Cabana, L. Monconduit, D. Larcher, M. R. Palacín, *Adv. Mater*. **2010,** 22:E170-E192.
5. F. Wang, R. Robert, N. A. Chernova, N. Pereira, F. Omenya, F. Badway, X. Hua, M. Ruotolo, R. Zhang, L. Wu, V. Volkov, D. Su, B. Key, M. S. Whittingham, C. P. Grey, G. G. Amatucci, Y. Zhu, J. Graetz, *J. Am. Chem. Soc.* **2011**, 133:18828-18836.
6. C. Qing, Y. Bai, J. Yang, W. Zhang, *Electrochimi. Acta* **2011**, 56:6612-6618.
7. D. R. Rolison, J. W. Long, J. C. Lytle, A. E. Fischer, C. P. Rhodes, T. M. McEvoy, M. E. Bourg, A. M. Lubers, *Chem. Soc. Rev.* **2009**, 38:226-252.
8. F. M. Courtel, S. Niketic, D. Duguay, Y. A. Lebdeh, I. J. Davidson, *J. Power Sources* **2011**, 196:2128-2134.
9. J. M. Tarascon, A. S. Gozdz, C. Schmutz, F. Shokoohi, P. C. Warren, *Solid State Ionics* **1996**, 86:49-54.
10. H. Zheng, R. Yang, G. Liu, X. Song, V. S. Battaglia, *J.Phys.Chem C*. **2012**, 116:4875-4882.
11. B. Lestriez, *C.R. Chim* **2010**, 13:1341-1350.
12. S. S. Zhang, T. R. Jow, *J. Power Sources* **2002**, 109:422-426.
13. A. Guerfi, M. Kaneko, M. Petitclerc, M. Mori, K. Zaghib, *J. Power Sources* **2007**, 163:1047-1052.
14. J. H. Lee, J. S. Kim, Y. C. Kim, D. S. Zang, Y. M. Choi, W. I. Park, U. Paik, *Electrochem. Solid-State Lett*. **2008**, 11:A175-A178.

15. S. F. Lux, F. Schappacher, A. Balducci, S. Passerini, M. Winter, *J. Electrochem. Soc*. **2010**, 157:A320-A325.

16. B. Lestriez, S. Bahri, I. Sandu, L. Roué, D Guyomard, *Electrochem. Commun*. **2007**, 9:2801-2806.

17. Z. Wang, N. Dupré, A. C. Gaillot, B. Lestriez, J. F. Martin, L. Daniel, S. Patoux, D. Guyomard, *Electrochim. Acta* **2012**, 62:77-83.

18. I. Kovalenko, B. Zdyrko, A. Magasinski, B. Hertzberg, Z. Milicev, R. Burtovyy, I. Luzinov, G. Yushin, *Science*, **2011**, 334:75-79.

19. H. K. Park, B. S. Kong, E. S. Oh, *Electrochem. Commun*, **2011**, 13:1051-1053.

20. Z. Zhang, W. Bao, H. Lu, M. Jia, K. Xie, Y. Lai, J. Li, *ECS Electrochem. Lett*, **2012** 1:A34-A37.

21. F. Zeng, W. Wang, A. Wang, K. Yuan, Z. Jin, Y. S. Yang, *ACS App. Mat. Interfaces* **2015**, 7 :26257-26265.

22. N. Loeffler, T. Kopel, G .T. Kim, S. Passerini, *J. Electrochem. Soc*. **2015,** 162: A2692-A2698.

23. H. Buqa, M. Holzapfel, F. Krumeich, C. Veit, P. Novák, *J. Power Sources* **2006**, 161:617-622.

24. K. Prasanna, T. Subburaj, Y. N. Jo, W. J. Lee, C. W. Lee, **2015**, *ACS App. Mat. Interfaces* 7:7884-7890.

25. Q. F. Yuan, F. G. Zhao, Y. M. Zhao, Z. Y. Liang, D. L. Yan, *J. Solid.State. Electrochem*. **2014**, 18:216.

26. J. Xu, S. L. Chou, Q. F. Gu, H. K. Liu, S. X. Dou, *J. Power Sources* **2013**, 225:172-178.

27. S. Komaba T. Ozeki, K. Okushi, *J. Power. Sources* **2009**, 189:197-203.

28. Y. Hao, Q. Lai, Z. Xu, X. Liu, X. Ji, *Solid State Ionics* **2005**, 176:1201-1206.

29. S. W. Woo, K. Dokko, K. Kanamura, *Electrochim. Acta* **2007**, 53:79-82.

30. J. Huang, Z. Jiang, *Electrochim. Acta* **2008**, 53:7756-7759.

31. S. L. Chou, J. Z. Wang, H. K. Liu, S. X. Dou, *J. Phys.Chem C*. **2011**, 115:16220-16227.

32. S. Karuppiah, S. Franger, K. Nallathamby, *ChemElectroChem*. **2017**, 4:1-8

33. D. V. Carvalho, N. Loeffler, G.-T. Kim, M. M. Margret, W. Mehrens, S. Passerini *Polymer* **2016**, 8:276

34. M. R. Harrison, P. P. Edwards, J. B. Goodenough, *Philos. Mag. B* **1985**, 52:(3) 679–699.

35. X. Li, M. Qua, Y. Huai, Z. Yua, *Electrochim. Acta* **2010**, 55:2978 – 2982.

36. R. Wang, L. Feng, W. Yang, Y. Zhang, W. Bai, B. Liu, W. Zhang, Y. Chuan, Z. Zheng, H. Guan, *Nanoscale Research Letters* **2017**, 12:575.
37. J. Liu, Q. Zhang, T. Zhang, J.-T. Li, L. Huang, S. G. Sun*, Adv. Funct. Mater*. **2015**, 25:3599-3605.
38. J.-T. Li, Z. Wu, Y. Qiu, Y. Zhou, Q.-S. Huang, L. Huang, S.-G. Sun, *Adv. Energy Mater*. **2015**, 1701185.
39. Y. Guan, L. Shao, D. Dong, F. Wang, Y. Zhang, Y. Wang, *RSC Adv*. **2016**, 6: 69966-69972.
40. J. P. Soares, J. E. Santos, G. O. Chierice, E .T. G. Cavalheiro, *Eclética Química* **2004**, 29:57-64.
41. X. Zhang, T. M. Devine, *J. Electrochem.Soc*. **2006**, 153:B344-B351
42. D. Aurbach, M. Daroux, P. Faguy, E. Yeager, *J.Electroanal.Chem. & Interfacial Electrochem* **1991**, 297:225-244.
43. B. R. Lee, E. S. Oh, *J. Phys.Chem. C.* **2013**, 117:4404-4409.
44. C. P. Sandhya, B. John, C. Gouri, *J. Mater. Sci.* **2013**, 48:5827-5832.
45. H. Ge, T. Hao, B. Zhang, L. Chen, L. Cui, X. M. Song. *Electrochim. Acta* **2016**, 211:119-125.
46. S. H. Yu, A. Pucci, T. Herntrich, M. G. Willinger, S. H. Baek, Y. E. Sung, N. Pinna, *J. Mater.Chem.* **2011**, 21:806-810.
47. S. Huang, Z. Wen, J. Zhang, Z. Gu, X. Xu, *Solid State Ionics* **2006**, 177:851-855.
48. L. Gong, M. H. T. Nguyen, E. S. Oh, *Electrochem. Commun*. **2013**, 29:45-47.
49. Q. Wu, S. Ha, J. Prakash, D. W. Dees, W. Lu, *Electrochim. Acta* **2013**, 114:1-6.
50. H. Zhenga, T. Li, G. Liub, X. Song, V. S. Battaglia, *J. Power Sources* **2012**, 208:52–57.
51. P. Kritil, D. Fattachova, *J. Electrochem Soc.* **2001**, 148:A1045.
52. F. Wang, L. Luo, J. Du, L. Guo, B. Li, Y. Ding, *RSC Adv*. **2015**, 5:6359-46365.
53. S. Sijiang, Y. Li, J. Yin, H. Wang, X. Yuan, Q. Li. *Chem. Eng. J.* **2014**, 237: 497-502.
54. G. Qian, L. Wang, Y. Shang, X. He, S. Tang, M. Liu, T. Li, G. Zhang, J. Wang. *Electrochim. Acta* **2016**, 187:113-118.
55. Z. Zhang, T. Zeng, Y. Lai, M. Jia, J. Li, *J. Power Sources* **2014**, 247:1-8.
56. M. O. Broniarz, A. Martyla, L. Majchrzycki, M. Nowicki, A. Sierczynska, *Eur. J. Chem.* **2016**, 7 (2):182-186.
57. F. Bigoni, F. D. Giorgio, F. Soavi, C. Arbizzani, *J. Electrochem Soc*. **2017**, 164 (1): A6171-A6177.

# Chapter 4

# A sustainable tamarind kernel powder based aqueous binder for graphite anode in lithium-ion batteries

# 4. A sustainable tamarind kernel powder based aqueous binder for graphite anode in lithium-ion batteries

## 4.1. Introduction

Lithium-ion batteries are the present and future energy storage device for Electric Vehicle (EV), Hybrid Electric Vehicle (HEV), as well as renewable energy storage applications [1]. In this context, various efforts have been focused on the development of novel cathodes, anodes, electrolytes and binders for the next generation lithium-ion batteries [2,3]. Currently the commercial lithium-ion batteries (LIBs) use lithium iron phosphate or lithium layered oxides as cathode and graphite as anode. Although the binder plays a vital role in the performance of LIBs, its significance has been least discussed in the battery applications [4,5]. Hence, uplift of binders is trivial for better performance of LIB, especially at high C-rate application like EVs.

Graphite is used extensively as an anode for LIB due to its structural stability, low operating potential vs lithium, less volumetric expansion, high electrical conductivity and better cyclic stability [6,7]. In addition, polarization between the charge and discharge capacity is less in graphite anode, which enables better energy efficiency for LIBs. The formation of a stable Solid Electrolyte Interface (SEI) layer on the graphite surface during the initial charging plays a pivotal role in establishing the reversibility and long cyclic life of LIBs [8–10]. Apart from the active material and conductive carbon, binder plays a crucial role on influencing of conductivity, irreversible capacity loss and delamination at higher C-rates. The polymeric binders are used to bind the active materials and conductive additives together for better electrical connectivity by the cohesion of particles and mechanical integrity by adhesion with the current collector [11]. These binders also facilitate the path for lithium-ion transport during charge/discharge of LIBs and in this perspective, polyvinylidene fluoride (PVDF) binder is used predominantly in the fabrication of LIB electrodes [12]. However, PVDF has several disadvantages such as chemical and thermal instabilities, swelling behaviour in organic solvents, limited electrical and ionic conductivities, volume expansion and requires environmentally hazardous N-methyl-2-pyrrolidone (NMP) solvent for slurry preparation [13]. In addition, recycling of PVDF binders at the end of the life of battery remains a challenging task. Hence, intensive research efforts are in progress to replace the existing PVDF binder with a suitable alternative aqueous binder for the fabrication of LIB electrodes [14]. Furthermore, the electrodes prepared by aqueous binders have shown high capacity, better reversibility, good rate capability and prolonged cycle life than that of PVDF counterpart [15]. Besides, the drying process is simpler for the fabrication of aqueous-based electrodes than the non-aqueous based ones. Moreover, the aqueous binders have been used predominantly due to their flexibility, high safety, low cost and environmental friendly nature [16,17].

Numerous binders have been studied for the graphite anode, and most of the electrodes were fabricated either with conductive or natural polymers for better coulombic efficiency and cyclic stability [18,19]. Yuan et al. have reported a cross linked ionomer, which can facilitate a better electronic connectivity and lowers the resistance during charge/discharge of graphite anode in LIB applications [20]. In addition, the major limiting step for graphite anode is lithium transference to the graphite surface, which can be enhanced by decreasing the interfacial resistance between electrode-electrolyte interface. Hence, the above factors aid to fasten the lithium movement into the solid particle [20,21]. The bio-degradable binders like chitosan, sodium alginate, xanthan gum, gum karaya, guar gum, and carboxymethyl cellulose are well-known in LIBs [22-27]. Some of them are used as an aqueous binder for graphite anode. Tamarind kernel powder (TKP), a biodegradable natural polysaccharide, extracted from the seeds of *Tamarindus indica* Linn is abundant in India, Pakistan, Bangladesh and Srilanka. TKP belongs to the Leguminosae family having a branched structure with a molecular weight of 720-880 kDa, and it forms a viscous solution in water [28]. It constitutes of (1→4) β-D-glucan backbone with a link of α-D-xylopyranose and β-D-galactopyranosyl linked (1→2)-α-D-xylopyranose linked (1→6) to glucose residues. Further, glucose, xylose, and galactose moieties (Fig. 4.2a) are in the ratios of 2.8:2.25:1.0, respectively. TKP is also termed as Tamarind seed polysaccharide (TSP) and was used as a lithium dendrite suppression in lithium metal batteries [29]. In addition, TSP has also been explored as solid biopolymer electrolytes and also for lithium conducting batteries [30,31]. In addition, it is also used as a thickening, stabilizing and gelling agents for the various food industries [32]. Moreover, TKP has wide pH tolerance, high solubility, good ionic conductivity, good thermal/electrochemical stabilities and mechanical strength, which are highly desirable properties for a binder [33]. The chemical structure of TKP is similar to that of Galactomannan, except the xylose group. The other common factor between Galactomannans and TKP is the absence of carboxyl groups. Galactomannan has already been established as a better aqueous binder for both cathode and anode materials for LIBs than non-aqueous PVDF [17,26,34]. In addition, we believe that TKP also forms hydrogen bonding with a particle as well as the substrate from all three main moieties i.e., glucose, xylose and galactose, which is similar to that of silicon anode with

Galactomannan. In spite of the above discussed wide characteristics of TKP, it has not yet been explored as an aqueous binder for any kind of battery applications.

Hence, we explored using TKP as a novel binder for the fabrication of graphite anode for LIBs and studied its electrochemical performance. The physical and chemical properties like amorphicity, viscosity, wettability of the binder and swelling of the graphite electrode were studied and compared with PVDF analogue.

## 4.2. Experimental

### 4.2.1. Materials

Potato-shaped graphite particles (d = 10-20 µm) (Superior graphite), NMC532 (Targray, Canada), carbon black (CB) (Super C65, TIMCAL Graphite & Carbon, Switzerland), TKP (A. K. Products, India), TRD 202A (JSR Corporation, Japan) and polyvinylidene fluoride (PVDF, Kynar, Arkema) were used as such without any further purification. 1M $LiPF_6$ in a mixture of ethylene carbonate (EC): dimethyl carbonate (DMC): diethyl carbonate (DEC) (1:1:1 by v/v BASF, Germany) was used as the electrolyte. The Ultrapure water of 18.2 MΩ $cm^{-1}$ was used for the preparation of binder solution and slurries.

### 4.2.2. Electrode fabrication and electrochemical testing

Graphite, carbon black and TKP binder were used as such for the preparation of slurries. For this, graphite of 87–85 wt.% and carbon black of 10 wt.% were premixed homogenously, and then the mixtures were added to three different (3–5 wt.%) aqueous TKP binder solutions. The slurries were coated on 10 µm Cu foil (Table 4.1) and the coated electrodes were dried under vacuum at 120 °C for 24 h. To compare the aqueous-based graphite electrodes, a similar electrode was prepared with non-aqueous PVDF binder (4 wt.%). All the electrodes were calendared to the desired thickness and porosity and were slit into 15 mm diameter disks for the cell fabrication. Further, to check the electrochemical stability of the binder, a similar coating procedure was adopted for pure TKP binder (4 wt.%) on copper foil. The loading of active material was found to be in the range 4.2 to 4.4 mg $cm^{-2}$ for all the compositions.

**Table 4.1.** TKP and PVDF binder-based electrodes with different active material ratios.

| S.No | Materials | Weight ratios of (GT:CB:TKP/PVDF) in slurry | Electrode Identification |
|---|---|---|---|

| | | | |
|---|---|---|---|
| 1 | Graphite: CB: TKP | 87:10:03<br>86:10:04<br>85:10:05 | C–TK3<br>C–TK4<br>C–TK5 |
| 2 | Graphite: CB: PVDF | 86:10:04 | C–PF4 |

The coin cells (CR2032) were prepared inside the argon-filled glovebox ($O_2$ and $H_2O$ limit of <1 ppm) by using graphite as the working electrode and lithium foil as a reference/counter electrode. The Whatman glass microfiber filter paper (GF/D) was used as a separator and 1M $LiPF_6$ in EC: DMC: DEC (1:1:1 by v/v) was used as electrolyte. Galvanostatic charge/discharge cycling was carried out in the voltage range 0.005–3.0 V vs. $Li/Li^+$ using BT-2000 Arbintester (USA). The rate capability experiments were performed by two methods: in the first method, identical currents were applied for both charge/discharge steps (symmetric method) up to 6C-rates and in the second method, charge current (lithiation) was kept constant at 0.2C-rate and the discharge current (de-lithiation) was varied (asymmetric method) up to 50C-rates. The Cyclic voltammetry (CV) studies were carried out for the pure TKP binder and graphite half cells in the voltage range of 0.005–3.0 V vs. $Li/Li^+$ at a scan rate of 0.05 mV $s^{-1}$ using BioLogic Science Instruments (France). The electrochemical impedance spectroscopy (EIS) data with an amplitude of 10 mV in the frequency range of 1 MHz to 0.01Hz was performed using Parstat MC Electrochemical Workstation (Princeton Applied Research, USA). In addition, a minimum of 2 to 3 cells were fabricated for all electrochemical tests in order to see the reproducibility of the results. All the electrochemical tests were measured/conducted at room temperature (25 $^{\circ}$C).

For the full cell analysis, cathode was fabricated using NMC532 (86 wt.%), conductive carbon (8 wt.%) and TRD202A binder (6 wt.%) on aluminium foil (20 µm). The active mass loadings of 7.1 mg $cm^{-2}$ (cathode) and 3.8 mg $cm^{-2}$ (anode) was maintained for assembling the coin cell. Galvanostatic charge/discharge studies for the full cell were carried out in the voltage range 3.0-4.2 V by constant current/constant voltage (CC/CV) mode.

### 4.2.3. Characterization of materials, slurries and coated electrodes

XRD analysis was performed by using Smart lab Rigaku X-ray diffractometer with a monochromatic $CuK_{\alpha}$ radiation in the 2θ range 10–80$^{\circ}$. The pristine and cycled electrode morphologies were analyzed by Field Emission Scanning Electron Microscope (FE-SEM), Carl Zeiss (Germany) with an accelerating voltage of 15 kV. Electrolyte stains on cycled electrodes were removed by dimethyl carbonate in glove box. Thermogravimetric analysis (TGA) of TKP binder was carried out under argon atmosphere by SDT Q600, TA instruments (USA). Rheological studies of all the pure binder solutions as well as aqueous graphite slurries were carried out using Anton Parr MCR102 (USA). The Fourier Transform Infrared spectroscopy (FTIR) spectra were recorded at 4 $\text{cm}^{-1}$ resolution by Attenuated Total Reflectance (ATR) method using Perkin Elmer analyzer (USA). The peel strength tests of the coated graphite electrodes were conducted at an angle of 180° and speed of 25 mm/min [Mecmesin peel tester, (UK)]. The contact angle (CA) measurements were carried out inside a dehumidified room (<10% relative humidity) using Kyowa-601 (Kyowa Interface Science Co, Ltd along with USB 3.0 CCD Camera, Japan). For this study, pure TKP binders (3–5 wt.%) casted on glass substrates were exposed to the electrolyte droplet for 5 s, and the pure TKP binder casted substrates are denoted as P-TK3, P-TK4 and P-TK5. The Swelling studies were conducted to check the increase in weight percentages of the graphite electrodes after soaking them in the electrolyte for 7days. Subsequently, after the swelling measurements, the moisture content in the left out electrolyte was determined using Karl-Fischer Titrator (Methrohm, 901 Titrando, Switzerland). In addition, these measurements were performed thrice to obtain the average value. The zeta potential measurements were carried out for aqueous graphite slurries at room temperature with the time duration of 5 min using Colloidal Dynamics Inc, (USA). The electrical resistivity for the coated electrodes was measured by four-probe method (Keithley Model 6621 current source and 2180 V source). To perform this, alternating current (AC) was employed in the current range 10–50 µA and voltage was measured across the electrode thickness. Optical microscopy analysis was carried out on pure binder solution of TKP (4 wt.%) casted on a glass substrate using Olympus, GX51 (Japan).

### 4.3. Results and discussion

XRD pattern of TKP (Fig. 4.1a) exhibited a broad peak suggesting that it is in amorphous form [31]. The FTIR spectrum of TKP (Fig. 4.1b) showed a wide band at 3285 $\text{cm}^{-1}$ for the stretching vibration of O–H groups. The peak at 2924 $\text{cm}^{-1}$ corresponds to the asymmetric stretching of the alkane C–H bond. The stretching vibration of C=C bond appeared at 1638 $\text{cm}^{-1}$ and the stretching of cyclic ether C–O–C of glucan moiety showed a peak at 1017 $\text{cm}^{-1}$. The bending vibrations of the O–H group of TKP showed a broad band at 555 $\text{cm}^{-1}$ [30,32]. The TKP exhibits three-stages of degradation in its TGA plot (Fig. 4.1c); (i) In the stage 1, the initial weight loss occurred at 65 °C corresponds to the evaporation of moisture,

(ii) the second stage represents the degradation of polysaccharide backbone in the region between 250 and 325 °C, and (iii) the third stage is due to the decomposition of volatile organic compounds above 400 °C. The differential scanning calorimetry (DSC) data showed an endothermic peak at 65 °C and an exothermic peak at 319 °C [35]. Since the thermal decomposition occurs apparently above 300 °C, it can be used as a binder for LIB electrode fabrication. The optical microstructure of P-TK4 (Fig. 4.1d) shows a uniform layer without any pores, indicating that P-TK4 is of amorphous nature, which is suitable for enhancing the wettability of the electrode. The viscosity measurements of pure TKP binder solutions (3–5 wt.%) are shown in Fig. 4.2b. The data show that the viscosity decreases as the binder content increases and all the three binder solutions are found to exhibit shear thinning behaviour. The CA data revealed that the wetting angle of the pure binder is in the order of P-TK5<P-TK4<P-TK3 (Fig. 4.2c). The binder content directly equates the number of hydroxyl groups, which enhances the hydrophilicity and hence the contact angle decreases as the binder content increases. The CV curve of pure TKP binder electrode (P-TK4, Fig. 4.2d) exhibited a small redox wave at 0.8 V vs. Li/Li$^+$. However, the current density of the redox peak (~3 μA g$^{-1}$) is negligible, suggesting that the binder is electrochemically inactive. A similar observation was reported in the literature for other aqueous binders [17,25,36]. Hence, TKP can be used as a binder for anodes in LIBs.

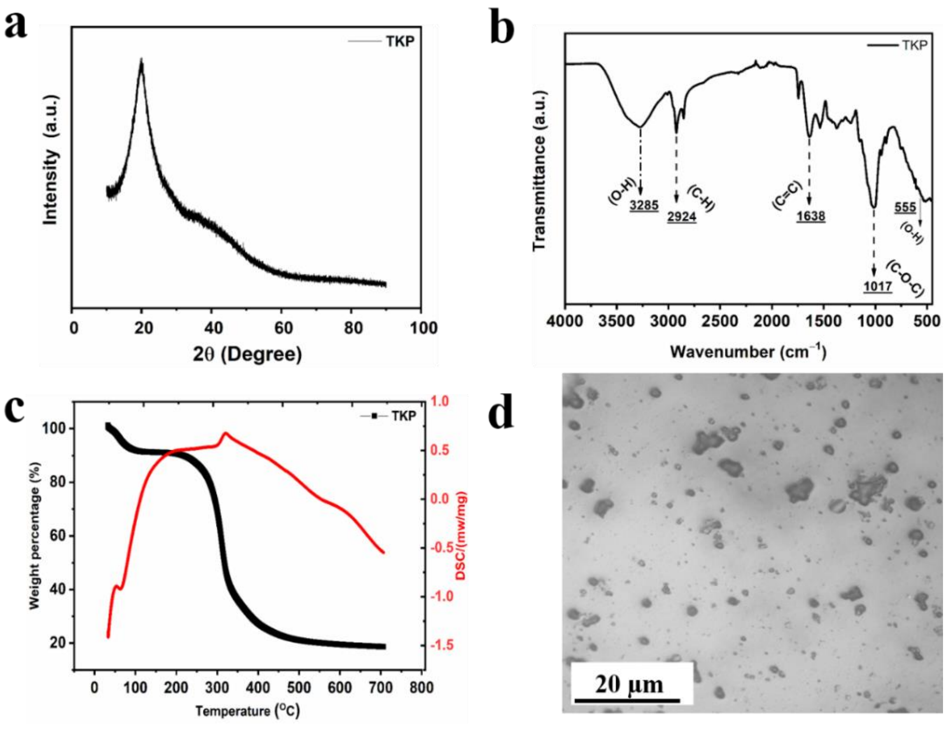

**Figure 4.1.** a) XRD of pure TKP powder, b) FTIR spectrum of pure TKP powder, c)

TGA/DSC of TKP powder, d) Optical microscopic image of pure TKP binder film (P-TK4).

The anode slurries and the electrodes were prepared (See Table 4.2) by varying the binder content of 3, 4 and 5 wt.%, which are abbreviated as C-TK3, C-TK4, and C-TK5, respectively. Similarly, the slurry and the electrode prepared using the PVDF binder (4 wt.%) are abbreviated as C-PF4 (Table 4.2).

**Table 4.2.** TKP and PVDF binder-based electrodes with different active material ratios.

| **S.No** | **Materials** | **Weight ratios of (GT:CB:TKP/PVDF) in slurry** | **Electrode Identification** |
|---|---|---|---|
| 1 | Graphite: CB: TKP | 87:10:03<br>86:10:04<br>85:10:05 | C–TK3<br>C–TK4<br>C–TK5 |
| 2 | Graphite: CB: PVDF | 86:10:04 | C–PF4 |

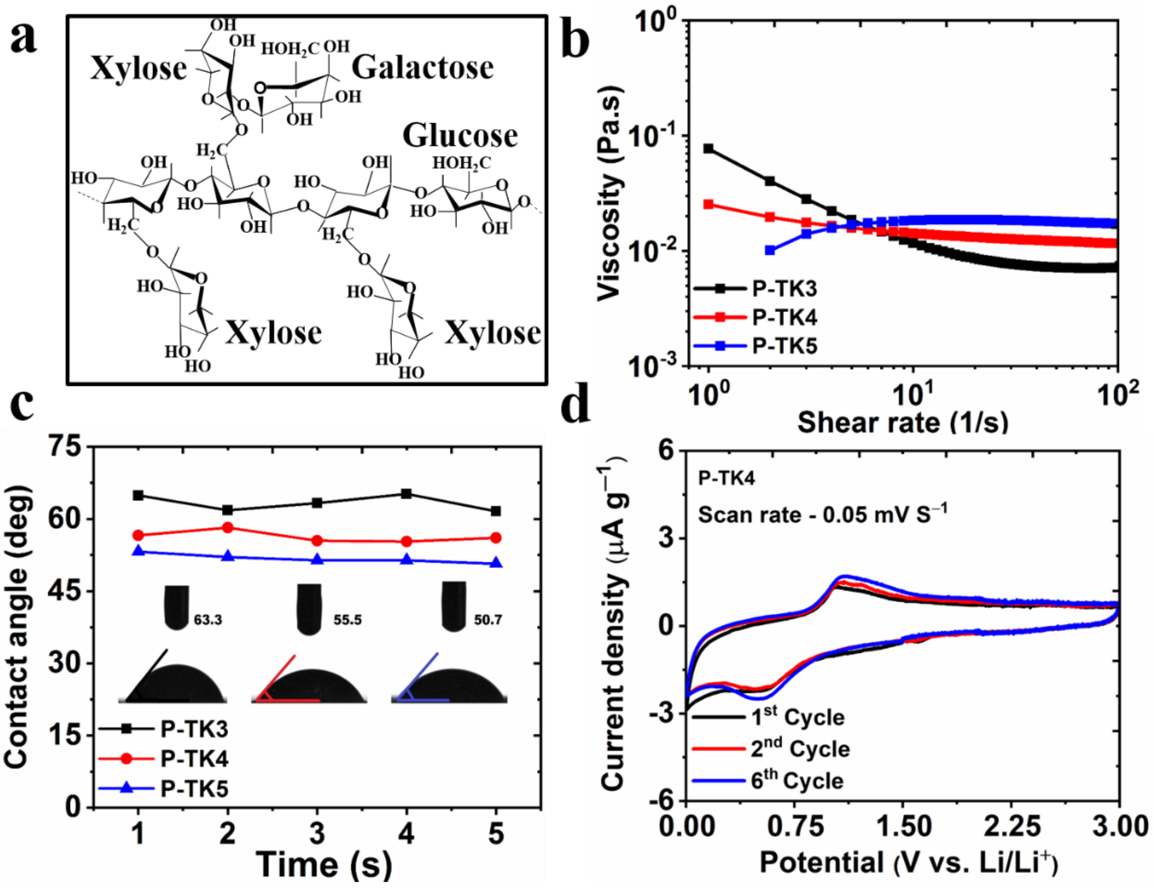

**Figure 4.2.** a) Molecular structure of TKP, b) Viscosity vs Shear rate profile of TKP's at various concentrations, c) Contact angle vs time profile of 3–5 wt.% of TKP solution at room

temperature, and d) Successive cyclic voltammograms of pure TKP film (P-TK4) in the range between 0.005 and 3.0 V vs. Li/Li$^+$ at a scan rate of 0.05 mV s$^{-1}$.

Rheological studies were conducted for C-TK3, C-TK4 and C-TK5 slurries at room temperature (Fig. 4.3). The viscosities at the shear rate of 1 s$^{-1}$ are in the order of C-TK4>C-TK5>C-TK3. In all the three cases, the shear thinning (non-Newtonian) behaviour was observed, which is more favorable for large scale electrode coating process that usually carried out at medium / high shear rate. The Zeta potential measurements of the slurries (Fig. 4.4 and Table 4.3) revealed that the surface charge stability of the slurries is in the following order C-TK4>C-TK5>C-TK3. The conductivity of the graphite slurries was in the range of 1.03 to 1.10 mS cm$^{-1}$. The C-TK4 exhibits a higher conductivity and Zeta potential values (Fig. 4.4), which are better than the reported values for graphite slurries with different aqueous binders of LA133 and CMC/SBR [37,38]. Thus it suggests that a homogeneous slurry of C-TK4 can be formed without any coagulation and flocculation. Hence, a uniform anode framework and better electrochemical performance can be anticipated from C-TK4 electrode.

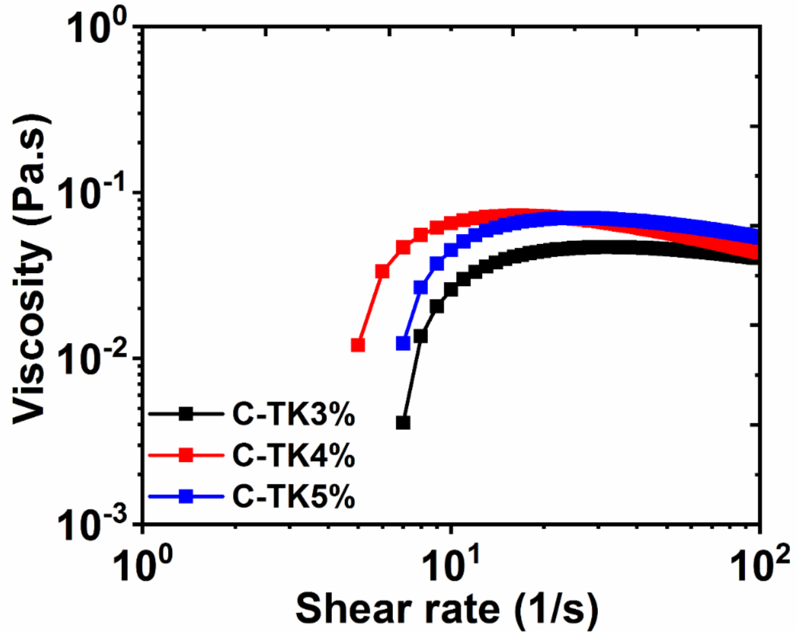

**Figure 4.3.** Rheology of C-TK3, C-TK4 and C-TK5 graphite slurries.

The peel strength of the electrodes was measured by 180° peel test and the values are found to be 0.09, 0.11, 0.65 and 1.6 N cm$^{-1}$ for C-TK3, C-TK4, C-TK5 and C-PF4, respectively. The increase in peel strength (seven-fold higher for C-TK5 w.r.t. C-TK3) with an increase in binder content is correlated to the increase of protein content present in the TKP binder. The swelling and moisture content studies were carried for C-TK4 and C-PF4 electrodes (Fig. 4.5) and the calculation for the swelling studies was done as reported in the literature [39]. The C-TK4 showed 7.25% swelling in the electrolyte, while the C-PF4 had shown 9.63% of swelling. Due to the linear polymer chain structure as well as its instability in organic solvents a higher swelling was observed for PVDF. The moisture content of the electrolyte solution which was used for the swelling studies of C-TK4 and C-PF4 measured as 55.2 ppm and 62.6 ppm, respectively. The electrical resistivity measurements were performed for C-TK4 and C-PF4 electrodes using four-probe technique. The C-TK4 exhibited lower resistivity value (2.25 μΩ cm$^{-2}$) than C-PF4 (3.5 μΩ cm$^{-2}$), which could be due to the presence of more number of hydroxyl groups in TKP polymer structure contributing to free mobility of the lithium-ions as reported by Finkenstadt [40]. The higher resistivity value obtained in C-PF4 is due to the insulating behaviour of PVDF as well as the low segmental motion of the lithium ions in the semi-crystalline binder. This is expected to result in a better electrochemical performance for C-TK4 than C-PF4.

**Table 4.3.** Zeta potential values for aqueous graphite slurries of C-TK3, C-TK4 and C-TK5.

| **S.No** | **Electrode** | **Zeta potential value (mV) for 5 mins** | **Conductivity (mS cm$^{-1}$)** |
|---|---|---|---|
| 1 | C-TK3 | -0.63; -0.58; -0.62; -0.63; -0.62 | 1.06:1.05:1.07:1.07:1.07 |
| 2 | C-TK4 | -0.27; -0.25; -0.27; -0.28; -0.27 | 1.09:1.10:1.10:1.10:1.10 |
| 3 | C-TK5 | -0.43; -0.45; -0.47; -0.41;- 0.47 | 1.03:1.03:1.03:1.03:1.05 |

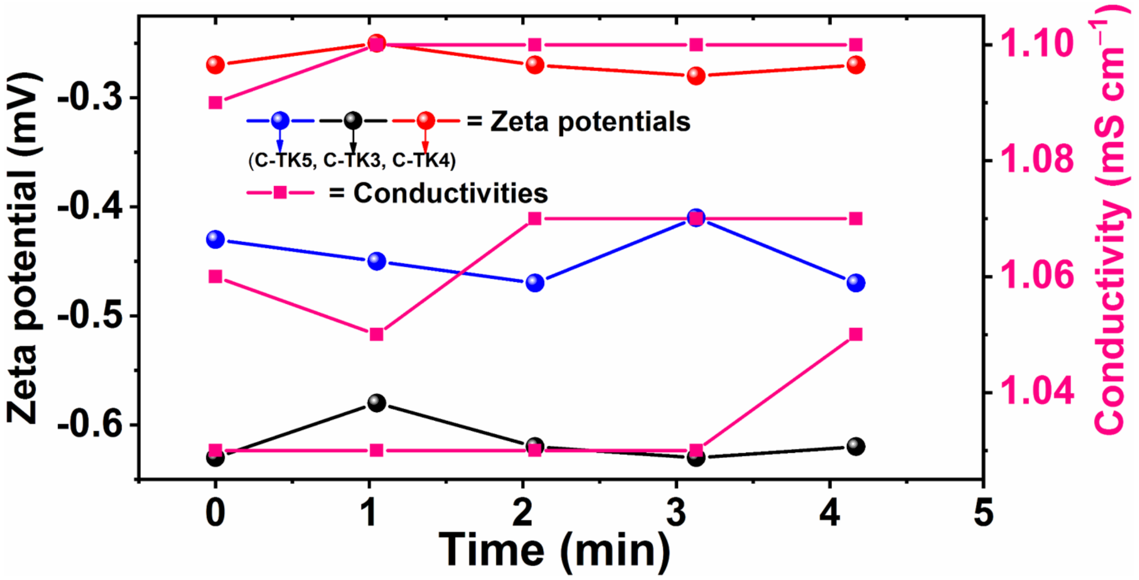

**Figure 4.4.** Zetapotential measurements for C-TK3, C-TK4 and C-TK5 graphite slurries.

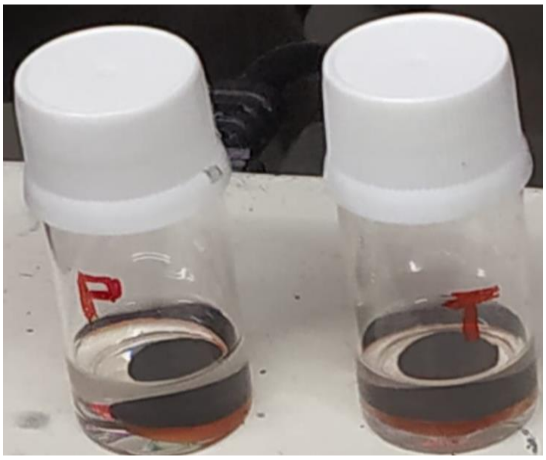

**Figure 4.5.** Swelling and electrolyte digital images of C-PF4 and C-TK4 electrodes.

Cyclic voltammograms of C-TK4 and C-PF4 electrodes were recorded for six successive cycles at 0.05 mV $s^{-1}$. Figure 4.6 shows the CVs of C-TK4 and C-PF4 for the 1st, 2nd and 6th cycles. Both the CVs of C-TK4 and C-PF4 (Fig. 4.6a,b) showed reversible redox peaks in the voltage range of 0.05 to 0.80 V. A cathodic peak appeared at 0.65 V in the first cycle and it disappeared in the consecutive cycles which is ascribed for the formation of the SEI layer. The three cathodic peaks at 0.19, 0.12 and 0.06 V of graphite electrodes were attributed to the presence of stage IV, stage II and stage I graphite intercalation compounds, respectively. It can also be noticed that the de-intercalation peaks for both electrodes are positioned at 0.22 V. There is no significant potential shift in the redox peaks of graphite electrodes in the first cycle with TKP (or) PVDF binder. In addition, first cycles of graphite showed similar small peaks for both C-TK4 and C-PF4 electrodes (Inset Fig 4.6a, b). At the first cycle, the peak current of C-PF4 is lower than the C-TK4 electrode, and it might be due to the slow formation of SEI at first cycle [41]. However, at 6th cycle, C-PF4 has shown marginally higher peak current than the C-TK4 electrode, which resembles to the higher rate of lithiation in the graphite lattice of C-PF4 than the former electrode [42]. Hence, these redox peaks are clear indication for intercalation/de-intercalation potentials for graphite anode.

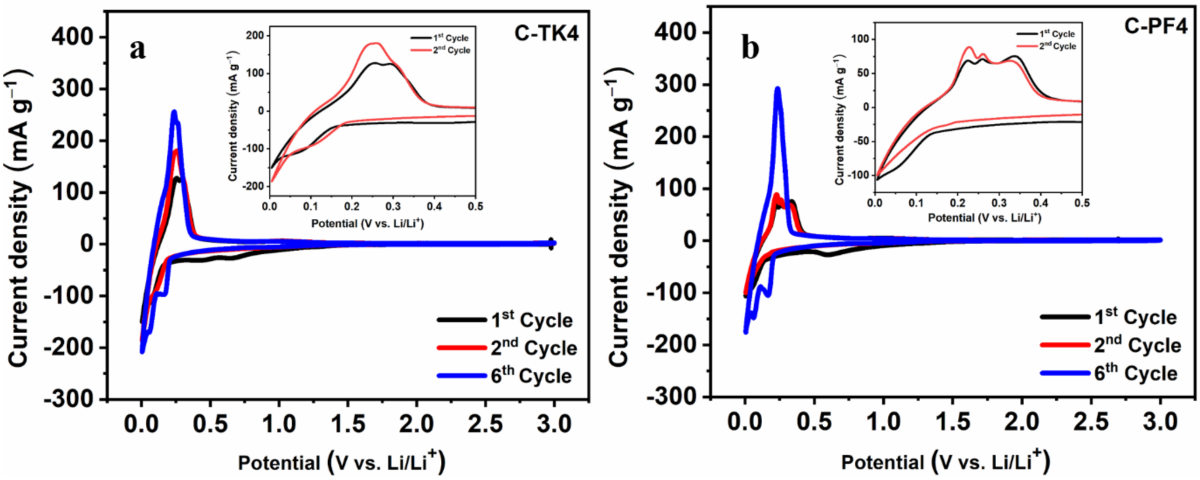

**Figure 4.6.** Cyclic voltammograms of a) C-TK4 and b) C-PF4 electrodes at 0.05 mV s$^{-1}$ for 1st, 2nd and 6th cycles.

Figure 4.7 displays the galvanostatic charge/discharge and cyclic stability profiles of all the four electrodes in the voltage range 0.005 V to 3.0 V vs. Li/Li$^+$. The different stages of lithium intercalation and de-intercalation in graphite anode can be ascertained by differential capacity vs potential profile (Fig. 4.8) plotted for 1st cycle of C-TK4 and C-PF4 electrodes.

The cathodic peaks at 0.19, 0.1 and 0.06 V can be described to the various intercalation stages of lithium into the graphite anode. In addition, the peak at 0.66 V for both the electrodes corresponds to the formation of the SEI layer as shown in inset Fig. 4.8. Furthermore, all peak potetials are well matched with our CV data. In the case of C-PF4, the potential shift was larger while compared to that of C-TK4 electrode indicating that more polarization was observed in the former electrode. As a result, a sluggish movement of lithium can be expected in C-PF4. The initial reversible specific capacities of C-TK3, C-TK4, C-TK5 and C-PF4 are found to be 422, 426, 396 and 367 mAh g$^{-1}$ at 0.1C-rate (0.1C = 37.2 mA g$^{-1}$) with coulombic efficiencies of 88.1, 87.3, 79.5 and 92.6%, respectively (Fig. 4.7a). The observed lower coulombic efficiencies of the aqueous based binder system compared to the PVDF system might be due to the parasitic reactions as well as non-uniform SEI layer formation at the surface of graphite anode for the first cycles of C-TK electrodes. After hundred cycles, the same electrodes delivered reversible capacities of 310, 343, 342 and 215 mAh g$^{-1}$ (Fig. 4.7b) with capacity retentions of 85.4, 80.5, 86.3 and 58.6%, respectively. In all the cases, the coulombic efficiencies were found to be in the range of 97 to 99% at 100th cycles. All three aqueous binder-based graphite electrodes exhibited high discharge capacities and high-capacity retentions than the PVDF counterpart. This can be due to the presence of hydroxyl groups in TKP binder and their interaction with active material as well as low polarization of the electrodes during cycling [43]. The obtained discharge capacities of C-TK3, C-TK4 and C-TK5 are significantly higher than that of the graphite electrodes prepared by other aqueous binders reported in the literature at various C-rates and different cycles (Table 4.4). In addition, the first cycle irreversible capacities of these electrodes are lower than the reported graphite anodes with other aqueous binders [44]. The first cycle irreversibility was mainly due to the formation of the SEI layer [44].

Specifically, the reversible plateaus occurred in the voltage range between 0.3 and 0.005 V vs. Li/Li$^+$ are in agreement with the reported literature [45]. Further, C-PF4 has yielded the lower de-lithiation capacity than C-TK electrodes (Fig. 4.7b), which is due to the fact that more polarization occurs during charge/discharge cycling as shown in Fig. 4.7b. The cycle number and specific capacity profile at 0.1C-rate are shown in Fig. 4.7c. It is apparent that the TKP based graphite electrodes displayed a stable cycling behaviour due to more flexibility, heterogeneous surface, and conductive nature of the binder [26,46]. Among the three electrodes, C-TK4 exhibited a better discharge capacity and stability, and it can be explained based on high zeta potential and optimal binder content present in the electrodes [15]. Yuan et al. have discussed the importance for minimum usage of the binder content in the graphite anode, wherein the electrode with minimum binder content is expected to result in high specific capacity as well as stable cycle life due to the homogenous networking of binder with active material. The low binder content makes the particle to particle coherence as close as possible, which facilitates free movement of lithium-ions across the electrode surface [47].

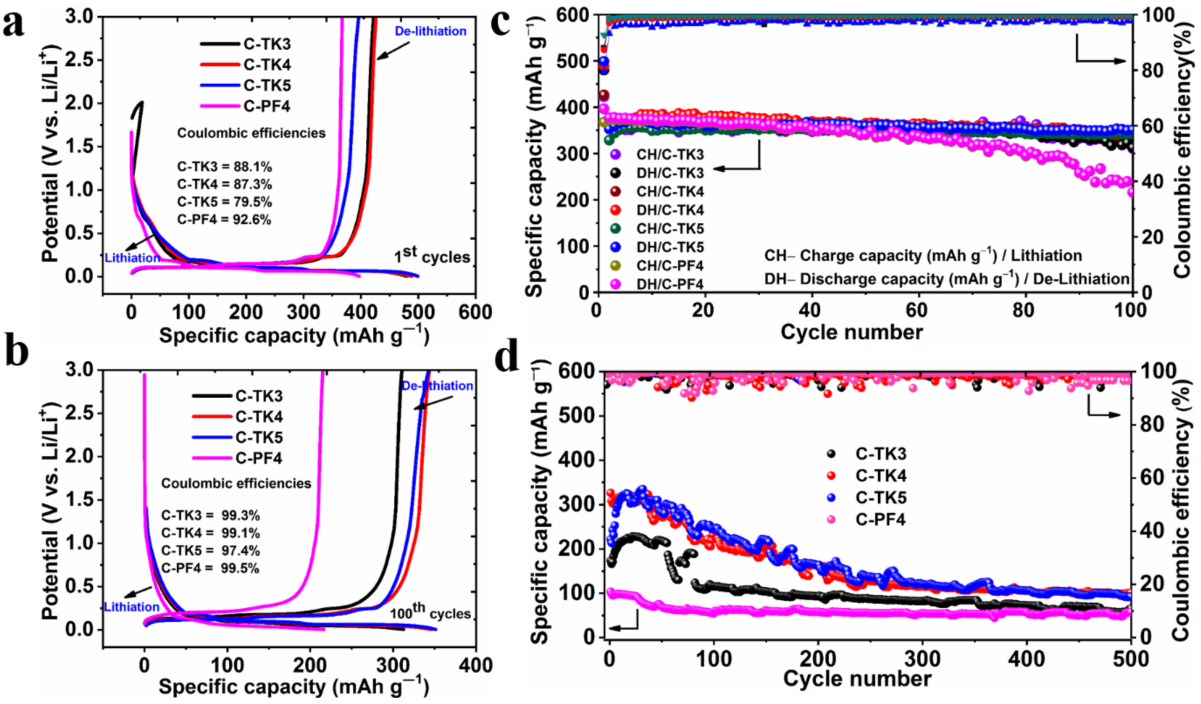

**Figure 4.7.** Galvanostatic charge/discharge profiles of C-TK3, C-TK4, C-TK5 and C-PF4 electrodes a) at first cycle and b) after 100 cycles. The cyclic stability profile of C-TK3, C-TK4, C-TK5 and C-PF4 electrodes for c) 100 cycles at 0.1C-rate and d) 500 cycles at 1C-rate.

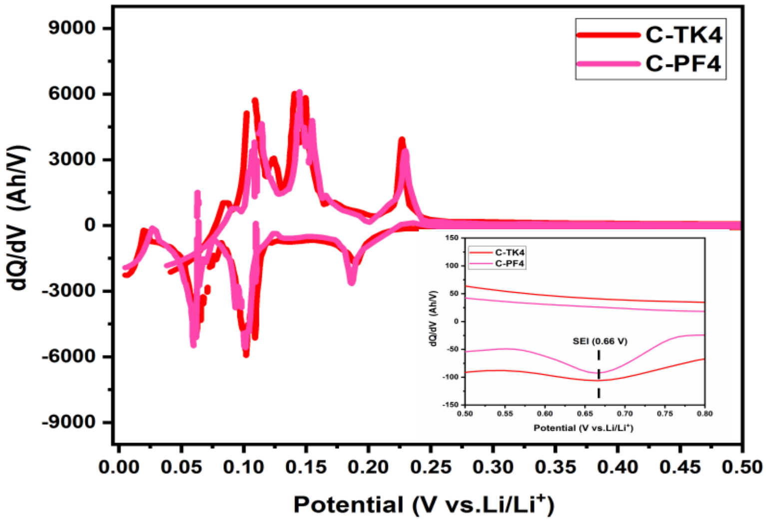

**Figure 4.8.** Differential capacity (dQ/dV) vs. potential graph for 1st cycle of C-TK4 and C-PF4 electrodes.

Figure 4.7d displays capacity vs cycle number profile of all four electrodes at 1C-rate (1C= 372 mA $g^{-1}$) for 500 cycles. The electrode C-TK4 exhibited high initial (de-lithiation) specific capacity of 326 mAh $g^{-1}$ than C-TK5 (221 mAh $g^{-1}$) and C-TK3 (173 mAh $g^{-1}$) electrodes. After 500 cycles, the de-lithiation capacities of C-TK3, C-TK4, and C-TK5 are 65, 101 and 92 mAh $g^{-1}$, respectively. The coulombic efficiencies for all these electrodes are >95% after 500 cycles. In the case of C-PF4, electrode has shown the initial de-lithiation capacity of 103 mAh $g^{-1}$ and 57 mAh $g^{-1}$ after the 500th cycle. The lower capacity of C-PF4 can be attributed to four factors: (i) the poor van der Waal interactions, (ii) swollen behavior, (iii) blockage of $Li^+$ migration and (iv) modest flexibility of the PVDF binder [48,49]. However, the C-TK4 electrode has shown a prominent specific capacity which is due to the formation of stable SEI after cycling as well as due to the presence of more active bonding sites in the branched TKP binder [25,50]. Additionally, the TKP binder could form 3D network interaction with graphite particles. Both C-TK4 and C-TK5 showed capacity retention of 45% at the end of 500 cycles. Although C-TK5 exhibited higher specific capacities and good capacity retention over C-TK4 for a longer cycling period from 20 to 400 cycles, a high-capacity decay was observed for C-TK5 on further cycling from 401 to 500 cycles. Moreover, C-TK5 electrode showed the highest first cycle irreversible capacity (102 mAh g$^{-1}$) and less coulombic efficiency (79.5%) than C-TK4. Hence, the C-TK4 is the better electrode composition due to its longevity and stability with respect to cycling. The obtained results of C-TK4 in terms of capacity and long cycle life are also found to be better than the other aqueous binder-based graphite anodes reported in the literature [51–54].

**Table 4.4.** Aqueous binders reported in the literature at various C-rates and different cycles.

| **S.No** | **Aqueous Binders** | **Binder (wt.%)** | **Initial Specific capacity (mAh g$^{-1}$) 1st cycle** | **Reversible discharge capacity (mAh g$^{-1}$) 100th cycle** | **C-rate/ Current density** | **Reference** |
|---|---|---|---|---|---|---|
| 1 | Xanthan gum | 1 | 375 | 350 | 0.083 | 14 |
| 2 | Na-CMC | 5 | 375 | 310 | 0.083 | 14 |
| 3 | LiCMC | 2.5 | 290 | 300 | 0.083 | 14 |
| 4 | AMAC | 5 | 200 | 200 (60th) | 0.5 mA cm$^{-2}$ | 56 |
| 5 | AMMA | 5 | 200 | 210 | 0.3 mA cm$^{-2}$ | 49 |
| 6 | PEDOT:PSS | 1.5 | 375 | 330 | 0.083 | 14 |
| 7 | Natural cellulose | 5 | ~320 | - | 0.1 | 18 |
| 8 | PMMA-5% PTEGMA | 5 | 330.8 | 330.12 | 0.1 | 19 |
| 9 | PolyVC (2%) | 10 | 300 | ~ 257 (20th) | 0.1 | 54 |
| 10 | C-Li-PSBM | 1.5 | 365 | ~310 (50th) | 0.5 | 20 |
| 11 | GA | 5 | 292 | 201 (50th) | 0.1 | 44 |
| 12 | Na-Alg | 5 | 382 | 299 (50th) | 0.1 | 23 |
| 13 | TKP | 3 | 422<br>173 | 310<br>65 (500th) | 0.1<br>1.0 | This work (C-TK3) |
| 14 | TKP | 4 | 426<br>326 | 343<br>101 (500th) | 0.1<br>1.0 | This work (C-TK4) |

| | | | | | | |
|---|---|---|---|---|---|---|
| 15 | TKP | 5 | 396<br>221 | 342<br>92 (500th) | 0.1<br>1.0 | This work<br>(C-TK5) |

Figure 4.9 displays the scanning electron microscopy (SEM) images of C-TK4 and C-PF4 electrodes at the pristine and after cycling at 1C-rate for 500 cycles. Both the pristine electrodes (Fig. 4.9a and e) have revealed that the active materials are distributed homogenously without any cracks. The C-TK4 electrode shows more pores and voids than the C-PF4 electrode. This could be due to the tendency of aqueous based slurry compared to the non-aqueous slurry used in the electrode fabrication. The higher magnification images of the fresh electrodes (Fig. 4.9b and f) displayed the potato-shaped graphite particles and the conductive carbon dispersed on the graphite particle. The SEM image of C-TK4 electrode after 500 cycles (Fig. 4.9c) showed a similar morphology as that of the pristine electrode without any cracks. On the other hand, the SEM images of the C-PF4 electrode after 500 cycles (Fig. 4.9g) showed deep cracks on the surface of the electrode. The cracks in C-PF4 might have originated due to the poor van der Waal interactions of PVDF with graphite anode. However, in the case of C-TK4, no such cracks were observed because of the presence of more binding sites in TKP binder. Furthermore, a small number of white crystals were observed on the graphite surface (Fig. 4.9d and h), which is due to the decomposition of the electrolyte to form lithium carbonate as confirmed by Energy Dispersive X-ray spectroscopy (EDS) analysis, and a similar observation has also been reported by Komaba et al. [45]. Although, the C-TK4 electrode shows more porosity and voids, still it could provide a better capacity and higher capacity retention than C-PF4. It is also observed that morphology of pure TKP is in spherical shape as shown in Fig. 4.10.

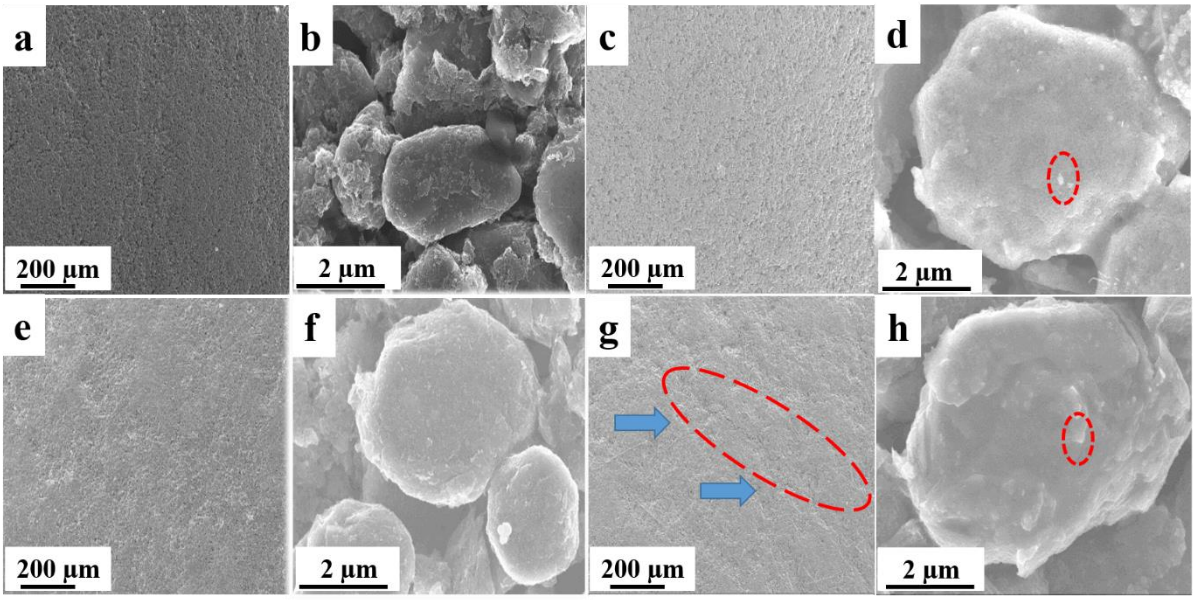

**Figure 4.9.** SEM morphology of C-TK4 (a,b,c,d) and C-PF4 (e,f,g,h) graphite electrodes for pristine (a,b,e,f) and after 500 cycles (c, d,g,h) at 1C-rate.

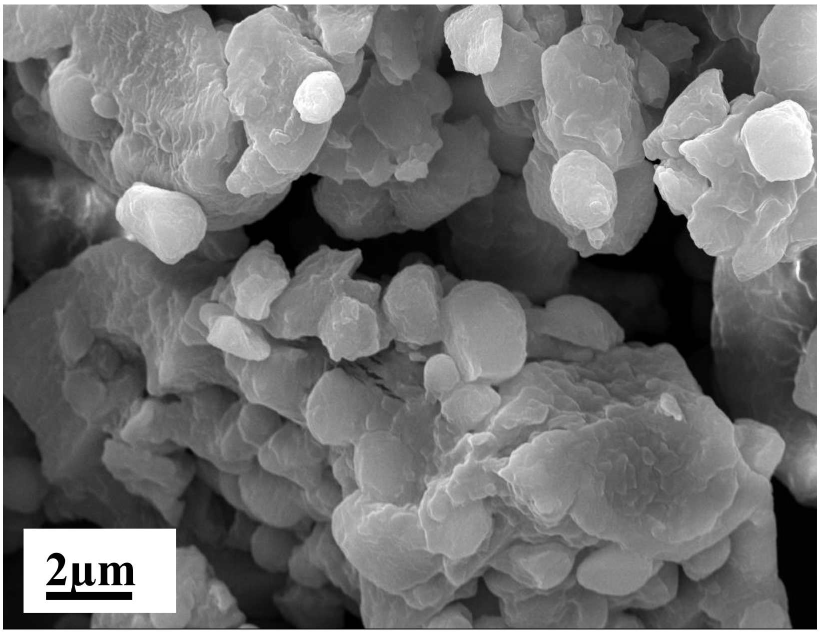

**Figure 4.10.** SEM morphology of pure TKP powder

To assess the rate capabilities of the graphite electrodes, charge/discharge studies were carried out at different C-rates (Fig. 4.11). For this purpose, two types of charge/discharge studies were performed. In the first method, identical charge/discharge currents were applied (symmetric) for every ten cycles, and the applied currents were varied up to 6C (Fig. 4.11a). In all the cases, except at lower C-rates (<0.5C), the discharge capacity decreases as the C-rate increases. Among the four electrodes, C-TK4 showed a better rate capability than all the other electrodes. Even though the obtained capacity of C-TK4 is low at 6C (35 mAh $g^{-1}$), it was reputable to see that the cell works for such a high current, especially for the graphite anode with a natural polysaccharide binder. It can also be seen that a high-capacity fade occurred after 1C-rate for C-TK4, but it showed the high-capacity retention of >86% up to 1C-rate in ten cycles. Further, the obtained de-lithiation capacities at high C-rates (1C and 2C) are far better than the reported results in the literature [44]. Subsequently, when the applied current was reduced again after 70 cycles to 0.1C, all aqueous-based electrodes showed good specific capacities and better cyclic stability. Among aqueous electrodes, the C-TK4 showed the highest specific (de-lithiation) capacity of 420 mAh $g^{-1}$ with the capacity retention of 98% for the given ten cycles. However, in the case of C-PF4, when the applied current was reduced back to 0.1C after 70 cycles, a gradual decrease in the capacity was found within the ten cycles.

In the second method (asymmetric), after the initial cycling at 0.1C-rate for 5 cycles, the charging current was kept constant at 0.2C rate and the discharge current was varied at every 5 cycles up to 50C for C-TK4 and C-PF4 electrodes (Fig. 4.11b). As known well, the discharge capacity shows a decreasing trend with the increase in C-rate. However, the obtained specific capacity value of C-TK4 is minimum six-fold higher than that obtained at the corresponding C-rate value from the first method (symmetric). For example, at the discharge rate of 6C, C-TK4 electrode delivered a specific discharge capacity of only 36 mAh $g^{-1}$ in the first method, whereas, it delivered 180 mAh $g^{-1}$ in the second method. In addition, it shows worthy performance even at very high C-rates. In the case of 20C and 50C-rates, it delivered 125 mAh $g^{-1}$ and 55 mAh $g^{-1}$, respectively. After the analysis up to 50C-rate, the discharging current was reversed back to 0.2C-rate, where the C-TK4 electrode attained its original capacity of 360 mAh $g^{-1}$, with nearly 100% capacity retention for the given five cycles. Although C-PF4 displayed higher specific capacity than C-TK4 at lower C-rates (0.2-2C), the specific capacity of C-PF4 decreased significantly at higher C-rates, i.e., 4C to 50C. After the analysis up to 50C rate, the discharging current was decreased to 0.2C, where the C-PF4 electrode gave 250 mAh $g^{-1}$ with a capacity retention of 73% only. In addition, to confirm the cyclic stability of C-TK4 at high C-rates, the electrode was cycled at a 0.2C-rate charging (lithiation) and 6C-rate discharging (de-lithiation) for 60 cycles (Fig. 4.11c). It delivered the initial de-lithiation capacity of 318 mAh g$^{-1}$ and the final capacity of 191 mAh g$^{-1}$ with a capacity retention of 60% at the end of the 60th cycle.

The improved electrochemical performance with TKP graphite anode is possibly due to the dispersion of electrolyte solvent on graphite surface uniformly with the branched structure of TKP polymer. Hence, it enhances the lithium transference number in C-TK4 electrode than the C-PF4 linear structure electrode, and a similar phenomenon for lithium polymer batteries also was observed by Watanabe et al. [55]. Thus, the observations confirmed that C-TK4 is much better and sustainable electrode in terms of cyclic stability and rate capability for the application of LIBs.

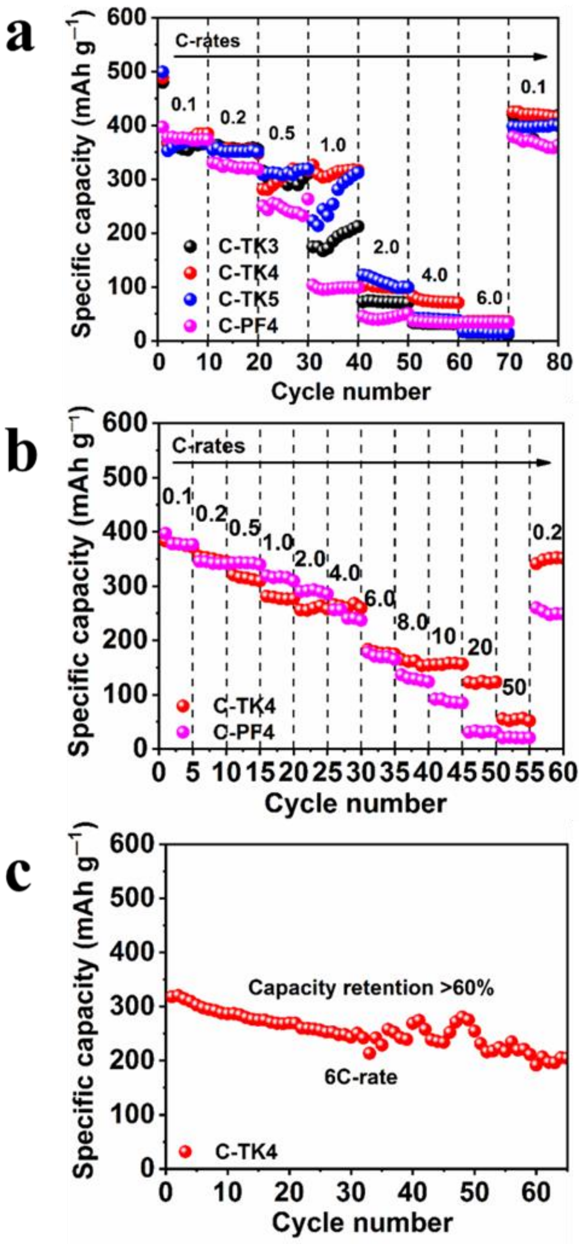

**Figure 4.11.** a) Rate capability profile of C-TK3, C-TK4, C-TK5 and C-PF4 electrodes using symmetrical charge/discharge currents up to 6C-rate. b) Rate capability profile of C-TK4 and C-PF4 electrodes with 0.2C charging (not shown) and different discharge current rates up to 50C-rate. c) Cycling stability profile of C-TK4 electrodes at 0.2C charge (not shown) and 6C discharge.

Figure 4.12 displays the Nyquist plots of fresh and cycled C-TK electrodes. Both the fresh and cycled spectra consists of depressed semi-circles at medium frequency range and an inclined line at low-frequency range. These semi-circles are attributed to the diffusion kinetics of Li-ion through SEI layer, charge transfer resistance between particles to electrolyte and mass transport in the solid-state particle of above said frequency ranges. Both the plots were fitted by Randel equivalent circuit using Zview software (Inset Fig. of 4.12a and b) and their corresponding values are given in Table 4.5.

The fitted elements are as follows: solution resistance ($R_S$), charge transfer resistance ($R_{CT}$), constant phase element ($CPE_{SEI}$), film capacitance ($C_F$), film resistance ($R_F$) and Warburg resistance ($W_S$). For the fresh TKP electrode plots (Fig. 4.12a), the increase in $R_{CT}$ with an increase in the binder content is noticed. The possible reason might be due to the increase in binder weight percentage, which impedes the lithium diffusion for the fresh cells. But, in contrast to the fresh TKP, the plots of the cycled electrode (Fig. 4.12b) exhibited the reverse trend and showed the reduction of $R_{CT}$ with an increase in the binder content. The significant reduction of $R_{CT}$ after charge/discharge cycles is mainly ascribed due to the improved interface properties of SEI after the first cycling [16,56,57]. Further, we also expected that, for cycled TKP electrodes, the higher film capacitance ($C_F$) from the circuit fitting values are further evidenced in the reduction of $R_{CT}$. Hence, these factors might be the reason for the C-TK4 electrode exhibited the low charge transfer resistance and higher electrochemical performance for 500 cycles than the C-TK5 and C-TK3 electrodes.

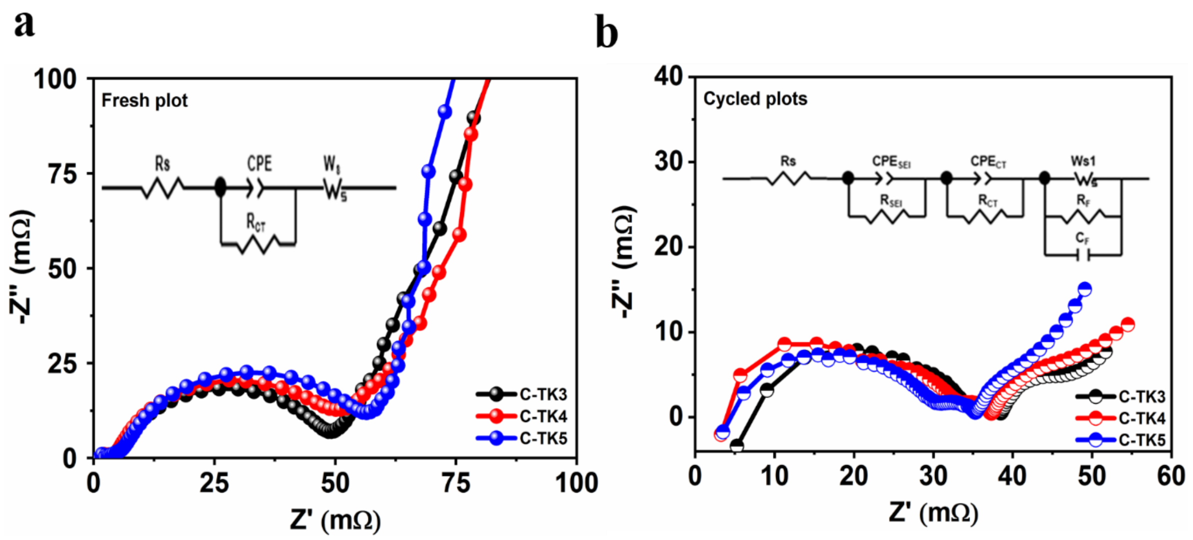

**Figure 4.12.** Nyquist plots of EIS for C-TK3, C-TK4 and C-TK5 electrodes a) fresh plot and b) cycled plot (after 500 cycles).

**Table 4.5.** Equivalent circuit fitted for C-TK3, C-TK4 and C-TK5 values for fresh and after cycling of 500 cycles at 1C-rate.

| **S.No** | **Electrode** | **Fresh cycles** | | **After 500 cycles** | | | | |
|---|---|---|---|---|---|---|---|---|
| | | $R_s$ (mΩ) | $R_{CT}$ (mΩ) | $R_s$ (mΩ) | $R_{SEI}$ (mΩ) | $R_{CT}$ (mΩ) | $W_{S1}$-R | $C_F$ (μF) |
| 1 | C-TK3 | 4.469 | 47.05 | 5.49 | 6.53 | 24 | 42.04 | 0.14552 |
| 2 | C-TK4 | 4.398 | 52.90 | 5.07 | 5.57 | 27.08 | 55.21 | 0.07479 |
| 3 | C-TK5 | 5.21 | 56.04 | 1.20 | 2.20 | 34.56 | 20.71 | 0.08423 |

In addition, the preliminary full cell analysis was demonstrated for real-time applications using aqueous NMC532 cathode and C-TK4 anode in the voltage range 3.0-4.2 V for various C-rates using coin cell as shown in Fig. 4.13. C-TK4 was selected for full cell analysis due to the higher cyclic stability, and rate capability as shown in the half cell studies. The formation study of the cell was done at 0.05C rate for 3 cycles (not shown). Subsequently, charge/discharge measurement was carried out at 0.2C for one cycle and then by 0.2C charging and 1C discharging for 50 cycles (Fig. 4.13). The inset (Fig. 4.13) shows the charge/discharge profile of the full cell at 0.2C-rate. It exhibits the charge and discharge specific capacities of 135 and 126 mAh $g^{-1}$, respectively. In the case of 0.2C charge/1C discharge, it exhibited the initial discharge capacity of 121 mAh $g^{-1}$ at 1C with good cycling stability. Even after 50 cycles, it displayed the discharge capacity of 102 mAh $g^{-1}$ with a capacity retention of >84%. Although the NMC532 cathode was not treated with any inorganic acids during electrode fabrication under aqueous condition for exhibiting the better performance, it could be able to provide a better capacity at 1C-rate. Furthermore, the obtained full cell result is almost equivalent to the reported value found in the literature [58,59]. Hence, TKP is a potential low-cost aqueous binder for the fabrication of graphite anode for lithium-ion batteries.

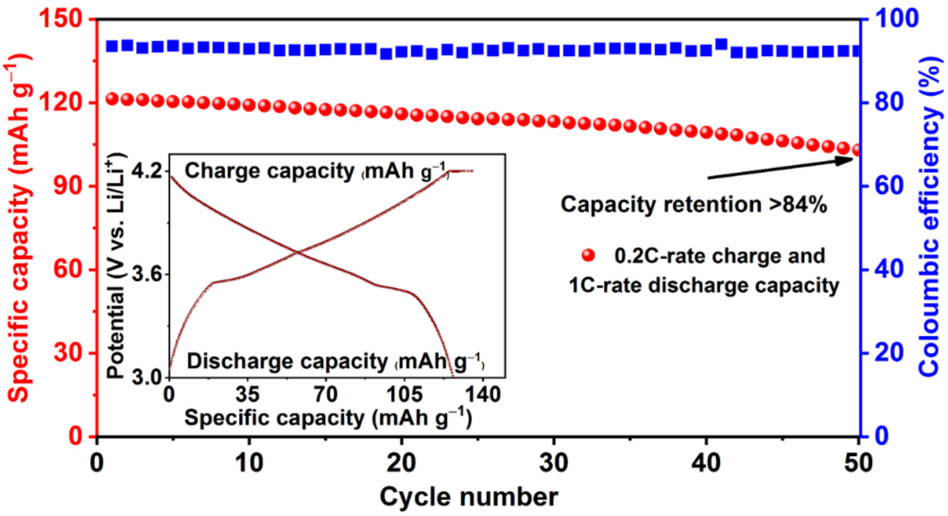

**Figure 4.13.** Cyclic stability and specific capacity profile of NMC532/C-TK4 cell at 0.2C charging/1C discharging for 50 cycles. Inset: Specific capacity vs. voltage profile of the cell at 0.2C charge/discharge.

## 4.4. Conclusions

Herein, we reported a graphite electrode using natural polysaccharide TKP as an alternative to conventional PVDF binder for the application in lithium-ion batteries. Graphite electrodes with various TKP binder contents (3 to 5%) as well as 4% PVDF binder were prepared and characterized systematically. The coated electrodes retained the original morphology of the active material confirming that binder did not react to active material. The electrodes with TKP binder showed much better cycling performance and rate capability than the C-PF4 electrode. For example, the C-TK4 electrode at 1C-rate demonstrated an initial capacity of 326 mAh $g^{-1}$ with excellent cycling stability up to 500 cycles, whereas the C-PF4 electrode delivered an initial capacity of 103 mAh $g^{-1}$ under similar conditions. In addition, the C-TK4 electrode exhibited a discharge capacity of 55 mAh $g^{-1}$ at 50C, while the C-PF4 displayed only 20 mAh $g^{-1}$. The full cell studies also showed the initial discharge capacity of 121 mAh $g^{-1}$ at 1C with capacity retention of >84% after 50 cycles. The enhanced performance of C-TK4 electrode can be ascribed to the following factors. a) High surface charge stability of the slurry, b) Low swelling of the binder, c) High conductivity of the electrode, and d) Branched chemical structure with more hydroxyl bonding sites. Moreover, it has advantages of easy handling and reduced processing cost than the toxic and high-cost PVDF binder. Hence, TKP could be used as a potential binder not only for the fabrication of graphite anode, but also it can be extended to other electrode materials as well as other chemistries like lithium sulfur in lithium-ion batteries for stationary/mobility applications.

### 4.5. References

[1] L. Dai, D. W. Chang, J. B. Baek, W. Lu, *Small* **2012**, 8, 1130-1166.

[2] G. N. Zhu, Y. G. Wang, Y.Y. Xia, *Energy Environ. Sci.* **2012**, 5, 6652-6667.

[3] N. Nitta, F. Wu, J. T. Lee, G. Yushin, *Mater. Today* **2015**, 18, 252-264.

[4] J. -T. Li, Z. -Y. Wu, Y.-Q. Lu, Y. Zhou, Q. -S. Huang, L. Huang, S. -G. Sun, *Adv. Energy Mater.* **2017**, 1701185.

[5] L. Luo, Y. Xu, H. Zhang, X. Han, H. Dong, X. Xu, C. Chen, Y. Zhang, J. Lin, *ACS Appl. Mater. Inter.* **2016**, 12, 8154-8161.

[6] S. Goriparti, E. Miele, F. D. Angelis, E. D. Fabrizio, R. P. Zaccaria, C. Capiglia, *J. Power Sources* **2014**, 257, 421-443.

[7] V. Sharova, A. Moretti, G. A. Giffin, D. V. Carvalho, S. Passerini, C-*J. Carbon Res.* **2017**, 3, 22.

[8] M. Chengyu, M. Wood, L. David, S. J. An, Y. Sheng, Z. Du, H. M. Meyer, R. E. Ruther, D. L. Wood, *J. Electrochem. Soc.* **2018**, 165, A1837-A1845.

[9] M. Nie, D. Chalasani, D. P. Abraham, Y. Chen, A. Bose, B. L. Lucht, *J. Phys. Chem C.* **2013**, 117, 1257−1267.

[10] V. R. Rikka, S. R. Sahu, A. Chatterjee, P. V. Satyam, R. Prakash, M. S. Ramachandra Rao, R. Gopalan, G. Sundararajan, *J. Phys. Chem. C.* **2018**, 122, 28717-28726.

[11] Z. Chen, L. Christensen, J. R. Dahn, *Electrochem commun.* **2003**, 5, 919-923.

[12] A. Nagai, M. Yoshio, R. J. Brodd, A. Kozawa (eds) Lithium-Ion Batteries. Science and Technologies, Springer, New York, NY, Chapter-6, **2009**, 155-161.

[13] V. V. N. Phanikumar, V. R. Rikka, B. Das, R. Gopalan, B.V. Appa Rao, R. Prakash, *Ionics* **2019**, 25, 2549-2561.

[14] F. M. Courtel, S. Niketic, D. Duguay, Y. A. Lebdeh, I. J. Davidson, *J. Power Sources* **2011**, 196, 2128-2134.

[15] D. Bresser, D. Buchholz, A. Moretti, A. Varzi, S. Passerini, *Energy Environ. Sci.* **2018**, 11, 3096-3127.

[16] T. Mochizuki, S. Aoki, T. Horiba, M. S. Dobrick, Z. J. Han, S. Fukuya, H. Oji, S. Yasuno, S. Komaba, *ACS Sustainable Chem.Eng.* **2017**, 5, 6343-6355.

[17] M. K. Dufficy, S. A. Khan, P. S. Fedkiw, *J. Mater. Chem. A.* **2015**, 3, 12023-12030.

[18] S. S. Jeong, N. Bockenfeld, A. Balducci, M. Winter, S. Passerini, *J. Power Sources* **2012**, 199, 331-335.

[19] N. Yuca, H. Zhao, X. Y. Song, M. F. Dogdu, W. Yuan, Y. B. Fu, V. S. Battaglia, X. C. Xia, G. Liu, *ACS Appl. Mater. Interfaces* **2014**, 6, 17111-17118.

[20] S. Huang, J. Ren, R. Liu, M. Yue, Y. Huang, G. Yuan, *New. J. Chem.* **2017**, 41, 11759-11765.

[21] Q. Shi, W. Liu, Q. Qu, T. Gao, Y. Wang, G. Liu, V. S. Battaglia, H. Zheng, *Carbon* **2017**, 111, 291-298.

[22] L. Chai, Q. Qu, L. Zhang, M. Shen, L. Zhang, H. Zheng, *Electrochim. Acta* **2013**, 105, 378-383.

[23] I. Kovalenko, B. Zdyrko, A. Magasinski, B. Hertzberg, Z. Milicev, R. Burtovyy, I. Luzinov, G. Yushin, *Science* **2011**, 334, 75-79.

[24] J. He, H. Zhong, J. Wang, L. Zhang, *J. Alloy. Compd.* **2017**, 714, 409-418.

[25] Y. Bie, J. Yang, Y. Nuli, J. Wang, *J. Mater. Chem A* **2017**, 5, 1919-1924.

[26] Q. Li, H. Yang, L. Xie, J. Yang, Y. Nuli, J. Wang, *ChemComm.* **2016**, 52, 13479-13482.

[27] J. Drofenik, M. Gaberscek, R. Dominko, F. W. Poulsen, M. Mogensen, S. Pejovnik, J. Jamnik, *Electrochim. Acta* **2003**, 48, 883-889.

[28] M. Razavi, S. Nyamathulla, H. Karimian, S. Z. Moghadamtousi, M. I. Noordin, *Molecules* **2014**, 19, 13909 - 13931.

[29] J. You, S. J. Zhang, L. Deng, M. Z. Li, X. M. Zheng, J. T. Li, Y. Zhou, L. Huang, S. G. Sun, *Electrochim. Acta* **2019**, 299, 636-644.

[30] L. Sampathkumar, P. C. Selvin, S. Selvasekarapandian, P. Perumal, R. Chitra, M. Muthukrishna, *Ionics* **2019**, 25, 1067-1082.

[31] L. Sampathkumar, P. C. Selvin, S. Selvasekarapandian, R. Manjuladevi, S. Monisha, P. Perumal, *Ionics* **2018**, 24, 3793-3803.

[32] K. Chawananorasest, P. Saengtongdee, P. Kaemchantuek, *Molecules* **2016**, 21, 775.

[33] E. Quartertones, P. Mustarelli, *Chem. Soc. Rev.* **2011**, 40, 2525-2540.

[34] D. V. Carvalho, N. Loeffler, G.T. Kim, M. M. Margret, W. Mehrens, S. Passerini, *Polymers* **2016**, 8, 276.

[35] P. Goyal, V. Kumar, P. Sharma, *J. Appl. Polym. Sci.* **2009**, 114, 377-386.

[36] J. Liu, Q. Zhang, T. Zhang, J. T. Li, L. Huang, S. G. Sun, *Adv. Funct. Mater.* **2015**, 25, 3599-3605.

[37] A. N. Jansen, G. K. Krumdick, Chemical Sciences and Engineering Division and Energy Systems Division, Final CRADA report, Argonne National Laboratory. December 22, **2016**.

[38] W. Wang, X. Yue, J. Meng, X. Wang, Y. Zhou, Q. Wang, Z. Fu, *J. Phys. Chem. C.* **2019**, 113, 250-257.

[39] G. Qian, L. Wang, Y. Shang, X. He, S. Tang, M. Liu, T. Li, G. Zhang, J. Wang, *Electrochim. Acta* **2016**, 187, 113-118.

[40] V. L. Finkenstadt, *Appl. Microbiol. Biotechnol.* **2005**, 67, 735-745.

[41] E. Peled, S. Menkin, *J. Electrochem. Soc.* **2017**, 164, A1703-A1719.

[42] N. A. Laziz, J. A. Rjeily, A. Darwiche, J. Toufaily, A. Outzourhit, F. Ghamouss, M.T. Sougrati, *J. Electrochem. Sci. Technol.* **2018**, 9, 320-329.

[43] H. K. Park, B. S. Kong, Oh. Eun-Suok, *Electrochem. Commun.* **2011**, 13, 1051-1053.

[44] N. Cuesta, A. Ramos, I. Camean, C. Antuna, A. B Garcia, *Electrochim. Acta* **2016**, 155, 140-147.

[45] S. Komaba, T. Ozeki, K. Okushi, *J. Power Sources* **2009**, 189, 197-203.

[46] N. Yabucchi, K. Shimomura, Y. Shimbe, T. Ozeki, J.-Y. Son, H. Oji, Y. Katayama, T Mura, S. Komaba, *Adv. Energy Mater.* **2011**, 5, 759-765.

[47] M. O. Broniarz, A. Martyla, L. Majchrzycki, M. Nowicki, A. Sierczynska, *Eur. J. Chem.* **2016**, 7, 182-186.

[48] F. S. Li, Y. S. Wu, J. Chou, M. Winter, N. L. Wu, *Adv. Mater.* **2015**, 27, 130.

[49] S. S. Zhang, T. R. Jow, *J. Power Sources* **2002**, 109, 422-426.

[50] Y. Ma, J. Ma, G. Cui, *Energy Storage Mater.* **2019**, 20, 146-175.

[51] D. Versaci, R. Nasi, U. Zubair, J. Amici, M. Sgroi, M. A. Dumitrescu, C. Francia, S. Bodoardo, N. Penazzi, *J. Solid State Electrochem.* **2017**, 21, 3429-3435.

[52] J. Chong, S. Xun, H. Zheng, X. Song, G. Liu, P. Ridgway, J. Q. Wang, V. S. Battaglia, *J. Power Sources* **2011**, 196, 7707-7714.

[53] H. Chen, M. Ling, L. Hencz, H. Y. Ling, G. Li, Z. Lin, G. Liu, S. Zhang, *Chem. Rev.* **2018**, 118, 8936-8982.

[54] H. Zhao, X. Zhou, S. J. Park, F. Shi, Y. Fu, M. Ling, N. Yuca, V. S. Battaglia, G. Liu, *J. Power Sources* **2014**, 263, 288-295.

[55] S. Seki, S. Tabata, S. Matsui, M. Watanabe, *Electrochim. Acta* **2004**, 50, 379-383.

[56] S. S. Zhang, K. Xu, T. R. Jow, *J. Power Sources* **2004**, 18, 226-231.

[57] S. R. Sahu, V. R. Rikka, P. Haridoss, R. Gopalan and R. Prakash, *Energy Technol.* **2019**, 7, 1900849.

[58] J. Paulsen, H. Hong, Hyosun AHN, United States Patent Application Publication, Pub.No: US2016/0218356A1 **2016**. Jul.25.

[59] D. V. Carvalho, N. Loeffler, M. Hekmatfar, A. Moretti, G. T. Kim, S. Passerini, *Electrochim. Acta* **2018**, 265, 89-97.

# Chapter 5

# Effectual investigation of fenugreek powder as an aqueous binder for graphite anode in lithium-ion batteries

# 5. Effectual investigation of fenugreek powder as an aqueous binder for graphite anode in lithium-ion batteries

## 5.1. Introduction

Rechargeable lithium-ion batteries (LIBs) are escalated to a higher position due to their reliable performances, particularly for e-transportation and energy storage applications. Infact, electric vehicle (EV) sales and their usage are increased with an emphasis on the reduction of carbon footprint [1]. Not only EVs, the high energy/power density of lithium-ion batteries (LIBs) afford as a worthy choice to most of the electronic gadgets such as mobile phones, laptops and other miniatures. Therefore, the fabrication of LIBs is of utmost importance. Although these batteries are in high demand for regular usage, manufacturing them is quite complex as well as expensive. Electrodes are fabricated using N-methyl-2-pyrrolidone (NMP) solvent and polyvinylidene difluoride (PVDF) binder under humidity-controlled atmosphere. NMP is a highly volatile, flammable, and explosive organic solvent [2]. Even though, PVDF shows better adherence, chemical, and electrochemical stability for various LIB materials, but it cannot offer the required conductivity and binding strength for the electrode. Hence, carbon black is required to improvise electronic connectivity and to enhance the binding strength of the fabricated electrode [3]. Thus, it is highly urged to seek an alternative method of electrode fabrication for LIBs. On the other hand, aqueous binders have been explored for the fabrication of electrodes due to good dispersion, environmental benign and low-cost process [4-6]. Carboxymethyl cellulose (LiCMC), Styrene butadiene rubber with sodium methyl cellulose and poly (acrylamide-co-diallyl dimethylammonium chloride (AMAC) have been used for the fabrication of graphite anode [7-9]. Silicon and Tin anodes prepared by aqueous binder route show good cyclic stability and rate capability, despite their high-volume expansion during the electrochemical cycling [10,11].

Graphite materials with large particle size and smaller specific surface area are beneficial for large scale electrodes. It provides very low irreversible capacity at the initial electrochemical insertion of lithium during cycling. Thus, it is advantageous in terms of the safety of the full cell and the modules. Herstedt et al. have explained that the surface properties can stimulate the rate capability of graphite materials [12]. It is also claimed that the rate capability of graphite can be improved by an engineering prerequisite for the manufacturing of electrodes as demonstrated by Buqa et al. [13]. In a real viewpoint, graphite demonstrates slow kinetics as well as limitations in a solid-state diffusion during charge and discharge time, hence it cannot deliver or sustain high currents. Forever, the crucial part for the performance of lithium-ion batteries at high rates is the diffusion of lithium-ions from either side of the electrodes. The other factors like binder percent, lithium conducting salt, and additives of electrolyte also may influence the high-rate performance of the graphite electrode in LIBs. Higher cell capacities do require more active material along with higher thickness of an electrode [13]. High thickness affects the electrode porosity and also lowers the electrolyte permeability. Furthermore, it directs to poor lithium-ion kinetics during cycling. Like non aqueous electrode, aqueous based electrodes also have this limitation with thick and dense formats. Hence, the electrode with more thickness ensues the non-uniform formation of solid electrolyte interface (SEI) on the edges of the graphite layer by exposing to the electrolyte. This results in the amputated loss in the active sites and cyclic performance of the cells [14,15,16].

The vital role of the functional group of a binder is well studied with polyacrylic acid (PAA) and poly (methyl acrylate (PMA in order to get better binding strength during the cycling, since they contain a large number of functional sites than the carboxy methyl cellulose (CMC). Therefore, they can adsorb very strongly on the graphite surface by the hydrogen bonding [17]. Above all, polyacrylates are being considered for cross linking PAA with CMC to fabricate high thick graphite electrodes >13.8 mg/cm$^2$. These binders also exhibit the low glass transition temperature (Tg), hence the soft, molten and rubbery nature offer better mechanical stability and flexibility to the electrodes [1]. Moreover, these binders are projected as fluorine free and provided the eco-friendly route for the LIB electrode manufacturing. At first, CMC was explored as water-based binder for electrode manufacturing in LIB applications by Drofenik et al [18]. Furthermore, it has better adhesive strength and lower solvent absorption than the PVDF binder, hence it led to the superior cycling with various active materials [2]. Apart from CMC and polyacrylates, other binders have been investigated, especially natural polysaccharides like guar gum, karaya gum, sodium alginate, chitosan, xanthan gum, Gelatin, tamarind kernel powder, and gellan gum are used for various electrode materials of LIBs [19-26]. These binders are chemically inactive in the potential range between 0 and 3 V vs. Li/Li$^+$. Generally, aqueous based electrodes are prone to be more hydrophilic, however drying temperature >120 $^{O}$C emerges the reduction in residual water content level to < 50 ppm as reported in literature [27,28].

Currently, natural and artificial polymers are explored intensively as binders to understand their potentiality for concerned applications. Explicitly for energy storage requirements, they have great attention due to sustainability, abundance, and low-cost nature [29-31]. Recently, for secondary batteries like LIBs, they employed as a binder for providing better dispersion and adhesion during the slurry preparation rather than the semi-crystalline PVDF binder [32,33]. In most of the cases, Galactomannans are heterogeneous polysaccharides consisting of β-(1-4)-D-mannan backbone having a D-galactose chain with a link of α-(1-6) have been used as binders for LIBs. In addition, it forms viscous, colloidal dispersion when hydrated in water due to the presence of galactose group [34]. But, the conformation of the 1→4-linked β-D-mannan backbone is equivalent to the cellulose. Hence, it cannot be dissolved in water. The galactose group which is attached as a side chain to backbone moiety causes steric disturbance, interchain association, and crystallization. Consequently, the galactose group renders the water solubility to the galactomannans, moreover, the increase in the degree of galactosyl percentage enhances the water solubility [34]. Similarly, the molecular structure of FG binder also consists of β, 1→4 linked mannopyranosyl units and each individual backbone monomer comprises an α, 1→6 linked galactopyranosyl residues. Therefore, the natural polysaccharides of fenugreek and guar gum do have more solubility than any other natural existing polysaccharides, since their galactose to mannose ratios are almost the same i.e., 1.0:1.0-1.1 and 1.0:1.6-1.8 respectively. The FG binder is a non-toxic polysaccharide with a molecular weight of ~30kDa, which corresponds to an average of 180-190 monosaccharides (mannose + galactose) units in the moiety. It is derived from the endosperm of fenugreek seeds with high branching random coil polymer structure, which reveals that it is highly flexible, and provides more binding sites [34]. It is also used for the reduction of surface tension by lowering the interfacial free energy. This further helps in the reduction of the surface energy of the electrode and enhances the wettability of the LIB cell [35]. On the other hand, cross linkings of in-situ grafting, addition reaction, and coordination reaction are successfully employed to reduce the volume expansion of silicon anode in LIBs, further they also provide better cyclic stability to cathode sulphur composite considerably [36,37,38]. Furthermore, as mentioned in literature, galactomannan binder does help in the usage of less binder amount as compared to the CMC binder for better electrochemical performance. It confirms that carboxyl and hydroxyl groups of the biopolymer are bonded via hydrogen bonding with the active material and provided decent cycling performance for LIBs [39].

In this work, we report for the first time the preparation of graphite electrode with FG binder and its electrochemical performances including cycling stability at high C-rates. The importance of intra/inter hydrogen bonding with graphite anode has been elucidated for better electrochemical performance. Besides, the advantage of FG binder has also been revealed over the standard PVDF binder used in LIB applications.

## 5.2. Experimental

### 5.2.1. Materials

Potato-shaped graphite particles (d = 10-18 µm, Superior graphite), NMC532 (Targray, Canada), carbon black (CB, Super C65, TIMCAL Graphite & Carbon, Switzerland), FG binder (Local market, India), and polyvinylidene fluoride (PVDF, Kynar, Arkema) were used as such without any further purification. 1M $LiPF_6$ in a mixture of ethylene carbonate (EC): dimethyl carbonate (DMC): ethyl methyl carbonate (EMC) (1:1:1 v/v enchem, Korea) was used as the electrolyte. Ultrapure water of 18.2 MΩ $cm^{-1}$ was used for the preparation of binder solution and slurries.

### 5.2.2. Electrode preparation and electrochemical measurements

Graphite electrode of three different ratios were fabricated by varying graphite (84 to 86 wt.%), fenugreek binder (4 to 6 wt.%) and keeping conductive carbon (10 wt.%) content constants as given in Table 5.1. Conventional graphite electrode was prepared with graphite (86 wt.%), conductive carbon (10 wt.%) and PVDF binder (4 wt.%). The desired compositions of graphite and conductive carbon were premixed together, to this mixture the required quantity of FG binder solution (~ 4 to 6 ml) was added and mixed in a mortar pestle to get a homogenous slurry. Then, the slurry was cast on a copper substrate (10 µm thickness) under ambient atmosphere. In a similar process, PVDF-based graphite electrode was fabricated with NMP inside a glove box. The coated electrodes were dried in a vacuum oven for 12 h then the electrodes were calendared and punched to 15 mm discs. The obtained active material loading of the electrodes was in between 4.5 and 5.5 $mg/cm^2$.

To investigate the electrochemical performance of graphite anode using FG and PVDF binders, the CR2032 coin cells were fabricated in a glove box (oxygen and moisture contents <1.0 ppm). Lithium foil was used as reference and counter electrode. Whatman Glass microfiber paper (GF/D) used as a separator and 1 M $LiPF_6$ in EC: DMC: EMC (1:1:1 v/v) was used as electrolyte. Galvanostatic charge/discharge analysis was carried out in the voltage range 0.005–3.0 V vs. Li/Li$^+$ using BT-2000 Arbintester (USA). The rate capability experiments were done by two methods: In the first method, the same currents were applied for both charge/discharge steps up to 6C-rate (symmetric method) and in the second method, the charge current (lithiation) was kept constant at 0.2C-rate and the discharge current (de-lithiation) varied up to 6C-rates (asymmetric method). Cyclic voltammetry (CV) studies were carried out for pure FG binder and graphite electrode half cells in the voltage range 0.005–3.0 V vs. Li/Li$^+$ at a scan rate of 0.05 mV s$^{-1}$ using BioLogic Science Instruments (France). Electrochemical impedance spectroscopy (EIS) analysis was performed with an amplitude of 10 mV in the frequency range of 1 MHz to 0.01Hz using a Parstat MC Electrochemical Workstation (Princeton Applied Research, USA). All electrochemical tests were performed at room temperature of 25 $^{o}$C.

**Table 5.1.** FG and PVDF binder-based graphite electrodes with different active material ratios.

| **S. No** | **Materials** | **Weight ratios of (GT: CB: FG/PVDF) in slurry** | **Electrode Identification** |
|---|---|---|---|
| 1<br>2<br>3 | Graphite: CB: FG | 86:10:04<br>85:10:05<br>84:10:06 | G-FG4<br>G-FG5<br>G-FG6 |
| 4 | Graphite: CB: PVDF | 86:10:04 | G-PF4 |

### 5.2.3. Characterization of materials, slurries, and coated electrodes

X-ray diffraction analysis (XRD) analysis was done for pure binder as well as FG based pristine/cycled graphite electrodes by using a Smart lab Rigaku X-ray diffractometer with monochromatic CuK$_\alpha$ radiation in the 2θ range 10–80$^{\circ}$. For the pure FG binder, the Fourier Transform Infrared spectroscopy (FTIR) spectrum was recorded at 2 cm$^{-1}$ resolution by the Attenuated Total Reflectance (ATR) method using the Perkin Elmer analyzer. Rheological studies were measured for all pure binder solutions and for FG based aqueous graphite slurries using Anton Parr MCR102. The Peel strength of the fabricated graphite electrodes were conducted at an angle of 180$^{o}$ and speed of 25 mm/min using Mecmesin peel tester. The pristine and cycled electrode morphologies were characterized by a Field Emission Scanning Electron Microscope (FE-SEM), Carl Zeiss with an accelerating voltage of 15 kV supported with an energy dispersive X-ray spectrometer (EDS). For the cycled electrodes, the electrolyte salt marks were washed with dimethyl carbonate and dried in the glove box.

Thermogravimetric analysis (TGA) of FG binder was carried out under argon atmosphere by LABSYS EVO STA (Simultaneous thermal analysis). Contact angle (CA) measurements were carried out under ambient room condition (<50% relative humidity condition) using DSA25 (KRUSS). To enact this analysis, pure 4, 5, and 6 wt.% FG binder aqueous solutions were cast on glass slides, and the pure FG binder films are called as P-FG4, P-FG5 and P-FG6, respectively. Average contact angles of electrolyte droplets on the surface of FG cast films recorded for 10 s. Swelling studies were done to find the increase in weight percentages of the pure binders and graphite electrodes after soaking them in the electrolyte for 2 and 15 days, respectively. Successively, after swelling studies, the moisture content in the left out electrolyte was ascertained using Karl-Fischer Titrator (Metrohm, 901, Titrando). Ionic conducivity was measured for pure FG binder solutions i.e., 4-6 wt.% using Metrohm 914 pH/Conductometer. Optical microscopy analysis conducted for pure binder solutions of FG (6 wt.%) and PVDF (4 wt.%) cast on glass substrate using Olympus microscope, (GX51). Raman analysis performed with Alpha 300R WITEC Spectrometer with a wavelength of 532 nm for the FG based graphite electrodes.

### 5.3. Results and discussion

Figure 5.1 shows the XRD, FTIR, CV, and viscosity studies of pure FG binder. The XRD pattern of FG binder (Fig. 5.1a) exhibited a broad peak at 21.11$^{o}$ and a sharp peak at 34.83$^{o}$ [40]. The FTIR spectrum (Fig. 5.1b) of FG binder shows a wide band at 3288 cm$^{-1}$ for hydroxyl group, and the other peaks at 1017, 1399, 1641 and 2924 cm$^{-1}$ are related to the C-O-C stretching of ether, C-H bonding of methyl group, stretching vibration of C=C bond and asymmetric stretching of the alkane C-H bond, respectively [41]. TG/DSC and Optical microscopy analysis are given in Fig. 5.2. The FG binder exhibits three types of weight losses in the range from 30 to 800 $^{O}$C as shown in Fig. 5.2a. The first weight loss (9%) occurred at 40-180 $^{O}$C corresponds to the loss of a small amount of moisture; the second major weight loss (>50%) happened at 180-350 $^{O}$C, which is ascribed for the polymer decomposition; the third weight loss from 350 to 510 $^{O}$C is due to the combustion and decomposition of the FG binder [42]. The Differential scanning calorimetry (DSC) data showed an endothermic peak at 107 $^{O}$C and an exothermic peak at 334 $^{O}$C. The endo peak is attributed to the loss of absorbed water, also it is an indicator of polymer/water interaction, whereas, the exothermic peak refers to the polymer degradation [43]. Since, the main thermal decomposition occurred apparently after 300 $^{O}$C, FG can be used as binder for LIB applications. To check the electrochemical stability of pure FG binder, the binder coated copper film was studied by CV in the potential range of 0.005 to 3.0 V vs. Li/Li$^{+}$ at 0.05 mV s$^{-1}$ (Fig. 5.1c). The observed small reduction peak at 1.4 V in the bare CV is due to the reduction of moisture present in the electrolyte [44]. Apart from that, it displayed a small quasi reversible redox wave at 1.0 V which could be due to intrinsic conductivity of binder. But it is a negligible current, hence this binder can be used for LIB applications [45-46]. The viscosity values of pure FG binder solutions (4 to 6wt.%) were measured and depicted in Fig. 5.1d. The viscosity order for pure binder solutions was found as follows P-FG5>P-FG4>P-FG6. In addition, all three binder percentages showed the shear thinning behaviour (i.e., Pseudo plastic) [41]. Specifically, among the three binder solutions, P-FG6 had given the lower viscosity than the other binder concentrations. So, it is obvious that, the aggregates which will form during the G-FG6 slurry preparation would be minimum than the other G-FG slurries used for the electrode fabrication. Therefore, better electrochemical result could be predicted from G-FG6 graphite electrode than the other electrodes. Optical microscopy analysis (Fig. 5.2b, c) reveals that more porosity can be achieved with FG based film than PVDF counterpart, which could be due to amorphous nature of FG binder than PVDF. The better porosity led to enhanced electrolyte penetration into the electrode as suggested by H. Buqa et.al. [13]. Swelling analysis for pure binders of PVDF, FG and G-FG electrodes are executed as shown in Fig. 5.3. The pure PVDF binder was swollen as represented in the digital image (Fig. 5.3b), while pure FG binder did not show any swelling behaviour, except the solution turns to pale yellow colour (Fig. 5.3b). In the case of graphite electrodes, G-FG5 and G-FG6 displayed the swelling behaviour in the electrolyte (Fig. 5.3c), whereas, G-FG4 and G-PF4 electrodes fragmented completely during the swelling period (Fig. 5.3c) and hence, their swelling properties could not be measured. The obtained swelling values for G-FG5 and G-FG6 electrodes are 20.39 and 23.93% respectively. It is known that FG binder has a branched polymer structure with less amounts of carbohydrates and proteins, hence it has shown the closest swelling values for either of the electrodes [34]. After the swelling studies, the moisture content of the remained electrolyte has been studied. The obtained moisture values are 156, 155, 118 and 213 ppm for G-FG4, G-FG5, G-FG6 and G-PF4, respectively. The lowest residual moisture observed for G-FG6 sample suggesting that the side reactions encompassed with this electrode might be lowered than the rest of the electrodes. Rheological studies were performed for G-FG4, G-FG5 and G-FG6 electrode slurries (For the Table 5.1 electrodes) at room temperature. All three slurries exhibited the shear thinning behaviour (Pseudo plastic/non-Newtonian) with an increase in the shear rate (Figure not shown). The obtained viscosity of slurries at the shear rate of 1 $s^{-1}$ is in the order of G-FG4>G-FG6>G-FG5. In contrast to the viscosities of pure binder, G-FG5 slurry displayed lower viscosity than the other two slurries. All three cases, no agglomeration was formed during the slurry preparation, thus achieved uniform coatings with FG binder.

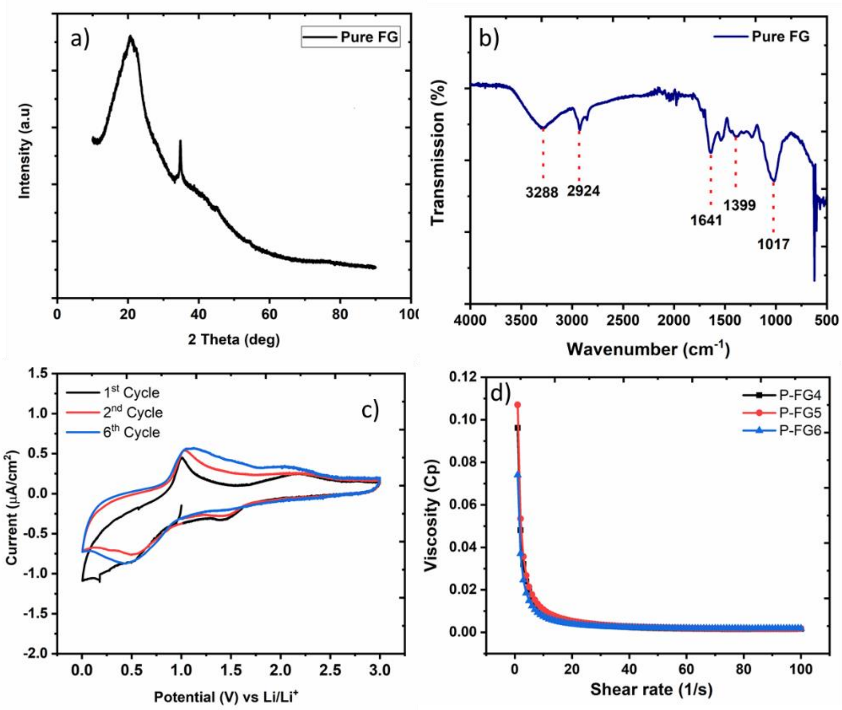

**Figure 5.1.** a, b) XRD and FTIR of pure FG binder, c) Successive cyclic voltammogram of FG in the range between 0.005 and 3.0 V vs. Li/Li$^+$ at a scan rate of 0.05 mV $s^{-1}$, d) Viscosity vs Shear rate profile of pure FG binder at various concentrations.

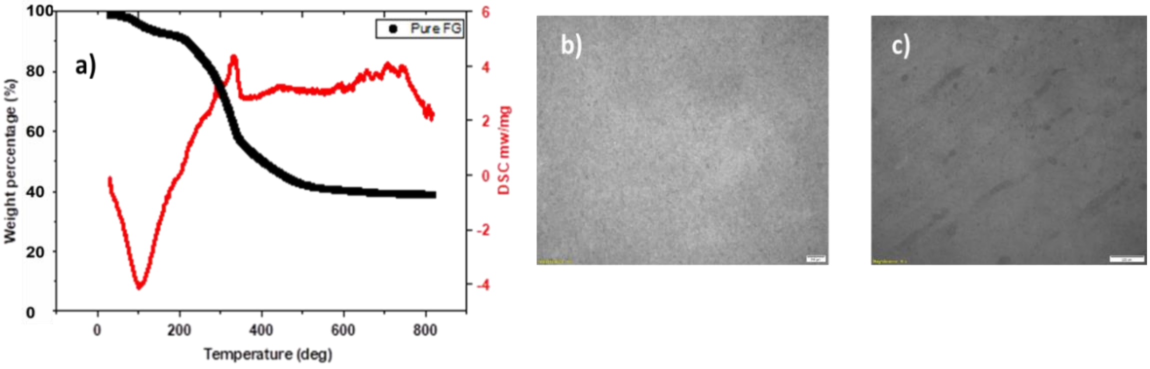

**Figure 5.2.** a) TG/DSC of FG binder, b-c) Optical microscopy images of FG and PVDF binder.

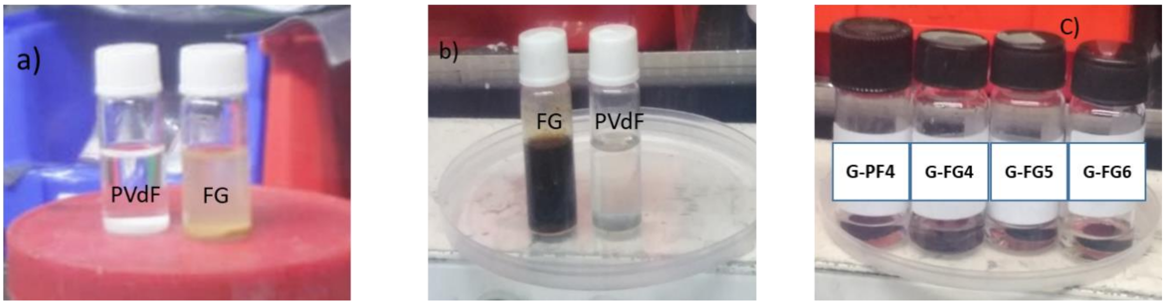

**Figure 5.3.** Digital images of a) PVDF and FG binders dissolved in electrolyte b) Swollen PVDF and colour changed FG binders dissolved in the electrolyte c) Swelled G-FG and PVDF based graphite electrodes after kept in the electrolyte for a duration of 15 days.

Contact angle measurements (Fig. 5.4) were evaluated for pure binder (4 to 6wt.%) to find the wettability of the electrolyte and peel strength of the coated aqueous based graphite electrode. The average contact angle was obtained by applying an electrolyte droplet on the surface of the binder film for a time of ten seconds. The obtained values are 30.1, 30.4 and 25.9 degrees for P-FG4, P-FG5 and P-FG6, respectively (Fig. 5.4a). P-FG6 showed a lower contact angle value than the other two samples, which is ascribed to the increase of galactose content in the FG binder [34, 41]. Thus it indicates that as the binder content increases, the electrolyte wettability also increases. Ionic conductivity is measured for pure FG binder solutions for all three weight percentages i.e., (4 to 6wt.%). The attained ionic conductivities are 462, 335, and $740\ \mu\text{S cm}^{-1}$ for P-FG4, P-FG5 and P-FG6, respectively. P-FG6 has given higher conductivity than the other binder solutions. Thus, ionic conductivity measurements also support the contact angle values and provided the correlation like increase in inter hydrogen bonding leads to higher conductivity and lower wettability. These wettability and conductivity studies further confirms the P-FG6 binder may improve electrochemical performance, cyclic stability, and rate capability of the G-FG6 electrode. However, all three aqueous based graphite electrodes give the peel strength value of 0.0149 N/cm as given in Fig. 5.4b.

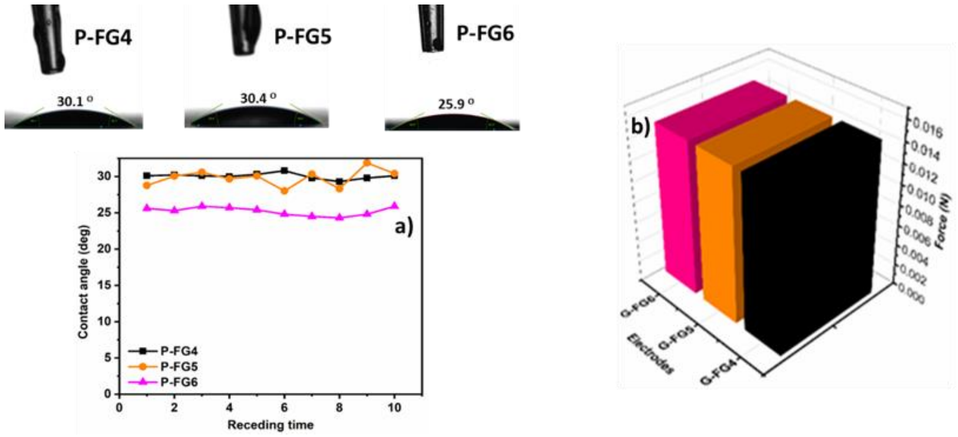

**Figure 5.4.** a, b) Contact angle of pure binders and peel strength of the coated electrodes. a) Contact angle vs receding time profile of P-FG4, P-FG5 and P-FG6 using 1M $LiPF_6$ electrolyte conducted at room temperature. b) Peel strength of aqueous coated graphite (G-FG) electrodes.

Cyclic voltammetric studies have been carried out for G-FG4, G-FG5 and G-FG6 electrodes for six successive cycles in the voltage range between 0.005 and 3.0 V vs. $Li/Li^+$ at 0.05 mV $s^{-1}$ is shown in Fig. 5.5. The first and sixth cycles of G-FG6 are shown in Fig. 5.5a and 5.5b, respectively. Both the first and sixth cycle CVs have shown the reversible redox peaks in the voltage range between 0.01 and 0.30 V. A peak observed at 0.66 V in the cathodic scan in the first cycle is ascribed as SEI layer [47]. High-intensity peaks were observed for G-FG6 sample than the other graphite electrodes. All three stages of graphite intercalation are clearly revealed in G-FG6. The increase in current could be due to the better dispersion of binder with the graphite particles leading to high rate of lithiation of the anode [25]. Additionally, more binder content may lead to better hydrogen bonding with active material and conductive carbon. The increase in binder concentration facilitates better solubility, wettability and dispersion by the enhancement of galactose moiety on the mannan backbone of the FG polymer binder [34].

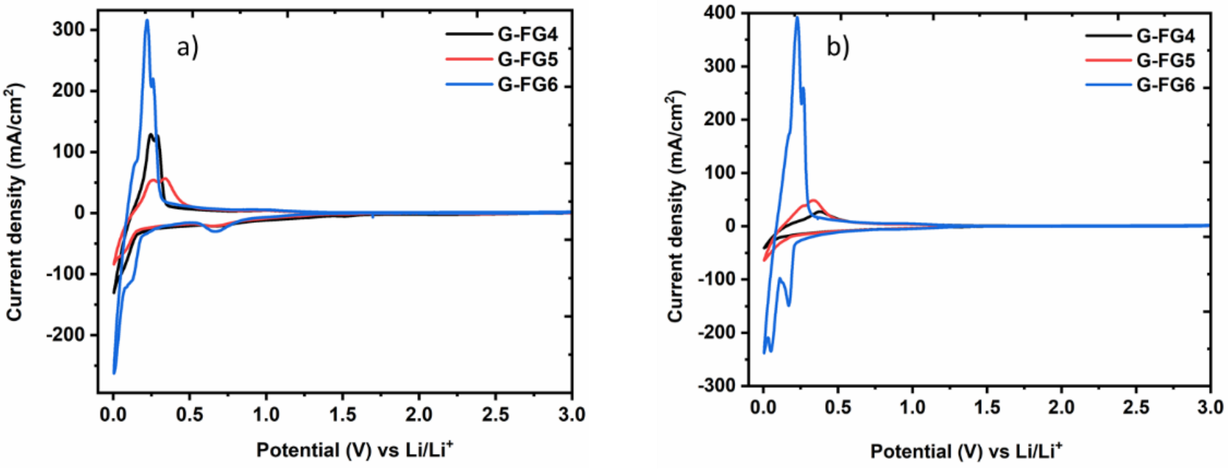

**Figure 5.5.** Cyclic voltammograms of G-FG electrodes at 0.05 mV $s^{-1}$ for 1st cycles a) and b) 6th cycles.

Figure 5.6. shows the galvanostatic charge/discharge analysis and cyclic stability profiles of G-FG4, G-FG5, G-FG6 and G-PF4 electrodes in the voltage range 0.005 to 3.0 V vs. Li/$Li^+$. All electrodes exhibited a small plateau at ~0.6 V in the first lithiation profile for the formation of SEI layer, which usually occurs in the voltage range between 0.8 and 0.06 V vs. Li/$Li^+$ [46]. The obtained reversible capacities varied by changing the composition of graphite electrodes. First cycle de-lithiation capacities of G-FG4, G-FG5, G-FG6, and G-PF4 are found to be 347, 359, 377 and 367 mAh $g^{-1}$ at 0.1C-rate with coulombic efficiencies (CEs) of 83.1, 86.11, 84.39 and 92.6%, respectively (Fig. 5.6a). It is noticed that CEs of aqueous based electrodes were lower as compared to the PVDF based electrode. This could be due to the high irreversible capacities, i.e., 70.76, 58.43, 69.88, and 29.38 mAh $g^{-1}$ was obtained by during initial cycle due to the formation of SEI layer and other side reactions [48]. However, at the end of hundred cycles (Fig. 5.6b) the reversible capacities of G-FG4, G-FG5, G-FG6, and G-PF4 are 264, 272, 265 and 215 mAh $g^{-1}$ with capacity retentions of 70.2, 75.8, 69.3 and 58.6%, respectively. In all cases, the coulombic efficiencies are determined to be >99.7%. Polarization between charge/discharge process plays a prominent role for the better electrochemical performance and cyclic stability of the lithium-ion cells. The corresponding polarization values for G-FGs and G-PF4 electrodes were found to be 0.13, 0.1, 0.06 and 0.16 V, respectively (Figure not shown). The polarization between the cyclings of G-FG electrodes expresses a decreasing trend with an increase in FG binder concentration and also their values are smaller than that of compared to G-PF4 electrode. It signifies that the G-FG6 electrode has higher conductivity and better electrochemical performance than the other graphite electrodes. This result complies with the CVs of G-FG electrodes, where the peak current increases with increase in the binder content. Although G-PF4 showed better CE at the initial cycle, it exhibited lower de-lithiation capacity even at 0.1C-rate due to higher polarization than G-FG electrodes [25]. Cycle number vs. specific capacity profiles of all the G-FGs and G-PF4 electrodes at 0.1C for hundred cycles are shown in Fig. 5.6c. The specific capacity of G-FG4 is marginally higher than G-FG6 as well as other electrodes for the initial ten cycles, after that G-FG6 showed better specific capacity and cyclic stability for the given hundred cycles. Although G-PF4 showed high initial specific capacities, it fails to maintain the cyclic stability. It is noteworthy to be mentioned that the obtained discharge capacities of G-FG electrodes are

better than various other aqueous binder-based electrodes reported in the literature as mentioned in Table 5.2.

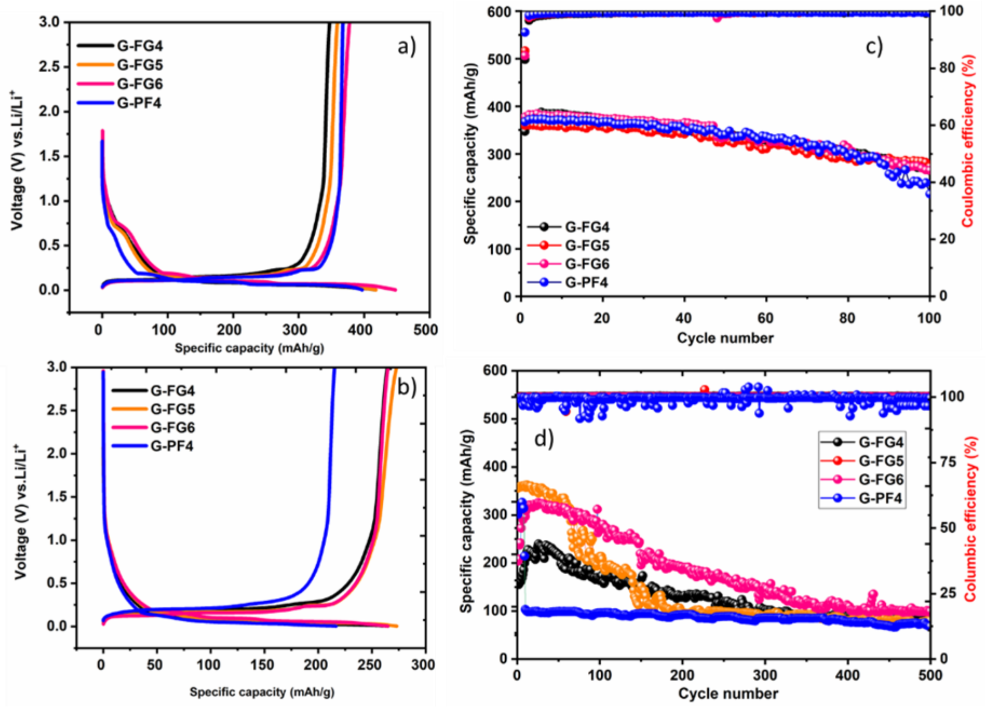

**Figure 5.6.** Galvanostatic charge/discharge profiles of G-FG4, G-FG5, G-FG6 and G-PF4 electrodes a) at first cycle and b) after 100 cycles. Cyclic stability profiles of G-FG4, G-FG5, G-FG6 and G-PF4 electrodes for c) 100 cycles at 0.1C-rate and d) 500 cycles at 1C-rate.

**Table 5.2.** Comparison of aqueous FG graphite electrodes with other aqueous binders at various C-rates.

| S.No | Aqueous binders | Wt.% of binder | Initial Specific capacity (mAh $g^{-1}$) 1st cycle | Reversible discharge capacity (mAh $g^{-1}$) 100th cycle | C-rate | Reference |
|---|---|---|---|---|---|---|
| 1 | AMAC | 5 | 200 | 200 (60th) | 0.5mA $cm^{-2}$ | 9 |
| 2 | AMMA | 5 | 200 | 210 | 0.3 mA $cm^{-2}$ | 49 |
| 3 | Xanthan gum | 8 | ~280 | ~250 (180th) | 0.5 | 50 |

| | | | | | | |
|---|---|---|---|---|---|---|
| 4 | Natural cellulose | 5 | ~320 | - | 0.1 | 51 |
| 5 | Acryl S020 | 6 | 355 | 177 | 0.1 | 52 |
| 6 | PAA | 6 | 349 | 315 (50th) | 0.1 | 53 |
| 7 | C-Li-PSBM | 1.5 | 365 | ~310 | 0.5 | 54 |
| 8 | G-FG4<br>G-FG5<br>G-FG6 | 4<br>5<br>6 | 347/157<br>359/355<br>377/203 | 264/85 (500th)<br>272/80 (500th)<br>265/99 (500th) | 0.1/1.0<br>0.1/1.0<br>0.1/1.0 | This work |

In order to evaluate the cyclic stability, the charge/discharge process was carried out for all four electrodes at 1C-rate for 500 cycles as depicted in Fig. 5.6d. After initial three cycles at 0.1C, the cells were cycled at 1C-rate for 500 cycles. The first discharge capacities at 1C were found to be 157, 355, 203 and 301 mAh g$^{-1}$ for G-FG4, G-FG5, G-FG6, and G-PF4 with coulombic efficiencies of 99.9, 99.7, 99.6, and 99.6%, respectively. Whilst, they showed the discharge capacities of 85, 80, 99 and 67 mAh g$^{-1}$ with capacity retentions of 54, 22, 48 and 21%, respectively at 500th cycle. The coulombic efficiencies for all four cases remain >99% even at 500 cycles. To decipher the cycling stability of G-FG electrodes, it is crucial to understand the influence of binder during charge/discharge of the cells. The initial cyclings (i.e., up to 20 to 30 cycles) of all G-FG electrodes displayed gradual increase in capacity, after that they showed the decreasing trend up to the 500 cycles. The electrodes of G-FG5 and G-FG6 had given better capacities than G-FG4. The G-FG4 does not contribute any significant performance, and also the low binder percent may not be sufficient enough to adhere the coated graphite with copper substrate. Whereas, in the case of G-FG5, the capacity and cyclic stability were far better than G-FG4 and G-FG6 electrodes up to 70-80 cycles. Subsequently, both capacity and stability were reduced drastically and became lesser compared to both G-FG4 and G-FG6 at the end of ~170 cycles. The reduction in the specific capacity of this electrode (i.e., G-FG5) is further explained in the SEM section (*vide infra*). While in G-FG6, the specific discharge capacity increased for the first 25 cycles, and then decreased gradually. Nevertheless, it bestowed highest capacity than the other G-FG electrodes at the end of ~60th cycle and it remained high till the end of 500 cycles. The better electrochemical performance of G-FG6 might be due to the increase in binder content which leads to the better wettability and cohesion of the electrode as more intact during the cycling. In the case of G-PF4 one, after a few cycles, the specific capacity dropped to a minimum value of about 100 mAh g$^{-1}$ and it remained stable for 500 cycles. Hence, G-FG6 electrode exhibited better electrochemical performance than other electrodes.

Figure 5.7 shows the schematic representation of intra and inter hydrogen bond formation in the G-FG electrodes. As per the report by R. R. Jonnalagadda. et al. [35], FG binder has two types of hydrogen bonding interactions i.e., intra and inter hydrogen bonding as in other galactomannan polysaccharides [35]. Both these bondings are marked accordingly in the schematic representation. Among these bondings, intra hydrogen bonding always forms aggregation within the structure by a strong bonding. Whereas, inter hydrogen bonding helps to make a network with neighbouring groups of the FG binder for effective bonding. G-FG4 and G-FG6 electrodes having lowest and highest intra/inter bondings due to the change in binder concentration. Accordingly, the electrochemical stability for the former electrode showed mediocre performance and the later exhibited better performance. In the case of the G-FG5 electrode, the intra bonding may have been pronounced than the inter hydrogen bonding.

Therefore, this electrode displayed more agglomeration as well as cracks in the SEM morphology (SEM section), which further leads to the modest electrochemical performance during the cycling at 1C-rate. G-PF4 was not discussed in this schematic representation, since its cyclic stability was poor compared to all three G-FG electrodes. In the report on Nano silicon electrode with FG binder [41] was observed that as the binder concentration increases from 3-10 wt.%, the optimized 5 wt.% binder has demonstrated higher cyclic stability for silicon anode. But in the present study, 6 wt.% binder composition has been performed satisfactory cyclic stability at various C-rates for graphite anode.

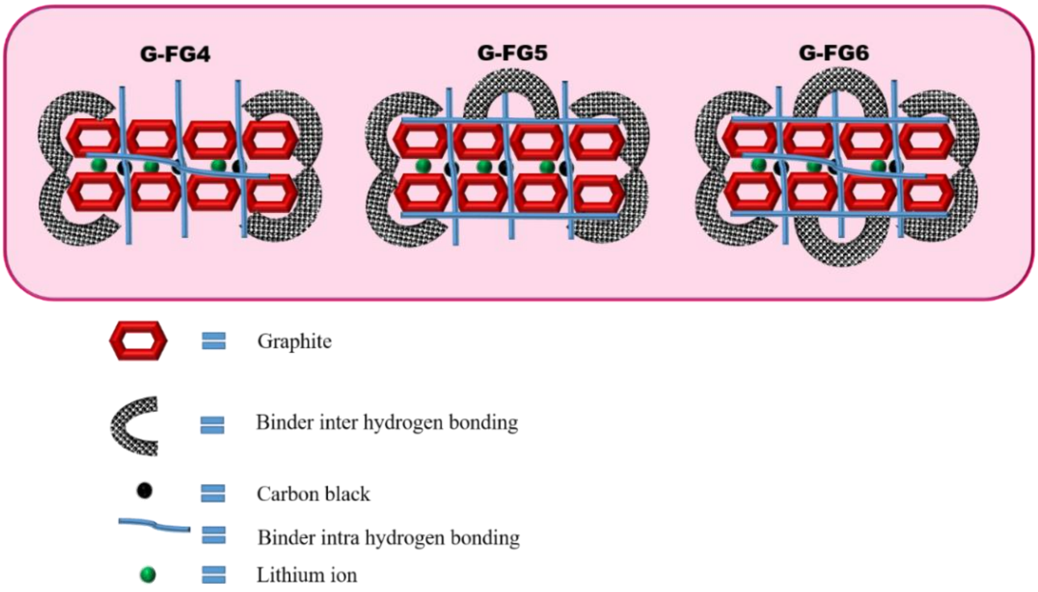

**Figure 5.7.** Schematic representation of FG binder for all the G-FG electrodes.

Figure 5.8 shows the rate capability and cyclic stability profiles of G-FG4, G-FG5, G-FG6 and G-PF4 by applying symmetric (same current rate for both charge and discharge) and asymmetric (different current rate for charge and discharge) current rates (0.1C to 6C for symmetric and 0.2C to 6C asymmetric). The charge /discharge analyses were carried out for five cycles for every given C-rate. In the symmetric rate capability analysis (Fig. 5.8a), the specific capacity decreases with increase in current rate up to 1C. Interestingly, after 1C, the discharge capacities of the G-FG electrodes are quite constant until 4C. At 4C-rate the obtained capacity retentions were 52, 85, 76 and 9% for G-FG4, G-FG5, G-FG6 and G-PF4, respectively with respect to the discharge capacities of 0.1C-rate. In addition, G-FG5 and G-FG6 electrodes at 4C-rate displayed the discharge capacity of >300 mAh $g^{-1}$. Furthermore, the obtained electrochemical performances at 4C-rate are much better than the reported values in literature [25,55]. But after 4C-rate, the reversible capacities of all electrodes faded significantly. Nevertheless, when electrodes were switched back to 0.1C-rate after 35 cycles, the G-FG6 electrode has given a remarkable reversible capacity of 415 mAh $g^{-1}$ than any other G-FG electrodes.

For asymmetric rate capability studies, the cells were cycled at 0.1C for five cycles, and then they were charged at a constant current rate of 0.2C and the discharge current rates varied from 0.2 to 6C for five cycles each (Fig. 5.8b). The electrodes G-FG6 and G-FG5 displayed higher discharge capacities than G-FG4 and G-PF4 electrodes. G-FG4 showed the decreasing capacity trend for all the C-rates. However, both G-FG5 and G-FG6 had shown almost similar capacities from 0.2C to 6C-rates. In addition, at 2C-rate the G-FG6 electrode displayed the discharge capacity of >300 mAh $g^{-1}$ with a decent consistency for five cycles. Even more, in the case of G-FG6, remarkable specific capacity of 270 mAh $g^{-1}$ was observed at 6C-rate, which is nine-fold higher than the corresponding symmetric rate capability data. The non-aqueous G-PF4 displayed a reduction in capacities at high rates from 2C to 6C. It reveals that, PVDF binder-based graphite electrode could not sustain the high current due to the weak Van der Walls forces between the active material and binder. Whereas, aqueous FG aqueous binder-based graphite electrodes exhibit better electrochemical performance irrespective of the C-rates. Besides, when the current was switched back to the 0.1C-rate after 35 cycles, the G-FG6 electrode regained the capacity with 100% retention compared to other electrodes. Hence, mostly in all the cases, G-FG6 electrode study is viable for the graphite anode with a fenugreek binder. Further, to find the lithium storage at an asymmetric rate, galvanostatic charge/discharge analysis was performed only for G-FG electrodes w.r.t. $Li/Li^+$ in the voltage range 0.005 to 3.0 V, as shown in Fig. 5.8c. To enact this, all G-FG electrodes were charged (lithiation) at 0.2C and discharged (de-lithiation) at 1C-rate for 200 cycles. The initial charge/discharge capacities were found to be 304/302, 349/347, and 287/286 mAh $g^{-1}$ for G-FG4, G-FG5, and G-FG6 respectively as presented in Fig. 5.8c. The attained CEs of these electrodes are 99.75, 99.26, and 99.69%, respectively. After two hundred cycles, the same electrodes delivered the specific capacities of 30/29, 31/22, and 187/187 correspondingly. From Fig. 5.8c, it can be seen that the capacities of both G-FG4 and G-FG5 are reduced with an increase in cycling. Especially, after 80 cycles, the capacity decay was even more and discharge capacities were ended with lower values. However, G-FG6 displayed a much better and higher performance for the complete cycles with good cyclic stability. Even though the initial capacities of G-FG6 were lower than the other electrodes, still it could afford the stable and at least three times higher discharge capacities than G-FG4 and G-FG5 electrodes for the corresponding cycles from 150 to 200. Significantly, CEs of these electrodes are 96.5, 73.4 and 99% at the 200th cycle. The higher CE of G-FG6 also validates that this particular binder concentration provided more pronounced performance than the routine low binder content generally used in the electrode fabrication of LIBs. Furthermore, to understand the potency of this G-FG6 electrode, charge/discharge study was conducted at 0.2C charge (lithiation) and 10C discharge rate (de-lithiation) for 100 cycles as illustrated in Fig. 5.8d. The obtained initial de-lithiation capacity was 319 mAh $g^{-1}$ whereas the final capacity was 144 mAh $g^{-1}$ with a capacity retention of 47% at the end of the 100th cycle. Although the capacity is declining from the initial cycle to the final cycle, it is still an exemplary performance with relevance to the reported results of graphite anode with various aqueous binders at 10C-rate [25,56]. The better performance of graphite electrode even at 10C-rate may be due to the branched structure of the FG binder, since the branched structure could absorb more electrolyte and distribute on the graphite surface uniformly. Thus, the lithium-ion mobility would have been enhanced and delivered the better capacity for FG based graphite electrodes.

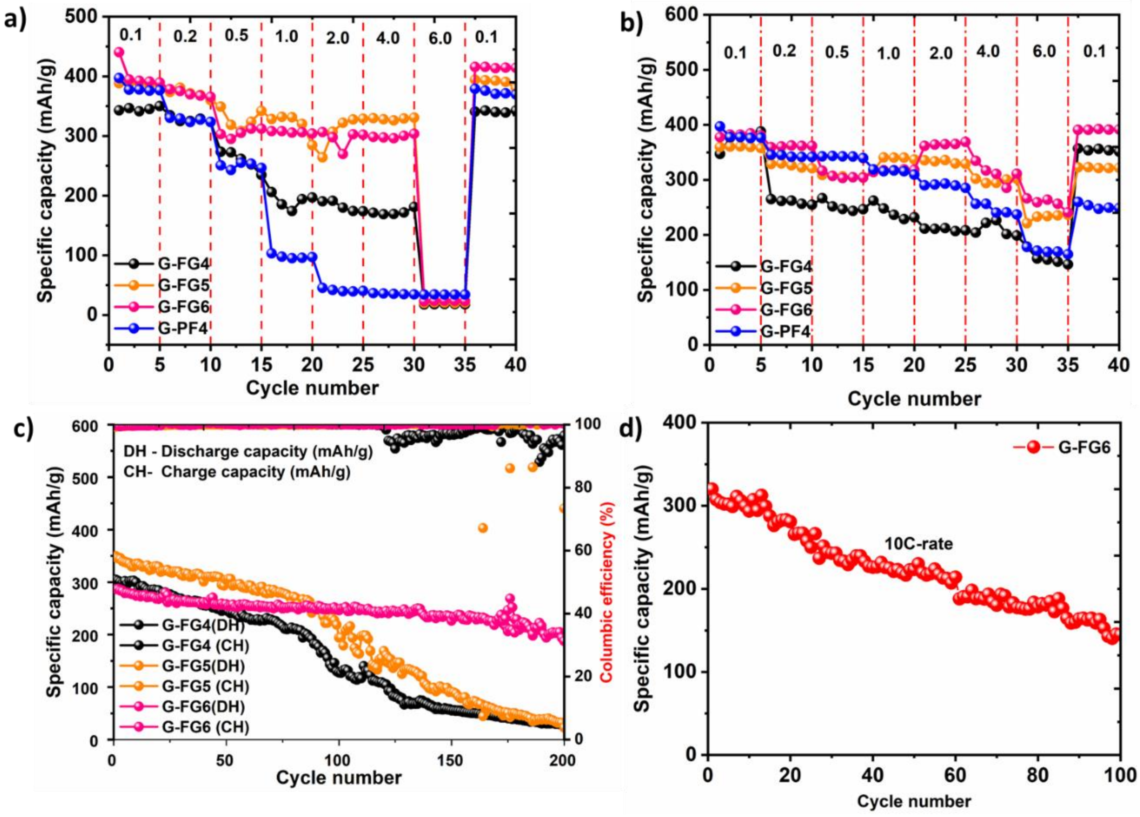

**Figure 5.8.** a) Symmetric rate capabilities (same current) of G-FG4, G-FG5, G-FG6, and G-PF4 electrodes from 0.1C to 6C-rate, b) asymmetric rate capabilities (different current) of G-FG4, G-FG5, G-FG6, and G-PF4 electrodes (0.2C charge/ various discharge currents up to 6C-rate c) Cyclic stability of G-FG4, G-FG5 and G-FG6 electrodes at 0.2C charging and 1C-rate discharging for 200 cycles and d) Cyclic stability of G-FG6 electrode at 0.2C-rate charging and 10C-rate discharging for 100 cycles.

Figure 5.9 shows the Raman spectra of pristine G-FG4, G-FG5 and G-FG6 graphite electrodes. The analysis was carried out with 2.33 eV (532 nm) laser excitation to understand the structural defects and electronic information of graphite electrodes. Moreover, for graphite anode, it reveals a single mode at ~1575-1580 cm$^{-1}$. These bands are assigned as $E_{2g}$ mode. But it is also called as G band which signifies the crystallinity and graphitic nature for the graphite materials. In addition, for most of the graphite materials, a D band at ~1360 cm$^{-1}$ can also be seen. It attributes to defects in the graphitic structure. The intensity ratio $I_D/I_G$ between the D and G bands is extensively used to differentiate the amount of defects in graphite [57]. In this context, the pristine G-FG electrodes also showed the D, G and 2D bands at 1343, 1564 and 2705 cm$^{-1}$ in their respective spectra as shown in Fig. 5.9. However, the difference in intensities was observed for all these bands. The inset Fig. 5.9a corresponds to the G band (1564 cm$^{-1}$) and Fig. 5.9b is for the D band (1360 cm$^{-1}$). The calculated $I_D/I_G$ ratios for G-FG electrodes are as follows, 0.042, 0.083, and 0.01 for G-FG4, G-FG5 and G-FG6 respectively. To compare further, as per the $I_D/I_G$ ratios, G-FG6 electrode showed lesser defects when compared to G-FG5 and G-FG4 electrodes. It implies that G-FG6 electrode must have better crystallinity and higher graphitic nature than both G-FG5 and G-FG4 electrodes. The very low disorder of G-FG6 conveys that the electrode is less defective than G-FG5 and G-FG4 electrodes. In fact, G-FG4 showed a high disorder than the other electrodes. Besides, the Raman data also corroborate with the electrochemical performance of the G-FG electrodes. The relatively high intense G band of the G-FG6 electrode could be linked to the better and stable cyclic performance than the other two electrodes. Further, among the other two electrodes, G-FG5 electrode with moderately high $I_D/I_G$ ratio has shown relatively good electrochemical performance, specific capacity and cyclic stability next to G-FG6 electrode. Finally, the 2D band at 2705 cm$^{-1}$ infers that the materials are of few layers of graphene for G-FG electrodes [58]. In addition, XRD patterns of pristine and cycled (1C-rate) G-FG electrodes are shown in Fig. 5.10. As seen from the figure, diffraction patterns of pristine and cycled G-FG electrodes exhibited the main peak aligned at an angle of 2θ = 26.65°, and also, they are matched with standard JCPDS card number i.e., 41-1487 of graphite anode. Henceforth, it conveys that, using fenugreek binder with graphite anode does not change the crystal structure of graphite even by changing the binder and active material compositions in the case of pre and

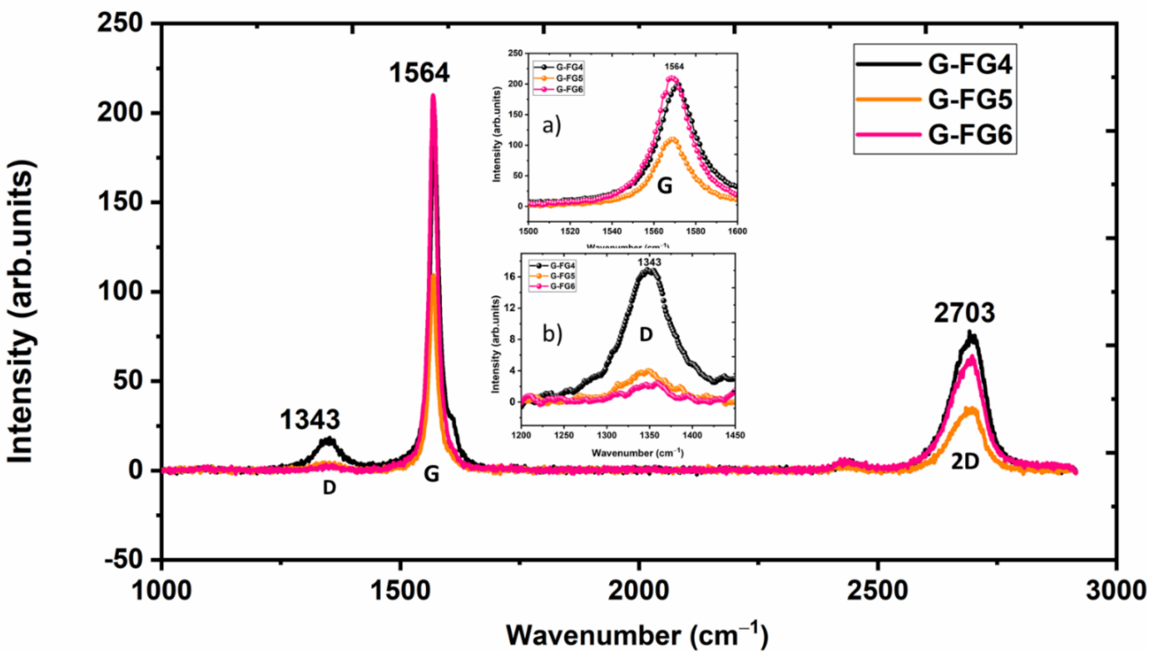

**Figure 5.9.** Raman spectrum of G-FG4, G-FG5 and G-FG6 electrodes; insets: expanded views of a) G-bands b) D-bands of the spectrum.

post cycling conditions. Moreover, the respective lines are indexed to the hexagonal crystal structure with $P6_3/mmc$ space group of the graphite anode.

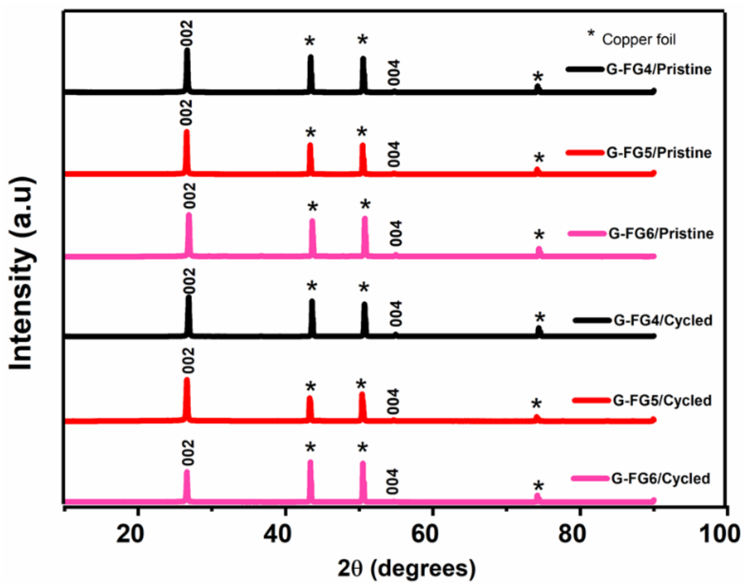

**Figure 5.10.** X-ray diffraction of pristine and cycled (at 1C-rate) G-FG electrodes.

Further to evaluate the electrochemical nature with FG as a binder for graphite anode, morphology studies were carried out using SEM analysis. To do this, G-FGs primitive and 1C-rate cycled electrodes (after 500 cycles) were examined as shown in Fig. 5.11. Pristine G-FG electrodes (Fig. 5.11a-c) displayed no cracks and exhibited similar morphology even with the change in the binder concentration. However, G-FG4 and G-FG5 (Fig. 5.11a and 5.11b) have shown more pores/voids than G-FG6 electrode. The morphology of the cycled electrodes varied with the change in the binder concentration as depicted in Fig. 5.11d-f. Cycled G-FG4 and G-FG6 electrodes exhibited similar morphology as the pristine electrodes displayed in Fig. 5.11d and 5.11f. Whereas, G-FG5 (Fig. 5.11e) after the cycling showed wide/long cracks. The attained electrochemical performance values of G-FG electrodes are also consistent with the morphology of electrodes. The electrodes of G-FG4 and G-FG6 revealed better cyclic stability for more number of cycles, while G-FG5 exhibited higher initial specific capacity and poor cyclic profile after 80 cycles (As shown in Fig. 5.6d). The low electrochemical performance of

G-FG5 after those cycles could be ascribed to the cracks developed during electrochemical cycling as well as the presence of more agglomerated particles that appeared on the cycled electrode as shown in Fig. 5.11e. Besides, both G-FG4 and G-FG6 electrodes (Fig. 5.11d and 5.11f) showed relatively equal porosity without any aggregation of conductive carbon along with graphite particles. Higher performance and durability of the electrodes are predominantly dependent on the peel strength and viscosity of the slurry as evident from the morphology analysis. All cycled electrodes were also examined by EDS analysis to determine the carbon and oxygen percentages as represented in Fig. 5.12. Both these elements are noteworthy for the studies of electrochemical performance and for the electrode binding during the cycling. The percentage difference between carbon and oxygen was clearly seen after the cycling of graphite electrodes. Carbon percentage was observed more for G-FG4 than G-FG5 and G-FG6 electrodes as displayed in Fig. 5.12(a-c). In addition, their EDS spectrum along with percentages was provided in Fig. 5.12 (d-f). The initial better specific capacity of G-FG4 might be ascribed to the presence of more conductive carbon on the electrode. Although it had more conductive carbon, it could not sustain and provide better and prolonged electrochemical performance as compared to G-FG5 and G-FG6 electrodes. The elemental oxygen percentages also varied in all three electrodes as represented in Fig. 5.12 (g-i). G-FG4 electrode (Fig. 5.12g), showed less oxygen content than G-FG5 (Fig. 5.12h) and G-FG6 (Fig. 5.12i) electrodes. Hence, G-FG4 could enable only low electrostatic interaction between the binder and conductive carbon, and therefore lower specific capacities have been observed. While, G-FG5 (Fig. 5.12b) possessed a relatively good carbon content, the carbon percentage is lesser than G-FG4 and G-FG6 electrodes (Fig. 5.12d and 5.12f). Along with, the capacity was suppressed inevitably because of the cracks generated during the cycling. Even though G-FG5 contains more oxygen content than the G-FG4 and G-FG6 electrodes, somehow G-FG5 could not endure the mechanical strength and resulted in the crack formation. In the case of G-FG6 (Fig. 5.12c), the carbon content was lower than G-FG4 and greater than G-FG5, but it yielded higher cyclic stability than all the other electrodes. Here, oxygen content of G-FG6 is relatively quiet higher than G-FG4 and nearly equivalent to that of G-FG5, and thus it strengthens the electrostatic interaction between carbon and oxygen for forming a stable bond with lithium-ion and oxygen. Further, it leads to good integrity between the copper substrate and the active material. Moreover, it facilitated fast lithium kinetics during the cycling of the G-FG6 electrode. Hence, G-FG6 (FG Binder 6%) remarkably displayed the better electrochemical performance in this study.

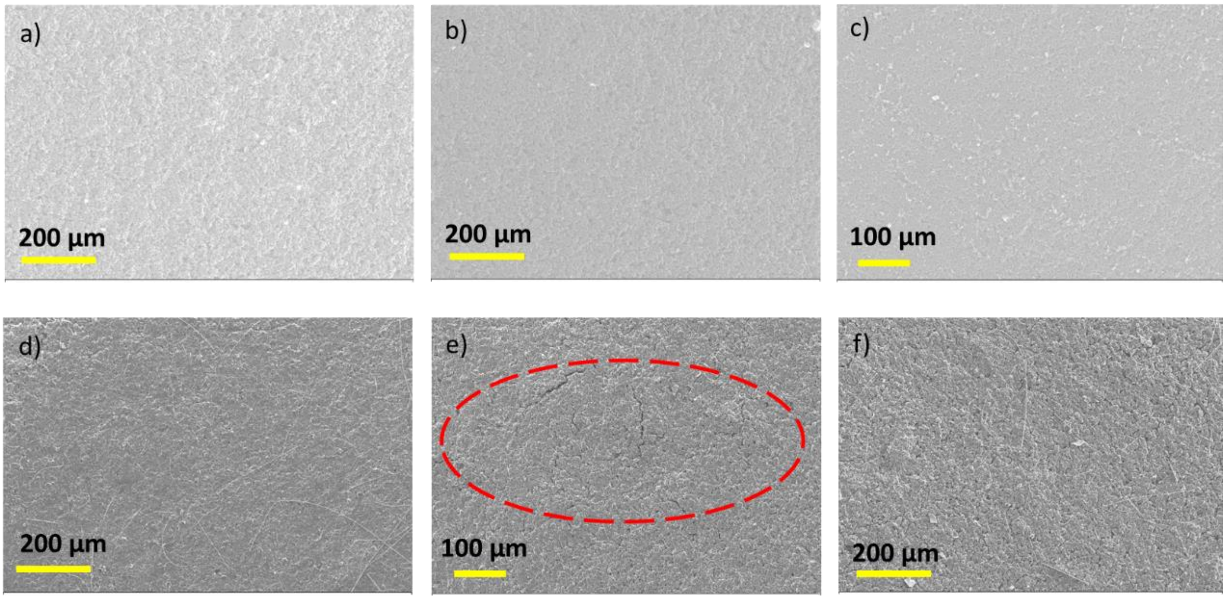

**Figure 5.11.** SEM of pristine and cycled G-FG electrodes; a-c) pristine G-FG4, G-FG5, and G-FG6 electrodes d-f) cycled electrodes of G-FG4, G-FG5 and G-FG6 after 500 cycles at 1C-rate.

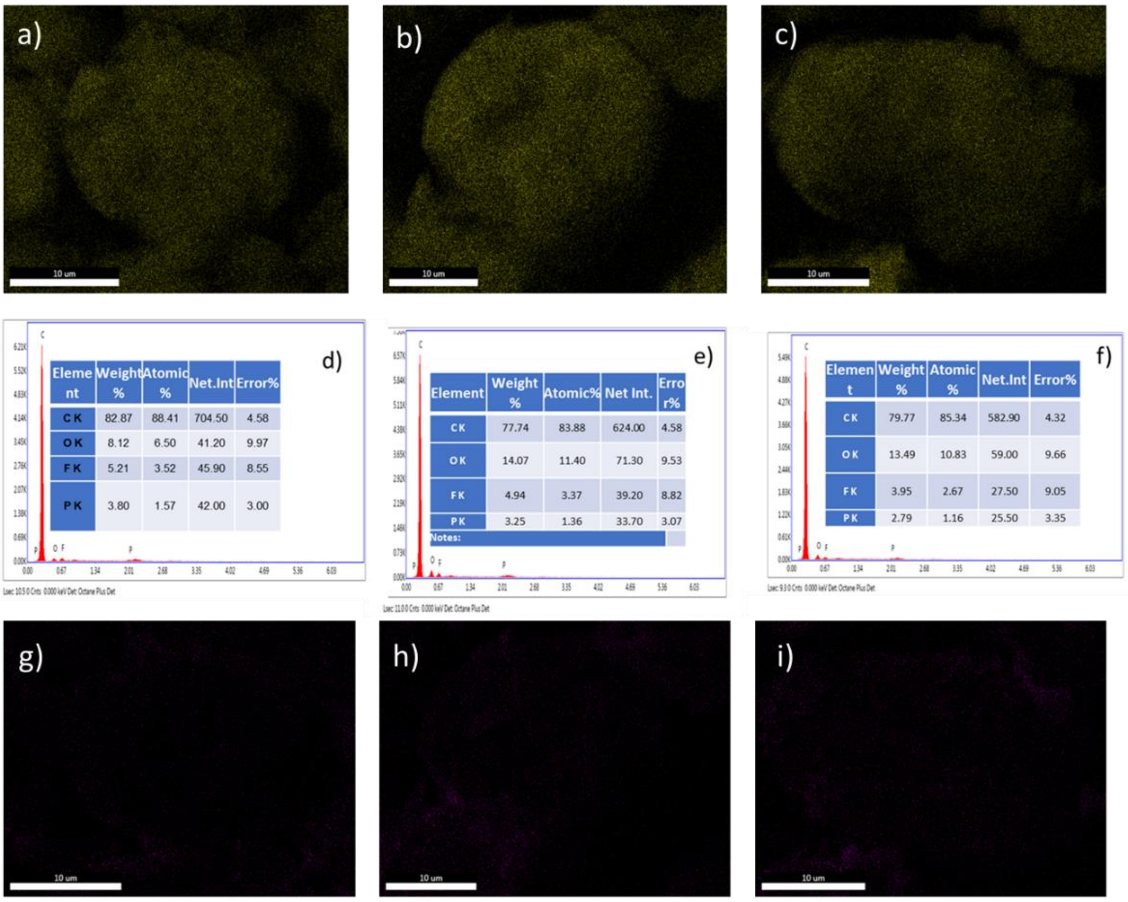

d)

| Element | Weight % | Atomic % | Net.Int | Error% |
|---|---|---|---|---|
| C K | 82.87 | 88.41 | 704.50 | 4.58 |
| O K | 8.12 | 6.50 | 41.20 | 9.97 |
| F K | 5.21 | 3.52 | 45.90 | 8.55 |
| P K | 3.80 | 1.57 | 42.00 | 3.00 |

e)

| Element | Weight % | Atomic% | Net Int. | Error% |
|---|---|---|---|---|
| C K | 77.74 | 83.88 | 624.00 | 4.58 |
| O K | 14.07 | 11.40 | 71.30 | 9.53 |
| F K | 4.94 | 3.37 | 39.20 | 8.82 |
| P K | 3.25 | 1.36 | 33.70 | 3.07 |
| Notes: | | | | |

f)

| Element | Weight % | Atomic % | Net.Int | Error% |
|---|---|---|---|---|
| C K | 79.77 | 85.34 | 582.90 | 4.32 |
| O K | 13.49 | 10.83 | 59.00 | 9.66 |
| F K | 3.95 | 2.67 | 27.50 | 9.05 |
| P K | 2.79 | 1.16 | 25.50 | 3.35 |

**Figure 5.12.** EDS mapping of carbon and oxygen for cycled G-FG4, G-FG5 and G-FG6 electrodes; carbon mapping (a-c), EDS spectra of corresponding above line mentioned G-FG electrodes for carbon and oxygen (d-f); Oxygen mapping of corresponding G-FG electrodes (g-i).

Figure 5.13. displays the Nyquist plots of fresh and cycled G-FG electrodes recorded at 3.0 V Vs. Li/$Li^+$. The electrochemical impedance spectra of fresh and cycled electrodes comprised of depressed semi circles at medium frequency range and an inclined line at low-frequency range. They represent the diffusion kinetics of Li-ion through SEI layer, a charge transfer resistance between particles to electrolyte and mass transport in the solid-state particle of above said frequency ranges [44]. The Nyquist plots are fitted with Randel equivalent circuits using ZsimpWin software (Inset Fig. 5.13a-f) and the fitted values are tabulated in Table 5.3. In this study, two different equivalent circuits were used for fitting the fresh and cycled G-FG based graphite electrodes. The fitted components are solution resistance (Rs), charge transfer resistance ($R_{CT}$), double layer capacitance ($Cdl_{SEI}$), Constant phase element ($CPE_{CT}$), SEI resistance ($R_{SEI}$), film resistance ($R_f$), film capacitance ($C_f$) and Warburg resistance ($W_o$). As seen in Fig. 5.13a-c, it is quite interesting to note that, the fresh G-FG cells with an increase in FG binder concentration for graphite anodes exhibited the decrease in charge transfer resistance ($R_{CT}$) of the electrodes. In addition, double layer capacitance ($Cdl_{SEI}$), SEI resistance ($R_{SEI}$) and film resistance ($R_f$) are also reduced with an increase in binder concentration as displayed in Table 5.3. In the case of cycled electrodes also (Fig. 5.13d-f) the charge transfer resistance ($R_{CT}$) decreased with an increase in binder concentration for graphite anodes i.e., (G-FG6<G-FG5<G-FG4). But, in contrast to the fresh cells, the SEI resistance ($R_{SEI}$) was increased with an increase in binder concentration for the cycled electrodes. Actually, this increased electrical resistance infers the uniform formation of SEI for the better percolation of lithium after the cycling. It is known that SEI is ionically conductive and electronic insulator behaviour. Except for the fresh G-FG6 electrode, the double layer capacitance ($Cdl_{SEI}$) is in the same order for all the electrodes, and their magnitude varied with an increase in FG binder concentration for the graphite anodes. For cycled electrodes, the effective decrease of charge transfer resistance ($R_{CT}$) is mostly due to the improved interfacial properties of SEI after the first cycling [59]. Furthermore, except for the cycled G-FG4 electrode, the film resistance ($R_f$) is quite the same even after the cycling of the electrodes at 1C-rate. Hence, the ameliorated electrochemical performance of G-FG6 electrode after 500 cycles at 1C-rate may be due to the decreased $R_{CT}$ and $R_f$ resistances of graphite anode. Further,

ionic conductivity measurements also corroborate the impedance analysis. It elucidates that, the study of graphite anode with aqueous based FG binder is beneficial for LIB applications.

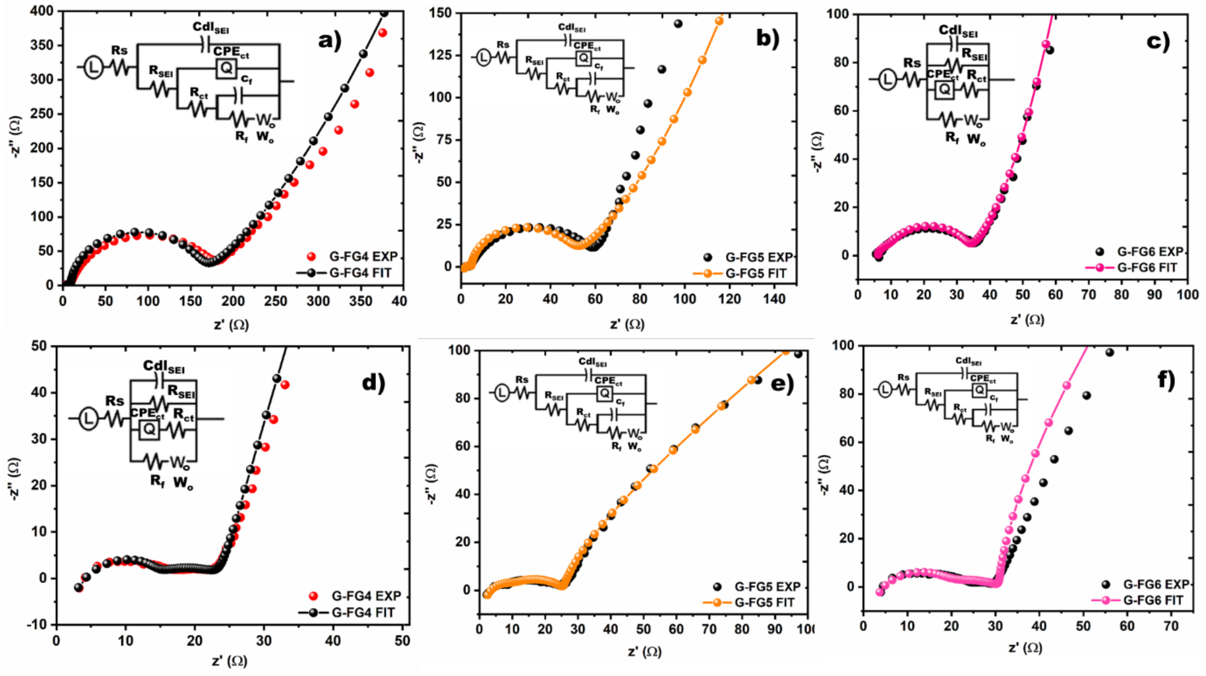

**Figure 5.13.** Nyquist plots of G-FG electrodes a-c) fresh and d-f) cycled (after 500 cycles).

**Table 5.3.** EIS analysis data of G-FG4, G-FG5 and G-FG6 electrodes fitted with equivalent circuit for fresh and after cycling 500 cycles at 1C-rate.

| **S.No** | **Electrode** | **Fresh cycles** | | | | | | | |
|---|---|---|---|---|---|---|---|---|---|
| | | $R_S$ (Ω) | $Cdl_{SEI}$ (F) | $R_{SEI}$ (Ω) | $R_{CT}$ (Ω) | $CPE_{CT}$ (S.sec^n) | $R_f$ (Ω) | $W_o$ (S.sec^0.5) | Error (%) |
| 1 | G-FG4 | 0.01 | 3.6 X $10^{-8}$ | 7.90 | 184.18 | 0.0003 | 1.260 | 0.0010 | <9.86 |
| 2 | G-FG5 | 0.01 | 4.8 X $10^{-8}$ | 4.20 | 61.87 | 0.0500 | 0.010 | 0.0010 | <5.71 |
| 3 | G-FG6 | 6.30 | 4.2 X $10^{-6}$ | 1.03 | 35.91 | 0.0035 | 0.010 | 0.0004 | <9.35 |
| **After 500 cycles** | | | | | | | | | |
| 4 | G-FG4 | 0.26 | 2.2 X $10^{-8}$ | 1.81 | 24.00 | 0.0054 | 31.23 | 0.0002 | <3.16 |
| 5 | G-FG5 | 1.00 | 2.7 X $10^{-8}$ | 8.77 | 17.40 | 0.0001 | 0.011 | 0.0060 | <5.16 |
| 6 | G-FG6 | 0.64 | 1.9 X $10^{-8}$ | 16.64 | 14.22 | 0.0007 | 0.018 | 0.0023 | <5.06 |

## 5.4. Conclusions

In this investigation, we reported a graphite electrode using a natural polysaccharide fenugreek binder as an alternative to standard polyvinylidene binder for the application in lithium-ion batteries. Graphite electrodes with different FG binder contents (4 to 6%) as well as 4% PVDF binder were prepared and illustrated methodically. The coated graphite electrodes retained the original morphology of the active material, conforming that binder did not react to active material. Notably, the graphite electrodes with FG binder displayed much better cycling performance and rate capability than the PVDF based graphite electrode. For example, one of the FG based graphite electrode at 1C demonstrated an initial capacity of 203 mAh $g^{-1}$ with good cyclic stability up to 500 cycles, whereas the PVDF based electrode delivered an initial capacity of 103 mAh $g^{-1}$ under similar conditions. In addition, the same aqueous based electrode has also delivered the very high specific capacity of >300 mAh $g^{-1}$ at 10C-rate. The enhanced performance of FG based electrodes can be ascribed due to the following factors. 1) Better inter hydrogen bonding of binder at higher concentration 2) Optimized swelling order 3) High conductivity of the electrode. 4) Branched chemical structure with more hydroxyl binding sites. Besides, Raman data also proved the importance of graphitization for better electrochemical performance. Moreover, aqueous based binders will have better flexibility to enhance the binding strength. Production of aqueous based electrodes can be scaled up with lower cost than the high-cost and toxic PVDF binder-based LIB electrodes. Thus, FG binder can’t be limited only for the fabrication of graphite anode, but also it can be used to other chemistries available in lithium-ion batteries for the electronic mobility applications.

## 5.5. References

[1] D. Bresser, D. Buchholz, A. Moretti, A. Varzi, S. Passerini, *Energy Environ. Sci*. **2018**, 11, 3096-3127.

[2] J. T. Li, Z. -Y. Wu, Y. -Q. Lu, Y. Zhou, Q. -S. Huang, L. Huang, S. -G. Sun, *Adv. Energy Mater*. **2017**, 1701185.

[3] M. Ling, J. Qiu, S. Li, C. Yan, M. J. Kiefel, G. Liu, S. Zhang, *Nano Lett*. **2015**, 15, 7, 4440-4447.

[4] P. S. Salini, S. V. Gopinadh, A. Kalpakasseri, B. Jhon, T. Mercy, *ACS Sustainable Chem. Eng*. **2020**, 8, 4003-4025.

[5] D. V. Carvalho, N. Loeffler, M. Hekmatfar, A. Moretti, G. T. Kim, S. Passerini, *Electrochim. Acta* **2018**, 265, 89-97.

[6] K. Prasanna, T. Subburaj, Y. N. Jo, W. J. Lee, C. W. Lee, *Acs Appl. Mater. Interfaces* **2015**, 7, 7884-7890.

[7] K. C. Kil, U. Paik, *Macromol. Res.* **2015**, 23, 719-725.

[8] H. Buqa, M. Holzapfel, F. Krumeich, C. Veit, P. Novak, *J. Power Sources* **2006**, 161, 617-622.

[9] S. S. Zhang, K. Xu, T. R. Jow, *J. Power Sources* **2004**, 138, 226-331.

[10] D. Shao, H. Zhong, L. Zhang, *ChemElectroChem.* **2014**, 0000, 00, 1-10.

[11] S. R. Sahu, V. R. Rikka, P. Haridoss, R. Gopalan, R. Prakash, *Energy Technol.* **2019**, 1900849.

[12] M. Herstedt, L. Fransson, K. Edstrom, *J. Power Sources* **2003**, 124, 191-196.

[13] H. Buqa, D. Goers, M. Hozapfel, M. E. Spahr, P. Novak, *J. Electrochem. Soc.* **2005**, 152 (2) A474-A481.

[14] D. W. Kim, W. Y. Jo, C. W. Park, S. M. Hwang, J. B. Yoo, Y.-J. Kim, *Electrochim. Acta* **2020**, 341, 1359362.

[15] M. Singh, J. Kaiser, H. Hahn, *J. Electrochem. Soc.* **2015**, 162 (7) A1196-A1201.

[16] L. Kremer, A. Hoffmann, T. Danner, S. Hein, B. Prifling, D. Westhoff, C. Dreer, A. Latz, V. Schmidt, M. W. Mehrens, *Energy Technol.* **2019**, 1900167.

[17] J. -H. Lee, U. Paik, V. A. Hackley, Y. -M. Choi, *J. Power Sources* **2006**, 161, 612-616.

[18] J. Drofenik, M. Gaberscek, R. Dominko, F. W. Poulsen, M. Mogensen, S. Pejovnik, J. Jamnik, *Electrochim. Acta* **2003**, 48, 883-889.

[19] Q. Li, H. Yang, L. Xie, J. Yang, Y. Nuli, J. Wang, *Chem. Commun.* **2016**, 52, 13479-13482.

[20] Y. Bie, J. Yang, Y. Nuli, J. Wang, *J. Mater. Chem. A* **2017**, 5, 1919.

[21] F. C. De Godoi, D. -W. Wang, Q. Zeng, K. -H. Wu, I. R. Gentle, *J. Power Sources* **2015**, 288, 13.

[22] L. Chai, Q. Qunting, L. Zhang, M. Shen, L. Zhang, H. Zhang, *Electrochim. Acta* **2013**, 105, 378-38.

[23] Y. K. Jeong, T. -W. Kwon, I. Lee, T. -S. Kim, A. Coskun, J. W. Choi, *Energy Environ. Sci.* **2015**, 8, 1224-1230.

[24] J. Sun, Y. Huang, W. Wang, Z. Yu, A. Wang, K. Yuan, *Electrochem.Commu.* **2008**, 10, 930-933.

[25] V. V. N. Phanikumar, B. V. Appa Rao, K. V. Gobi, R. Gopalan, R. Prakash, *ChemistrySelect* **2020**, 5, 1-11.

[26] S. Klamor, M. Schroder, G. Brunklaus, P. Niehoff, F. Berkemeier, F. M. Schappacher, M. Winter, *Phys. Chem. Chem. Phys.* **2015**, 17, 5632-5641.

[27] D. L. Wood, J. D. Quass, J. Li, S. Ahmed, D. Ventola, C. Daniel, *Drying Technol.* **2017**, 1-11.

[28] J. Li, C. Daniel, J. An, D. Wood, *MRS Adv.* **2016**, 1, 1029-1035.

[29] Y. Ma, J. Ma, G. Cui, *Energy storage materials* **2019**, 20, 146-175.

[30] J. He, H. Zhong, J. Wang, L. Zhang, *J. Alloys Comp.* **2017**, 714, 409-418.

[31] J. Liu, Q. Zhang, T. Zhang, J.-T. Li, L. Huang, S. G. Sun, *Adv. Funct. Mater.* **2015**, 25, 3599.

[32] B. Lestriz, *C. R. Chimie* **2010**, 13, 1341-1350.

[33] S. H. Lee, J. H. Lee, D. H. Nam, M. Cho, J. Kim, C. Chanthad, Y. Lee, *ACS Appl. Mater. Interfaces* **2018**, 10, 16449-16457.

[34] V. D. Prajapati, G. K. Jani, N. G. Moradiya, N. P. Randeria, B. J. Nagar, N. N. Naikwadi, B. C. Variya, *International Journal of Biological Macromolecules* **2013**, 60, 83-92.

[35] I. Kanungo, N. N. Fathima, R. R. Jonnalagadda, B. U. Nair, *Phys. Chem. Chem. Phys.* **2015**, 17, 2778-2793.

[36] L. M. Wei, C. C. Chen, Z. Y. Hou, H. Wei, *Sci. Rep.* **2016**, 6, 19583.

[37] C. Chen, S. H. Lee, M. Cho, J. Kim, Y. Lee, *ACS. Appl.Mat.Interfaces* **2016**, 8, 2658.

[38] J. Liu, Q. Zhang, Z. Y. Wu, J. H. Wu, J. T. Li, L. Huang, S. G. Sun, *Chem.commun.* **2014**, 50, 6386.

[39] M. K. Dufficy, S. A. Khan, S. Fedkiw, *J. Mater. Chem. A* **2015**, 3, 331-340.

[40] A. K. Sav, R. A. Fule, M. T. Ali, P. Amin, *J. Pharm. Investig.* **2013**, 43:417-429.

[41] L. Qiu, Y. Shen, H. Fan, X. Yang, C. Wang, *International Journal of Biological Macromolecules* **2018**, 115, 672-679.

[42] C. Liu, F. Lei, P. Li, J. Jiang, K. Wang, *Carbohydr. Polym.* **2020**, 236, 116100.

[43] B. Pallavi, K. Gurpreet, *Eur. J. Pharm. Biopharm.* **2015**, 96, 173–184.

[44] V. V. N. Phanikumar, V. R. Rikka, B. Das, R. Gopalan, B. V. Appa Rao, R. Prakash, *Ionics* **2019**, 25, 2549–2561.

[45] F. M. Courtel, S. Niketic, D. Duguay, Y. A. Lebdeh, I. J. Davidson, *J. Power Sources* **2011**, 196, 2128-2134.

[46] J. Liu, Q. Zhang, T. Zhang, J. T. Li, L. Huang, S. G. Sun, *Adv. Funct. Mater.* **2015**, 25, 3599-3605.

[47] S. Komaba, T. Ozeki, K. Okushi, *J. Power Sources* **2009**, 189, 197-203.

[48] P. Ganesh, P. R. C. Kent, D. Jiang, *J. Phys. Chem. C* **2012**, 116, 24476-24481.

[49] S. S. Zhang, T. R. Jow, *J. Power Sources* **2002**, 109, 422-426.

[50] Z. Wang, G. Dang, Q. Zhang, J. Xie, *Int. J. Electrochem. Sci*. **2017**, 12, 7457-7468.

[51] S. S. Jeong, N. Bockenfeld, A. Balducci, M. Winter, S. Passerini, *J. Power Sources* **2012**, 199, 331-335.

[52] E. Pohjalainen, O. Sorsa, J. Juurikivi, T. Kallio, *Energy Technology* **2016**, 4, 470-472.

[53] K.-F. Chiu, H.-J. Leu, S.-H. Su, R.-Z. Wu, *ECS Transactions* **2016**, 73, 289-304.

[54] S. Huang, J. Ren, R. Liu, M. Yue, Y. Huang, G. Yuan, *New J. Chem.* **2017**, 41, 11759.

[55] N. Cuesta, A. Ramos, I. Camean, C. Antuna, A. B. Garcia, *Electrochim. Acta* 155, **2015**, 140-147.

[56] C. Toigo, M. Singh, B. Gmeiner, M. Biso, K.-H. Pettinger, *J. Electrochem. Soc*. **2020**, 167, 020514.

[57] D. Li, D. L. Danilov, L. Gao, Y. Yang, P. H. L. Notten, *Electrochim. Acta* **2016**, 210, 445-455.

[58] L. Liu, N. Solin, O. lnganas, *Rsc Adv.* **2019**, 9, 39758-39767.

[59] S. S. Zhang, K. Xu, T. R. Jow, *J. Power Sources* **2004**, 18, 226-231.

# Chapter 6

# Large scale fabrication of graphite anode using carboxymethyl cellulose and styrene butadiene rubber as aqueous binders in lithium-ion batteries

# 6. Large scale fabrication of graphite anode using carboxymethyl cellulose and styrene butadiene rubber as aqueous binders in lithium-ion batteries

## 6.1. Introduction

The significant revolution is seen in electric vehicles because of lithium-ion batteries (LIBs). These batteries are comparatively better in terms of volumetric (Wh/L) and gravimetric (Wh/kg) energy densities as compared to the lead and nickel metal hydride batteries being used in various applications. The major applications of LIBs are energy storage systems (ESS), uninterrupted power supply (UPS), electric vehicle (EV), power tools, electronic gadgets and various other applications. Currently, with one charge, batteries in EVs are able to sustain the energy storage for a travel of 300 miles. At present, the extensively used cathodes are $LiCoO_2$, $LiMn_2O_4$, $LiFePO_4$ and $LiNi_{0.8}Co_{0.15}Al_{0.05}O_2$, whereas anodes are graphite and LTO for LIBs. Although the technology is matured in various levels, still the improvement is profoundly considered for better cyclic and rate capabilities in current LIB materials [1]. In this context, most of the researchers are finding the alternatives to cope the current electrochemical performance by adopting novel modifications for materials as well as in the electrode fabrication process for LIBs. In electrode fabrication procedure, the replacement of non-aqueous polyvinylidene difluoride (PVDF) binder with aqueous binders is successfully established with ameliorated standards in LIB process. The advantages of aqueous binders are well known, since these binders are lower in cost, eco-friendly and little conductive in nature. However, in terms of aqueous fabrication of cathodes, aqueous binders do face challenges like integrity in electrode coating, crack generation with increase of electrode thickness, leaching of lithium ions, corrosion of aluminium foils and cavity formation because of hydrogen generation during the drying process [2]. These above said issues already have been resolved to a better extent by adding organic/inorganic acids, metal oxide coatings on aluminium current collector, coating of carbon paste on current collector to circumvent the corrosion and also by adding some additives during the slurry preparation. In the case of anodes, the aforementioned issues are almost minimal and playing the pivotal role in the electrode fabrication process. Some of the aqueous binders which are being used for various anode materials are Na-CMC, SBR, PAA, Gelatine, Guar gum, Karaya gum, Xanthan gum, Chitosan and Tamarind kernel powder [3-4]. Moreover, aqueous binders effectively mitigated the high-volume expansion of anode materials like silicon, tin, silicon/carbon and $SnO_2$/C at low and high C-rates. These anode materials are also in higher capacity as compared to the graphite anode [5]. Few studies for silicon anode also revealed the copolymerization of PAA polymer with different monomers led to better mechanical, chemical and electrochemical performance. In addition, some cross-linked polyacrylates and branched polymers were used to increase the contact points between polymer and high-volume expansion active materials. The silicon anode fabricated with branched β-cyclodextrin binder had given more adhesion strength than the alginate binder and granted higher capacity retention due to the self-healing properties of the binder. Even more, some natural polymers like guar and gellan gums offer the lone pair of the oxygen atoms for the movement of lithium-ions in the polymer chain. In recent times, poly (3,4-ethylenedioxythiophene): poly (styrene sulfonate) (PEDOT:PSS) is often used as conductive polymer binder as well as water soluble binder for volume expansion materials. The advantageous PEDOT:PSS binder could reduce the conductive carbon black usage and would withstand the volume expansion during the charge/discharge cycles of the electrode materials. Thus, like aforementioned binder, multiple aqueous binders have been studied for silicon anode and for other prominent volume expansion materials in order to enhance the cyclic and rate capabilities for EV industry [6]. Such an equivalent performance is not seen with non-aqueous PVDF binder for any LIB materials. Moreover, in commercial view point, graphite is highly considered anode material for both non-aqueous and aqueous based electrodes in LIBs. The theoretical capacity of the graphite is 372 mAh $g^{-1}$, and it is quite low as compared to the other high-capacity anode materials. Yet it is relatively better in terms of low average voltage i.e., 0.150 V vs $Li/Li^+$, which is essentially benefit to increase the cell voltage. Graphite also exhibits minimum voltage hysteresis, which further provides the higher energy efficiency for LIBs. All these properties can boost to oeuvre on graphite anode for commercial and research pursuits [7]. As compared to the other anode materials, graphite electrode fabrication with aqueous binder is more prominent in terms of reduction in drying temperature, eco-friendliness, low irreversible capacity loss during cycling, formation of thin and stable SEI layer, decrease in binder usage and its cost [8]. Many aqueous binders have been employed for graphite anode as mentioned in literature reports, but among them the CMC/SBR is the most studied aqueous binder for LIBs. The remarkable benefits of SBR binder are heat resistance, flexibility, good cohesion and adhesion between the graphite particles and the current collector [9]. Whereas, CMC is a thickening agent and it is a linear polymeric derivative of cellulose which consists of β-linked glucopyranose moieties with different levels of carboxymethyl substitution. The carboxymethyl moiety renders CMC soluble in aqueous medium relative to the insoluble pure cellulose [10]. Further, CMC plays a wide role in graphite slurry dispersion, which promotes the electrical conductivity of the electrodes. The degree of substitution (DS) functions lead role on CMC, since the charge density of polymeric chains in water depends on it [11]. But, the use of SBR binder must be optimum, and it has been reported that the usage of higher amount of SBR elastomer does lead to decrease in electronic conductivity [12]. C. C. Li et al. have pointed the amount of distribution of these binders on electrode also affects the cell performance [13]. Considering the copious properties of this binder, in this work we investigated the effect of CMC/SBR binder on graphite anode and optimized the amount of carbon black for better cyclic stability and rate capability by implementing half and full cells approach. The obtained results are also in good agreement with literature reports [14-15].

## 6.2. Experimental

### 6.2.1. Materials

Potato shaped graphite (10-20 µm) (Superior graphite, USA), Super C65 carbon black (Timcal, Switzerland), Polyvinylidene difluoride (PVDF), sodium carboxymethyl cellulose (Na-CMC), styrene butadiene rubber (SBR) binders from MTI Corporation and TRD102A from JSR corporation were used as received. 1M $LiPF_6$ in a mixture of ethylene carbonate (EC): dimethyl carbonate (DMC): ethyl methyl carbonate (EMC) (1:1:1 v/v, enchem, Korea) was used as the electrolyte. Ultrapure water of 18.2 MΩ $cm^{-1}$ was used for the preparation of binder solution and slurries.

### 6.2.2. Electrode preparation and electrochemical measurements

To study the lab and large-scale electrodes, two different anode slurries for lab scale were prepared using ball mill method by varying graphite and carbon black ratios for a duration of 3 h. Subsequently corresponding electrodes were fabricated by using comma bar coating technique. The first slurry consists of graphite (90 wt.%), carbon black (4 wt.%), carboxymethyl cellulose (3 wt.%) and styrene butadiene rubber (3 wt.%) from MTI Corporation). The second slurry contains of graphite (88 wt.%), carbon black (6 wt.%), carboxymethyl cellulose (3 wt.%) and styrene butadiene rubber (3 wt.%) from MTI Corporation). The fabricated electrodes are named as AGT-90 and AGT-88, respectively. Further, AGT-90 was also fabricated by large-scale method using the pilot plant slurry mixture and comma bar coater for a length of 40 meters. The composition used for pilot plant slurry was 90:4:6 i.e., graphite (90 wt.%), carbon black (4 wt.%), carboxymethyl cellulose (3 wt.%) and styrene butadiene rubber (3 wt.% TRD102A from JSR Corporation). To compare the performance of graphite electrodes prepared by aqueous method (AGT- 88 and 90), the conventional non-aqueous graphite electrode was fabricated with doctor blade by using the slurry of graphite (90 wt.%), carbon black (4 wt.%) and PVDF (6 wt.%) binder. The fabricated electrode is named as PGT-90. The $LiNi_{0.5}Mn_{0.3}Co_{0.2}O_2$ and $LiFePO_4$/C non-aqueous cathodes were prepared and fabricated by using the appropriate quantities of NMC532 (86 wt.%), carbon black (8 wt.%) and PVDF binder (6 wt.%), whereas $LiFePO_4$/C (83 wt.%), carbon black (13 wt.%) and PVDF binder (4 wt.%) in large scale for the full cell analysis. The electrochemical performance was tested with BT-2000 Arbintester (USA) in the voltage range of 0.005 to 2.5 V vs. $Li/Li^+$ (for small scale electrodes) and 0.005 to 3.0 V vs. $Li/Li^+$ metal (for large scale electrodes) using CR2032 coin cell for the half-cell analysis. The rate capability experiments were carried out by applying the asymmetric current i.e., same charge current (0.2C-rate) and different discharge currents up to the 50C-rate for graphite half cells. Full cells were tested in the voltage range of 3.0 to 4.2 V using polypropylene (PP) prismatic cells for NMC532/Graphite cell and pouch cells were fabricated for LFP/Graphite cell and tested in the voltage range of 2.7 to 3.65 V. Electrochemical impedance spectroscopy (EIS) analysis was performed with an amplitude of 10 mV in the frequency range of 1 MHz to 0.01Hz using a Parstat MC Electrochemical Workstation (Princeton Applied Research, USA). All electrochemical tests were done at room temperature of 25 $^{o}$C. The Whatman glass microfiber filter paper (GF/D) and polypropylene were used as a separator and 1M $LiPF_6$ in EC: DMC: EMC (1:1:1 v/v) was used as an electrolyte.

### 6.2.3. Characterization of materials, slurries and coated electrodes

The spectrum of pure CMC powder was recorded at a resoluiton of 2 $cm^{-1}$ by Fourier Transform Infrared spectroscopy (FTIR) with Attenuated Total Reflectance (ATR) method using the Perkin Elmer Spectrometer (USA). Rheological studies were carried out for aqueous and non-aqueous based graphite slurries using Anton Parr MCR102 (USA). The peel strength tests of the fabricated graphite electrodes were performed at an angle of 180$^{\circ}$ with a speed of 25 mm/min using Mecmesin peel tester (UK). Surface morphologies of graphite electrodes were analyzed by a Field Emission Scanning Electron Microscope (FE-SEM, Carl Zeiss, Germany) with an accelerating voltage of 15 kV. Swelling studies were executed to check the increase in weight percentage of aqueous and non-aqueous based graphite electrodes after soaking them in the electrolyte for 15 days.

## 6.3. Results and Discussion

The FTIR of CMC binder is depicted in Fig. 6.1. The vibration bands in the region of 1000-1200 cm$^{-1}$ are the characteristics of glycoside cycle and the C-O-C ether chain as seen in Fig. 6.1. The C=O stretching vibrations of Na-CMC groups are indexed at 1583 cm$^{-1}$. The wide band at 3200-3300 cm$^{-1}$ is attributed to the vibrations of the –OH groups from the water molecules and all the peaks are in concurrence with literature reports [16].

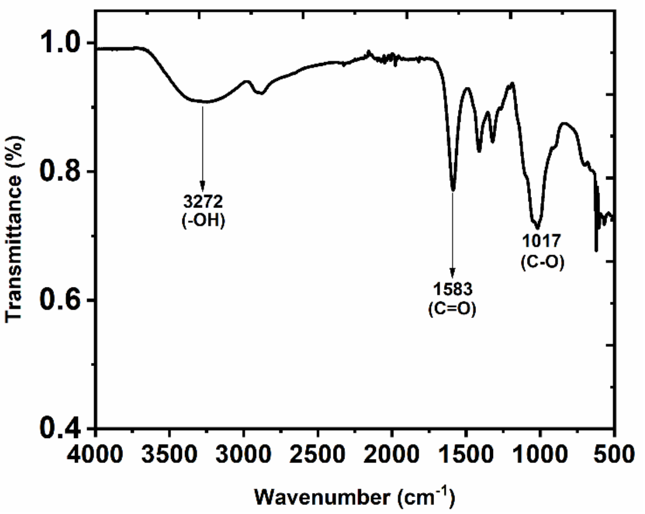

**Figure 6.1.** FTIR spectrum of pure CMC binder powder

Rheology measurements were performed for plant scale aqueous (AGT-90) and non-aqueous based slurries (PGT-90) and the results are given in Fig. 6.2. Both the slurries showed the shear thinning behaviour with increase in shear rate as shown in Fig. 6.2a. It is noticed that aqueous based slurry had shown the higher viscosity (24,400 cP) than the non-aqueous slurry (18,400 cP) at 1 (1/s) shear rate. In addition, the amplitude sweep studies of AGT-90 and PGT-90 slurries also indicated the gel behaviour (i.e., G'>G") for either the cases with low strength rate for aqueous and higher strength rate for non-aqueous slurry as represented in Fig. 6.2b. The peel strength of the lab scale electrodes is measured by 180° peel test and the values are found to be 2.5, 1.8 and 2.1 N cm$^{-1}$ for AGT-88, AGT-90 and PGT-90, respectively. The peel strength of AGT-88 was higher than the other two electrodes, and it could be attributed to the more amount of carbon black present in the electrode. The swelling analysis was carried out for the aforementioned electrodes by soaking in the electrolyte for fifteen days as represented in Fig. 6.3. The attained swelling values are 46.02, 47.12 and 40.91% for AGT-88, AGT-90 and PGT-90, respectively. The non-aqueous electrode i.e., PGT-90 has given lower value as compared to the other aqueous based electrodes. The low swelling value for PGT-90 is unexpected as compared to the results being reported in literature [17].

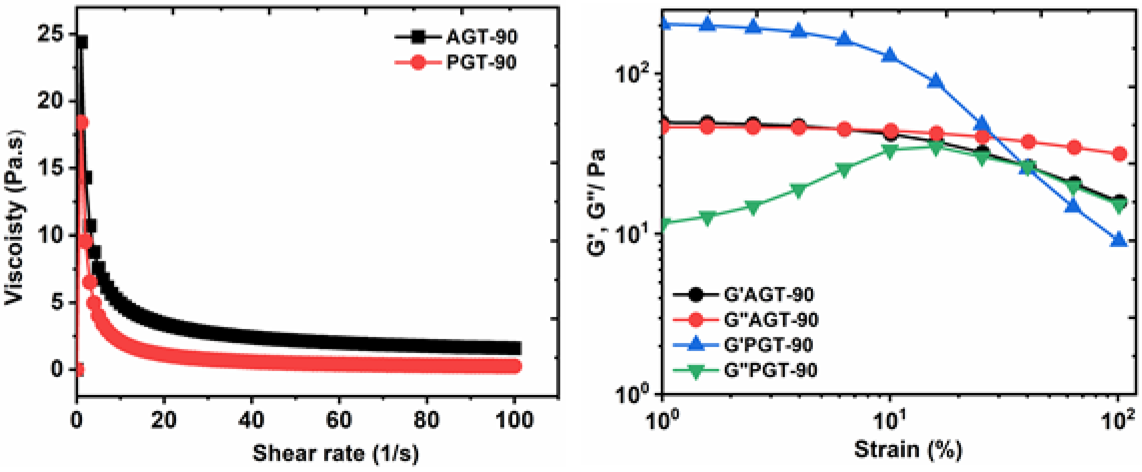

**Figure 6.2.** a) Flow curve profiles and b) amplitude sweep profiles for AGT-90 and PGT-90 slurries.

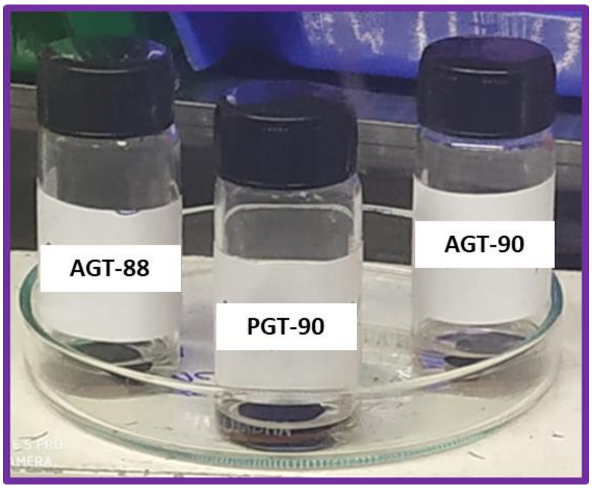

**Figure 6.3.** Swelling analysis of AGT-88, AGT-90 and PGT-90 electrodes soaked in 1M $LiPF_6$ electrolyte.

Cyclic voltammetry analysis was carried out for lab scale AGT-90 electrode at 0.05 mV $s^{-1}$ in the voltage range of 0.005 to 3.0 V vs $Li/Li^+$ for six consecutive cycles as shown in Fig. 6.4. First cycle of the CV displays the reduction peak in the voltage range of 0.6 to 0.8 V, which is attributed as the formation of solid electrolyte interface (SEI) layer on the graphite anode as indicated in Fig. 6.4. The continuation cycles have shown the reversibility in peaks with an increase in the peak current from one cycle to the other cycle. In addition, all the intercalation stages of graphite anode at 0.16, 0.12 and 0.04 V are clearly seen in the corresponding CV [18]. The de-intercalation potential for all these cycles is observed at 0.23 V. Thus, the obtained voltammogram is as equivalent to the reported results with other aqueous binders of graphite anode [19].

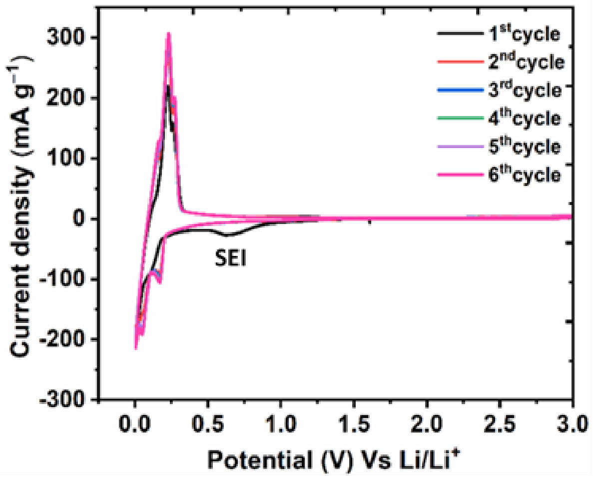

**Figure 6.4.** Cyclic voltammetry of AGT-90 vs. Li/Li$^+$ at 0.05 mV s$^{-1}$ for six cycles.

Galvanostatic charge/discharge analysis and cyclic stability were studied for lab scale ball milled aqueous electrodes and non-aqueous electrode at 0.1C-rate in the voltage range of 0.005 to 2.5 V vs. Li/Li$^+$ for a number of 65, 100 and 40 cycles for AGT-88, AGT-90 and PGT-90, respectively, as shown in Fig. 6.5. The initial discharge capacities (de-intercalation) of aforementioned electrodes are found to be 400, 370 and 373 mAh g$^{-1}$ (Fig. 6.5a-c) with coulombic efficiencies of 71, 94 and 84% respectively. But, the AGT electrodes at 40th cycle showed the discharge capacities of 357 and 384 mAh g$^{-1}$ respectively. The final discharge capacities (de-intercalation) of electrodes for corresponding cycle number were noted to be 373, 366, and 373 mAh g$^{-1}$ for AGT-88, AGT-90 and PGT-90, as shown in Fig. 6.5a-c. The highest discharge capacity of AGT-88 at the initial and final discharge cycles could be due to the presence of more carbon black percentage among the two aqueous based electrodes. The cyclic stability (charge/discharge) profile of above-mentioned electrodes for respective cycles i.e., 65, 100, and 40 at AGT-88, AGT-90 and PGT-90 is represented in Fig. 6.5d. All electrodes have shown a steady profile for complete cycles at 0.1C-rate. The aqueous AGT-88 electrode displayed high and stable discharge capacities for total cycles than AGT-90 and PGT-90 electrodes. The capacity retentions of these electrodes at final cycle were noticed to be 93, 96, and 99%, respectively. The electrodes of AGT-90 and PGT-90 also have demonstrated the stable performances, but PGT-90 has been noticed with higher capacities than AGT-90, as seen in Fig. 6.5d. The low swelling value also might have promoted higher performance for PGT-90 electrode. In the case of AGT-88 electrode, better cyclic stability could be due to the well dispersion of CMC/SBR binder with graphite anode and higher carbon black additive as discussed in charge/discharge cycle. However, for all the cases, each individual electrode showed the coulombic efficiencies of >90%.

The cycle number vs. discharge capacity profile at 1C-rate for 100 cycles of AGT-88 and AGT-90 and asymmetric charge/discharge currents from 0.2C to 50C-rate of AGT-90 and PGT-90 electrodes are shown in Fig. 6.5e and 6.5f. Both 1C-rate and rate capability studies were executed for lab scale electrode in the voltage range of 0.005 to 3.0 V vs $Li/Li^+$ in order to compare the existing literature reports. As seen from Fig. 6.5e, AGT-88 and AGT-90 aqueous based electrodes exhibited a stable electrochemical performance at 1C-rate for the complete 100 cycles. The initial discharge capacities of AGT-88 and AGT-90 were 334 and 364 mAh $g^{-1}$, respectively. Although the cyclic stability is stable with cycle number, the difference of discharge capacity between AGT-88 to AGT-90 for each cycle is noted to be ~ 20 mAh $g^{-1}$ for the entire cycles. The obtained capacity retention for AGT-88 and AGT-90 electrodes at 100th cycle is 94 and 96%, respectively. Importantly, the AGT-88 electrode displayed higher performance at 0.1C-rate, but the same is not witnessed at 1C-rate even after the voltage window was varied for the cells. The reason for better discharge capacity at 1C-rate might due to the homogenous distribution of binder and optimum amount of carbon black in order to provide better cyclic stability as reported in literature [20]. For asymmetric charge/discharge C-rates, initially both AGT-90 and PGT-90 electrodes were initially cycled with same charge/discharge current at 0.1C for five cycles, but subsequently the charge current of 0.2C-rate was made constant and the discharge currents were varied up to 50C-rate, as shown in Fig. 6.5f. The discharge capacity values of AGT-90 are higher than PGT-90 for all the C-rates. Especially, the discharge capacities of AGT-90 are >300 mAh $g^{-1}$ up to 6C-rate. Thereafter, the discharge capacities decreased with the increase in C-rates and bestowed 100 mAh $g^{-1}$ at 50C-rate. The PGT-90 electrode could not be able to maintain the higher current beyond 1C-rate and kept reduced its capacities with the increase in the current up to the 50C. The weak van der Walls attraction in PVDF binder is ascribed to the capacity fade for PGT-90 during the cycling [21]. Therefore, as demonstrated by other researchers, in the current study also the aqueous based graphite anode with CMC/SBR binder had offered a higher electrochemical performance even at high C-rates [8, 22].

After ascertaining the lab scale results with ameliorated performance for AGT-90, the same composition has been used for large scale electrode fabrication as mentioned in section 6.2.2. The fabricated electrode is studied for half-cell analysis w.r.t. Li/Li$^+$ metal. The galvanostatic charge/discharge and cyclic stability profiles of AGT-90 electrode at 0.1C and 1C-rates for 1, 30 and 15 cycles are represented in Fig. 6.6. The first cycle reversible capacity (de-intercalation) of the electrode is 248 mAh g$^{-1}$, as given in Fig. 6.6a. The same has been continued for thirty cycles, and a specific discharge capacity of 258 mAh g$^{-1}$ (30th cycle) attained at 0.1C-rate, as seen in Fig. 6.6b. It is perceived that the large-scale electrode gave lower specific capacities than the lab scale electrode. The reason for lower capacity is attributed due to the presence of higher active material loading in the electrode [23]. In addition, the cycle number vs specific capacity profile at 1.0C-rate for 15 cycles was studied for AGT-90 as given in Fig. 6.6c. The obtained discharge capacities are lower in both the C-rates, even then they exhibited quite constant capacities without any capacity degradation for respective cycles as displayed in Fig. 6.6c.

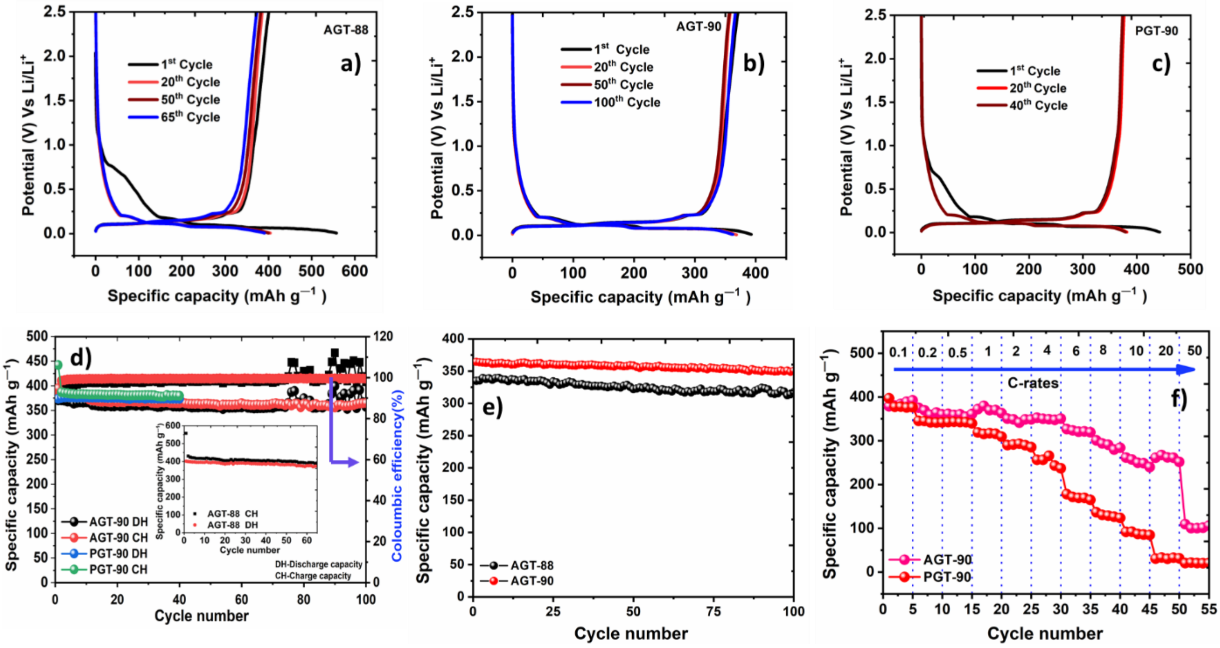

**Figure 6.5.** (a-c) Galvanostatic charge/discharge profiles and d) cyclic stability profiles of AGT-88, AGT-90, PGT-90 electrodes at 0.1C-rate for 65, 100 and 40 cycles, respectively. e) Cyclic stability of AGT-88 and AGT-90 at 1.0C-rate for 100 cycles, and f) rate capability of AGT-90 and PGT-90 electrodes from 0.1C to 50C-rate.

Following the half-cell analysis, the AGT-90 large scale graphite anode electrode along with NMC532 cathode (non-aqueous) was used to fabricate prismatic type PP full cells for 10 and 15 Ah capacities as shown in Fig. 6.7. The fabricated cells were tested at 0.05C and 0.5C-rate for three cycles and hundred cycles, respectively, in the voltage range between 3.0 and 4.2 V as shown in Fig. 6.7. At initial formation, both 10 and 15 Ah cells have yielded the discharge capacities of 10 and 17Ah for three cycles (Figure not shown).

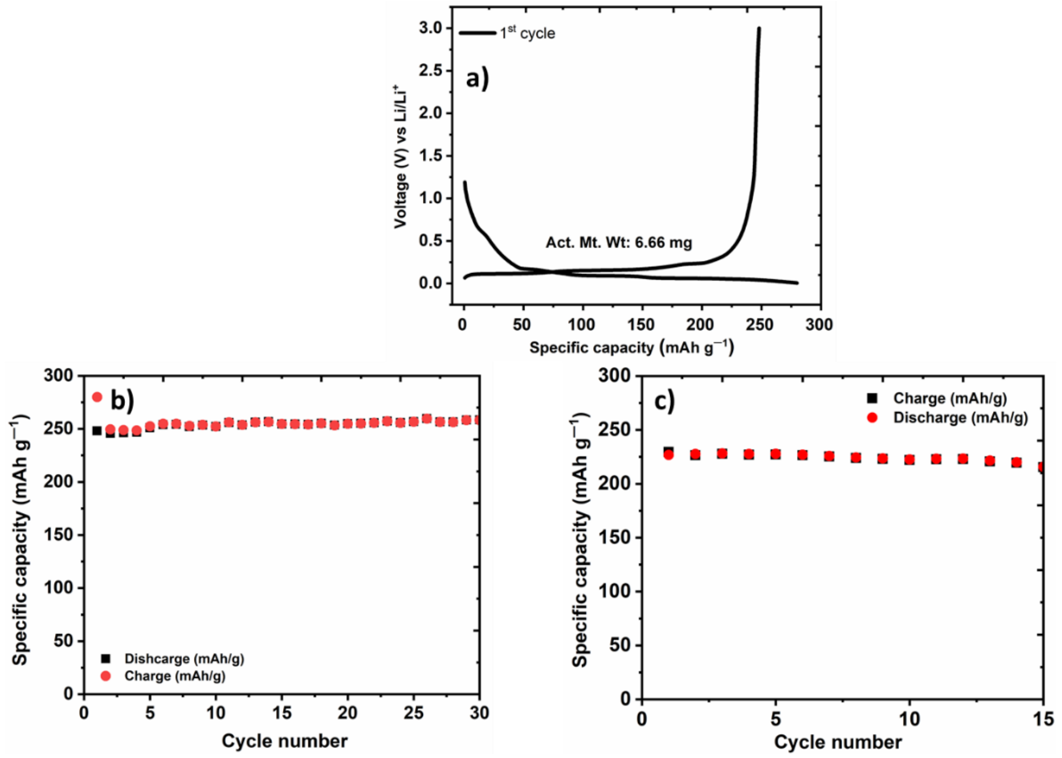

**Figure 6.6.** a) Galvanostatic charge-discharge of AGT-90 at first cycle, and cyclic stability profiles of AGT-90 b) at 0.1C-rate for 30 cycles and c) at 1C-rate for 15 cycles.

The coulombic efficiencies at initial cycle are found to be 87.7 and 93.3% for 10 and 15 Ah capacities, respectively. The more capacity for 15 Ah cells is due to the presence of excess active material present in the electrode. The cycle number vs capacity of aforementioned cells at 0.5C-rate for 100 cycles are mentioned in Fig. 6.7. The first cycle of cells had given the discharge capacities of 9 and 14 Ah for the cell capacities of 10 and 15 Ah, respectively. After the first cycle, the discharge capacities were started to reduce with an increment of cycles and the PP cell delivered the discharge capacities of 7 and 10 Ah with capacity retentions of 79 and 80%, respectively, at 100th cycle. Although the achieved capacities decreased with the increase in cycle number, it can be minimized by further modifications like secondary drying of electrodes, etc. The obtained electrochemical performances are also aligned with the existing literature reports of LIBs [24].

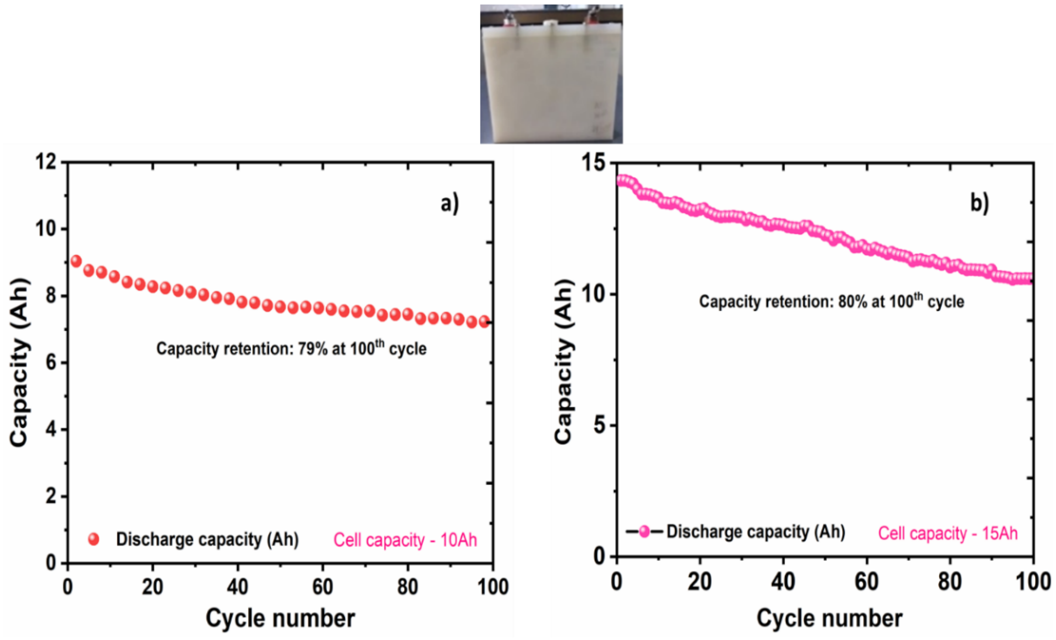

**Figure 6.7.** a, b) Cyclic stability of 10 and 15 Ah PP cells at 0.5C for 100 cycles.

To support the electrochemical performances, SEM studies were performed for as fabricated lab scale AGT-88, AGT-90 and large scale AGT-90 aqueous based electrodes, as depicted in Fig. 6.8. The different magnifications of lab scale AGT-88 (Fig. 6.8a-d), AGT-90 (Fig. 6.8e-h) and large scale AGT-90 (Fig. 6.8i-l) electrodes clearly revealed the difference in carbon percentage depositions, as seen in Fig. 6.8. The SEM images of AGT-88 lab scale electrode exhibited a quite low amount of carbon black deposition on graphite particles, and non-uniform dispersion in spite of higher carbon black percentage is obvious in corresponding electrode magnifications, as seen in Fig. 6.8a-d. But, the AGT-90 of lab and large-scale electrodes (Fig. 6.8e-l) exhibit the carbon black deposition homogenously on graphite particles for all the morphologies even though the used carbon black amount was less for either the cases. In fact, the carbon black is seen higher and covered homogeneously on graphite particles for the large-scale electrode (Fig. 6.8k and l), and this might have happened because of the difference in slurry mixing process. The lab and large-scale aqueous based electrodes also reveal that there are no crack or agglomerations on the surface of the electrodes (Fig. 6.8a, e and i). In addition, the fabricated electrodes had retained their original morphology i.e., potato shaped morphology for all the electrodes [25]. Henceforth, the electrochemical performance of AGT-90 electrode would have demonstrated improved electrochemical performances for either electrode fabrications in the current study. In general, for LIBs, AGT-90 electrode is favoured than AGT-88, because of the presence of higher active material in AGT-90 electrode.

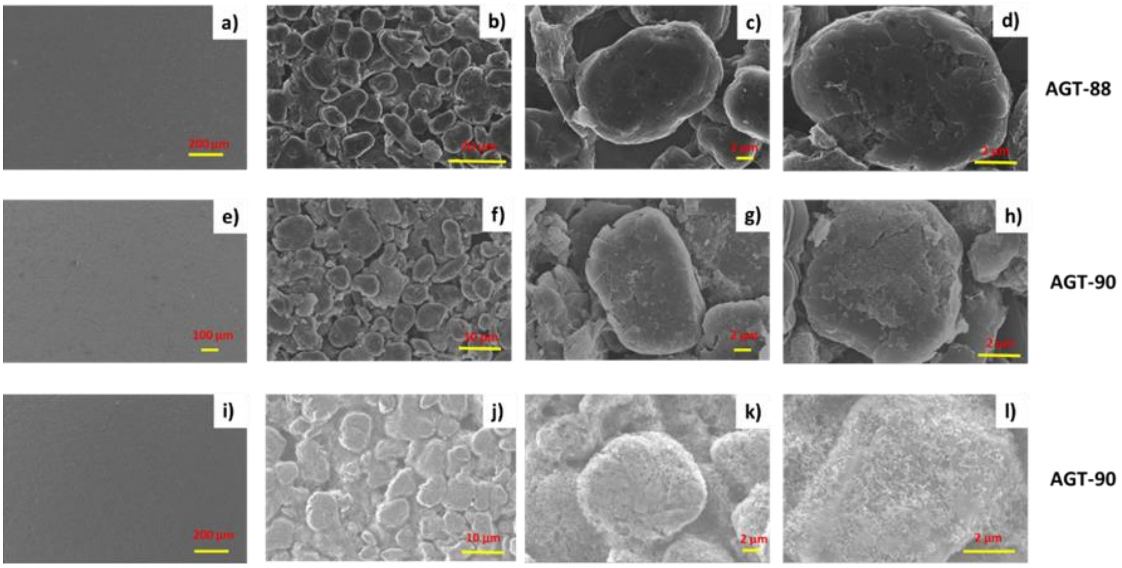

**Figure 6.8.** SEM morphologies of as fabricated a-d) AGT-88, e-h) AGT-90 and i-l) large scale AGT-90 electrodes.

Full cell analysis is performed by pouch cell fabrication for LFP vs graphite electrodes. For this, galvanostatic charge/discharge and cyclic stability profiles of full cells comprised non-aqueous LFP cathode and aqueous large-scale graphite anode (AGT-90) were studied in the voltage range of 2.7-3.65 V at 0.05C and 0.1C-rate for 10 and 50 cycles, as depicted in Fig. 6.9. The fabricated cell at 0.05C exhibited the initial charge/discharge capacities of 125 and 100 mAh g$^{-1}$ with coulombic efficiency of 80%, as represented in Fig. 6.9a. The discharge capacity of 100 mAh g$^{-1}$ is stable for all ten cycles as seen in Fig. 6.9b. Afterwards, the cell displayed a reasonable specific capacity of >90 mAh g$^{-1}$ at 0.1C with capacity retention of 85% for 50 cycles, as shown in Fig. 6.9c. The fabricated aqueous graphite electrode (AGT-90) might be stable and it fetched the reasonable performance for both NMC532 and LFP full cells. Therefore, these cells can cut down the cost partially by employing aqueous binder for graphite anode with various cathode materials in the LIB manufacturing process.

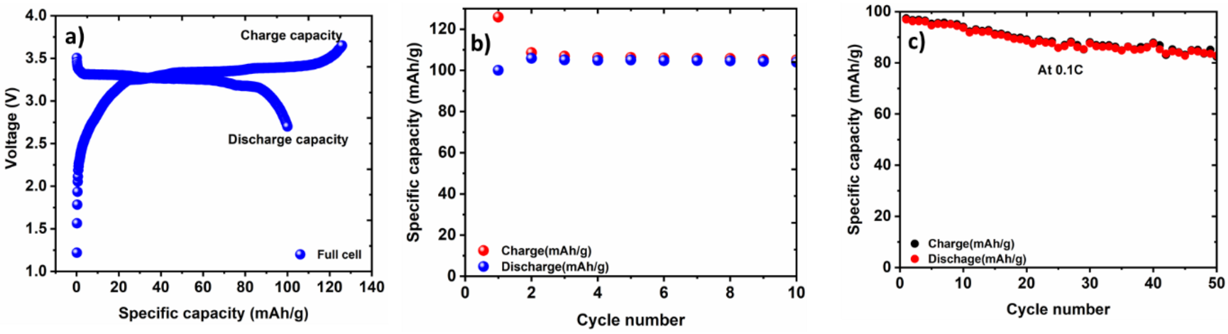

**Figure 6.9.** a) Galvanostatic charge/discharge capacity profiles of LFP/Graphite cell at 0.05C-rate, and cyclic stability profiles of LFP/Graphite cell b) at 0.05C for 10 cycles and c) at 0.1C-rate for 50 cycles.

Figure 6.10 displays the cycle number vs specific capacity of AGT-90 small scale electrode at room temperature (RT) and 50 $^{O}$C at 0.1C-rate for 75 cycles. The temperature setup for charge/discharge is also shown in the inset of Fig. 6.10. The initial discharge capacities are found to be 370 and 359 mAh g$^{-1}$ with coulombic efficiencies of 93% and 81%, respectively, at RT and 50 $^{O}$C conditions. The continuation cycles for either of the electrodes have demonstrated the steady performance with reversible capacities of 365 and 358 mAh g$^{-1}$ at the 75th cycle. The attained capacity retentions at the end cycles are 98 and 100%, respectively. Although the discharge capacities at RT are higher than those at 50 $^{O}$C, the actual difference is ~10 mAh g$^{-1}$ for each respective cycle. In addition, the coulombic efficiency resulted at 50 $^{O}$C is comparatively higher than that at RT one. The results at 50 $^{O}$C are expected to show capacity fade with the increase in cycles because of a raise in the internal resistance, but in contrast to that, it displayed a stable performance as equivalent to the RT condition. Therefore, this study even discloses that the aqueous based cells can be used at high temperature conditions like 50 $^{O}$C and more for LIB applications [26].

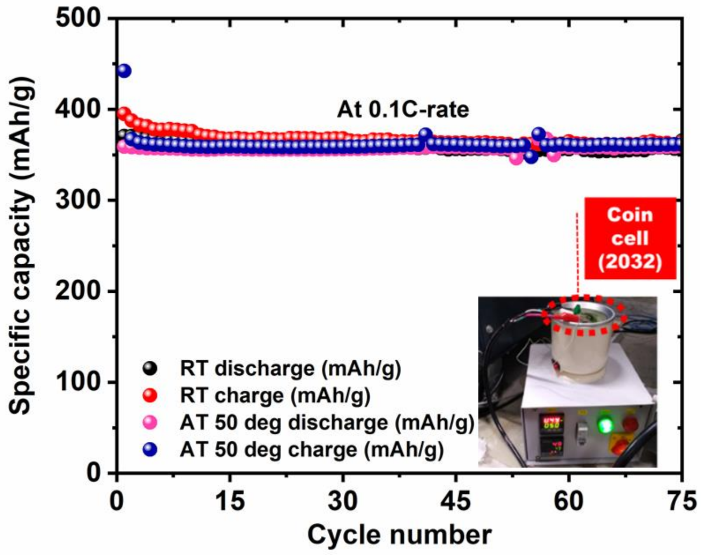

**Figure 6.10.** Cyclic stability of AGT-90 for RT and 50 $^{O}$C conditions at 0.1C-rate for 75 cycles.

The impedance analysis is demonstrated for as fabricated AGT-90 (small scale) electrode using the Nyquist plot, as depicted in Fig. 6.11. The plot exhibits a single depressed semi-circle along with $45^{O}$ slope line called Warburg diffusion for the electrode [27]. The charge transfer resistance ($R_{ct}$) of AGT-90 is smaller, as noticed from Fig. 6.11. The Warburg region is also seen normal for AGT-90 electrode. Hence, the small $R_{ct}$ value reflects that the aqueous based AGT-90 is conducive for better cycling, which also implies that the lithium diffusion kinetics is much faster in AGT-90. Hence, AGT-90 had exhibited better electrochemical performances with high-rate capability in the present study [28].

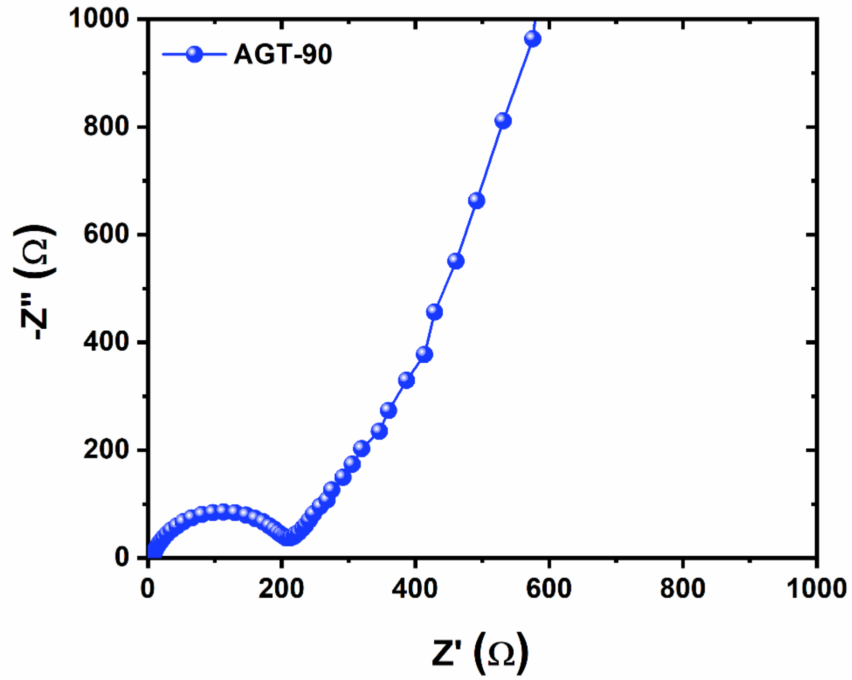

**Figure 6.11.** The Nyquist plot of as fabricated AGT-90 electrode.

## 6.4. Conclusions

Herein, we investigated the effect of CMC/SBR aqueous binder on graphite anode for the applications of LIB. In this work, electrode fabrication has been done in lab scale and large-scale methods. Graphite anode in lab scale has shown the electrochemical performance close to the theoretical capacity of graphite at 0.1C-rate. Moreover, even at 1C-rate, graphite electrode displayed good cyclic stability for 100 cycles. The large scale coated aqueous graphite electrode studied in full cell configuration with NMC532 cathode had shown high and stable specific capacity and cyclic stability profiles. The prismatic cells of 10 and 15 Ah delivered more than 65% rated capacity with the capacity retentions of ≥ 80% for 100 cycles. The obtained capacity retention is almost equivalent to the commercial cells. In addition, the electrochemical performances of the fabricated electrodes observed at high temperature are almost equivalent to those resulted at room temperature. Hence, the electrodes fabricated in this study with aqueous binder would reduce the cost of the lithium-ion batteries and would also become environmental friendly. Thus, aqueous based electrodes could be implemented in commercial line of LIBs.

## 6.5. References

[1] J. Lu, Z. Chen, F. Pan, Y. Cui, K. Amine, *Electrochemical Energy Reviews* **2018**, 1, 35-53.

[2] R. Sahore, D. L. Wood III, A. Kukay, K. M. Grady, J. Li, I. Belharouak, *ACS Sustainable Chem. Eng*. **2020**, 8, 3162-3169.

[3] D. Bresser, D. Buchholz, A. Moretti, A. Varzi, S. Passerini, *Energy Environ. Sci.* **2018**, 11, 3096-3127.

[4] V. V. N. Phanikumar, B. V. Appa Rao, K. V. Gobi, R. Gopalan, R. Prakash, *ChemistrySelect* **2020**, 5, 1199-1208.

[5] S. R. Sahu, V. R. Rikka, P. Haridoss, R. Gopalan, R. Prakash, *Energy Technol*. **2019**, 1900849.

[6] H. Chen, M. Ling, L. Hencz, H. Y. Ling, G. Li, Z. Lin, G. Liu, S. Zhang, *Chemical Reviews* **2018**, 118 (18), 8936-8982.

[7] C. Mao, M. Wood, L. David, S. J. An, Y. Sheng, Z. Du, H. M. Meyer III, R. E. Ruther, D. L. Wood III, *J. Electrochem. Soc.* **2018**, 165 (9) A1837-A1845.

[8] F. Jeschull, D. Brandell, M. W. Mehrens, M. Memm, *Energy Technol*. **2017**, 5, 2108-2118.

[9] H. Buqa, M. Holzapfel, F. Krumeich, C. Veit, P. Novak, *J. Power Sources* **2006**, 161, 617-622.

[10] J. H. Lee, S. Lee, U. Paik, Y. M. Choi, *J. Power Sources* **2005**, 147, 249-255.

[11] J. H. Lee, U. Paik, V. A. Hackley, Y. M. Choi, *J. Electrochem. Soc.* **2005**, 152, A1763.

[12] J. Chong, S. Xun, H. Zheng, X. Song, G. Liu, P. Ridgway, J. Q. Wang, V. S. Battaglia, *J. Power Sources* **2011**, 196, 7707-7714.

[13] C. C. Wu, C. C. Li, *ACS Sustainable Chem. Eng.* **2020**, 8, 6868−6876.

[14] E. Pohjalainen, O. Sorsa, J. Juurikivi, T. Kallio, *Energy Technology* **2016,** *4*, 470-472.

[15] P. S. Salini, S. V. Gopinadh, A. Kalpakasseri, B. Jhon, T. Mercy, *ACS Sustainable Chem. Eng.* **2020**, 8, 4003-4025.

[16] A. V. Sorokin, V. A. Kuznetsov, M. S. Lavlinskaya, *Polym.Bull.* **2020**.

[17] R. Wang, L. Feng, W. Yang, Y. Zhang, Y. Zhang, W. Bai, B. Liu, W. Zhang, Y. Chuan, Z. Zheng, H. Guan, *Nanoscale Research Letters* **2017**, 12:575.

[18] N. Cuesta, A. Ramos, I. Cameán, C. Antuña, A. B. García, *Electrochim. Acta* **2015**, 155, 140-147.

[19] V. R. Rikka, S. R. Sahu, A. Chatterjee, P. V. Satyam, R. Prakash, M. S. R. Rao, R. Gopalan, G. Sundararajan, *J. Phys. Chem. C* **2018**, 122, 50, 28717-28726.

[20] H. Huo, Z. Lin, S. Guo, J. Shao, G. Zhang, Q. Wang, *New J. Chem*. **2017**, 41, 14228.

[21] S. J. Rezvani, M. Pasqualini, A. Witkowska, R. Gunnella A. Birrozzi, M. Minicucci, H. Rajantie, M. Copley, F. Nobili, A. Di. Cicco, *Applied Surface Science* **2018**, 435, 1029-1036.

[22] D. Shin, H. Park, U. Paik, *Electrochem commun*. **2017**, 77, 103-106.

[23] J. Liang, H. Sun, Z. Zhao, Y. Wang, Z. Feng, J. Zhu, L. Guo, Y. Huang, X. Duan, *Science* **2019**, 19, 728-736.

[24] Z. Du, K. M. Rollag, J. Li, S. J. An, M. Wood, Y. Sheng, P. P. Mukherjee, C. Dan, D. L. Wood III, *J. Power Sources* **2017**, 354, 200-206.

[25] X. Zheng, Q. Shi, Y. Wang, V. S. Battaglia, Y. Huang, H. Zheng, *Carbon* **2019**, 148, 105-114.

[26] F. Zou, A. Manthiram, *Adv. Energy Mater*. **2020**, 2002508.

[27] V. V. N. Phanikumar, V. R. Rikka, B. Das, R. Gopalan, B. V. Appa Rao, R. Prakash, *Ionics* **2019**, 25, 2549-2561.

[28] Y. Li, Q. Zeng, I. R. Gentle, D. W. Wang, *J. Mater. Chem. A* **2017**, 5, 5460.

# Chapter 7

# Summary and conclusions

## 7. Summary and conclusions

The present thesis consists of seven chapters. Chapter-1 describes the overall introduction, focused binder introduction, scope and objectives of the study. Chapter-2 describes the methodology and in detailed characterization required for the thesis work. Chapters-3 to 6 discussed about the usage of artificial and natural polymers as aqueous binders for the anode materials of LIBs. Chapter-7 summarizes and concludes the present work.

Chapter-3 discussed about the fabrication and electrochemical performance of LTO anodes using the aqueous binders i.e., PVA and Na-Alg (control experiments with PVDF) and demonstrated the cyclic and rate capability studies against $Li/Li^+$. The capacity of LTO anode decreased with the increase in binder concentration. The LTO electrodes with aqueous binders have shown lower charge transfer resistance, less polarization behaviour than the corresponding electrode prepared with PVDF binder. Among the three electrodes, LTO electrode with PVA binder exhibited better and long cyclic stability than the other electrodes. Although LTO/Na-Alg electrode exhibited lower electrochemical performance than LTO/PVA, still the obtained performance is as equivalent to the non-aqueous based LTO/PVDF anode. Hence, aqueous based binders are beneficial in terms of efficiency, cost, eco-friendly and safety for LIB applications.

For Chapter-4, we have reported the graphite electrode using a natural polysaccharide TKP binder as an alternative to the conventional non-aqueous PVDF binder for the application in LIBs. For this, graphite electrodes with various TKP binder contents (3 to 5 wt.%) as well as 4 wt.% PVDF binder were prepared and characterized systematically. The coated electrodes retained the original morphology of the active material during the usage for as much as 500 cycles confirming that the aqueous TKP binder did not react to active material. Among the aqueous based electrodes, the graphite anode with 4 wt.% binder demonstrated an initial capacity of 326 mAh $g^{-1}$ at 1C-rate with an excellent cycling stability up to 500 cycles, whereas the PVDF based electrode delivered an initial capacity of 103 mAh $g^{-1}$ under similar conditions. Moreover, the aqueous based electrode showed a specific capacity of 55 mAh $g^{-1}$ at 50C-rate, while the non-aqueous based electrode displayed only 20 mAh $g^{-1}$ for the same rate. The better performance of the aqueous based electrodes could be due to the branched chemical structure of binder with more hydroxyl bonding sites and high surface charge stability of the slurry. Hence, aqueous based electrodes displayed better performance than the non-aqueous based electrodes.

Chapter-5 described the effect of Fenugreek (FG) natural polymer as an aqueous binder on graphite anode for LIBs. For the first time the use of Fenugreek binder (FG) as an aqueous binder for the graphite anode was studied. The graphite electrodes have been fabricated using 4, 5 and 6 wt.% of FG binder and their electrochemical performances were studied. Among all the electrodes, the electrode with 6 wt.% binder content shows the best electrochemical performance. It exhibits the reversible capacities of >220 mAh $g^{-1}$ at 1C for 175 cycles and noticed the stable specific capacities by increasing the cycle number up to 500 cycles. The obtained capacity is much better than the conventional PVDF binder (first cycle: 103 mAh $g^{-1}$ at 1C). Besides, the fabricated FG/Graphite electrode exhibits a discharge capacity of >300 mAh $g^{-1}$ at 10C. In addition, the effect of intra/inter hydrogen bonding of fenugreek binder has been described by varying the binder concentration for the graphite anode. Raman analysis also discloses the graphite electrode with high degree graphitization as well as low disorder, which is prominent for cyclic stability. Electrochemical impedance studies exhibited that the graphite electrode with high binder percentage possessed the lowest charge transfer resistance even after charge/discharge of 500 cycles at 1C-rate. Comprehensively, the better performance of the aqueous binder-based graphite electrode can be ascribed to the better solubility, high lithium-ion conductivity and improved wettability of the FG binder. Hence, FG aided as a crucial binder in the electrode fabrication of graphite anode for the application of lithium-ion batteries.

In Chapter-6, we investigated the effect of CMC/SBR aqueous binder on graphite anode for the applications of LIB. In this work, electrode fabrication has been done in lab scale and large-scale methods. Graphite anode in lab scale has shown the electrochemical performance close to the theoretical capacity of graphite at 0.1C-rate. Moreover, even at 1C-rate, graphite electrode displayed good cyclic stability for 100 cycles. The large scale coated aqueous graphite electrode was studied in full cell configuration with NMC532 cathode. The prismatic cells of 10 and 15 Ah delivered more than 85% rated capacity with the capacity retentions of ≥ 80% for 100 cycles. The obtained capacity retention is almost equivalent to the commercial cells. Hence, the electrodes prepared with aqueous binder would reduce the cost of the lithium-ion batteries and also environmental friendly. Thus, aqueous based electrodes could be implemented in commercial line of LIBs.

Finally, the electrochemical performance values of aqueous binders which were used for anode materials of this thesis are compared with literature reported values and the same has been provided in Table 7.1.

**Table 7.1.** Electrochemical performance values of aqueous binders used for anode materials.

| S.No | Binder | Material | C-rate | Theoretical specific capacity (mAh $g^{-1}$) | Obtained specific capacity (mAh $g^{-1}$) | Reported maximum result (mAh $g^{-1}$) [Ref.] |
|---|---|---|---|---|---|---|
| 1 | PVA/Na-Alg | $Li_4Ti_5O_{12}$ | 1.0 | 175 | 140/110 | 150 [1] |
| 2 | TKP | Graphite | 1.0 | 372 | 326 | 360 [2] |
| 3 | FG | Graphite | 1.0 | 372 | 220 | 360 [2] |
| 4 | CMC/SBR | Graphite | 1.0 | 372 | 360 | 360 [2] |

Hence, the aqueous binders have been investigated systematically for LTO/Graphite anodes in terms of half and full cell configurations. The obtained electrochemical performance is as equivalent to the non-aqueous based electrode with high capacity, rate capability and cyclic stability. Thus, the aqueous binders laid the new path by the increase in energy density, reducing the manufacturing cost and eco-friendliness for LIB applications. These binders can be further developed by cross linking or grafting to enhance the properties like amorphocity, adhesion-cohesion, conductivity, swelling, thermal and chemical stabilities. By achieving the aforementioned properties, probably these binders will be further robust and would play a vital role for LIB applications.

## 7.1. References

[1] D. V. Carvalho, N. Loeffler, G. T. Kim, M. M. Margret, W. Mehrens, S. Passerini, *Polymer* **2016**, 8:276.

[2] L. Chai, Q. Qu, L. Zhang, M. Shen, L. Zhang, H. Zhenga, *Electrochim. Acta* **2013**, *105, 378-383.*

## LIST OF PUBLICATIONS & BIO-DATA

### Publications in Peer-Reviewed/Refereed International Journals

1) A novel and sustainable tamarind kernel powder based aqueous binder for graphite anode in lithium-ion batteries, **V.V.N. Phanikumar**, K. V. Gobi, B. V. Appa Rao, R. Gopalan and R. Prakash, *ChemistrySelect*, **2020**, 5, 1199 –1208, **DOI: 10.1002/slct.201903374**

2) Investigation on polyvinyl alcohol and sodium alginate as aqueous binders for lithium titanium oxide anode in lithium-ion batteries, **V.V.N. Phanikumar**, V. R. Rikka, B. K. Das, B.V. Appa Rao, R. Gopalan and R. Prakash *Ionics*, June 2019, Volume 25, Issue 6, pp 2549–2561**,** ***DOI:*** **10.1007/s11581-018-2751-8**

3) Effectual investigation of fenugreek powder as an aqueous binder for graphite anode in lithium-ion batteries, **V.V.N. Phanikumar**, K.V. Gobi, R. Gopalan and R. Prakash. **(To be communicated)**

4) A study of large-scale graphite anode fabrication using aqueous CMC/SBR binder for lithium-ion battery applications, **V.V.N. Phanikumar**, K.V. Gobi, R. Gopalan and R. Prakash. **(To be communicated)**

5) Tamarind seed skin derived fiber like carbon nanostructures as novel anode material for lithium-ion battery, **V.V.N. Phanikumar**, S. R. Sahu, R. Prakash, R. Gopalan and B.K.Das *Ionics*, November 2018, Volume 24, Issue 11, pp 3413–3421; ***DOI***: **10.1007/s11581-018-2498-2 (Other work)**

# BIO-DATA

**V. V. N. Phanikumar**
C/o. M. Ranganathan,
Plot.no. 3/1,
Devi Karumari Amman Nagar,
Velachery, Chennai.
Tamil Nadu- 600042, India.
Email: vphani.edu@gmail.com
Mobile: 9003208419 / 6374084290

---

**Education:**

**Dec-2013 to Present** **Ph.D. Thesis submitted**
**NIT-Warangal**
**Research scholar in Department of Chemistry**
**Thesis title: "Investigation on natural and synthetic polymers as aqueous binder for anodes of lithium-ion batteries."**

**Course Work :** As a part of PhD programme, mandatory Course Work have been completed on the following courses.

1. Advanced Analytical Methods
2. Surface Analytical Techniques
3. Advanced Electrochemical Methods
4. Electrochemical Energy Systems
5. English for Scientific Communication

Cumulative Grade Obtained: **A**

**Nov 2007- Nov 2009** **M.Sc.** Organic Chemistry, Andhra University- **75.70%**

**Apr 2005- Mar 2007** **B.Sc.** Maths, Physics and Chemistry, Andhra University**- 65.52%**

## Experience:

**Nov 2017 to till date** Project. Scientist -B in CAEM, ARCI, Chennai

**May 2013 to Oct 2017** Senior /Junior Fellowship in CAEM, ARCI, Chennai

| | |
|---|---|
| **Aug 2011 to Apr 2013** | Project Associate in CAEM, ARCI, Chennai |
| **May 2010 to Jul 2011** | Jr. Chemist in Quality Control Department- in Arch Pharma Labs, Sangareddy, Medak Dist. |
| **Nov 2009 to May 2010** | Associate in K. Ramachandra Transmissions and Pvt. Ltd, , Hyderabad. |

**Awards / Honours**

1) Received the **'Best Poster Award'** for the poster presentation on " Effect of polyvinyl alcohol and sodium alginate aqueous binders on lithium titanium oxide anode for lithium-ion batteries" at National conference on frontiers in chemical sciences and technologies (FCST) held at NIT-Warangal ,Warangal during 28 -29th January, 2016.
2) V.V.N. Phanikumar, B.V. Appa Rao, K.V. Gobi, R. Gopalan, and R. Prakash, Tamarind kernel powder as a novel aqueous binder for graphite anode in lithium-ion batteries, December 16- 8, 2019, IIT-Roorkee. (**Best Poster Award**)

**Conference / Workshop Attended**

1) V.V.N. Phanikumar, B.V. Appa Rao, K.V. Gobi, R. Gopalan, and R. Prakash, Tamarind kernel powder as a novel aqueous binder for graphite anode in lithium-ion batteries, December 16- 8, 2019, IIT-Roorkee.
2) V.V.N. Phanikumar, B.V. Appa Rao, R. Gopalan and R. Prakash, Polyvinyl alcohol and sodium alginate as alternate green binders of lithium titanium oxide anode for lithium-ion batteries.The 3rd National conference on Materials for energy conversion and storage, 8-20th October, 2018, IIT-BHU, Varanasi.
3) National conference on frontiers in chemical sciences and technologies (FCST) held at NIT-Warangal, 28 -29th January 2016, Warangal.
4) Oral presentation on Investigation on $LiFePO_4/C$ cathode prepared by eco-friendly polyvinyl alcohol (PVA) binder for lithium-ion battery at NMD-ATM, 13-16th November 2015, Coimbatore.
5) One day workshop on “Emerging applications of laser technology in manufacturing” held at VIT University, 13th February 2015, Vellore.